UNIVERSITY OF CALIFORNIA SAN DIEGO

Dark Matter Direct Detection via Multiphonon Excitations in Crystal Targets

A dissertation submitted in partial satisfaction of the
requirements for the degree Doctor of Philosophy

in

Physics

by

Ethan Phillip Gonzalez Villarama

Committee in charge:

Professor Tongyan Lin, Chair
Professor Monica Allen
Professor Stefan Llewellyn Smith
Professor Aneesh Manohar
Professor Vivek Sharma

2023

The Dissertation of Ethan Phillip Gonzalez Villarama is approved, and it is acceptable in quality and form for publication on microfilm and electronically.

University of California San Diego

2023

DEDICATION

To the people that I love and wouldn't be here without.

EPIGRAPH

And I get this feeling all the time that I'm an ape trying to put two sticks together, so I always feel stupid. Once in a while, though, the sticks go together on me and I reach the banana.

Richard Feynman

TABLE OF CONTENTS

LIST OF FIGURES

LIST OF TABLES

PREFACE

The main scope of my work throughout graduate school has focus on direct detection of sub-GeV dark matter in crystals, which is detailed in chapters 3 and 4. Chapter 5 studies a wildly different dark matter candidate, primordial black holes, which I have not worked on in quite some time. Though quite separate from my current work, I've chosen to leave this chapter in the text since it contributed to my growth as a graduate student. This chapter and various related subsections within the text are not necessary to understand overall story of dark matter direct detection in crystals. The reader may treat these sections as a sort of "bonus" to enjoy if they would like to.

ACKNOWLEDGEMENTS

As I sit at my desk editing the last few slides of my defense presentation, my parents arrive at my apartment with some gourmet donuts and a lychee green boba tea. I haven't been too communicative with them during the busy times in grad school especially these last few months, yet here they are, my greatest and most loving supporters. I don't think I could ever articulate the depth of gratitude that I feel for my family. I am certain that I could never have gotten this far without the comfort of knowing that they would be there for me no matter what. To my parents and my little brother, thank you for being my home.

Never in my life have I met someone who has understood me quite like Brian. Going through the trials of grad school and life together has been an immeasurably important and fulfilling experience that I cannot imagine having lived without. To be where and who I am today would have otherwise been impossible. Let me be clear, the profound positive impact our friendship has had on the person I am, the way I think, and how I interact with the world cannot be overstated. You would have to be a particularly remarkable individual to brave the chaos, uncertainty, and madness of reality without a "Brian" in your life. Down rabbit holes and through forests with magical mushrooms, I'm sure a myriad of adventures awaits us.

Natalie, my ex-neighbor, graduate school never felt quite the same after you moved away from just 25 feet down the hall. I was so lucky to have a friend like you close by during the early grad school years. Spending late nights chilling at your place are some of my fondest memories and definitely got me through classes, quals, and whatever other stresses of life. I can't wait until we live nearby again one day (or if not, I'll find my way onto a plane).

Shirell, thanks for being here for me all of these years. Every time work or personal life has hit me like a brick to the face, I've always had you. Never have I felt truly alone or hopeless knowing that you're just a phone call or a few hour drive away. Doubt and fear have certainly been themes throughout my grad school experience and somehow you've always been able to show me that I'm doing alright. Nowhere besides my your place (and my parents') have I felt truly at home. Underneath the starry Catalina sky lying down on those wooden tables chatting

late into the night is one of my first memories of us becoming real friends, and I'm forever grateful for that moment and the journey that it led us down. Despite whatever hardships we face, I know that you're someone that will always belong in my heart. Each day you're a part of is a day well spent and I hope that there are many more to come. So, whenever you come across this, this is a promise to see you soon.

Rory, I remember I used to write you fun little poems and I haven't in a while, so let me give it a shot. I call this poem/short story "Panera":

"Do you want to go to Panera?" you exclaim
Ecstatically I reply, "A panadería? What's the name?"
"Eh?" you question as you frown with confusion
"Zany as always," I chuckle, unaware of my delusion
"No, no, I said *Panera*," you retort, realizing my mistake
"Unless..?" as you laugh, an idea taking shape
"To Mexico?" I implore with a grin on my face
So a misunderstanding took us south, to sin, a new place

Okay, I hope you liked it, I think it depicts our friendship quite accurately. I don't know if there's much more I can convey here that I haven't told you so many times already. I'm sure you know how important you are to me and how happy I am to have you in my life.

Fatima, where would I be without you. Seriously, it's actually so sick that we met and became friends. I haven't typically been one to believe in any sort of fate, but I must admit that the astronomically improbable sequence of events that led us here does make me feel a little something. Speaking of fate, Jiraiya, sensei of the chosen ones, once said that "wherever someone thinks of you, that's where home is." So wherever I end up, you'll always have a place. Thanks for being so loving and supportive of me.

Georgia, if I had to go back in time and pick out a butterfly effect moment that shaped my life as a whole up until now, it probably would have something to do with you. I couldn't have gone through my first years in grad school without you and I'm grateful for all of those memories. I'm really glad that we managed to become friends in the end. I can't wait until you

get to finish grad school and get the chance to write sappy acknowledgements too! I'll be here for you always, like you've been for me.

Patricia, Chris, I wish I could've moved in with you back when you lived together so long ago now. I loved all of those times I'd show up to your place with little notice and we'd just chill and talk for hours. You really understand me in funny little ways that I have difficulty describing but nonetheless feel very deeply. You know how much I love you and thanks for always being there for me, I couldn't have done it without you.

I would like to also thank Angela, Exequiel, Pranati, Kat, Emma, AJ, Max, Mac, Evgueni, Ahmed, Avaneesh, Dani, and Brennan for being such supportive friends. Thanks also to all of my family around the globe that I love and appreciate spending time with even if only once every few years. Unfortunately, I cannot keep writing paragraphs for everyone that has profoundly impacted my life and grad school experience, or these acknowledgements would exceed the length of the main text. It is possible that I have missed some people as I'm writing this section in a tired post-defense haze, so just know that I am deeply thankful to everyone that's been there for me despite my current lack of conscious recollection.

I would also like to thank the people that I've spent my time working with. First, my advisor Tongyan, who is undoubtedly the best advisor I could have asked for. It has been a pleasure working with you, thanks for being so patient and supportive of me and helping me become the scientist I am today. I'm sure you know that at times, graduate school was quite an arduous experience for me, and I'm so thankful that you were able to guide me through it. Thanks for listening to and being receptive of all of my goofy ideas, both related and unrelated to physics. I can't wait to come back and chat about wherever our lives take us from here.

Vivek, you have been an incredible mentor and I am extremely glad that I got assigned to teaching for you all of those years ago. I wouldn't be the teacher I am today without your support and I'm happy that we got to help all of those students together. To the rest of my committee, thanks for being so easy to schedule with. To the post-docs I've written papers with, Simon, Mukul, Chia-Hsien, and Jonathan, you were all very enjoyable to work with and really made my

research experience great.

Chapter 3, in full, is a reprint of the material as it appears in Brian Campbell-Deem, Simon Knapen, Tongyan Lin, and Ethan Villarama, Dark matter direct detection from the single phonon to the nuclear recoil regime, Phys.Rev. D **106** (2022) no.3, 036019. The dissertation author was one of the primary investigators and authors of this paper.

Chapter 4, in full, is a reprint of the material as it appears in Tongyan Lin, Chia-Hsien Shen, Mukul Sholapurkar, and Ethan Villarama, Anharmonic effects in nuclear recoils from sub-GeV dark matter (e-print: 2309.10839 [hep-ph]), which is being prepared for journal submission. The dissertation author was one of the primary investigators and authors of this paper.

Chapter 5, in full, is a reprint of the material as it appears in Jonathan Kozaczuk, Tongyan Lin, Ethan Villarama, Signals of primordial black holes at gravitational wave interferometers, Phys.Rev. D **105** (2022) no.12, 123023. The dissertation author was one of the primary investigators and authors of this paper.

VITA

2017 B.S. in Physics, California State University Los Angeles, Los Angeles, CA

2023 Ph.D. in Physics, University of California San Diego, La Jolla, CA

PUBLICATIONS

Brian Campbell-Deem, Simon Knapen, Tongyan Lin, Ethan Villarama, Dark matter direct detection from the single phonon to the nuclear recoil regime, Phys.Rev. D **106** (2022) no.3, 036019, arXiv: 2205.02250 [hep-ph]

Jonathan Kozaczuk, Tongyan Lin, Ethan Villarama, Signals of primordial black holes at gravitational wave interferometers, Phys.Rev. D **105** (2022) no.12, 123023, arXiv: 2108.12475 [astro-ph]

ABSTRACT OF THE DISSERTATION

Dark Matter Direct Detection via Multiphonon Excitations in Crystal Targets

by

Ethan Phillip Gonzalez Villarama

Doctor of Philosophy in Physics

University of California San Diego, 2023

Professor Tongyan Lin, Chair

In dark matter direct detection experiments, the free nuclear recoil description breaks down as the de Broglie wavelength of dark matter approaches the typical atomic spacing of the target material. In this work, we investigate the particular case of scattering off of crystal targets, whose collective excitations are well understood as phonons. As experimental energy thresholds decrease, it becomes increasingly important to understand the response of targets to energy depositions below the nuclear recoil scale. For dark matter masses lighter than 1 MeV, the scattering rate is dominated by single phonons, while at masses larger than 100 MeV, we expect the scattering to approach the free nuclear recoil result. Starting from the phonon formalism in the harmonic crystal approximation, we perform the first calculations of scattering

rates in the intermediate 1-100 MeV mass regime where multiphonon process dominate and demonstrate how the multiphonon response smoothly approaches free nuclear recoil. We then drop the harmonic approximation and calculate possible corrections to the scattering rates due to crystal anharmonicity. We find these anharmonic corrections to be large at small dark matter masses $\sim$ MeV and large experimental thresholds $\sim$ 100 MeV, but approach the harmonic result as the DM mass increases.

Chapter 1

Introduction to Dark Matter

1.1 History and Evidence of Dark Matter

The matter that we see in our day to day lives is made up of mostly baryons and electrons, whose interactions are well known within the Standard Model. Despite being all that we have directly observed terrestrially, it is well-established that baryonic matter consists of only a small fraction of the total matter in the universe. In order to explain various astrophysical and cosmological phenomena, overwhelming evidence suggests that there must exist some other form of matter at a roughly 5 to 1 ratio to ordinary matter. Everything that makes up this "other" matter has thus far remained elusive to experiments and is appropriately dubbed dark matter. Uncovering the exact nature of dark matter continues to be one of the most compelling challenges in modern physics.

The strong evidence for the existence of dark matter began in the 1930s with Fritz Zwicky's observations of galaxy velocities within the Coma Cluster [1]. The velocity of individual galaxies within the cluster must be related to the total cluster mass via Newtonian gravity and the virial theorem, which tells us that the average kinetic and potential energy of a gravitationally bound system are related by

$$\langle T \rangle = -\frac{1}{2}\langle V \rangle. \tag{1.1}$$

This can be recast in terms of root-mean-squared velocity, total cluster mass, and cluster radius

$$\sqrt{\langle v^2 \rangle} \sim \sqrt{\frac{G_N M}{R}}, \tag{1.2}$$

where G_N is Newton's gravitational constant. Zwicky measured the velocity dispersion of the galaxies and estimated the cluster mass by observing the galactic luminosities and inferring the number of stars. Upon making these measurements, Zwicky found a quite peculiar result, which was that the root-mean-squared velocity predicted by the total luminous mass of the cluster was around 20 times smaller than the measured value. Zwicky concluded that if these measurements were correct, there must exist a large amount of unseen matter holding the cluster together. This missing matter became known as dark matter, which is now the primary candidate for explaining a large body of astrophysical and cosmological data.

The next historically important piece of evidence came in the form of velocity distributions of stars within galaxies. Newtonian gravity once again allows us to predict the velocity of objects given some mass distribution. In the case of typical galaxies, the luminous matter distribution is roughly constant outside of the galactic center, which corresponds to a galactic rotation curve that scales as

$$v(r) \propto \frac{1}{\sqrt{r}}. \tag{1.3}$$

This suggests that the velocity of stars inhabiting spiral arms distant from the galactic center should obey this speed drop with radius relationship if luminous matter is the bulk of the total matter distribution. However, measurements in the 1970s by Vera Rubin and company originally on the Andromeda galaxy [2], but later on many different spiral galaxies [3], show that the large radius tail of the stellar velocity distribution is actually constant. The original result by Rubin is depicted in Fig. 1.1. Since then, the universality of flat velocity tail has only been confirmed with greater precision and sample size. These measurements imply that the true matter distribution is significantly different than what one would expect from only stellar matter. It was then postulated

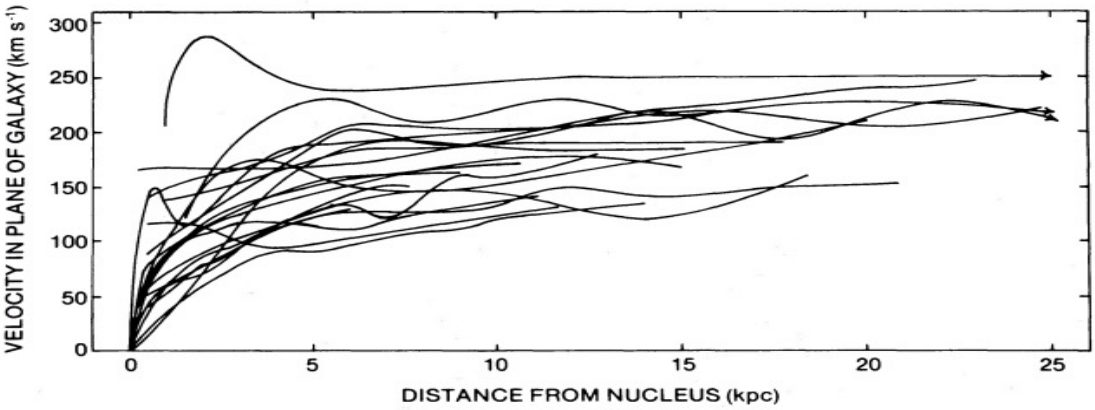

Figure 1.1. Rotation curves of 21 different galaxies reproduced from [3]. Objects far the from the center of the galaxy maintain a flat velocity dispersion.

that there must be some missing matter, possibly connected to the missing galaxy cluster mass conceived of by Zwicky. We now understand these galactic rotation curves as resulting from galaxies being embedded in large dark matter halos that share the galactic center.

Some more modern astrophysical signals of dark matter include gravitational lensing [4] and observations of the Bullet Cluster. Gravitational lensing is a phenomenon predicted by Einstein's general theory of relativity in which the path of light is deflected by massive objects. This phenomenon has been most clearly observed in the case of strong lenses such as black holes or galaxy clusters which can produce multiple images of a single background object. Gravitational lensing serves as an important probe of matter distributions since the scale of the visible distortions depend on the mass of the lens itself. One striking example of strong gravitational lensing is that of galaxy cluster Abell 370 [5], which acts as a lens for extremely distant galaxies. This lensing effect, pictured by the Hubble Space Telescope in Fig. 1.2, cannot be explained by the luminous matter in the foreground. There now also exist weak lensing surveys [6, 7] and galaxy-galaxy lensing studies [8, 9] that confirm the presence of invisible matter in the universe and can even infer details about its distribution.

The Bullet Cluster is the aftermath of two colliding galaxy clusters, which creates a particularly unique probe of dark matter. During the galactic collision, the hot gas that contains

Figure 1.2. This is an image captured by the Hubble Space Telescope of galaxy cluster Abell 370 acting as a gravitational lens. A careful observer can make out visual distortions of background galaxies such as arcing about the lens. Credits: NASA, ESA, Hubble SM4 ERO Team, and ST-ECF

most of the baryonic matter slowed due to friction. However, gravitational lensing observations of the cluster show that the majority of the matter is not in the same location as the gas [10] as depicted in Fig. 1.3. In fact, we can see that while the gas component shows experiences drag due to electromagnetic interactions, the majority of the matter content simply passed through each other, creating a clear offset between the luminous and non-luminous matter.

In addition to the astrophysical realm, significant evidence of dark matter lives in the field of cosmology. The cosmic microwave background (CMB), a cornerstone measurement in cosmology, is the remnant radiation from when the universe first became transparent at around 4×10^5 years old. Measurements of the CMB angular distribution tell us much about the matter content of the universe via its statistical properties. This relic radiation originated at the time when the universe cooled to a temperature where photons were no longer being constantly scattered off of baryonic matter and began free streaming. Both baryonic and dark matter introduce a

Figure 1.3. A composite image from Magellan and the Hubble Space Telescope with an overlayed projection of the matter distribution from lensing (blue) and hot gas distribution from Chandra X-ray observations (pink). Credits: X-ray: NASA/CXC/CfA/M.Markevitch et al.; Optical: NASA/STScI; Magellan/U.Arizona/D.Clowe et al.; Lensing Map: NASA/STScI; ESO WFI; Magellan/U.Arizona, [10].

gravitational potential that causes anisotropies in the CMB distribution, while radiation pressure counteracts this effect and washes out anisotropies. Thus, precise measurements of the CMB distribution allow us to infer the matter content of the universe, among other structural factors. The CMB power spectrum depicted in Fig. 1.4 is a measurement of anisotropies in the CMB. The exact strength of these anisotropies at different scales depends on the delicate balance of gravity and radiation pressure and requires the aforementioned 5 to 1 ratio of dark matter to baryonic matter to fit the data [11]. Other cosmological evidence include the matter spectrum of galactic to cosmic scale structures [12, 13] and primordial abundances of light elements [14, 15].

A plethora of astrophysical and cosmological evidence has solidified our current cosmological paradigm known as ΛCDM (cold dark matter), which postulates that the universe mainly consists of three components. The largest part by energy density is the cosmological constant Λ

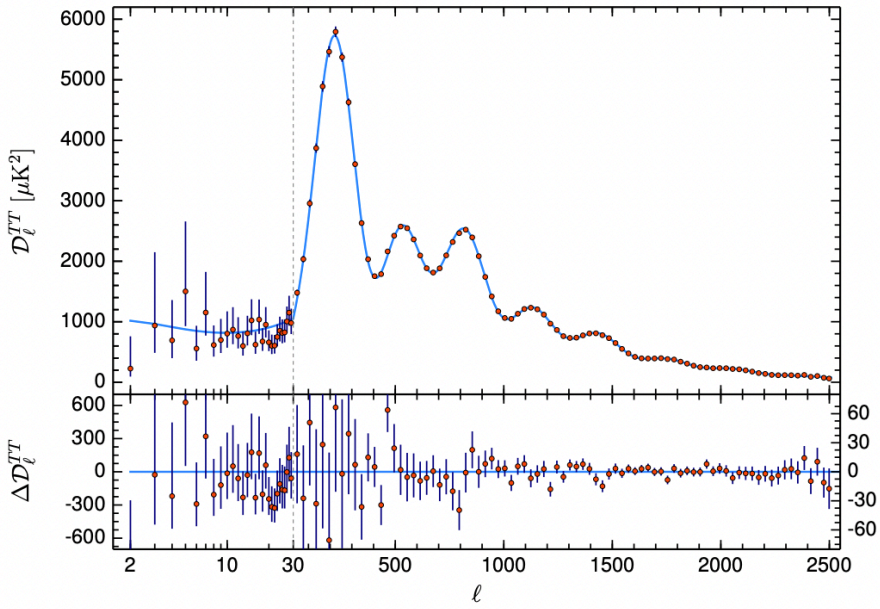

Figure 1.4. CMB power spectrum from *Planck* 2018 results, reproduced from [11]. The relative amplitudes of the peaks of the spectrum at different multipole moments l depend precisely on the ordinary and dark matter content of the universe.

responsible for the expansion of the universe, which is typically described by dark energy. The smallest component of the universe by energy fraction and most familiar to us is ordinary matter, which consists of baryons, electrons, etc.. Finally, we have cold dark matter, whose qualifier "cold" will be expounded on in detail the next section.

1.2 Dark Matter Models

Dark matter is the primary component of matter in the universe, yet its identity at a microscopic level is unknown. This chapter discusses the broad spectrum of dark matter models generally, while pointing out classes of candidates that are of particular interest to this work and investigated in the remaining chapters.

1.2.1 Particle Dark Matter

Before discussing particular theories, we first review the general constraints that dark matter models should obey in order to be consistent with the modern cosmological paradigm

ΛCDM:

- **Weakly interacting with Standard Model** - This is the most obvious constraint on dark matter originating from astrophysical, cosmological, and terrestrial observations. If dark matter were to interact with the Standard Model more than very weakly, we would simply be able to *see* the effects of these non-gravitational interactions via scatterings with Standard Model particles in the sky or on Earth or in their effects on the large scale structure of the universe.

- **Non-relativistic** - Dark matter must be non-relativistic by sufficiently early times in order to generate the structure formation and matter power spectrum that we observe today. If dark matter remains relativistic for too long, it the pressure it produces counteracts the gravitational potential necessary to birth galaxies and other structures.

- **Stable and weakly interacting with itself** - Dark matter decay on timescales shorter than the age of the universe lead to imprints on the CMB and matter power spectrum in the same vein as the previous bullet point. Decays and self-interactions necessitate some additional component to dark matter that prevents it from being pressureless at early enough times and is thus strongly constrained.

- **Produce the measured relic density**- Dark matter models must of course generate the correct amount of dark matter that exists today, i. e. 27% of the total energy density of the universe (68% being dark energy and the remaining 5% ordinary matter).

Despite these restrictions, there still remains an enormous theory space of allowed dark matter models depicted on its mass scale in Fig. 1.5.

The $\sim 10^{-22}$ eV to $\sim$ keV range consists of bosonic ultralight particles. Fermions below the keV scale are generally disallowed from saturating all of the DM due to the Tremaine-Gunn bound [17]. This bound arises from the Pauli exclusion principle in combination with typical galactic sizes and gravitational considerations. Fermionic DM lighter than a keV quickly

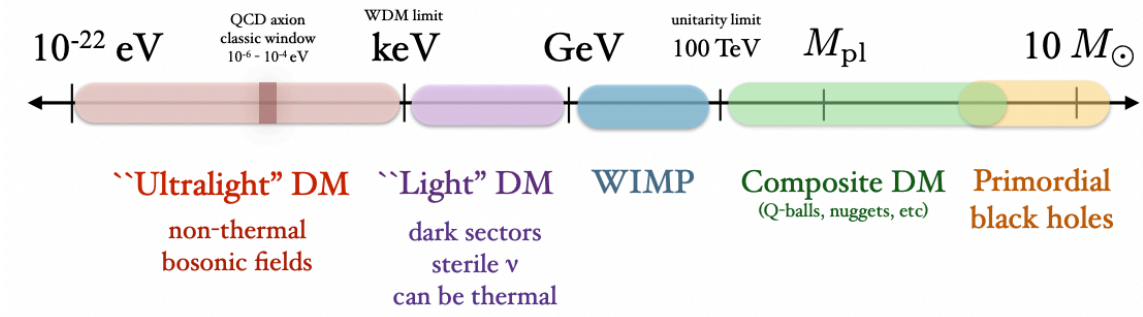

Figure 1.5. Cartoon of the theory space of DM candidates across mass scales, borrowed from [16]

oversaturates the allowed phase space of galaxies that we observe. In other words, they would lead to structures much too large. This leaves ultralight bosons as the remaining allowed candidate in this mass range. A key difference between the sub-keV and greater than keV mass regions is that sub-keV DM cannot be produced thermally, or it will remain relativistic for too long. Axions or axion-like particles (ALPs) are a type of bosonic particle whose relic density can be fixed non-thermally via the misalignment mechanism [18]. In this class of theories, the DM is a scalar field whose value is fixed in the early universe. The equation of motion for the scalar field causes the axion or ALP field to fluctuate at late times as the Hubble friction decreases, leaving a fluctuating field at late times which acts as cold dark matter. One popular model in this window is known as the QCD axion [19], which typically lives around 10^{-5} eV. The QCD axion is a small extension of the Standard Model, whose presence simultaneously solves the strong-CP problem, which would explain the anomalously small neutron electric dipole moment. DM belonging to this class of theories currently do not have direct detection prospects within the experimental setup that we focus on in the remainder of this work. Nonetheless, one can find discussions of the theoretical motivations and experimental prospects for various axion/ALP models in [20, 21, 22] and references therein.

In order of increasing mass, the next scale depicted in Fig. 1.5 is known as light DM, which is the main focus of this work. Before discussing models in this window, we briefly foray into a discussion of the next largest mass regime, the WIMP (Weakly Interacting Massive

Particles) scale DM. WIMP dark matter is of particular interest to this work since most existing direct laboratory probes target this regime. We will see that WIMPs are a nice baseline for a DM candidate easily consistent with ΛCDM while enjoying tractable direct detection prospects.

WIMP dark matter is a candidate whose relic abundance is typically set by a mechanism known as thermal freezeout [23]. Initially, WIMPs are produced in thermal equilibrium with the rest of the Standard Model in the early universe and maintain this equilibrium via creation and annihilation processes between the DM and SM. As the universe expands and cools, the Hubble rate eventually exceeds the DM annihilation rate. At this time, called "freezeout", the DM density is "frozen" other than the dilution due to an expanding universe, as annihilations to SM particles become inefficient and rare. Given the observed relic DM density today, we can work backwards to determine the necessary annihilation cross-section necessary for generating the correct amount of DM by freezeout. After freezeout, the ratio of dark matter number density to entropy density of CMB photons remains constant, since both of these quantities decrease with the scale factor cubed. In the literature, this ratio is known as the "abundance". Measurements of the CMB and DM density tell us that the abundance is roughly eV/m_χ today, where m_χ is the DM mass.

Now, we estimate the abundance at the time of freezeout in terms of the annihilation cross section. As discussed, freezeout occurs roughly when Hubble expansion exceeds the annihilation rate Γ, which depends on the equilibrium number density of DM (n_χ^{eq}) and the annihilation cross section:

$$\Gamma = n_\chi^{eq} \langle \sigma v \rangle = H, \tag{1.4}$$

where $\langle \sigma v \rangle$ is the thermally averaged cross section times velocity. Early universe thermodynamics [24] gives the entropy density of photons at freezeout in terms of temperature T and entropy degrees of freedom $g_{\star,S}(T)$

$$s_{fo} = \frac{2\pi^2}{45} g_{\star,S}(T) T^3, \tag{1.5}$$

while the number density of a non-relativistic spin-1/2 Dirac fermion species is

$$n_\chi^{eq} \approx 4\Big(\frac{m_\chi T}{2\pi}\Big)^{3/2} e^{-m_\chi/T}. \tag{1.6}$$

Combining results from equilibrium thermodynamics of the early universe soup (1.5) and (1.6) with the freezeout time condition (1.4) and today's measurement of eV/m_χ abundance gives the following benchmark for the annihilation cross section

$$\langle \sigma v \rangle \approx 2 \times 10^{-26} \mathrm{cm}^3/\mathrm{s} \tag{1.7}$$

[25]. If the thermally averaged cross section times velocity is anything below this condition, freezeout will occur too early to dilute the relic DM density to the correct abundance.

We are now quickly approaching the rationale for the name "Weakly" in Weakly Interacting Massive Particles. In the case of spin-1/2 Dirac fermions coupled to Standard Model fermions by a vector mediator, the annihilation cross section to SM fermions schematically is approximately given by

$$\langle \sigma v \rangle \sim \frac{\alpha_\chi \alpha_f}{m_\chi^2} \times \begin{cases} m_\chi^4/m_V^4 & m_\chi < m_V \\ 1 & m_\chi > m_V \end{cases} \tag{1.8}$$

where α_χ and α_f are coupling strengths between the DM fermions and mediator and SM fermions and mediator, respectively, and m_V is the mediator mass. By either coincidence or fate, one may notice that the required annihilation cross section for freezeout (1.7) closely matches (1.8) if we take the coupling strengths α_χ and α_f to be on the scale of $SU(2)_L$ weak interactions $\alpha_w \approx 0.03$ and the DM mass to be on the weak scale:

$$\langle \sigma v \rangle \approx \frac{\alpha_w^2}{1\ \mathrm{TeV}^2}. \tag{1.9}$$

This apparent match between the freezeout annihilation cross section and weak-scale cross sections is known as the "WIMP miracle". The implication here is that minimal extensions to the SM at the weak scale, such as supersymmetry [26], are excellent thermal candidates that easily produce today's relic abundance of DM. Several other concrete examples are elucidated in [23, 27, 28].

Given an annihilation cross section of the form (1.8), one finds that WIMP candidates generally belong in roughly the 1 GeV $-$ 100 TeV mass range in order to produce the correct annihilation rate while satisfying the perturbative unitarity bound. For dark matter masses below 1 GeV, the weak coupling strengths with a weak scale mediator will not produce enough annihilations, while DM masses near 100 TeV require coupling strengths $\alpha_{\chi,f}$ that exceed 1. There now exist many ongoing search avenues for WIMP dark matter including direct detection, which will be discussed in the next chapter. Unfortunately, search avenues in this mass regime have not yet borne fruit. Current experimental exclusion bands in this mass range are shown in Fig. 2.2. The continual narrowing of allowed WIMP parameter space motivates us to broaden our scope towards the sub-GeV range, known as "light dark matter" (LDM).

1.2.2 Light Dark Matter

Finally we arrive at the target parameter space for the bulk of this Dissertation, the keV$-$GeV dark matter mass range. Like WIMPS, light dark matter can also be produced thermally in the early universe and decay to the required relic density through thermal freezeout. The main difference between LDM and WIMP freezeout is that light dark matter typically requires new mediators away from the weak scale to achieve the necessary annihilation cross section (1.7). This means that dark matter populating this theory space may belong to some entirely new *dark sector* which interacts very weakly with the SM. The necessity of these new dark mediators allows for a rich tapestry of models [29, 28, 30, 31, 32, 33], so long as they preserve the successes of the current cosmological paradigm.

In this work, we aim to explore LDM direct detection in the most broad way possible

with respect to the allowed theory space. Therefore, we will usually work with effective DM-nucleon couplings instead of restricting to particular models. This is a sensible approach since fundamental interactions can typically be recast in terms of higher order effective couplings. As an example, let's introduce a dark sector copy of the electromagnetic (EM) part of the SM with some nonzero new mediator mass m_V. The EM component of the SM and new dark sector extension give the following Lagrangian

$$\mathscr{L} \supset -\frac{1}{4}F_{\mu\nu}F^{\mu\nu} - \frac{1}{4}V_{\mu\nu}V^{\mu\nu} + \frac{\kappa}{2}F_{\mu\nu}V^{\mu\nu} + \frac{1}{2}m_V^2 V_\mu V^\mu + eA_\mu J^\mu_{\rm EM} + g_\chi V_\mu J^\mu_D, \tag{1.10}$$

This dark sector can be connected to the SM via the kinetic mixing term $\frac{\kappa}{2}F_{\mu\nu}V_{\mu\nu}$. This mixing between the photon and new dark mediator allows for effective $\bar{e}e\chi\bar{\chi}$ and $\bar{p}p\bar{\chi}\chi$ interactions, where e are electrons, p are protons, and χ is a new dark fermion. Since this model includes a dark copy of EM, the mediator V is known as a dark photon. This particular case is explored further in Sec. 3.4.3. This kinetic mixing portal is one of many possible ways to generate effective interactions between SM and DM fermions through a new DM mediator. A dark sector extension with a scalar mediator ϕ can connect to the SM through a Higgs portal through terms $\phi H^\dagger H$ and $\phi^2 H^\dagger H$. Then, the $\phi\bar{\chi}\chi$ term along with effective couplings to SM fermions $\phi\bar{f}f$ result in DM-SM fermion scatterings. In order to remain agnostic to the specific model, the results presented in Chapters 3 and 4 are generalized to massless and massive scalar mediators between DM and nucleons, with the addition of the dark photon in Ch. 3. An exploration of the astrophysical, terrestrial, and cosmological constraints on these simplified models can be found in [34].

1.2.3 Primordial Black Holes

Primordial black holes (PBHs) are a particularly exotic dark matter candidate that form from rare overdensities in the early universe. PBHs with masses greater than $\sim 10^{15}$ g or $\sim 10^{-18} M_\odot$ (solar masses) are able to survive Hawking evaporation until today and can therefore

make up a component of DM today. Constraints on the allowed PBH parameter space near this evaporation threshold comes from γ-ray observations, as PBHs near this mass range would emit an appreciable amount of Hawking radiation. For larger PBHs ($\gtrsim 10^{23}$ g or $10^{-11} M_{\odot}$), gravitational lensing searches have excluded PBHs from making more than $\sim 10\%$ of today's DM density. Existing constraints are expounded on further in Sec. 5.3.4 and references therein. In Chapter 5, we calculate projected reaches for next generation gravitational wave experiments on the PBH parameter space and show that they may be competitive with current exclusion bounds for a wide range of PBH masses.

Chapter 2

Dark Matter Detection

2.1 Direct Detection

Direct detection is one of the primary search avenues for DM and refers to the attempted detection of DM via its scatterings with ordinary matter. Since DM must only interact very weakly with SM particles, constructing low background, low energy threshold laboratory experiments is a necessity. This challenge is technological frontier that continues to be an active field of research in experimental physics. Chapters 3 and 4 of this work aim to predict the response rates of theoretical future solid state experiments to the DM wind. We begin by reviewing the kinematics and responses of existing laboratory direct detection probes of dark matter.

2.1.1 Nuclear and Electronic Recoils

Existing dark matter direct detection experiments generally operate via the following schema. Some large volume of inert material sits within a heavily shielded tank waiting for the rare instance of a dark matter interaction. This interaction excites a nucleon or electron, whose energy is then carried away to the edge of material and then captured by some low energy-threshold apparatus. For a recent overview and specific details of the numerous ongoing experiments, see Ref. [35] and references therein. An example diagram for a crystal-based apparatus is shown in Fig. 2.1. The precise form in which the energy propagates and is measured depends on the details of the experiment, but we can still understand the kinematics of the nuclear

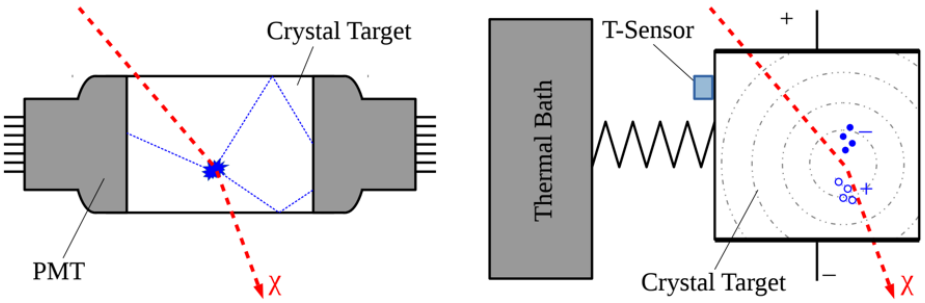

Figure 2.1. reproduced from [35].

and electronic recoils in a fairly general way as follows.

We will begin with a simple treatment of DM-nucleus scattering in the case where the DM-nucleon interactions are coherent across the nucleus. First, the incident momentum and energy of some incident DM particle χ are given by

$$\mathbf{p} = m_\chi, \quad E_i = \frac{\mathbf{p}^2}{2m_\chi}. \tag{2.1}$$

If the DM particle imparts momentum $\mathbf{q}$ upon scattering with a nucleus, the final dark matter energy is

$$E_f = \frac{(\mathbf{p}-\mathbf{q})^2}{2m_\chi} + \frac{\mathbf{q}^2}{2m_N}. \tag{2.2}$$

The key energy scale for the purpose of experimental detection is the amount of energy deposited into the system, or the final recoil energy of the nucleus. Applying energy and momentum conservation to the incident and final energy, one finds that when $\mathbf{p}$ and $\mathbf{q}$ are collinear, the dark matter imparts the maximum momentum and recoil energy onto the nucleus

$$|\mathbf{q}|_{\max} = 2\mu_{\chi N} v, \quad E_{NR} = \frac{|\mathbf{q}|^2}{2m_N} = \frac{2\mu_{\chi N}^2 v^2}{m_N}, \tag{2.3}$$

where v the incident DM speed and $\mu_{\chi N}$ is the DM-nucleus reduced mass. From simple kinematics, we see that the nuclear recoil energy scales with the square of the reduced mass. Thus, the recoil energy goes roughly as $2m_N v^2$ as long as the DM mass exceeds the nuclear

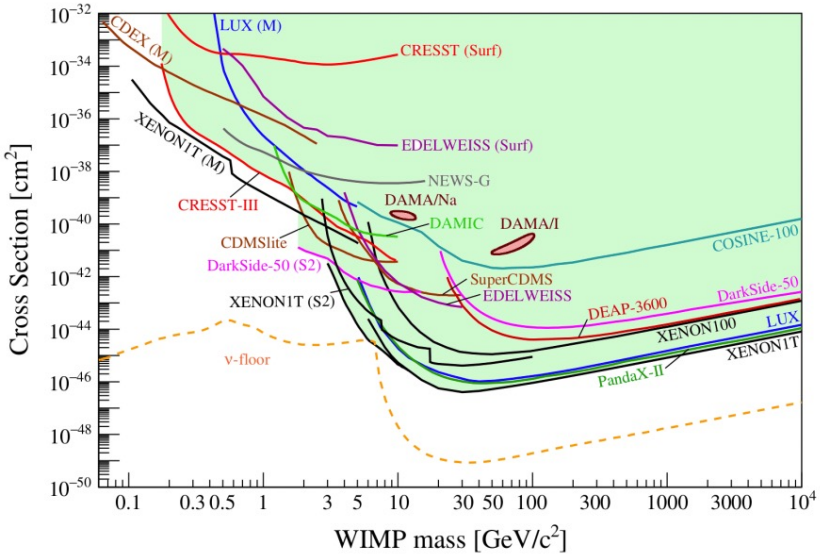

Figure 2.2. 90% confidence exclusion bounds for spin-independent DM-nucleon scatterings for various direct detection experiments, reproduced from [36]. The dashed line labeled ν-floor refers to the irreducible background from neutrino scattering.

mass. Taking a typical DM velocity of $v \sim 10^{-3}$, we find that recoils in this $m_\chi > m_N$ limit are of order $\mathcal{O}$(10-100) keV. Modern experiments have energy detection thresholds below this scale and thus are able to probe DM masses as low as 1 GeV. However, as the dark matter mass drops further below the nuclear mass, the imparted energy decreases with m_χ^2, rendering detection difficult via free nuclear recoils. In order to calculate the particular scattering rate and event energy spectrum, one would of course need to include the particular DM-nucleon interaction and possibly a nuclear structure factor if the dark matter de Broglie wavelength is smaller than the nuclear scale. For spin-independent nucleon couplings, Fig. 2.2 depicts many experimental bounds on the DM-nucleon cross section. As we can see, many direct detection experiments have already explored and excluded much of the WIMP parameter space.

In addition to nuclear recoils, modern experiments generally include some mode sensitive to DM-electron scatterings. The kinematics of electronic recoils differ from nuclear recoils due to the fact that electrons are much lighter than nucleons and have large average velocities compared to the DM. Following the similar analysis as for the nucleons, we calculate the electron

recoil energy, which gives

$$E_{eR} = \frac{\mathbf{p}\cdot\mathbf{q}}{m_\chi} - \frac{\mathbf{q}^2}{2m_\chi} \tag{2.4}$$

by kinematics. This recoil energy can be deposited if it corresponds to a difference between electron energy eigenvalues. This can be made precise upon careful study of the electronic structure of the material, but for the sake of a simple intuitive understanding, we treat the initial and final states as free momentum eigenstates with characteristic velocity of order of the fine structure constant α. In this case, the initial and final electron energies are given by

$$E_i = \frac{\mathbf{k}^2}{2m_e}, \;\; E_f = \frac{(\mathbf{k}+\mathbf{q})^2}{2m_e} \tag{2.5}$$

via momentum conservation, where $\mathbf{k}$ is the initial electron momentum. Combining this with the energy conservation condition gives

$$\frac{\mathbf{p}\cdot\mathbf{q}}{m_\chi} = \frac{\mathbf{k}\cdot\mathbf{q}}{m_e} - \frac{\mathbf{q}^2}{2\mu_{\chi e}}, \tag{2.6}$$

which is approximately

$$\frac{\mathbf{q}^2}{2\mu_{\chi e}} = \frac{\mathbf{k}\cdot\mathbf{q}}{m_e} \tag{2.7}$$

since the characteristic electron velocity $\sim \frac{\mathbf{k}}{m_e} \sim \alpha = \frac{1}{137}$ is much greater than the typical DM velocity $\sim \frac{\mathbf{p}}{m_\chi} \sim 10^{-3}$. Thus, the typical momentum transfer scales for electronic recoils are

$$|\mathbf{q}| \sim \mu_{\chi e}\alpha \tag{2.8}$$

For DM mass above the MeV scale, this corresponds energy depositions of order $m_e^2\alpha^2 \sim$ eV, which are accessible by modern experiments. Several experimental bounds on the DM-electron are illustrated in Fig. 2.3. Below the electron mass (~ 0.5 MeV), the phase space of allowed scatterings is heavily restricted since the electron mass becomes larger than the DM mass while having a much larger speed and thus would typically impart energy on the DM if they are both

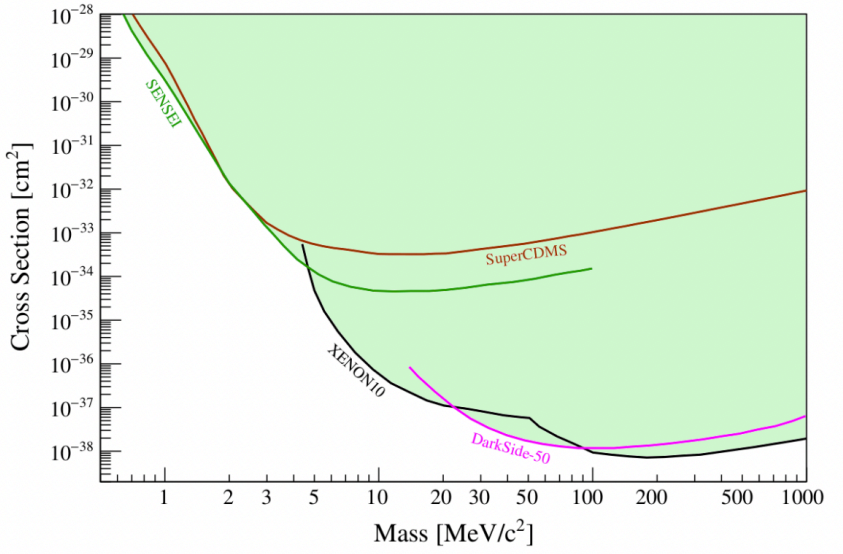

Figure 2.3. 90% confidence exclusion bounds for DM-electron scatterings mediated by a massive dark photon for various direct detection experiments, reproduced from [35].

free particles. In reality, the dark matter is can to impart its full kinetic energy $\frac{1}{2}m_\chi v^2$, but depositions are kinematically suppressed.

In this analytic discussion along with the experimental results in Figs. 2.2 and 2.3, we have found that DM-nucleon direct detection is only sensitive down to ~ 1 GeV DM mass while DM-electron sensitivity continues a few orders of magnitude further. This is primarily due to the fact that energy thresholds for nuclear and electronic recoils are quite different in existing experiments. We are able to detect electronic excitations down to the few eV scale, which allows for DM searches down to near the electron mass scale. However, nuclear recoils results at present are restricted to $\gtrsim 1$ keV thresholds. In the coming years, we expect the energy thresholds for DM-nucleon interactions to decrease significantly with new technologies. The next subsection discusses a promising experimental apparatus that may be able to probe DM-nucleon interactions below the GeV scale.

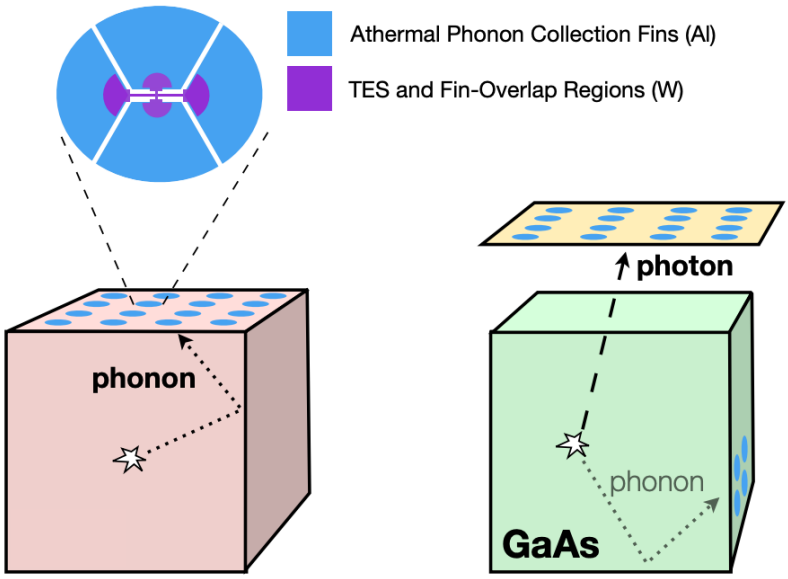

Figure 2.4. Illustrative diagram of the proposed "SPICE" experiment from the TESSERACT collaboration Snowmass 2021 Letter of Interest [37]. The left side depicts the mode that probes DM-nucleon interactions via phonons through frontier TES technology. The right side depicts the mode that exploits scintillation of the target crystal to probe DM-electron scatterings.

2.1.2 Solid State Detectors

In recent years, advancements in solid state physics have led to new prospects for experimental direct searches of dark matter through ultra-low energy threshold technology. One group leveraging these technological advancements is the TESSERACT collaboration, who is in their research and design phase for a liquid helium experiment called "HeRALD" and a polar crystal based experiment dubbed "SPICE" [37]. Here we review the SPICE experiment, which is a potential future apparatus for the scatterings discussed in Chapters 3 and 4.

The SPICE experiment will consist of a large number of gram-sized (or cm^3-sized by volume) crystal targets of sapphire and gallium arsenide totalling $\sim 0.1 - 1$ kg of each material. For each replica, there will be a low threshold athermal phonon detector on the surface. These surface detectors consist of superconducting Al fins and Transition Edge Sensors (TES) that work in conjunction to act as an athermal phonon calorimeter. The arrangement of Al fins and TESs on the surface are depicted in Fig. 2.4. The majority of area on the detector is composed

of the superconducting fins with small TESs at at the intersections of the fins. As particles scatter with nucleons in the crystal, phonons carry the imparted energy until they reach the superconducting fins. This energy is then converted into quasi-particles in the superconducting fins via broken Cooper pairs. These quasi-particles propagate within the fins until they are picked up by a TES, which are able to measure energy depositions by a simple mechanism. The TES is made of a metal with a narrow superconducting transition, which means that its resistance is highly temperature dependent. These sensors are operated near the transition temperature, thus small energy depositions may be detectable via sharp changes in the current through the TESs. Constructing real apparatuses using this concept is a topic of much ongoing research, one investigation of such a detector is detailed in Ref. [38]. The current frontier TESs [39] have been demonstrated to be able to reach thresholds as low as a few hundred meV. Chapters 3 and 4 of this Dissertation detail the theory of DM-nucleon/phonon scatterings and provide concrete tools for calculating experimental observation rates for meV to eV range, with particular emphasis on the intermediate regime around $100-200$ meV.

2.1.3 Phonons

As experimental energy thresholds decrease, we will begin to probe energy and momentum depositions on a scale that produce collective excitations in a crystal rather than single nuclear recoils. In crystal lattices, the pseudo-particle quantizing these collective excitations is the phonon [40], depicted for a simple chain in Fig. 2.5. We shall now review the kinematics of single phonon excitations, which typically carry energies of < 100 meV. This will serve as motivation for the rest of this work, which details the response of multiphonons.

In order to understand the basic physics of phonons, let's study the simple solvable model of a 1D harmonic chain of equal masses with only nearest neighbor interactions. The Hamiltonian of this theory is given by

$$H = \sum_i \left(\frac{p_i^2}{2m} + \frac{1}{2} m\omega_0^2 (x_i - x_{i+1})^2 \right), \tag{2.9}$$

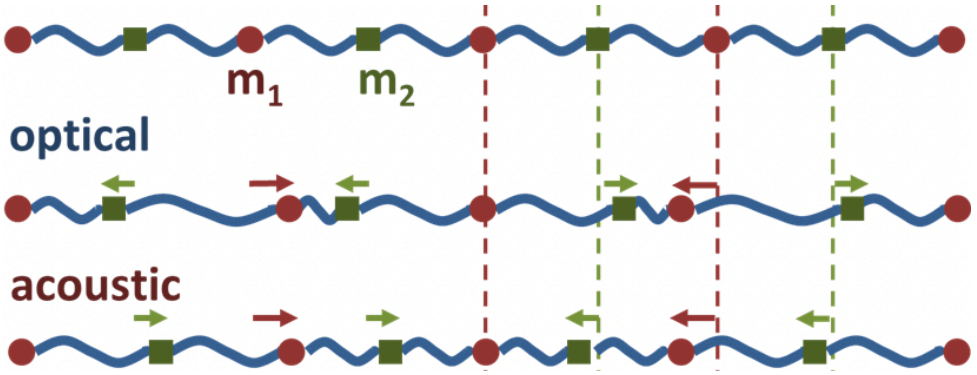

Figure 2.5. Cartoon of phonons moving along a 1D chain. At the top, the atoms are in equilibrium. The middle illustration shows optical phonons, which consist of neighboring atoms displaced in opposite directions. The bottom depicts acoustic phonons made of neighboring atoms displaced in the same direction. In both scenarios the phonons are longitudinal, since the direction of motion of individual atoms is parallel to the direction of motion of the phonon. In the 3D case, there will also be transverse acoustic and optical phonons whose atoms move orthogonally to the phonon propagation (which would be up and down in this diagram). Illustration Credit: Brews Ohare, Wikimedia Commons

where m is the mass, x_i, p_i are the displacement and momentum of mass i, and ω_0 is an energy scale that sets the strength of the nearest-neighbor interaction. We also constrain the system to have periodic boundary conditions, which makes it symmetric under translations of the equilibrium lattice spacing. This is simply a mathematical trick that provides the model with an exact symmetry. The boundary conditions are immaterial in the limit of a very large number of atoms. Since the Hamiltonian is invariant under translations of the equilibrium lattice spacing, it is diagonalizable in discrete Fourier modes

$$X_k = \frac{1}{\sqrt{N}} \sum_l e^{ikal} x_l, \; P_k = \frac{1}{\sqrt{N}} \sum_l e^{-ikal} p_l, \tag{2.10}$$

where N is the number of atoms and a is the lattice spacing. Straightforwardly inserting (2.10) into (2.9) gives the Hamiltonian in Fourier space

$$H = \frac{1}{2m} \sum_k \left(P_k P_{-k} + m^2 \omega_k^2 X_k X_{-k} \right), \tag{2.11}$$

where the sum is over all $k_n = \frac{2\pi n}{Na}$ such that $n \in \mathbb{Z}$ and $|n| \leq \frac{N}{2}$ and ω_k is given by

$$\omega_k = 2\omega \left| \sin \frac{ka}{2} \right|. \tag{2.12}$$

Now we fully diagonalize (2.11) by defining phonon creation and annihilation operators as satisfying $X_k = \sqrt{\frac{1}{2m\omega_k}}(a_k^\dagger + a_{-k})$ and $P_k = i\sqrt{\frac{m\omega_k}{2}}(a_k^\dagger - a_{-k})$:

$$H = \sum_k \omega_k (a_k^\dagger a_k + \frac{1}{2}). \tag{2.13}$$

We see that the proper commutation relations for creation and annihilation operators $[a_k, a_{k'}^\dagger] = \delta_{k,'k'}$ and $[a_k, a_{k'}] = [a_k^\dagger, a_{k'}^\dagger] = 0$ follow from $[x_i, p_j] = i\delta_{ij}$ and definitions of X_i, P_i. Finally, we find that single phonon eigenstates of the Hamiltonian ($a_k^\dagger|0\rangle$) are eigenstates of the total momentum operator and have energies that must satisfy the dispersion relation (2.12).

Given this dispersion relation, we can see that the kinematically accessible regime for single phonon production differs significantly from the free nuclear recoil response discussed around (2.3). The single phonon energies in our toy model scale linearly with the momentum at small momenta

$$\omega_k = 2\omega \left| \sin \frac{ka}{2} \right| \sim \omega a k \propto k, \tag{2.14}$$

which remains a feature of acoustic phonons in the full 3D crystal theory since acoustic phonons are the Goldstone bosons of broken translational symmetries. The proportionality constants between the energy and momenta in a realistic crystal are given by the sound speeds, which are typically $\mathcal{O}(\text{few}) - \text{O}(10)$ km/s. Thus, single acoustic phonon responses are possible for energy depositions in the $< \mathcal{O}(\text{few} \times 10)$ meV range as depicted in Fig. 2.7.

We would be remiss to neglect that this toy model does not capture the optical phonon modes present in real crystals. When neighboring atoms are non-identical as in crystals with multiple atoms per unit cell, there are modes where neighboring atoms move in opposite directions simultaneously, resulting in near-flat dispersions with finite energies at zero momentum.

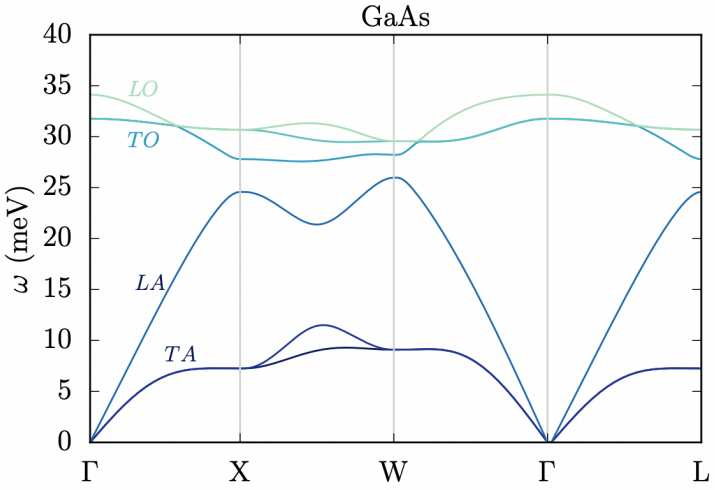

Figure 2.6. Dispersion relations for GaAs reproduced from [41]. The symbols X and W represent specific points along the edge of the Brillouin zone in reciprocal space while Γ is the zero momentum point. There are three acoustic (two transverse, one longitudinal) and three optical modes as expected for a two atom per unit cell crystal in 3D.

Fig. 2.6 illustrates a full set of dispersion relations for GaAs with optical phonon energies of $31 - 33$ meV. A complete numerical Density Functional Theory (DFT) calculation of scattering rates in the single phonon regime is performed in [41], while our full analytic prescription with both acoustic and optical modes is given in Sec. 3.3.1.

Prior to the work in this Dissertation, only the single phonon [41], diphonon [42], and free nuclear recoil responses to the dark matter wind had been formalized and calculated. In Chapters 3 and 4, we perform first calculations in the multiphonon regime, depicted as the wide yellow region in Fig. 2.7, and demonstrate its consistency with the single phonon and nuclear recoil limits. These results are the main goal and accomplishment of Chapters 3 and 4 of this thesis. As we can see from the figure, this is a necessity as we attempt to probe light dark matter with masses less than 100 MeV with experimental energy thresholds below 1 eV.

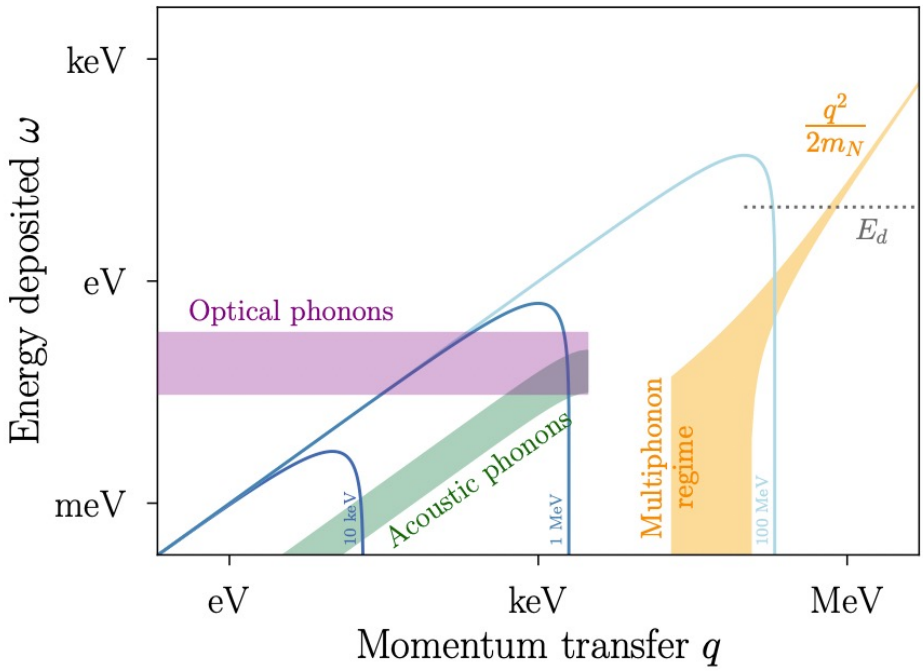

Figure 2.7. Schematic of the various DM-nucleon scattering regimes in crystals, reproduced from [43]. The purple and green shaded regions illustrate regions of momentum and energy transfers that can excite single phonons while the thin yellow shaded region above E_d refers to scatterings where the nucleus can be treated as free. The blue lines correspond to the kinematically accessible momentum and energy transfers for DM with velocity $v = 10^{-3}$. We see that DM masses below $\lesssim 1$ MeV typically excite single phonons, while DM masses $\gtrsim 1$ GeV effectively scatter off of single free nuclei. Understanding and calculating scatterings in the intermediate regime labeled "multiphonon regime" is one of the main accomplishments of this Dissertation.

2.2 Gravitational Waves

Einstein's general relativity predicts the formation of propagating ripples in spacetime in certain extreme circumstances. These ripples, known as gravitational waves, were first experimentally observed in 2015 by LIGO (Laser Interferometer Gravitational-Wave Observatory) [44] and were determined to be sourced by a merger of two black holes. Since then, many more observations have been made of gravitational waves originating from various combinations of neutron star and black hole mergers [45, 46]. While originally designed to find smoking-gun confirmation of Einstein's general relativity through merger measurements, gravitational wave detection may present a new probe into the existence of primordial black holes.

In theory, primordial black holes form due to large curvature perturbations in the early universe that cause rare overdensities. The mass and total energy density of PBHs are thus related to the cosmological metric at early times. While observations of gravitational waves today originate from large perturbations to the local spacetime metric near massive objects, GWs are also necessarily produced by large perturbations to the cosmological metric in the early universe. If such events occurred, the remnant GWs will have propagated and redshifted along with the rest of the universe and formed a GW stochastic background, similar to the CMB but with gravitational radiation instead of electromagnetic radiation. Data from existing GW interferometers LIGO and Virgo has been used to place constraints on the primordial curvature spectrum [47]. However, these results are not competitive with existing cosmological bounds on the primordial black hole parameter space. In Chapter 5, we carefully relate the population of PBHs to the strength and scales of primordial curvature perturbations. We investigate gravitational waves produced from PBH potentials, the cosmological metric, and various other sources and discuss the potential observational prospects of next generation gravitational wave experiments on these stochastic GW backgrounds.

Chapter 3

Dark matter direct detection from the single phonon to the nuclear recoil regime

3.1 Introduction

The effort to directly detect dark matter (DM) is entering the sub-GeV mass regime, thanks to experimental innovations which allow for ever lower energy thresholds. For kinematic reasons, this regime is especially challenging for DM which primarily couples to hadronic matter. For a DM mass (m_χ) below 1 GeV, the energy that the DM can deposit in an elastic collision with a nucleus of mass m_N is bounded by

$$E_N \leq \frac{2v^2 m_\chi^2}{m_N}. \tag{3.1}$$

For $m_\chi \ll m_N$ this is only a small fraction of the total available DM kinetic energy, which can make it very difficult to detect. This problem can be mitigated to some extent by choosing light element targets such as H [48], He [49, 50, 51], or diamond [52] and by pushing for lower thresholds. Alternatively, one may leverage inelastic processes such as the Migdal effect [53, 54, 55] or bremsstrahlung [56]. Inelastic processes occur at substantially lower rate, but are not subject to the constraint in (3.1) and can also yield signals that are more easily detected than a nuclear recoil, such as electronic excitations, ionizations or X-rays. Which approach is preferable depends on the characteristics of the detector.

At sufficiently low energy and momentum scales, DM-nucleus scattering is also not subject to (3.1) because atom-atom interactions become important. In particular, the relevant excitations in a crystal target are phonons instead of elastic nuclear recoils. For $m_\chi \lesssim$ MeV, the momentum transfer from DM scattering corresponds to wavelengths comparable or larger than the interatomic spacing of a typical target. In this regime, the dominant process will be coherent scattering off multiple atoms, with creation of a single phonon. For crystalline targets with phonon energies as high as $\sim$100 meV, the energy deposited from DM can be well above the naive estimate in (3.1). Single phonon excitation has been studied extensively for sub-MeV dark matter, where numerical and analytic calculations by different groups are in good agreement [57, 41, 58, 59, 60, 61, 62, 63]. These calculations have also been extended to diphonon production from sub-MeV dark matter[1] [42] as well as to single phonon production from MeV-GeV dark matter by including Umklapp processes [58, 60]. However, so far there has not been a complete description of DM scattering for intermediate energy and momentum transfers, where multiphonon processes are expected to dominate.

In this work, we develop an analytic treatment of DM scattering that interpolates between the single phonon and nuclear recoil regimes. The relevant approximations are set primarily by the momentum transfer q. For single phonon excitations and $q < 2\pi/a$, where a is typical atomic lattice spacing, we use a long-wavelength approximation used earlier in the literature [57, 41, 59, 42]. For $q > 2\pi/a$, we employ the incoherent approximation, which neglects interference effects between the response of neighboring atoms. This allows us to organize the calculation as a systematic expansion in the number of final state phonons, where each additional phonon comes with a factor of $q/\sqrt{2m_d\bar{\omega}_d}$. Here, m_d and $\bar{\omega}_d$ are the mass and average oscillation frequency of the atom in the position indexed by d. For $q < \sqrt{2m_d\bar{\omega}_d}$ it is numerically practical to compute the rate order-by-order in terms of the phonon density of states of the material. For $q \gg \sqrt{2m_d\bar{\omega}_d}$, scattering into many phonons dominates and the perturbation series

[1] Analogous calculations were performed for superfluid He [64, 65, 66, 67, 68, 69, 70], for which diphonon production is the leading observable process for $m_\chi \lesssim 1$ MeV.

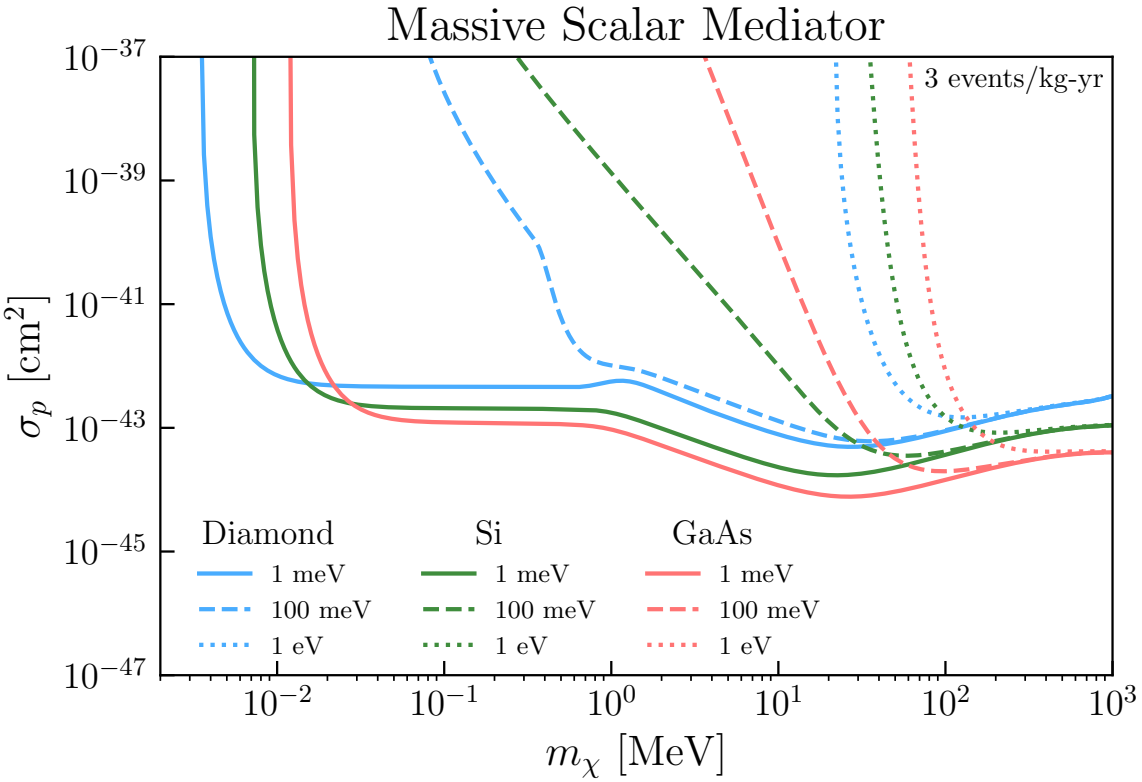

Figure 3.1. Cross sections needed for 3 events/kg-year for various target materials and threshold energies. A massive hadrophilic mediator is assumed.

requires increasingly large orders in $q/\sqrt{2m_d\bar{\omega}_d}$ to converge. It can however be resummed by making use of the impulse approximation, which in turn smoothly matches onto the free nuclear recoil regime. A similar expansion in number of modes has been performed previously for the integrable toy model that is the harmonic oscillator [71]. Here we have generalized the approach to a harmonic *crystal*, analogous to the procedure followed in [72] and [73], in calculations of the Migdal effect and X-ray backgrounds, respectively. Fig. 3.1 illustrates our results from applying these approximations. All of our calculations are implemented as part of the `DarkELF` public code [74].[2]

The remainder of this paper is organized as follows: In Sec. 3.2 we introduce the dynamic structure factor, which captures the material-dependence of the DM scattering cross section,

[2]https://github.com/tongylin/DarkELF

and motivate the incoherent approximation for the structure factor. In Sec. 3.3, we describe our analytic approximations in detail across the different regimes in energy and momentum transfer. We perform checks on our use of the incoherent approximation by comparing with previous calculations for single-phonon production and analytic calculations for diphonon production. Our results for GaAs are discussed in detail in Sec. 3.4 and we conclude in Sec. 3.5. Appendix 3.A contains the formulas for diphonon production and Appendix 3.B provides details on the impulse approximation. The implementation in `DarkELF` is documented in Appendix 3.C. We further provide numerical results for Ge, Si and diamond in Appendix 3.D.

3.2 Dynamic structure factor

Our starting point will be a general potential for spin-independent DM-nucleus interactions, although the formalism below could also be applied to spin-dependent interactions. For a DM particle of mass m_χ incident on a crystal with N unit cells and $\mathfrak{n}$ ions per unit cell, the potential in Fourier space is given by

$$\tilde{\mathscr{V}}(\mathbf{q}) = \frac{2\pi b_p}{\mu_\chi} \tilde{F}(\mathbf{q}) \sum_{\ell}^{N} \sum_{d=1}^{\mathfrak{n}} f_{\ell d} e^{i\mathbf{q}\cdot\mathbf{r}_{\ell d}}. \tag{3.2}$$

Here, we sum over the N unit cells, labeled by lattice vectors ℓ, and atoms within the unit cell, labeled with the index d, such that all atoms in the crystal with positions $\mathbf{r}_{\ell d}$ are summed over. The DM-proton scattering length b_p is defined by the DM-proton scattering cross section $\sigma_p \equiv 4\pi b_p^2$ at some reference momentum, and μ_χ is the DM-proton reduced mass. We first consider a general coupling strength $f_{\ell d}$ of the nucleus labeled by ℓ, d relative to that of a single proton. $f_{\ell d}$ is specified for various interactions in Section 3.4, such as nucleon number for scalar mediators and the effective electric charge for scattering via a dark photon mediator. In the latter case $f_{\ell d}$ is $\mathbf{q}$ dependent when accounting for screening effects.

We consider two form factors in (3.2) representing limiting cases of interactions: scattering via a heavy mediator, where $\tilde{F}(\mathbf{q}) = 1$; and scattering via a massless mediator, where

$\tilde{F}(\mathbf{q}) = q_0^2/q^2$ with a model-dependent reference momentum q_0.

Collecting the overall factor $2\pi b_p \tilde{F}(\mathbf{q})/\mu_\chi$, we define the differential cross section as

$$\frac{d\sigma}{d^3\mathbf{q}\,d\omega} = \frac{b_p^2}{\mu_\chi^2}\frac{1}{v}\frac{\Omega_c}{2\pi}|\tilde{F}(\mathbf{q})|^2 S(\mathbf{q},\omega)\,\delta\left(\omega - \omega_{\mathbf{q}}\right) \tag{3.3}$$

where v is the initial velocity of the dark matter (incident on a target at rest), $\Omega_c = V/N$ is the volume of the unit cell in the crystal, and $\omega_{\mathbf{q}} = \mathbf{q}\cdot\mathbf{v} - q^2/2m_\chi$ is the kinematic constraint on the momentum and energy transfers to the crystal $\mathbf{q}$ and ω. We have in turn also defined the dynamic structure factor

$$S(\mathbf{q},\omega) \equiv \frac{2\pi}{V}\sum_f \left|\sum_\ell^N \sum_{d=1}^{\mathrm{n}} \left\langle \Phi_f \middle| f_{\ell d} e^{i\mathbf{q}\cdot\mathbf{r}_{\ell d}} \middle| 0 \right\rangle\right|^2 \delta\left(E_f - \omega\right). \tag{3.4}$$

Note that the convention for $S(\mathbf{q},\omega)$ varies across the literature; here we use the convention that gives a similar $S(\mathbf{q},\omega)$ definition for both phonon interactions and DM-electron interactions [58, 43]. We also assume the system is initially in its ground state $|0\rangle$ prior to the collision, corresponding to a zero temperature system. We sum over final states with energies E_f, such that each term represents the probability to excite the final state $\left|\Phi_f\right\rangle$.

3.2.1 Coherent and incoherent structure factors

For a given crystal there are many possible configurations of interaction strengths $f_{\ell d}$ which may vary even for different samples of the same material, e.g. the exact distribution of spins or isotopes in the material for spin-dependent[3] or mass-dependent interactions, respectively. This can be accounted for by averaging over a large collection of target samples. With a large number of nuclei in the crystal, we expect the exact distribution of interaction strengths in a given sample to be inconsequential relative to the result averaged over many samples. We can keep track of fluctuations away from the average configuration by splitting the scattering rate

[3]For spin-dependent interactions, $f_{\ell d}$ is an operator rather than a parameter, but otherwise the analysis proceeds analogously.

into a coherent and incoherent contribution, as explained below.

We follow the procedure of Refs. [75, 76] and first re-express (3.4) by expanding the square and Fourier transforming the δ-function, giving

$$S(\mathbf{q},\omega) = \sum_{\ell,\ell'}^{N} \sum_{d,d'}^{\mathfrak{n}} f_{\ell d} f^*_{\ell' d'} \mathscr{C}_{\ell' d' \ell d} \tag{3.5}$$

where $\mathscr{C}_{\ell' d' \ell d}$ is the time-dependent two-point function:

$$\begin{aligned} \mathscr{C}_{\ell' d' \ell d} &\equiv \frac{1}{V} \int_{-\infty}^{\infty} dt \sum_f \left\langle 0 \middle| e^{-i\mathbf{q}\cdot\mathbf{r}_{\ell' d'}(0)} \middle| \Phi_f \right\rangle \\ &\qquad \times \left\langle \Phi_f \middle| e^{i\mathbf{q}\cdot\mathbf{r}_{\ell d}(t)} \middle| 0 \right\rangle e^{-i\omega t} \\ &\equiv \frac{1}{V} \int_{-\infty}^{\infty} dt \, \langle e^{-i\mathbf{q}\cdot\mathbf{r}_{\ell' d'}(0)} e^{i\mathbf{q}\cdot\mathbf{r}_{\ell d}(t)} \rangle e^{-i\omega t}. \end{aligned} \tag{3.6}$$

In the second line we used the completeness of the basis of states. It will also be advantageous to define a shorthand notation for the *auto-correlation function* for an atom with itself as

$$\begin{aligned} \mathscr{C}_{\ell d} &\equiv \mathscr{C}_{\ell d \ell d} \\ &\equiv \frac{1}{V} \int_{-\infty}^{\infty} dt \, \langle e^{-i\mathbf{q}\cdot\mathbf{r}_{\ell d}(0)} e^{i\mathbf{q}\cdot\mathbf{r}_{\ell d}(t)} \rangle e^{-i\omega t}. \end{aligned} \tag{3.7}$$

We assume that the $f_{\ell d}$ are random throughout the crystal. Under this assumption, the average of $f_{\ell d} f^*_{\ell' d'}$ over target configurations, $\overline{f_d f^*_{d'}}$, must be independent of the lattice sites ℓ, ℓ'. Making this replacement in (3.5) gives

$$S(\mathbf{q},\omega) = \sum_{\ell,\ell'}^{N} \sum_{d,d'}^{\mathfrak{n}} \overline{f_d f^*_{d'}} \mathscr{C}_{\ell' d' \ell d} \tag{3.8}$$

where the averages may be written as

$$d \neq d' : \qquad \overline{f_d f_{d'}^*} = \overline{f_d}\,\overline{f_{d'}^*},$$
$$d = d' : \qquad \overline{f_d f_{d'}^*} = \overline{f_d^2}.$$

For the $d \neq d'$ case we assumed that the expectation values of the f_d for different atoms in the unit cell are uncorrelated. This allows one to split the structure factor into two contributions:

$$S(\mathbf{q},\omega) = \sum_{\ell\neq\ell'}^{N}\sum_{d\neq d'}^{\mathrm{n}} \overline{f_d}\,\overline{f_{d'}^*}\,\mathscr{C}_{\ell' d' \ell d} + \sum_{\ell}^{N}\sum_{d}^{\mathrm{n}} \overline{f_d^2}\,\mathscr{C}_{\ell d} \tag{3.9}$$

$$= \sum_{\ell,\ell'}^{N}\sum_{d,d'}^{\mathrm{n}} \overline{f_d}\,\overline{f_{d'}^*}\,\mathscr{C}_{\ell' d' \ell d} + \sum_{\ell}^{N}\sum_{d}^{\mathrm{n}} \left(\overline{f_d^2} - (\overline{f_d})^2\right)\mathscr{C}_{\ell d} \tag{3.10}$$

$$\equiv S^{(\mathrm{coh})}(\mathbf{q},\omega) + S^{(\mathrm{inc})}(\mathbf{q},\omega) \tag{3.11}$$

where the second line is obtained by adding and subtracting the term proportional to $(\overline{f_d})^2$ and regrouping. The first and second term in (3.11) are usually referred to as the *coherent* and *incoherent* structure factors in the neutron scattering literature.

The coherent structure factor relays the scattering rate if the interaction strengths of all atoms in equivalent lattice sites are equal to a common value $\overline{f_d}$. For example, one can consider low energy, spin-independent neutron scattering in a very pure crystal with only a single isotope per atom type. This implies $f_d = f_{\ell d} = A_d$, with A_d the atomic mass number, such that the incoherent contribution in (3.11) vanishes exactly. The sum in (3.10) then crucially includes position correlators between differing nuclei, which capture the interference between different lattice sites. In practice, this interference leads to a coherence condition, which demands that the momentum in the scattering process must be conserved up to a reciprocal lattice vector. In particular, the 0th order term in a low $\mathbf{q}$ expansion of (3.6) corresponds to Bragg diffraction.

The incoherent structure factor on the other hand accounts for the statistical variations in interaction strengths between different scattering centers in the lattice. The second sum in (3.10)

contains no cross terms and thus does not include interference between different lattice sites. There is therefore no corresponding coherence condition and the incoherent structure factor does not enforce momentum conservation.[4]

For most earlier DM direct detection calculations the focus has been on spin-independent scattering in high purity crystals with little isotopic variation. In this scenario, we take the single isotope approximation $\overline{f_d^2} - (\overline{f_d})^2 = 0$, implying that only the coherent scattering contributes. For spin-dependent dark matter scattering, the average will be the quantum expectation value of the spin operator, resulting in $\overline{f_d^2} \neq (\overline{f_d})^2$. We therefore expect the incoherent piece in (3.11) to be important in this case. In this paper we focus exclusively on spin-independent scattering in the single isotope limit and the corresponding coherent structure factors. The coherent structure factors are however more difficult to evaluate, due to the conservation of crystal momentum that is built into (3.6). This results in increasingly complicated phase space integrals for multiphonon processes [42]. For our purposes, the utility of studying the incoherent structure factor will be that the auto-correlation function can be used to obtain a reasonable and more manageable approximation of the coherent structure factor at sufficiently high momenta. Our results can also be extended to the case of spin-dependent scattering, but we leave this for future work.

Before venturing further into this approximation and its validity, we must first develop the structure factors into a form which lends itself to a direct calculation. In order to evaluate the structure factors in (3.4)–(3.8), the position vector of each atom may be decomposed in terms of the equilibrium lattice positions and displacement vectors, $\mathbf{r}_{\ell d} = \ell + \mathbf{r}_d^0 + \mathbf{u}_{\ell d}$. Here $\mathbf{r}_d^0$ is the equilibrium location of atom d relative to the origin of the primitive cell and $\mathbf{u}_{\ell d}$ is the displacement relative to that equilibrium. Following this decomposition, we quantize the

[4] An alternative but equivalent point of view is that for coherent scattering, translation symmetry is broken up to a shift symmetry, since all unit cells are identical. For incoherent scattering the scattering centers are treated as independent and translation invariance is therefore fully broken, resulting in the complete loss of momentum conservation.

displacement vector in the harmonic approximation with a phonon mode expansion

$$\mathbf{u}_{\ell d}(t) = \sum_{\nu}^{3\mathfrak{n}} \sum_{\mathbf{k}} \frac{1}{\sqrt{2Nm_d\omega_{\nu,\mathbf{k}}}} \Big(\mathbf{e}_{\nu,d,\mathbf{k}} \hat{a}_{\nu,\mathbf{k}} e^{i\mathbf{k}\cdot(\ell+\mathbf{r}_d^0)-i\omega_{\nu,\mathbf{k}}t} + \mathbf{e}^*_{\nu,d,\mathbf{k}} \hat{a}^\dagger_{\nu,\mathbf{k}} e^{-i\mathbf{k}\cdot(\ell+\mathbf{r}_d^0)+i\omega_{\nu,\mathbf{k}}t} \Big) \tag{3.12}$$

The index ν denotes the phonon branches, of which there are $3\mathfrak{n}$, and $\mathbf{k}$ labels the phonon momentum in the first Brillouin Zone (BZ). The $\hat{a}^\dagger_{\nu,\mathbf{k}}$ and $\hat{a}_{\nu,\mathbf{k}}$ are the creation and annihilation operators for the phonons, $\omega_{\nu,\mathbf{k}}$ is the energy of the phonon, $\mathbf{e}_{\nu,d,\mathbf{k}}$ is the phonon eigenvector for atom d normalized within a unit cell, $\sum_d \mathbf{e}^*_{\nu,d,\mathbf{k}} \cdot \mathbf{e}_{\mu,d,\mathbf{k}'} = \delta_{\mu\nu}\delta_{\mathbf{k},\mathbf{k}'}$, and m_d is the mass of atom d.

The structure factor in (3.8) can then be explicitly evaluated by applying (3.12) to (3.6). For a pure single isotopic crystal with $\overline{f_d^2} = (\overline{f_d})^2$, this is given by [42]

$$S^{(\mathrm{coh})}(\mathbf{q},\omega) = \frac{2\pi}{V} \sum_f \left| \sum_{\ell}^{N} \sum_{d}^{\mathfrak{n}} \overline{f_d}\, e^{-W_d(\mathbf{q})} \mathscr{M}_{\ell d} \right|^2 \delta\left(E_f - \omega\right) \tag{3.13}$$

where

$$\mathscr{M}_{\ell d} \equiv e^{i\mathbf{q}\cdot(\ell+\mathbf{r}_d^0)} \left\langle \Phi_f \right| \exp\left[i \sum_{\mathbf{k},\nu} \frac{\mathbf{q}\cdot\mathbf{e}^*_{\nu,\mathbf{k},d}}{\sqrt{2Nm_d\omega_{\nu,\mathbf{k}}}} \hat{a}^\dagger_{\nu,\mathbf{k}} e^{-i\mathbf{k}\cdot(\ell+\mathbf{r}_d^0)} \right] |0\rangle \tag{3.14}$$

is the matrix element for scattering into the final state of the crystal denoted by f. The Debye-Waller factor $e^{-W_d(\mathbf{q})}$ is given in terms of the function $W_d(\mathbf{q}) \equiv \frac{1}{2}\langle(\mathbf{q}\cdot\mathbf{u}_{\ell d}(0))^2\rangle$. We may Taylor expand the inner exponential in powers of $\mathbf{q}$ where the nth term can excite a final state consisting of n phonons. The phonon eigenvectors and energies may be obtained numerically using Density Functional Theory (DFT) (see e.g. [77]); using these, the leading single phonon structure factor has been calculated [41, 60, 63]. These DFT-based calculations quickly become cumbersome, however, and have not yet been performed for generic n-phonon terms. Analytic calculations may be performed more easily, and have been carried out for the single- and two-phonon terms [42], but are only tractable when assuming an isotropic crystal and that $|\mathbf{q}|$ is small relative to the size of the first Brillouin zone. Such analytic calculations likewise lack scalability for higher order

phonon terms.

In summary, since the direct evaluation of (3.13) is very tedious and not always possible, we will rely instead on an approximate form of $S^{(\mathrm{coh})}(\mathbf{q},\omega)$, bypassing the need to deal with (3.13). This is described in the next section.

3.2.2 Incoherent approximation

The incoherent approximation amounts to dropping the cross terms in ($\ell \neq \ell'$ or $d \neq d'$) from the sum in (3.10), thus neglecting the interference between non-identical atoms. In other words, one approximates the coherent structure factor by

$$S^{(\mathrm{coh})}(\mathbf{q},\omega) \approx \sum_{\ell}^{N} \sum_{d}^{\mathfrak{n}} (\overline{f_d})^2 \mathscr{C}_{\ell d}. \tag{3.15}$$

The incoherent structure factor remains unchanged, and the total structure factor is then given by $S^{(\mathrm{tot})}(\mathbf{q},\omega) \approx \sum_{\ell}^{N} \sum_{d}^{\mathfrak{n}} \overline{f_d^2} \mathscr{C}_{\ell d}$. In this work we will focus only on pure crystals with a single isotope for each type of atom, so that the total structure factor can be computed with (3.15). The incoherent approximation is expected to be a good approximation when the momentum transfer is larger than $2\pi/a$ with a the inter-particle spacing. Then the phase factors associated with the interference terms are expected to add up to a small correction compared to the $\ell = \ell', d = d'$ terms in the sum. For an argument justifying (3.15) we refer to [75, 78].

For momentum transfers within the first Brillouin zone, single phonon scattering always dominates the inclusive scattering rate. It is however possible that the detector threshold is such that single phonon processes cannot be accessed but the double or multiphonon processes can. In this case the incoherent approximation cannot a priori be taken for granted. We nevertheless use it, but verify the results against our earlier two-phonon calculations [42] whenever possible (Sec. 3.3.2), finding satisfactory agreement. The accuracy of the calculations in this part of phase space is however less well understood and further work is needed.

To evaluate the auto-correlation function, we first replace the atomic positions $\mathbf{r}_{\ell d}$ in

(3.11) with their displacement operator decomposition, noting that the $\ell + \mathbf{r}_d^0$ constant cancels, amounting to a simple substitution of $\mathbf{r}_{\ell d} \to \mathbf{u}_{\ell d}$:

$$\mathscr{C}_{\ell d} = \frac{1}{V} \int_{-\infty}^{\infty} dt \, \langle e^{-i\mathbf{q}\cdot\mathbf{u}_{\ell d}(0)} e^{i\mathbf{q}\cdot\mathbf{u}_{\ell d}(t)} \rangle e^{-i\omega t} \tag{3.16}$$

The expectation value may be rewritten with an application of the Baker–Campbell–Hausdorff formula, Bloch's identity $\langle e^{\hat{A}} \rangle = e^{\frac{1}{2}\langle \hat{A}^2 \rangle}$, and some matrix algebra [41] giving:

$$\mathscr{C}_{\ell d} = \frac{1}{V} \int_{-\infty}^{\infty} dt \, e^{-2W_d(\mathbf{q})} e^{\langle \mathbf{q}\cdot\mathbf{u}_{\ell d}(0)\, \mathbf{q}\cdot\mathbf{u}_{\ell d}(t) \rangle} e^{-i\omega t}. \tag{3.17}$$

When we deployed Bloch's identity, we implicitly used the harmonic approximation, by only considering displacement operators of the form in (3.12).

The correlator $\langle \mathbf{q}\cdot\mathbf{u}_{\ell d}(0)\, \mathbf{q}\cdot\mathbf{u}_{\ell d}(t) \rangle$ may be evaluated with the form of the displacement operator in (3.12), wherein the ℓ dependence cancels. This gives

$$\langle \mathbf{q}\cdot\mathbf{u}_d(0)\, \mathbf{q}\cdot\mathbf{u}_d(t) \rangle = \sum_{\nu} \sum_{\mathbf{k}} \frac{\left| \mathbf{q}\cdot\mathbf{e}_{\nu,\mathbf{k},d} \right|^2}{2Nm_d\omega_{\nu,\mathbf{k}}} e^{i\omega_{\nu,\mathbf{k}}t} \tag{3.18}$$

which can be simplified further by averaging over the direction of momentum vector $\mathbf{q}$

$$\langle \mathbf{q}\cdot\mathbf{u}_d(0)\, \mathbf{q}\cdot\mathbf{u}_d(t) \rangle \approx \frac{q^2}{3} \sum_{\nu} \sum_{\mathbf{k}} \frac{|\mathbf{e}_{\nu,\mathbf{k},d}|^2}{2Nm_d\omega_{\nu,\mathbf{k}}} e^{i\omega_{\nu,\mathbf{k}}t} \tag{3.19}$$

$$= \frac{q^2}{2m_d} \int_{-\infty}^{+\infty} d\omega' \frac{D_d(\omega')}{\omega'} e^{i\omega' t} \tag{3.20}$$

where we defined the *partial density of states* for each atom in the primitive cell as

$$D_d(\omega) \equiv \frac{1}{3N} \sum_{\nu} \sum_{\mathbf{k}} |\mathbf{e}_{\nu,\mathbf{k},d}|^2 \delta(\omega - \omega_{\nu,\mathbf{k}}). \tag{3.21}$$

The partial density of states was normalized to satisfy $\int_{-\infty}^{+\infty} d\omega D_d(\omega) = 1$. This can be shown by

using the eigenvector completeness condition, which imposes $\sum_\nu e^*_{\nu,\mathbf{k},d,i} e_{\nu,\mathbf{k},d,j} = \delta_{ij}$ for fixed $\mathbf{k}, d$, where i, j are spatial indices. In addition, the total density of states of the material is defined by

$$D(\omega) \equiv \sum_d D_d(\omega) = \frac{1}{3N} \sum_\nu \sum_{\mathbf{k}} \delta(\omega - \omega_{\nu,\mathbf{k}}), \tag{3.22}$$

which satisfies $\int_{-\infty}^{+\infty} d\omega D(\omega) = \mathfrak{n}$ with $\mathfrak{n}$ the number of atoms in the unit cell.[5] In materials such as Ge, Si, or GaAs all atoms in the primitive cell have the same or similar mass and as such contribute roughly equally to the density of states, see Fig. 3.2. One could therefore approximate $D_d(\omega) \approx D(\omega)/\mathfrak{n}$ in (3.20) for these materials. We however choose to keep track of the partial density of states, to keep the calculations as general as possible.

For mono-atomic lattices, the density of states can be extracted directly from neutron scattering data through the incoherent structure factor. This is not always possible for multi-atomic lattices, since the scattering is only sensitive to the combination $\sum_d |\overline{f_d}|^2 D_d(\omega)/m_d$. To infer the individual $D_d(\omega)$ as well as $D(\omega)$, one therefore needs a set of scattering techniques which allows one to effectively vary the $\overline{f_d}$. This is not available for all materials, and it is therefore often most convenient to extract the $D_d(\omega)$ from DFT calculations. A comprehensive library of results has been made available by the materials project [79].

Returning now to the calculation of the autocorrelation function, we can expand the exponential term in (3.17) using the form of the correlator in (3.20). This yields an explicit representation of $C_{\ell d}$ as an expansion in number of phonons n being excited:

$$\begin{aligned} \mathscr{C}_{\ell d} =& \frac{2\pi}{V} e^{-2W_d(\mathbf{q})} \sum_n \frac{1}{n!} \left(\frac{q^2}{2m_d} \right)^n \\ & \times \left(\prod_{i=1}^n \int d\omega_i \frac{D_d(\omega_i)}{\omega_i} \right) \delta \left(\sum_j \omega_j - \omega \right) \end{aligned} \tag{3.23}$$

where the delta function arises from the time integral $\frac{1}{2\pi} \int dt\, e^{i(\sum \omega_i)t} e^{-i\omega t}$ and ensures energy

[5] In the literature, the density of states is also sometimes normalized to $3n_a$, where n_a is the atomic density.

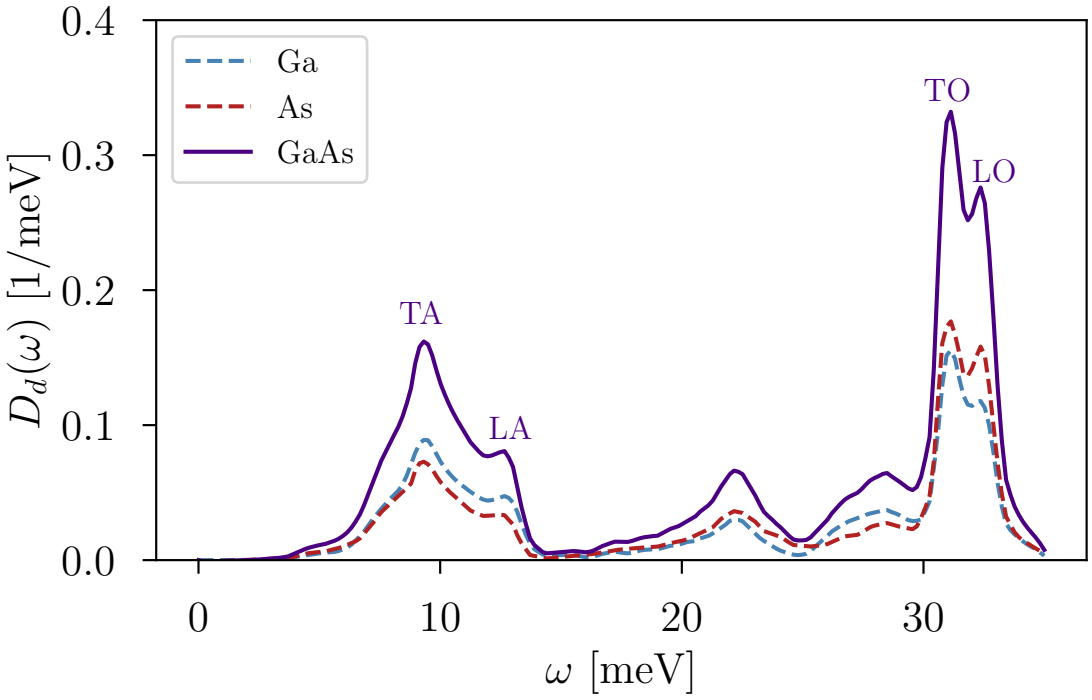

Figure 3.2. Partial and total density of states for GaAs [79]. Labels indicate the regions in which a particular phonon branch dominates.

conservation. Here, by using (3.20), the Debye-Waller function takes the form of

$$W_d(\mathbf{q}) = \frac{q^2}{4m_d} \int d\omega' \frac{D_d(\omega')}{\omega'}. \tag{3.24}$$

Thus, in comparison to the difficulties discussed surrounding (3.13), inputting this form of the correlator into (3.15) gives an analytic approximation for all phonon terms in the appropriate regime of validity.

In this paper, we utilize the incoherent approximation to calculate the contributions from higher-order phonon terms to an arbitrary degree in a simple and fast manner. This allow us to make rate predictions for the entire relevant mass range, going from the low-mass ($m_\chi \gtrsim$ keV) single phonon regime to the high-mass ($m_\chi \gtrsim 50$ MeV) nuclear recoil regime.

3.3 Processes

Using the autocorrelation function, (3.23), we can estimate the scale at which a generic n-phonon term starts becoming a relevant contribution to scattering. To organize the multiphonon expansion, it is useful to define an average phonon energy

$$\bar{\omega}_d \equiv \int d\omega' \omega' D_d(\omega'). \tag{3.25}$$

While $\bar{\omega}_d$ technically depends on the atom d, this just gives an $\mathcal{O}(1)$ dependence in the phonon scale. Since $n! \propto n^n$ at large n, we see that the nth term of the series (3.23) will roughly begin giving an $\mathcal{O}(1)$ contribution when

$$\frac{q^2}{2m_d \bar{\omega}_d} \sim n. \tag{3.26}$$

This means that for a given q (or consequently, m_χ) one can determine the dominant scattering processes. When $\frac{q^2}{2m_d\bar{\omega}_d} \lesssim 1$, single phonon excitations will be the primary channel; for $m_d \sim 30$ GeV and $\bar{\omega}_d \sim 30$ meV, this corresponds to $q \lesssim 30$ keV. Conversely, when $\frac{q^2}{2m_d\bar{\omega}_d} \gg 1$, phonons are no longer a suitable description and the scattering is instead well modeled by the recoil of a single nucleus. This transition occurs roughly at $q \gtrsim 2\sqrt{2m_d\bar{\omega}_d}$. In between these two extremes, we have $n \sim$ few, indicating multiphonon excitations as the primary process. The precise nature of the dominant process for a given m_χ will vary based on the mediator mass and experimental threshold.

In this section, we describe analytic approaches for characterizing the structure factor in crystal targets, broken into subsections corresponding to the previously mentioned processes. Secs. 3.3.1 and 3.3.2 deal with single phonon and two phonon excitations. Here we can also compare calculations of the full structure factor with the incoherent approximation. Sec. 3.3.3 deals with many phonon excitations, and Sec. 3.3.4 describes the impulse approximation, which gives a good approximation to the structure factor for momenta approaching the nuclear recoil

limit. For all numerical results in this section, we will assume a coupling to nucleons (replacing the generic average interaction strength $\overline{f_d}$ with the nucleon number A_d) for both massive and massless mediators, and take a GaAs target as a typical example of a simple cubic crystal of interest.

3.3.1 Single phonon production

If the unit cell contains at least two atoms, there are two types of phonons that can be produced: *acoustic* and *optical* phonons. As discussed in Sec. 3.2, DFT-based calculations for both single acoustic and single optical phonon excitations have been performed across a large dark matter mass range ($\sim$keV to GeV) [41, 60, 63]. Meanwhile analytic calculations so far have been limited $q \lesssim 1$ keV, which corresponds to $m_\chi \lesssim$ MeV [57, 42]. Although the DFT-based calculations span the entire mass range of interest and can provide information such as directional dependence, the numerics are more intensive; the phonon band structure, eigenvectors and structure factors must be calculated from first principles for each material. For high q, the sum over the reciprocal lattice must also be accounted for [58, 62]. Here we extend the analytic calculations to the high q regime by using the incoherent approximation. The comparison with the DFT results of [41] will also serve as a validation of the incoherent approximation.

To organize the calculations, it is useful to define a momentum scale ($q_{\rm BZ}$) which approximately reflects the size of the first Brillouin zone. We take $q_{\rm BZ} = \frac{2\pi}{a} \approx 2$ keV, where a is the lattice constant. We first review the single phonon response for $q < q_{\rm BZ}$. In this regime, we compute the structure factors in the isotropic approximation and in the limit $q \ll q_{\rm BZ}$. For this purpose we assume linear dispersions $\omega = c_s q$ for the longitudinal acoustic (LA) and transverse accoustic (TA) modes, with c_s replaced by $c_{\rm LA}$ and $c_{\rm TA}$ for the longitudinal and transverse sound speeds, respectively. The optical modes are assumed to have flat (constant) dispersions for the longitudinal optical (LO) and transverse optical (TO) phonon energies $\omega_{\rm LO}$ and $\omega_{\rm TO}$. The sound speeds and optical phonon energies are taken to be their long-wavelength values ($q = 0$). We

will refer to this set of assumptions as the *long-wavelength approximation*.

The matrix element is given by the leading non-trivial term in the small q expansion of (3.14). The only relevant contributions for $q \ll q_{\mathrm{BZ}}$ are those of the single LA and LO phonons. We approximate the long-wavelength acoustic eigenvectors as

$$\mathbf{e}_{\mathrm{LA},\mathbf{k},d} \approx \frac{\sqrt{A_d}}{\sqrt{\sum_{d'} A_{d'}}}\hat{\mathbf{k}}; \tag{3.27}$$

note that this form is valid for generic crystal targets and not limited to GaAs. For the LO phonon, we use the following eigenvectors, which are only valid for diatomic lattices [42]

$$\mathbf{e}_{\mathrm{LO},\mathbf{k},1} \approx \frac{\sqrt{A_2}}{\sqrt{A_1+A_2}}\hat{\mathbf{k}}, \tag{3.28}$$

$$\mathbf{e}_{\mathrm{LO},\mathbf{k},2} \approx -\frac{\sqrt{A_1}}{\sqrt{A_1+A_2}} e^{-i\mathbf{k}\cdot\mathbf{r}_2^0}\hat{\mathbf{k}} \tag{3.29}$$

where the first atom is taken to be at the origin of the primitive cell, and the second atom is taken to be at the coordinate $\mathbf{r}_2^0 = (a/4, a/4, a/4)$ for GaAs. The acoustic and optical transverse eigenvectors are orthogonal to these, but do not contribute to the scattering into a single phonon. With these approximations and taking $\overline{f_d} = A_d$, the analytic expressions for the single phonon contributions to the structure factor are [42]

$$S_{n=1,\mathrm{LA}}(q,\omega) \approx \frac{2\pi}{\Omega_c}\frac{(\sum_{d'} A_{d'})\,q^2}{2m_p\omega_{\mathrm{LA},q}}\delta(\omega-\omega_{\mathrm{LA},q})\Theta(\omega_{\mathrm{LO}}-\omega) \tag{3.30}$$

$$S_{n=1,\mathrm{LO}}(q,\omega) \approx \frac{2\pi}{\Omega_c}\frac{q^4a^2}{32\omega_{\mathrm{LO}}}\frac{A_1A_2}{m_p(A_1+A_2)}\delta(\omega-\omega_{\mathrm{LO}}) \tag{3.31}$$

$$S_{n=1}^{(q<q_{\mathrm{BZ}})}(q,\omega) = S_{n=1,\mathrm{LA}}(q,\omega) + S_{n=1,\mathrm{LO}}(q,\omega) \tag{3.32}$$

with Ω_c the volume of the primitive cell. Here we have introduced a cut-off of $\omega = \omega_{\mathrm{LO}}$ to the longitudinal acoustic branch to avoid overestimating the scattering rate with the LA mode near the edge of the Brillouin zone. The q^4 scaling and appearance of the lattice constant a

in the optical structure factor comes from averaging over angles with the eigenvectors, giving $(\mathbf{q}\cdot\mathbf{r}_2^0)^2 \approx q^2a^2/16$ [59].

For dark matter with a standard velocity dispersion $v \sim 10^{-3}$, the typical momentum transfer begins to fall outside the first Brillouin zone for $m_\chi \gtrsim 1$ MeV. Physically, this corresponds to the wavelength becoming smaller than the interatomic spacing, and the long-wave length formulas from (3.27) to (3.31) are no longer valid. We can however utilize the incoherent approximation in (3.15) and (3.23), which yields

$$S_{n=1}^{(q>q_{\rm BZ})}(q,\omega) \approx \frac{2\pi}{\Omega_c}\sum_d^{\rm n} e^{-2W_d(q)}(\overline{f_d})^2\,\frac{q^2}{2m_d}\frac{D_d(\omega)}{\omega}. \tag{3.33}$$

The forms of the structure factor are qualitatively quite different in the two q regimes. In the coherent regime $q < q_{\rm BZ}$, summing over the response of multiple atoms with constructive interference leads to a resonant response in (3.32). The impact of the interference is greatly reduced for $q > q_{\rm BZ}$, such that the incoherent approximation becomes a viable description.

While the sharp transition in the structure factor is an artifact of our approximations, (3.32)-(3.33) can accurately describe the integrated structure factor above or below $q_{\rm BZ}$. Fig. 3.3 compares our combined analytic single phonon description with numerical DFT calculations. For the DFT result we follow [41], computing the dynamical matrix and phonon dispersions with respectively VASP [80] and phonopy [77] (see also [60]), and take the angular average of $S(\mathbf{q},\omega)$ over all $\mathbf{q}$ directions for comparison with the isotropic approximation. The top panels show the structure factors in (3.32) as a function of q, integrated over ω. The top left panel shows $S(q,\omega)$ integrated over $\omega \in [1\,\text{meV}, 27\,\text{meV}]$ to select the acoustic phonon branches only and the top right panel shows the integral over $\omega \in [27\,\text{meV}, 40\,\text{meV}]$ for optical phonon branches. The analytic approximations are in good agreement with the DFT result in their respective regimes of validity. For $q < q_{\rm BZ}$, integrating (3.32) leads to respectively $\sim q$ and $\sim q^4$ scaling, while the incoherent approximation in (3.33) always scales as $\sim q^2$. As discussed above, the ω-dependence of the analytic structure factors is quite different in the two regimes, with the

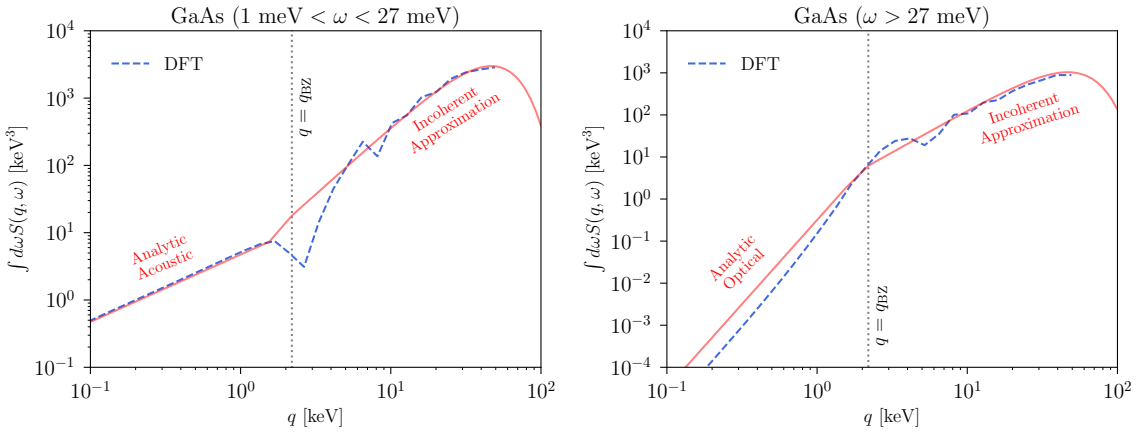

(a) Comparison of the integrated single phonon structure factor for GaAs. The left panel shows the structure factor integrated over $\omega = 1 - 27$ meV for acoustic phonon branches only and the right panel has $\omega = 27 - 40$ meV for optical phonon branches only. The dashed line shows the DFT result, averaged over all $\mathbf{q}$ directions, while the solid line shows our analytic approximation based on joining (3.32) (valid for $q < q_{\rm BZ}$) with the incoherent approximation (3.33) (valid for $q > q_{\rm BZ}$).

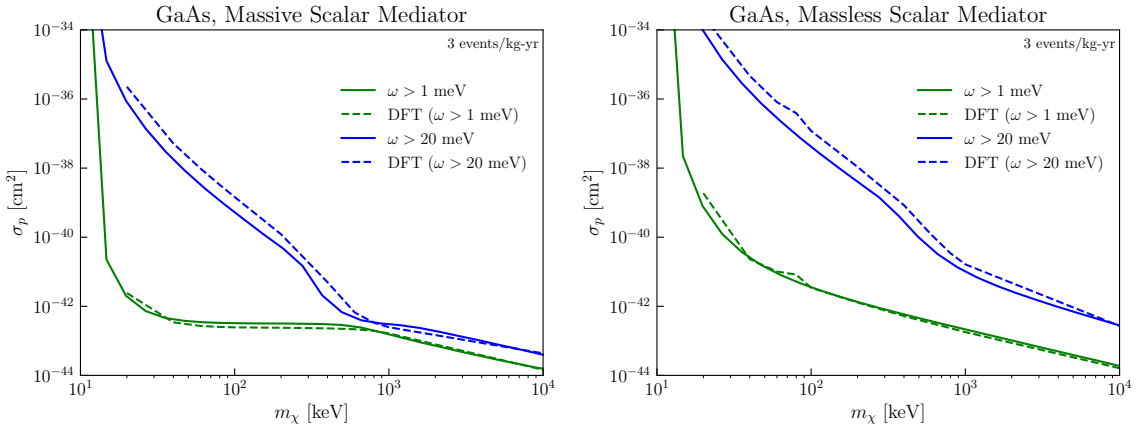

(b) Cross sections giving a rate of 3 events/kg-year, assuming $\overline{f_d} = A_d$. The rate is computed using our analytic single phonon structure factor approximation (solid) or with DFT calculations (dashed). We find that the analytic approach agrees with the DFT calculations within an $\mathcal{O}(1)$ factor.

Figure 3.3. Single phonon production.

coherent structure factor giving a resonant response around the single-phonon dispersion while the incoherent approximation is continuous in ω. However, the integrated result matches the full DFT calculation of the coherent structure factor well, indicating that the analytic approach will be useful in calculating integrated quantities such as rates. Furthermore, the analytic approach provides physical insight into the change in the q-scaling of the structure factor in Fig. 3.3a.

The plots in Fig. 3.3b show single phonon integrated rates for both massive and massless scalar mediators. For the massless mediator, scattering into the acoustic phonon specifically favors small q due to the $\propto q^{-4}$ contribution of the mediator form factor. The analytic result of (3.30) therefore applies across the entire DM mass range, as the large q contributions are negligible. For all other cases the structure factor scales with a positive power of q so that large q contributions are the most important. We therefore see a change in slope of the σ_p reach around $m_\chi \sim$ MeV, when $q \gtrsim q_{\rm BZ}$ becomes kinematically accessible. These features are captured by the $q > q_{\rm BZ}$ analytic description from the incoherent approximation, and again agree with the DFT results.

3.3.2 Two-phonon production ($q < q_{\rm BZ}$)

We next turn to the use and accuracy of the incoherent approximation for two-phonon production, in particular for $q < q_{\rm BZ}$. Single phonon production always dominates in this regime if above threshold [42]. It is however expected that there will be a phase in the experimental program for which the energy threshold will still be too high to access single optical and accoustic phonons, such that the formally subleading double phonon production can be relevant.

While the incoherent approximation is expected to be the least accurate for $q < q_{\rm BZ}$, it is still useful to compare it with existing analytical results for the structure factor. The analytic results are obtained in the long-wavelength approximation, as defined in Sec. 3.3.1. In this limit, the Wilson coefficients of the self-interaction operators for the acoustic modes can be extracted from the measured or calculated elasticity parameters. With these assumptions, one can explicitly evaluate (3.13) to second order in $q/\sqrt{m_d \omega}$ [42].

In this work, we will extend the long-wavelength calculations to all final states (see Appendix 3.A) and compare them with the incoherent approximation. For this purpose we extrapolate the results of Ref. [42] to higher q values and make a number of additional assumptions to model the self-interactions of the optical modes, thus giving the complete structure factor. For these reasons the calculations in this section should however be considered only a toy model of a GaAs-like crystal. We will show below that for this toy model and in the limit of small momentum transfer, the incoherent and long-wavelength approximations give qualitatively similar DM scattering rates.

From Ref. [42], the two-phonon structure factor can be written as

$$S(\mathbf{q},\omega) = S^{(\mathrm{harm})}(\mathbf{q},\omega) + S^{(\mathrm{anh})}(\mathbf{q},\omega) \tag{3.34}$$

in the long-wavelength limit. The first term is the structure factor in the harmonic limit (also referred to as the contact piece in [42]), where anharmonic corrections to the atomic potentials are neglected. It can be obtained by expanding (3.14) to second order, and evaluated analytically in the long-wavelength limit. The second term contains contributions to the structure factor from anharmonic interactions. In order to evaluate this, one needs to include a phonon self-interaction Hamiltonian in computing (3.14), as described in detail in [42]. The interactions of acoustic phonons are based on an effective three-phonon Hamiltonian valid in the long-wavelength limit, but to obtain a more complete picture we include a highly approximate three-phonon Hamiltonian for interactions involving optical phonons. These calculations are summarized in Appendix 3.A.

To perform the most meaningful comparison between the incoherent and long-wavelength approximations, we assume the following Debye model for the partial density of states for a diatomic crystal

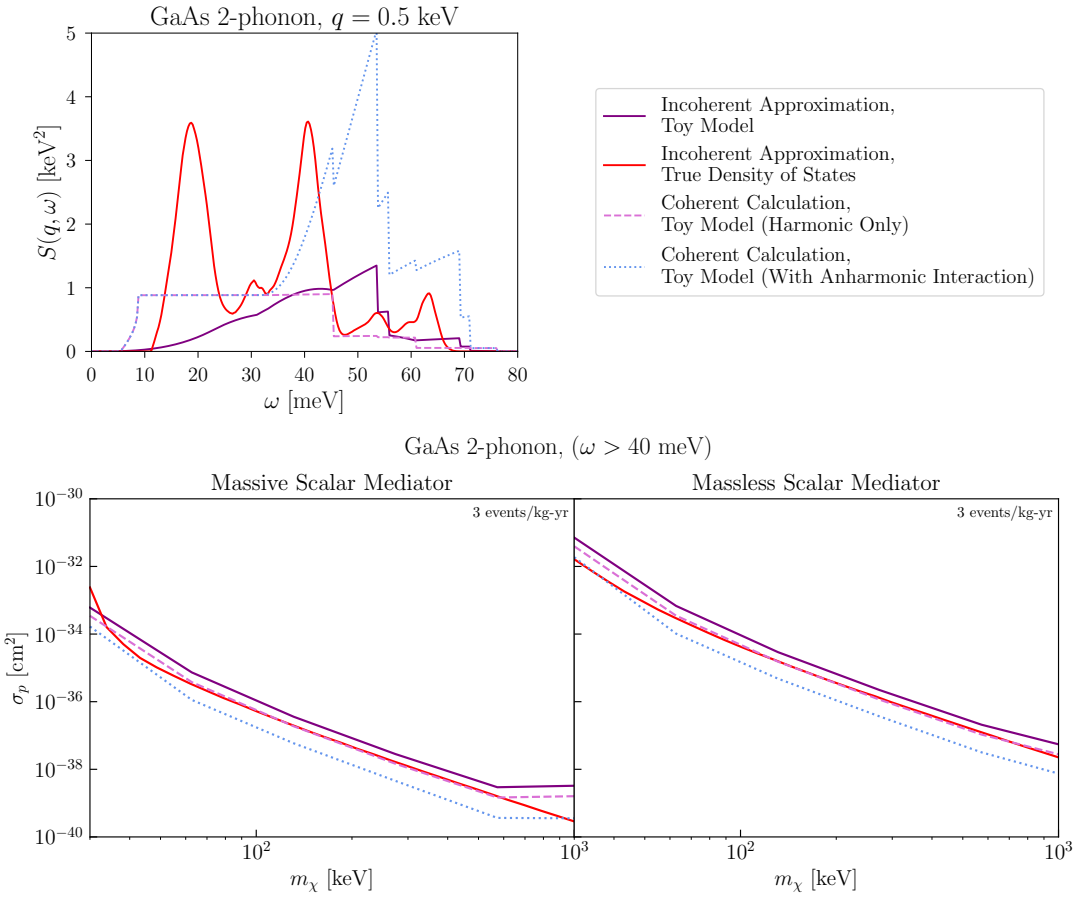

Figure 3.4. Two phonon production. *Top*: Comparison of the two-phonon structure factor calculated with various approximations, where the toy model assumes the long-wavelength approximation. Optical-optical channels give a δ-function and are not plotted. *Bottom*: Cross sections for producing two phonons at a rate of 3 events/kg-year using the same approximations as above. We restrict the mass range to $m_\chi \lesssim 1$ MeV so that typical q values are below $q_{\rm BZ}$, where our long-wavelength approximations are valid. The energy threshold is taken to be 40 meV, above the single phonon energies.

$$
\begin{aligned}
D_{1,2}(\omega) = \frac{1}{q_{\mathrm{BZ}}^3}\frac{1}{A_1+A_2} & \\
&\left(A_{1,2}\frac{\omega^2}{c_{\mathrm{LA}}^3}\Theta(c_{\mathrm{LA}}q_{\mathrm{BZ}}-\omega)\Theta(\omega)\right. \\
&+A_{1,2}\frac{2\omega^2}{c_{\mathrm{TA}}^3}\Theta(c_{\mathrm{TA}}q_{\mathrm{BZ}}-\omega)\Theta(\omega) \\
&+A_{2,1}\frac{q_{\mathrm{BZ}}^3}{3}\delta(\omega-\omega_{\mathrm{LO}}) \\
&\left.+A_{2,1}\frac{2q_{\mathrm{BZ}}^3}{3}\delta(\omega-\omega_{\mathrm{TO}})\right).
\end{aligned}
\tag{3.35}
$$

which is derived from the long-wavelength approximation as described in Sec. 3.3.1.[6] The explicit structure factor from using this toy density of states in (3.23) is given in Appendix 3.A, which for simplicity we evaluate with $A_1 = A_2$ for GaAs.

The top panel of Fig. 3.4 compares the calculations of the two-phonon structure factor in the incoherent and long-wavelength approximations. For the incoherent approximation, we show the result with the toy density of states in (3.35) as well as with the true density of states from Fig. 3.2. The dashed line shows the harmonic limit, meaning that $S^{(\mathrm{anh})}$ is neglected. This is the case that is most directly comparable to the incoherent approximation, which assumes the harmonic mode expansion in (3.12). For the dotted line, the leading phonon self-interactions were included.

In the harmonic limit, all modes scale as $\sim q^4$ except for optical-acoustic final state, which scales as $\sim q^6$. The incoherent approximation naturally misses these more subtle destructive interference effects, but still captures the correct q^4 scaling for most of the modes. We see in Fig. 3.4 that the incoherent approximation is within a factor of ~ 5 of the long-wavelength

[6] Here the maximum momentum of the modes is determined by requiring that the sum over all modes is equal to the total number of degrees of freedom. For GaAs and in the isotropic approximation, the exact momentum cutoff is about 2% different from $q_{\mathrm{BZ}} = 2\pi/a$. This error is negligible compared to the uncertainties on the other assumptions made in this section.

approximation for all $\omega > \omega_{\rm LO}$, for both the toy model and true density of states. The difference at smaller ω is not experimentally relevant, as the single phonon rate will completely dominate in this region. There are also delta-function terms from the optical-optical branches which do not appear in the plot; their contributions to the overall scattering rate are comparable for the incoherent and long-wavelength approximations as well. See Appendix 3.A for details. These terms dominate the scattering rate at higher energies, and overall we see in Fig. 3.4 that the incoherent approximation reproduces the structure factor in the harmonic limit to within a factor of few.

When anharmonic interactions are included, the difference becomes larger and the incoherent approximation may under-predict the rate by up to an order of magnitude in our estimate. However, as discussed above, the anharmonic Hamiltonian used is itself also only valid at the order of magnitude level, particularly for optical modes. We expect that our approach can model the rate in this regime at the order-of-magnitude level, but a proper DFT calculation is needed for it to be rigorously validated.

Finally, we show in the bottom panel of Fig. 3.4 a comparison of the cross sections corresponding to a rate of 3 events/kg year, with the different approximations for the two-phonon structure factor. We assume $\omega > 40$ meV, since for lower thresholds the rate is dominated by single-phonon production [42]. We emphasize that here we are only illustrating that the incoherent approximation is within a factor of few of the full structure factor, as long as the same assumptions are made for the phonon dispersion relations. Therefore, we restrict our comparison to $m_\chi <$ MeV such that we can restrict to $q < q_{\rm BZ}$. The incoherent approximation underestimates the rate by a factor of few in the harmonic limit, and up to an order of magnitude when anharmonic interactions are included. Using the true density of states slightly improves the agreement. Though this comparison only applies to a limited q range, our result suggests that the incoherent approximation should give a reasonable, order-of-magnitude estimate for multiphonon production even at low q. We expect this uncertainty to decrease for larger q where the incoherent approximation is most justified, and in particular we will see that the incoherent

approximation reproduces the expected rate in the free nuclear recoil limit, as discussed in the next sections.

3.3.3 Multiphonon production

In the previous section, where we dealt with $q < q_{\rm BZ}$, the incoherent approximation should be viewed as an order-of-magnitude estimate only. For $q > q_{\rm BZ}$, it is however on firm ground [75, 78] and is used routinely to measure the density of states from neutron scattering data [75]. Moreover, in the $q \gg q_{\rm BZ}$ regime multiphonon processes become important. This follows from the form of the structure factor, obtained by inserting (3.23) into the incoherent approximation (3.15):

$$S(\mathbf{q},\omega) \approx \frac{2\pi}{\Omega_c}\sum_d^{\mathfrak{n}} (\overline{f_d})^2 e^{-2W_d(\mathbf{q})} \sum_n \left(\frac{q^2}{2m_d}\right)^n \times \frac{1}{n!}\left(\prod_{i=1}^{n}\int d\omega_i \frac{D_d(\omega_i)}{\omega_i}\right)\delta\left(\sum_j \omega_j - \omega\right). \tag{3.36}$$

From the discussion around (3.26), the typical number of phonons is $n \sim \frac{q^2}{2m_d\bar{\omega}_d}$. With $\bar{\omega}_d \gtrsim 30$ meV and $m_d \gtrsim 30$ GeV for most crystals, the self-consistency condition for the incoherent approximation ($q \gtrsim q_{\rm BZ}$) is therefore always satisfied for $n > 2$ processes. The evolution of (3.36) for increasingly large q is shown in Fig. 3.5a.

We can obtain an approximate scaling for (3.36) by separating each term in the sum over n into q-dependent and ω-dependent parts. The ω-dependent part is given by the second line of the equation, which is only non-zero at $\omega \lesssim n\,\omega_{\rm LO}$ in order to satisfy the delta function. This part of the structure factor can be estimated to have at most the value of $1/(n!\,\bar{\omega}_d^{n+1})$; this is illustrated in Fig. 3.11 of Appendix 3.C, where we plot the numerical result. For $q \lesssim \sqrt{2m_d\bar{\omega}_d}$ (left and center panels of Fig. 3.5a), the Debye-Waller factor can be neglected and the structure factor then scales as $S(q,\omega) \propto \sum_n \frac{1}{n!}\left(\frac{q^2}{2m_d\bar{\omega}_d}\right)^n$. For $q^2/(2m_d\bar{\omega}_d) \lesssim 1$, the structure factor therefore scales as $S(q,\omega) \sim q^{2m}$, with m the lowest number of phonons that is kinematically allowed. This scaling

will be useful in Sec. 3.4, where we use it to extract the approximate scaling behavior of the DM cross section curves. It no longer holds for $q \gtrsim \sqrt{2m_d\bar{\omega}_d}$ (right-hand panel of Fig. 3.5a), where many modes contribute equally. This regime however can be understood in the impulse approximation, which is the subject of the next section.

3.3.4 The impulse approximation ($q \gg q_{\rm BZ}$)

For $q \gg q_{\rm BZ}$ the sum of the multiphonon terms asymptotes to an approximately Gaussian envelope, as can be seen most clearly from the rightmost panel in Fig. 3.5a. This asymptotic form can be derived directly with a steepest descent approximation, also known as the *impulse approximation*. It is valid whenever the interaction with the probe particle happens on a time scale short compared to that of the phonon modes.

To derive this, it is most insightful to take a step back from (3.36) and return to using (3.20) in (3.17). The auto-correlation function is then

$$\mathscr{C}_{\ell d} = \frac{1}{V} e^{-2W_d(\mathbf{q})} \int_{-\infty}^{\infty} dt\, e^{\frac{q^2}{2m_d}\int d\omega' \frac{D_d(\omega')}{\omega'} e^{i\omega' t}} e^{-i\omega t}. \tag{3.37}$$

When $q \gg \sqrt{2m_d\bar{\omega}_d}$, the exponent involving the density of states integral will be highly oscillatory in t, and the integral may be approximated by expanding about $t = 0$ through a steepest descent method. (See Appendix 3.B). Doing so gives

$$\mathscr{C}_{\ell d} \approx \frac{1}{V}\sqrt{\frac{2\pi}{\Delta_d^2}} \exp\left(-\frac{\left(\omega - \frac{q^2}{2m_d}\right)^2}{2\Delta_d^2}\right) \tag{3.38}$$

where $\Delta_d^2 \equiv \frac{q^2\bar{\omega}_d}{2m_d}$. This approximation is referred to as the impulse approximation since the saddle-point around $t = 0$ dominates the rate. The true peak is shifted slightly from the result (3.38), which can be corrected by including higher orders in the expansion [81]. Including these additional terms has negligible impact on later results.

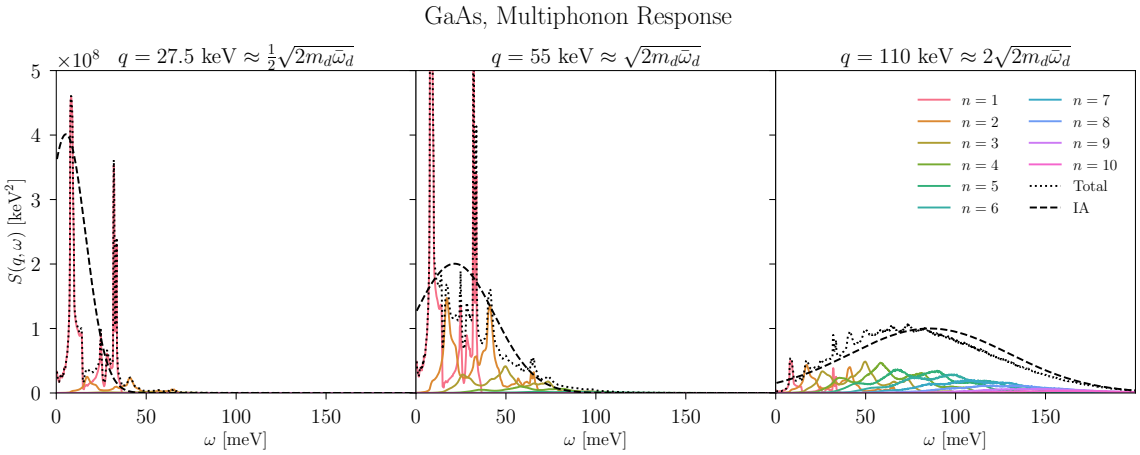

(a) The first ten phonon structure factors in the incoherent approximation for GaAs, plotted for various fixed q. At sufficiently large $q > \sqrt{2m_d\bar{\omega}_d}$, the total structure factor converges to the impulse approximation (IA, dashed line). In the right panel, there is a slight difference between the peak of the true structure factor and the impulse approximation. This can be accounted for in the impulse approximation by including higher orders in the steepest descent expansion [81].

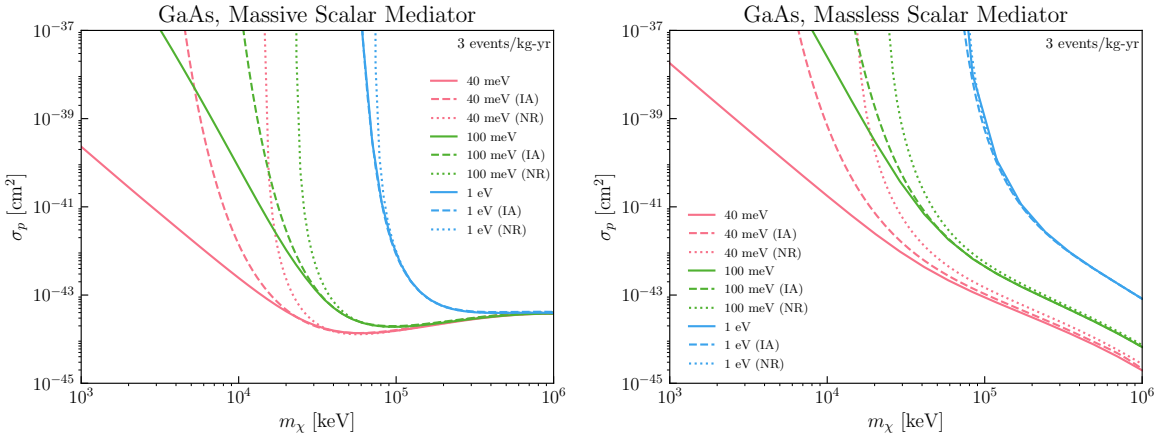

(b) Cross sections for 3 events/kg-yr in GaAs for a hadrophilic mediator. Rates are computed with the $n \leq 10$ phonon terms in the incoherent approximation (solid lines), the impulse approximation (IA; dashed), and the analytic free nuclear recoil result (NR; dotted). We see that at sufficiently high masses–and hence momentum transfers–the impulse approximation sufficiently recovers the result of summing the phonon terms. Likewise, for yet larger momenta the impulse approximation merges onto the free nuclear recoil result, as discussed in Sec. 3.3.4.

Figure 3.5. Multiphonon transition into the nuclear recoil regime.

From (3.38), we see that the structure factor in the impulse approximation is

$$S^{\mathrm{IA}}(q,\omega) = \sum_{d}^{\mathrm{n}} \frac{(\overline{f_d})^2}{\Omega_c} \sqrt{\frac{2\pi}{\Delta_d^2}} \exp\left(-\frac{\left(\omega - \frac{q^2}{2m_d}\right)^2}{2\Delta_d^2}\right) \tag{3.39}$$

which is a sum of Gaussians peaked around $q = \sqrt{2m_d\omega}$, one for each atom in the unit cell. In Fig. 3.5a we see that (3.39) is a reasonable approximation for $q \approx \sqrt{2m_d\bar{\omega}_d}$ and converges rapidly to the full result in (3.36) for $q \gtrsim 2\sqrt{2m_d\bar{\omega}_d}$. As expected, it does not capture the features in the structure factor for $q \lesssim \sqrt{2m_d\bar{\omega}_d}$. In our final results, we use (3.39) for $q > 2\sqrt{2m_d\bar{\omega}_d}$, as it is numerically much faster than (3.36). For crystals composed of multiple atoms, we define the boundary as $\max_d \left[2\sqrt{2m_d\bar{\omega}_d}\right]$. At this scale, the average number of phonons is about four, and it is sufficient to truncate the sum at $n = 10$ for all smaller q.

As we consider larger DM masses which access larger q and ω, the Gaussian becomes more sharply peaked. This can be seen by comparing the width Δ_d to the peak value $\omega = q^2/2m_d$. In the large-q limit, we have

$$\lim_{q\to\infty} \frac{\Delta_d}{\omega} \approx \sqrt{\frac{\bar{\omega}_d}{\omega}} \tag{3.40}$$

so the Gaussian becomes narrow for ω well above the typical phonon energy. Then the narrow width limit exactly reproduces the expected free nuclear recoil delta function response:

$$\lim_{q,\,\omega\to\infty} \mathscr{C}_{\ell d} = \frac{2\pi}{V}\delta\left(\omega - \frac{q^2}{2m_d}\right) \tag{3.41}$$

$$S^{\mathrm{FR}}(q,\omega) = \sum_{d} \frac{2\pi}{\Omega_c}(\overline{f_d})^2\,\delta\left(\omega - \frac{q^2}{2m_d}\right). \tag{3.42}$$

We therefore recover the familiar free nuclear recoil response for each individual atom in the unit cell.

In Fig. 3.5b we show cross section curves with a GaAs target, for both massive and massless scalar mediators. We compare the reach obtained with the full structure factor (in the incoherent approximation), the impulse approximation, and the free nuclear recoil limit. For

$m_\chi \lesssim 20-40$ MeV, the full structure factor must be used to capture the rate, depending on the mediator mass and threshold. For $m_\chi \gtrsim 20-40$ MeV, the q values compatible with the impulse approximation start to dominate, and we see that it reproduces the full result very closely. At even higher masses, the free nuclear recoil response becomes an excellent approximation, as expected.

A particular feature to notice from Fig. 3.5b is that the free nuclear recoil rate agrees with the impulse approximation result even in regions of the q, ω phase space where the Gaussian is not narrow. For example, for the massive mediator and $m_\chi = 50$ MeV, the rate will be dominated by momentum transfers $q \sim 2m_\chi v \sim 100$ keV, corresponding most closely to the rightmost panel of Fig. 3.5a. From (3.40) this gives $\Delta_d/\omega \approx 0.5$ which is not particularly small. The nuclear recoil approximation nevertheless works remarkably well. The reason is that phase space integral in (3.3) has a trivial ω dependence aside from the $S(\mathbf{q},\omega)$ factor, since the delta function in ω just determines the region of phase space that is integrated over. Therefore, as long as the energy threshold is small compared to the peak in ω, the phase space integral over (3.39) and (3.42) yields similar answers.

3.3.5 Summary

Fig. 3.6 schematically illustrates the various approximations for the structure factor discussed in this section. The boundaries reflect only our choice of approximation and not a sharp transition in the behavior of the structure factor. The dotted gray parabola represents the phase space boundary for a given m_χ and v (see Sec. 3.4). This parabola extends upwards and rightwards as m_χ is increased, such that multiple different regimes are sampled for high enough m_χ.

For the single phonon excitations ($n = 1$) described in Sec. 3.3.1, we use the long-wavelength and incoherent approximations for $q < q_{\mathrm{BZ}}$ and $q > q_{\mathrm{BZ}}$, respectively. This combination gives good agreement with a full DFT calculation of the scattering rate, at least for a cubic crystal such as GaAs.

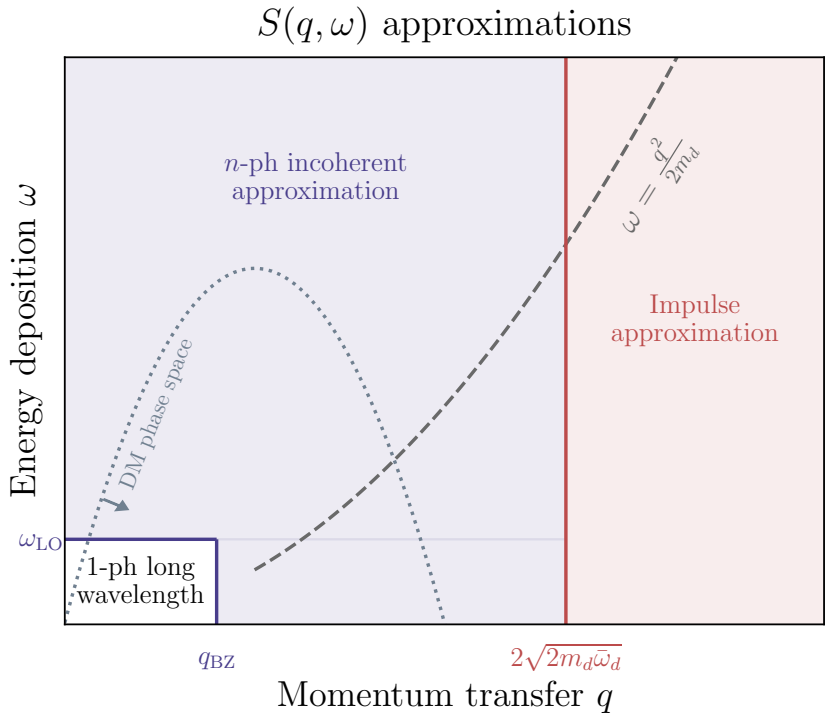

Figure 3.6. Schematic figure (not to scale) depicting the approximation used to calculate the structure factor in various regions of phase space. The "1-ph long wavelength" regime is discussed in Sec. 3.3.1, the "n-ph incoherent approximation" regime in Sec. 3.3.2 and 3.3.3 and the "Impulse approximation" region in Sec. 3.3.4.

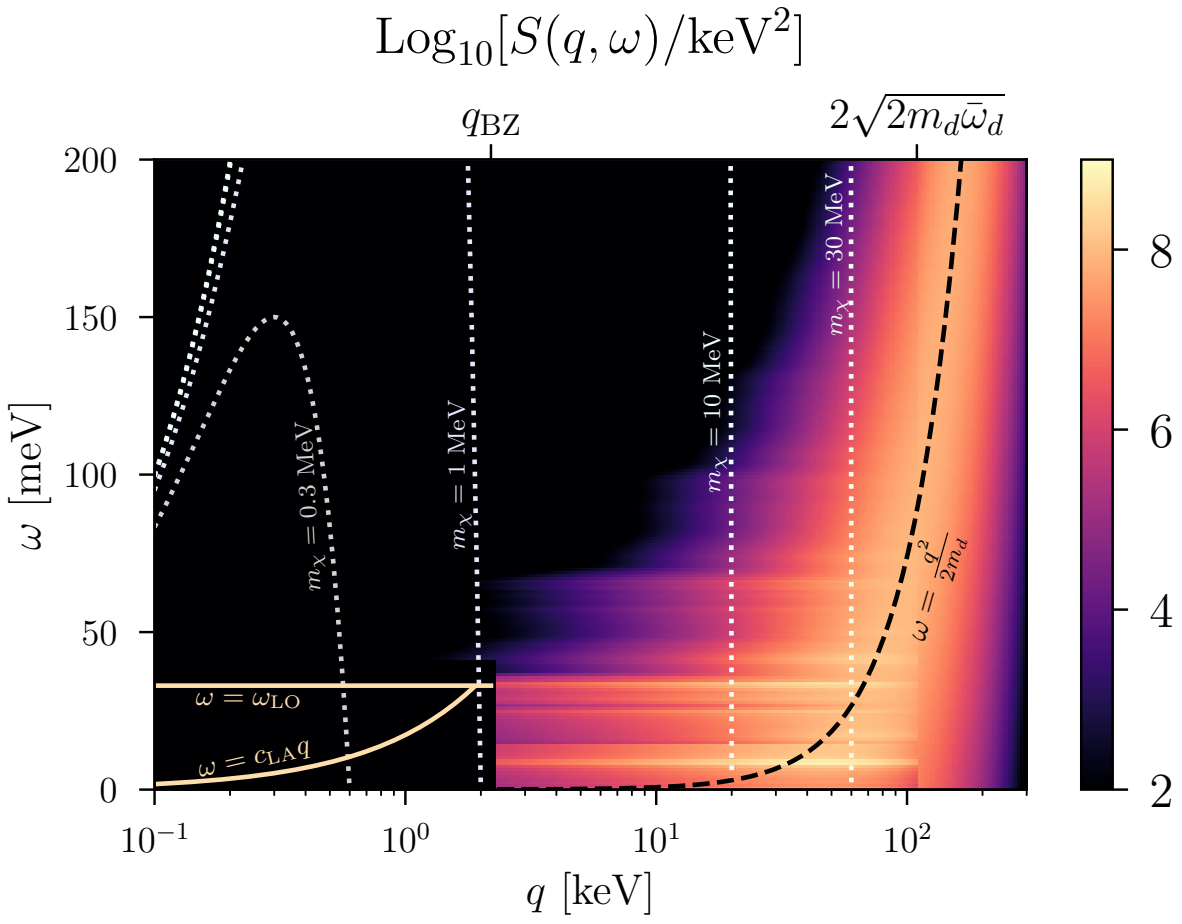

Figure 3.7. GaAs structure factor. Density plot of the structure factor in the same regimes of (q, ω) as shown in Fig. 3.6. Dotted lines are phase space boundaries for various DM masses with a typical initial velocity $v = 10^{-3}$. At low q and ω, the solid yellow lines are the dispersion relations of the single LA and LO phonons. At large q, the black dashed line is the free nuclear recoil dispersion relation; in general, there are separate lines for Ga and As but for clarity we show only one line corresponding to the average mass of Ga and As.

For multiphonon excitations ($n \geq 2$), we use the incoherent approximation for the structure factor for all q below $\max_d[2\sqrt{2m_d\bar{\omega}_d}]$. This is motivated by Sec. 3.3.2, where we argued that the incoherent approximation can serve as an order-of-magnitude estimate even for $q \ll q_{\rm BZ}$. Given the limitations of the long-wavelength approximation, a dedicated DFT calculation is needed in this regime. For multiphonon excitations, we sum terms in (3.36) until we achieve convergence, as explained in Sec. 3.3.3. Finally, for $q \geq \max_d[2\sqrt{2m_d\bar{\omega}_d}]$ we make use of the impulse approximation, which ultimately transitions into the well-known free nuclear recoil regime. This was explained in Sec. 3.3.4.

Fig. 3.7 shows our full calculation of the structure factor for GaAs, overlaid with the phase space boundaries for a few representative DM masses. In the low q, single phonon regime, the response is given by a set of δ-functions on the LO and LA phonon dispersions, represented by the orange curves. At intermediate and high q, the structure function is modeled by a continuous function, where the layered structure for $\omega \lesssim 50$ meV reflects the various single and multiphonon contributions. At higher q and ω the individual resonances cease to be visible and one transitions into the smooth $S(\mathbf{q},\omega)$ predicted by the impulse approximation. At very high ω the structure function converges towards its free nuclear recoil form, which is represented by the black dashed line.

3.4 Results

In this section we convert our newly-gained understanding of the structure factor into concrete predictions for the DM scattering rate in a crystal target. The event rate per unit of target mass is

$$R = \frac{1}{\sum_d m_d}\frac{\rho_\chi}{m_\chi}\int d^3\mathbf{v}\, v f(\mathbf{v}) \int d^3\mathbf{q}\, d\omega \frac{d\sigma}{d\mathbf{q}d\omega} \tag{3.43}$$

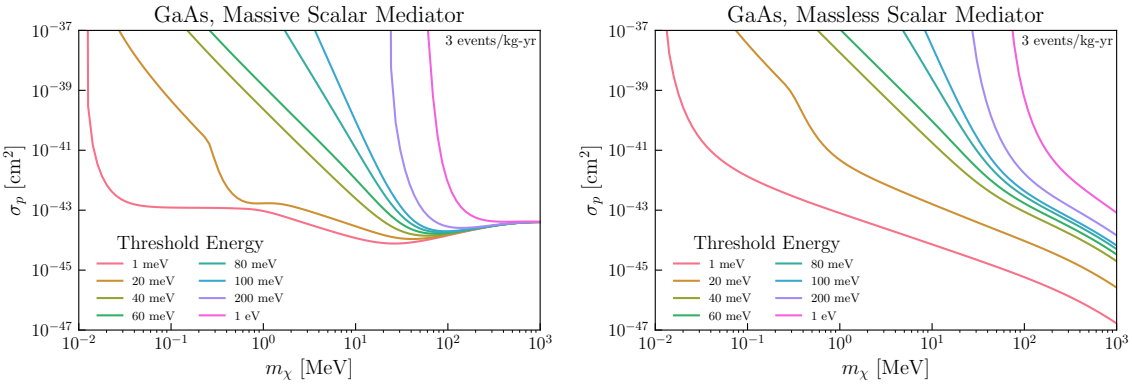

Figure 3.8. Cross section plots corresponding to a rate of 3 events/kg-yr for massive and massless scalar mediators in GaAs for various thresholds. The structure factors used are the analytic results demarcated in Fig. 3.6 for each corresponding regime in the (q,ω) phase space. For the massive mediator, we see the dominance of the single acoustic phonon at low masses and low thresholds, and of the optical phonon for intermediate thresholds. Eventually, for sufficiently high masses the process becomes dominated by the free nuclear recoil response. For the massless mediator, the q^{-4} form factor favors small momenta, and the rate is dominated by the lowest accessible mode for a given threshold.

where the experimental energy threshold is implicit in the boundary of the ω integral. $f(\mathbf{v})$ is the DM velocity distribution, which we take to be

$$f(\mathbf{v}) = \frac{1}{N_0}\exp\left[-\frac{(\mathbf{v}+\mathbf{v}_e)^2}{v_0^2}\right]\Theta\left(v_{esc}-|\mathbf{v}+\mathbf{v}_e|\right),$$
$$N_0 = \pi^{3/2}v_0^3\left[\mathrm{erf}\left(\frac{v_{esc}}{v_0}\right)-2\frac{v_{esc}}{v_0}\exp\left(-\frac{v_{esc}^2}{v_0^2}\right)\right], \tag{3.44}$$

with $v_0 = 220$ km/s, the Earth's average velocity $v_e = 240$ km/s, and $v_{\rm esc} = 500$ km/s the approximate local escape velocity of the Milky Way. The scattering rate can be further simplified in the isotropic limit; using (3.3),

$$R = \frac{1}{4\pi\rho_T}\frac{\rho_\chi}{m_\chi}\frac{\sigma_p}{\mu_\chi^2}\int d^3\mathbf{v}\frac{f(\mathbf{v})}{v}\int_{q_-}^{q_+}dq\int_{\omega_{\rm th}}^{\omega_+}d\omega\, q\,|\tilde{F}(q)|^2 S(q,\omega) \tag{3.45}$$

where $\omega_{\rm th}$ is the energy threshold of the experiment, and the other integration limits[7] are

$$q_\pm \equiv m_\chi v \left(1 \pm \sqrt{1 - \frac{2\omega_{\rm th}}{m_\chi v^2}}\right) \tag{3.46}$$

$$\omega_+ \equiv qv - \frac{q^2}{2m_\chi}. \tag{3.47}$$

Note (4.75) defines the phase space boundary shown in Fig. 3.6 for a given m_χ and v. Finally, ρ_T is the mass density of the target material and we have recast the rate in terms of the DM-proton scattering cross section $\sigma_p \equiv 4\pi b_p^2$.

3.4.1 Massive hadrophilic mediator

In the case of a massive mediator coupling to baryon number, we calculate the scattering rate by taking $\overline{f_d} = A_d$ and $\tilde{F}(q) = 1$. The cross sections corresponding to a rate of 3 events/kg-year exposure are shown in the left panel of Fig. 3.8, assuming a GaAs target and for different energy thresholds. The same figures for Si, Ge and diamond can be found in Appendix 3.D.

We can understand the numerical results in Fig. 3.8 analytically using the scaling of the structure factor discussed in Secs. 3.3.1–3.3.4. First, from (4.73), the m_χ dependence of the rate is contained in

$$R \propto \frac{\sigma_p}{m_\chi \mu_\chi^2} \int_{q-}^{q+} dq \int_{\omega_{\rm th}}^{\omega_+} d\omega\, q\, S(q,\omega). \tag{3.48}$$

The structure factor only contains positive powers of q across the entire phase space, so for a massive mediator, the integral (3.48) will be dominated by the largest kinematically accessible momentum transfers.

For $m_\chi \gg 30$ MeV, the kinematically allowed phase space is extended to q and ω where the free nuclear recoil approximation can be used. The rate therefore approximately scales as $R \sim 1/m_\chi$ for $m_p \gtrsim m_\chi \gg 30$ MeV. For low enough thresholds, this scaling holds even as the

[7] In numerical implementations of (4.73), as done in `DarkELF`, it is beneficial to change the order of integration by first integrating over v, then q, and finally over ω.

dark matter mass comes within $O(\text{few})$ of 30 MeV, where the structure factor is relatively broad in ω. The reason is that the kinematically allowed phase space is wide enough in ω that the integral over the Gaussian in the impulse approximation gives within a factor of few of the integral over the delta function in (3.42), as discussed earlier in Sec. 3.3.4.

For dark matter masses of 1 to 30 MeV, the allowed phase space is restricted to values of $q < \sqrt{2m_d\bar{\omega}}$. Here the structure factor can be expanded in powers of $q/\sqrt{2m_d\bar{\omega}}$ and favors small ω. As noted in Sec. 3.3.3 the structure factor scales as $\sim q^{2m}$, with m the smallest number of phonons whose total energy is above the energy threshold. We see there is significant threshold dependence: the single phonon final state strongly dominates the rate if it is above the energy threshold, while for higher thresholds only multiphonons contribute. The rate integral now scales as

$$R \propto \frac{\sigma_p}{m_\chi^3} \int^{2m_\chi v} dq\, q^{2m+1} \int_{\omega_{\text{th}}} d\omega \propto \sigma_p\, m_\chi^{2m-1}, \tag{3.49}$$

where q was evaluated at its maximum $q \sim 2m_\chi v$. The ω integral does not contribute to the m_χ scaling of the rate, since the integrand is peaked in ω somewhere near the energy threshold ω_{th}. This expression then gives the approximate scaling $R \propto m_\chi^{2m-1}$. Since m is dependent on the energy threshold, this explains why different thresholds in Fig. 3.8 result in a different scaling as a function of m_χ.

At even lower dark matter masses ($m_\chi < 1$ MeV), the phase space is restricted to q values within the first Brillouin zone, which is dominated by single phonon production in the long wavelength regime. If the threshold is low enough to access a single phonon, the scaling further depends on whether the threshold captures an appreciable part of the LA branch. If so, the leading contribution comes from the acoustic mode (3.30), which gives

$$R \propto \frac{\sigma_p}{m_\chi^3} \int^{2m_\chi v} dq\, q^2 \int d\omega\, \delta(\omega - c_{\text{LA}} q) \propto \sigma_p, \tag{3.50}$$

approximately independent of m_χ. This behavior is clearly reproduced in Fig. 3.8 for the 1 meV

threshold, for which the acoustic branch is always accessible. If the threshold is too high to access the acoustic branch, but can detect the optical branch, the structure factor has an extra q^3 scaling and we find $R \propto m_\chi^3$. This case occurs for $m_\chi \lesssim 0.3$ MeV on the 20 meV curve in Fig. 3.8. For $m_\chi \gtrsim 0.3$ MeV the DM can excite the acoustic branch, resulting in a sharp enhancement of the rate.

3.4.2 Massless hadrophilic mediator

If we instead have a massless mediator that couples to baryon number, then by convention, the mediator form factor is taken to be $|\tilde{F}(q)|^2 = \left(\frac{m_\chi v_0}{q}\right)^4$ with $v_0 = 220$ km/s. The cross section curves for this scenario are given in the right panel of Fig. 3.8 again for different thresholds.

As in Sec. 3.4.1, we can analytically explain the scaling of the different curves across the DM mass range. The main difference with the massive mediator case is that for a massless mediator, there is a $1/q^4$ scaling in the form factor, which leads to a scattering rate that generally favors low q and ω. The main contribution to the rate will therefore be much more threshold dependent across all DM masses.

If the threshold is small enough to access single acoustic phonon excitations, then this will be the dominant contribution to the rate at all masses. Again from (4.73) and using the analytic acoustic structure factor, the rate for thresholds that are sensitive to a single acoustic phonon scales as

$$R \propto \sigma_p m_\chi \int_{\omega_{\rm th}/c_{\rm LA}} dq \frac{1}{q^2} \int d\omega\, \delta(\omega - c_{\rm LA} q). \tag{3.51}$$

The integrand is largest at the smallest q, so we estimate the q integral by evaluating the integrand at $q \approx \omega_{\rm th}/c_{\rm LA}$ in (4.74). The integrand therefore has no m_χ dependence and gives the scaling $R \propto m_\chi$ for the $\omega > 1$ meV curve in Fig. 3.8. Note however that this scaling behavior is sensitive to our convention for the reference momentum in $\tilde{F}(q)$. For example, in models with both electron and nucleon couplings one often chooses to normalize the form factor with the reference momentum $q_0 = \alpha m_e$, which would yield $R \propto m_\chi^{-3}$.

If the LA branch is not accessible but the LO branch is, the production of a single LO mode will generally dominate. This introduces a different m_χ dependence, which can be seen in Fig. 3.8 by comparing the 1 meV and 20 meV curves in the region with $m_\chi \lesssim 30$ MeV. If $m_\chi < 1$ MeV, using the expression in (3.31) gives

$$R \propto \sigma_p m_\chi \int^{2m_\chi v} dq\, q \int d\omega\, \delta(\omega - \omega_{LO}). \tag{3.52}$$

Unlike for the acoustic phonon, the structure factor favors high q so that the largest contribution is near $q \sim 2m_\chi v$, giving $R \propto m_\chi^3$. If $m_\chi > 1$ MeV, the rate integrand is dominated by momentum transfers $q \sim q_{\rm BZ}$. This is because when $q > q_{\rm BZ}$ and $\omega \leq \omega_{\rm LO}$ we are using the incoherent approximation for single phonon production, where the q integrand drops as q^{-1}. Thus, we estimate the rate by integrating up to $q_{\rm BZ}$ only:

$$R \propto \sigma_p m_\chi \int^{q_{\rm BZ}} dq\, q \int d\omega\, \delta(\omega - \omega_{LO}), \tag{3.53}$$

and find that $R \propto m_\chi$. This is the reason why the 20 meV curve in Fig. 3.8 changes slope around $m_\chi \sim 1$ MeV.

We next turn to the intermediate mass range ($1 - 30$ MeV) with $\omega_{\rm th} > \omega_{\rm LO}$, such that $n \geq 2$ phonons. In Fig. 3.8 this corresponds to the curves with thresholds of 40 meV and above. As in Sec. 3.4.1, we again notice that the leading contribution to the structure factor will be given by the smallest number of phonons, m, that can exceed the threshold energy. In this regime, the integrand $\propto S(q,\omega)/q^3$ scales with positive powers of q for $m \geq 2$ phonons, since (3.23) grows faster than q^3. The analysis for multiphonons then follows exactly the same logic as the discussion in the previous section and we find that $R \propto m_\chi^{2m-1}$.

For large dark matter masses ($\gg 30$ MeV), again if the threshold is well above the single phonon energy, we can apply the free nuclear recoil approximation to obtain the scaling. Using

the free nuclear structure factor gives

$$R \propto \frac{\sigma_p}{m_\chi^3} \int_{\sqrt{2m_d\omega_{\rm th}}} dq\, q \Big(\frac{m_\chi v_0}{q}\Big)^4 \int d\omega\, \delta\big(\omega - \frac{q^2}{2m_d}\big). \tag{3.54}$$

The q-integral is dominated by low-momentum transfers along the free nuclear recoil dispersion, so we evaluate the integral at the intersection of $\omega = \omega_{\rm th}$ and $\omega = \frac{q^2}{2m_d}$, or $q = \sqrt{2m_d\omega_{\rm th}}$. Then, the approximate scaling in this regime is $R \propto m_\chi/\omega_{\rm th}$, which we verify numerically in Fig. 3.8.

3.4.3 Dark photon mediators

The defining feature of a dark photon mediator is that it couples to the electric charge of the SM particles. In the regime where phonons are the relevant degrees of freedom, the charge of the nucleus is (partially) screened by the electrons. This means that we need a notion of an *effective charge*, as seen by the DM, which is momentum dependent. For individual atoms, this effective charge interpolates between zero in the low momentum, fully screened regime and the nuclear charge in the high momentum regime. We use the calculations from Brown et. al. [82] of the effective charge for individual atoms, as shown in Fig. 3.9. We expect this approximation to hold only for $q \gtrsim q_{\rm BZ}$, since additional many-body effects should be relevant for $q < q_{\rm BZ}$. This is particularly true for a polar material such as GaAs, where the Born effective charge of the Ga and As atoms is non-zero in the $q \to 0$ limit. In this regime a full DFT calculation of the momentum dependence of the effective charge is needed, which we do not attempt here.

In this work, we will therefore focus on the momentum regime $q \gtrsim q_{\rm BZ}$, which corresponds to $m_\chi \gtrsim$ MeV. In this case we can use the incoherent approximation and take $\overline{f_d} = Z_d(q)$, with $Z_d(q)$ the atomic effective charges in Fig. 3.9. This allows us to compute scattering rates with dark photon mediators for the production of two or more phonons, which is dominated by the highest kinematically accessible momentum transfers.

The regime $q < q_{\rm BZ}$ is relevant primarily for massless dark photon mediators. (For massive dark photon mediators, there are strong BBN constraints that severely limit the scattering

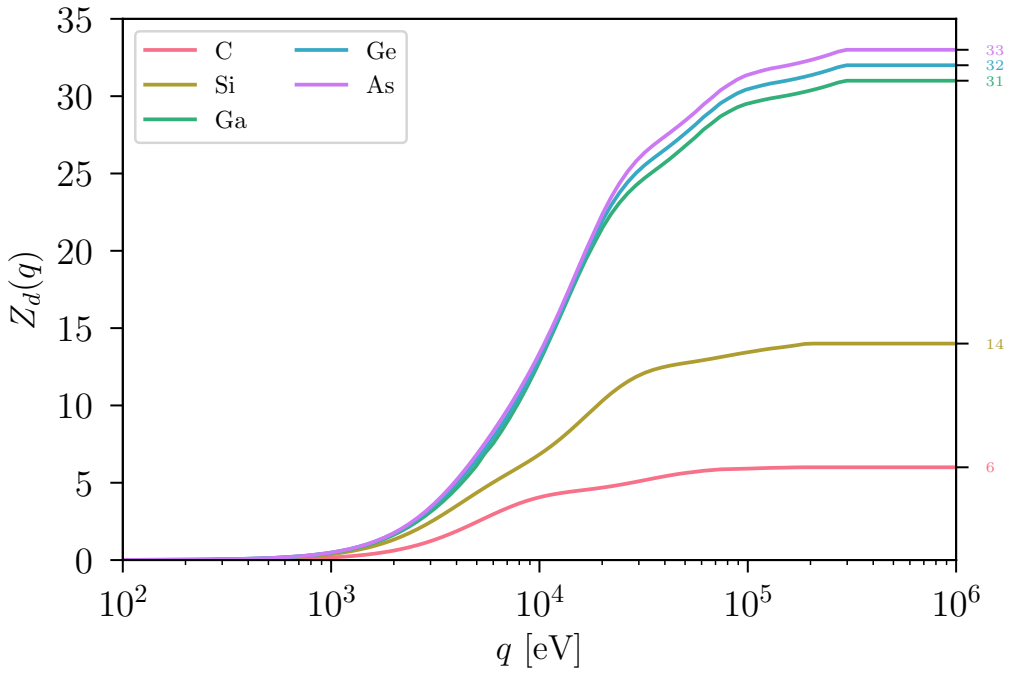

Figure 3.9. Momentum dependence of the effective ion charge for atomic elements, as computed in [82].

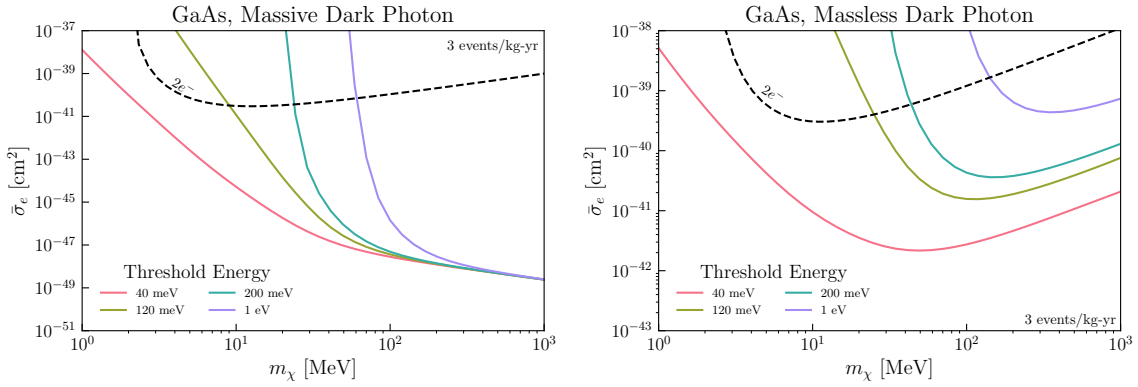

Figure 3.10. Cross section plots for a rate of 3 events/kg-year in GaAs, for massive and massless dark photon mediators. For comparison, the dashed black lines represent the cross sections required for DM-electron scattering with a $2e^-$ ionization threshold with the same exposure, as computed using `DarkELF` [83, 74].

rate for sub-MeV dark matter, see e.g. [34].) In this regime, there are substantial deviations from the atomic effective charges due to the delocalized nature of the valence electrons. For instance, a polar material such as GaAs, SiC and sapphire can have a residual dipole moment associated with atomic displacements even for $q \to 0$. The effective couplings $\bar{f}_d$ in this limit are given by Z_d^*/ε_∞, where Z_d^* is the Born effective charge and ε_∞ is a screening due to valence electrons; the Born effective charges can be calculated with DFT methods [41, 60, 62]. This was treated in previous studies of single-phonon production through a massless dark photon mediator [57, 41, 58, 59, 60, 61, 62, 63]. For non-polar materials such as Si, Ge and diamond, the Born effective charges vanish and instead multiphonon production is expected to dominate. This can be estimated with the energy loss function [74], at least for sub-MeV dark matter. Since this $q < q_{\rm BZ}$ regime is already included in `DarkELF` [74], we restrict our results here to multiphonon processes with $q > q_{\rm BZ}$ and $\omega > \omega_{\rm LO}$.

Our results are shown in Fig. 3.10 for GaAs; the results for Ge, Si and diamond are deferred to Appendix 3.D. As is conventional for dark photon mediators, we choose the reference momentum for the massless mediator to be $q_0 = \alpha m_e$ and present the results in terms of the effective DM-electron cross section $\bar{\sigma}_e$ [84], with

$$\bar{\sigma}_e = \frac{\mu_{\chi e}^2}{\mu_\chi^2}\sigma_p \tag{3.55}$$

and $\mu_{\chi e}$ the DM-electron reduced mass. In our calculations using the atomic effective charges, we impose $q > q_{\rm BZ}$ to ensure we are not sampling the area of phase space for which these charges are clearly invalid. This means that our rate calculations for $m_\chi \lesssim 10$ MeV are a slight underestimate of the true result.

3.5 Conclusions and outlook

It is well-known that DM scattering in crystals can lead to one or more phonons being produced if DM has MeV-scale mass, as well as a recoiling nucleus if DM has GeV or higher

mass. These processes are two sides of the same coin, depending on whether the momentum transfer is comparable to the inverse of the interparticle spacing and whether the energy deposition is comparable to the typical phonon energy $\sim \bar{\omega}$. When both momentum and energy scales are small, single phonon production dominates, and when both are large, nuclear recoils dominate. Here we studied the intermediate regime which is dominated by many phonons, which allows us to smoothly interpolate between single phonon production and nuclear recoils (see Fig. 3.8).

To make the multiphonon calculation tractable, we relied on the isotropic, incoherent, and harmonic crystal approximations. This allowed us to obtain analytic results for the scattering rate in terms of the phonon density of states in the crystal. These approximations are expected to be very good for $q \gg q_{\mathrm{BZ}}$ ($m_\chi \gg 1$ MeV), as they explicitly reproduce the nuclear recoil limit when $q \gg \sqrt{2 m_N \bar{\omega}}$. For $q \lesssim q_{\mathrm{BZ}}$ ($m_\chi \lesssim 1$ MeV) the experimental threshold determines which theoretical treatment is most appropriate: for single phonon production, one can obtain analytic formulas by instead using a long wavelength, isotropic approximation. These results are currently only valid for cubic crystals such GaAs, Si, Ge and diamond. For strongly anisotropic materials such as sapphire, one must find a way to generalize them further or rely on DFT calculations. For multiphonon production and $q \lesssim q_{\mathrm{BZ}}$, the situation is more complicated: in this case it cannot be taken for granted that anharmonic corrections to the various multiphonon channels can be neglected. The anharmonic multiphonon contributions involving optical modes are particularly difficult to model analytically, and at the moment we perform a simple estimate in a toy model to justify extrapolating the incoherent and harmonic approximations to $q \lesssim q_{\mathrm{BZ}}$. A dedicated DFT calculation is needed to improve their accuracy.

Our approach provides a smooth description of sub-GeV dark matter scattering down to keV masses for hadrophilic mediators. For dark photon mediators, a DFT calculation of the momentum-dependent couplings in the $q \sim q_{\mathrm{BZ}}$ regime is needed to complete the interpolation. For both mediators, we have provided results for multiple direct detection materials of interest, and also included our calculation as part of the `DarkELF` public code package. These will be essential to interpret direct detection results as experimental thresholds for calorimetric detectors

reach the eV scale and lower.

Acknowledgements

We are grateful to So Chigusa, Sinéad Griffin, Bashi Mandava and Mukul Sholapurkar for useful discussions. BCD, TL, and EV were supported with Department of Energy grants DE-SC0019195 and DE-SC0022104, as well as a UC Hellman fellowship. SK was supported by the Office of High Energy Physics of the U.S. Department of Energy under contract DE-AC02-05CH11231. EV is supported by a Sloan Scholar Fellowship. Chapter 3, in full, is a reprint of the material as it appears in Brian Campbell-Deem, Simon Knapen, Tongyan Lin, and Ethan Villarama, Dark matter direct detection from the single phonon to the nuclear recoil regime, Phys.Rev. D **106** (2022) no.3, 036019. The dissertation author was one of the primary investigators and authors of this paper.

Appendix

3.A Two phonon analytic structure factors

In Sec. 3.3.2 we compared the long-wavelength and incoherent approximations for the two-phonon final states, for q within the first BZ. In this appendix we provide the analytic expressions for both approximations.

3.A.1 Long-wavelength approximation

Here we discuss how we extend the analytic calculations from [42] for the coherent two-phonon structure factor to additional combinations of final state phonon pairs. As in Sec. 3.3.2, we assume a hadrophilic mediator with $\overline{f_d} = A_d$ throughout this appendix. It was shown in [42] that the structure factor separates into harmonic and anharmonic contributions

$$S(\mathbf{q},\omega) = S^{(\mathrm{harm})}(\mathbf{q},\omega) + S^{(\mathrm{anh})}(\mathbf{q},\omega) \tag{3.56}$$

which do not interfere at leading order in the long wavelength limit. The first term involves expanding (3.13) to second order; note that it was referred to as the contact term in [42]. The anharmonic term is computed using an anharmonic phonon interaction Hamiltonian to first order. The specific matrix elements to be used are given in equations (12) and (13) of [42]. We take the long-wavelength approximation for the phonon modes, as described in Sec. 3.3.1. For a crystal

with two atoms in the unit cell, the longitudinal eigenvectors can be approximated by

$$\mathbf{e}_{\mathrm{LA},\mathbf{k},1} \approx \frac{\sqrt{A_1}}{\sqrt{A_1+A_2}}\hat{\mathbf{k}}, \tag{3.57}$$

$$\mathbf{e}_{\mathrm{LA},\mathbf{k},2} \approx \frac{\sqrt{A_2}}{\sqrt{A_1+A_2}}e^{-i\mathbf{k}\cdot\mathbf{r}_2^0}\hat{\mathbf{k}} \tag{3.58}$$

$$\mathbf{e}_{\mathrm{LO},\mathbf{k},1} \approx \frac{\sqrt{A_2}}{\sqrt{A_1+A_2}}\hat{\mathbf{k}}, \tag{3.59}$$

$$\mathbf{e}_{\mathrm{LO},\mathbf{k},2} \approx -\frac{\sqrt{A_1}}{\sqrt{A_1+A_2}}e^{-i\mathbf{k}\cdot\mathbf{r}_2^0}\hat{\mathbf{k}}. \tag{3.60}$$

with $\hat{\mathbf{k}}$ the unit vector along the phonon propagation direction. Note that the $\mathbf{r}_2^0$ dependence was neglected in the LA eigenvector in (3.27) and in [42]; here we have kept this additional phase so that the acoustic and optical eigenvectors are explicitly orthogonal across a unit cell. This additional phase factor will only be relevant in cases where there is a destructive interference in the leading coupling to acoustic phonons, which occurs for some final states [59]. The transverse eigenvectors lay in the plane perpendicular to $\hat{\mathbf{k}}$ and have analogous normalizations.

Analytic expressions for the harmonic structure factor were provided in Ref. [42] for acoustic-acoustic final states only. We require expressions for the optical-optical and optical-acoustic final states as well to perform the comparison with the incoherent approximation. A straightforward application of (16) in [42] to the lowest order in q gives

$$\begin{aligned}
S^{(\mathrm{harm})}_{\mathrm{LOLO}} &= \frac{2\pi}{\Omega_c}\frac{\pi q^4}{120 m_p^2 \omega_{\mathrm{LO}}^2}\delta(\omega - 2\omega_{\mathrm{LO}}) \\
S^{(\mathrm{harm})}_{\mathrm{LOTO}} &= \frac{2\pi}{\Omega_c}\frac{\pi q^4}{90 m_p^2 \omega_{\mathrm{LO}}\omega_{\mathrm{TO}}}\delta(\omega - (\omega_{\mathrm{LO}} + \omega_{\mathrm{TO}})) \\
S^{(\mathrm{harm})}_{\mathrm{TOTO}} &= \frac{2\pi}{\Omega_c}\frac{\pi q^4}{45 m_p^2 \omega_{\mathrm{TO}}^2}\delta(\omega - 2\omega_{\mathrm{TO}})
\end{aligned} \tag{3.61}$$

for the optical-optical modes.

For the optical-acoustic modes, the harmonic structure factors are of the form

$$S^{(\mathrm{harm})}_{\mathrm{LOLA}} = \frac{2\pi}{\Omega_c} \frac{a^5}{2304\pi^2 c^2_{\mathrm{LA}} m_p^2 \omega_{\mathrm{LO}}} \frac{A_1 A_2}{(A_1+A_2)^2} \left(\frac{\omega - \omega_{\mathrm{LO}}}{c_{\mathrm{LA}}} \right)^7 \times g^{(\mathrm{harm})}_{\mathrm{LOLA}}(x)\, \Theta(c_{\mathrm{LA}} q_{\mathrm{BZ}} - (\omega - \omega_{\mathrm{LO}})), \tag{3.62}$$

where $x \equiv \frac{c_{\mathrm{LA}} q}{\omega - \omega_{\mathrm{LO}}}$. The other structure factors for optical-acoustic final states are given by relabelings LO $\to$ TO, LA $\to$ TA, where the expressions g expanded at small q are

$$\begin{aligned}
g^{(\mathrm{harm})}_{\mathrm{LOLA}}(x \ll 1) &\approx \frac{3}{10}x^6 - \frac{1}{7}x^8 + \frac{1}{15}x^{10} \\
g^{(\mathrm{harm})}_{\mathrm{LOTA}}(x \ll 1) &\approx \frac{1}{5}x^6 + \frac{12}{35}x^8 - \frac{4}{105}x^{10} \\
g^{(\mathrm{harm})}_{\mathrm{TOLA}}(x \ll 1) &\approx \frac{1}{5}x^6 + \frac{1}{7}x^8 - \frac{1}{15}x^{10} \\
g^{(\mathrm{harm})}_{\mathrm{TOTA}}(x \ll 1) &\approx \frac{4}{5}x^6 - \frac{12}{35}x^8 + \frac{4}{105}x^{10}.
\end{aligned} \tag{3.63}$$

We see that at leading order in small q, the optical-acoustic structure factors are all suppressed by an additional factor of q^2 relative to the optical-optical modes, which is due to destructive interference. Since we will be comparing with the incoherent approximation at small q, we can effectively neglect these final states.

We would also like to compute the anharmonic contributions to the 2-phonon structure factor, which we do with the inclusion of an anharmonic interaction Hamiltonian. For acoustic phonons in the long-wavelength limit, we have an effective Hamiltonian for acoustic phonons where the interactions are given in terms of macroscopic properties of the crystal through the Lamé parameters, as described in [42]. For the interactions of optical phonons, however, it is more difficult to write down a reliable analytic Hamiltonian. In this case we use (45) of Ref. [42], which comes from [85]. This Hamiltonian should be taken only at the order-of-magnitude level. We restrict the use of both effective Hamiltonians to the first BZ. The analytic expressions for the acoustic-acoustic and acoustic-optical final states are given already, so we complete this by

calculating the optical-optical terms. At leading order in q, this gives

$$\begin{aligned}
S^{(\mathrm{anh})}_{\mathrm{LOLO}} =& \frac{2\pi}{\Omega_c}\frac{\pi}{6m_p^2}\frac{c_{\mathrm{LA}}^2}{\bar{c}^2}\frac{\omega_{\mathrm{LO}}^2 q^4}{((2\omega_{\mathrm{LO}})^2-(c_{\mathrm{LA}}q)^2)^2} \\
&\times \delta(\omega - 2\omega_{\mathrm{LO}}) \\
S^{(\mathrm{anh})}_{\mathrm{LOTO}} =& \frac{2\pi}{\Omega_c}\frac{2\pi}{3m_p^2}\frac{c_{\mathrm{LA}}^2}{\bar{c}^2}\frac{\omega_{\mathrm{LO}}\omega_{\mathrm{TO}} q^4}{((\omega_{\mathrm{LO}}+\omega_{\mathrm{TO}})^2-(c_{\mathrm{LA}}q)^2)^2} \\
&\times \delta(\omega - \omega_{\mathrm{LO}} - \omega_{\mathrm{TO}}) \\
S^{(\mathrm{anh})}_{\mathrm{TOTO}} =& \frac{2\pi}{\Omega_c}\frac{2\pi}{3m_p^2}\frac{c_{\mathrm{LA}}^2}{\bar{c}^2}\frac{\omega_{\mathrm{TO}}^2 q^4}{((2\omega_{\mathrm{TO}})^2-(c_{\mathrm{LA}}q)^2)^2} \\
&\times \delta(\omega - 2\omega_{\mathrm{TO}}),
\end{aligned} \tag{3.64}$$

where $\bar{c} \equiv (c_{\mathrm{LA}} + c_{\mathrm{TA}})/2$. We have also assumed that the Grüneisen constant $\gamma_{\mathrm{G}} \approx 1$.

3.A.2 Incoherent approximation

The second result needed for the comparison in Sec. 3.3.2 is the two-phonon structure factor for GaAs in the incoherent approximation. To calculate this, we use the simplified density of states in (3.35) corresponding to the long-wavelength limit. Performing the $n = 2$ integral in (3.23) gives

$$S_{n=2}(q,\omega) = \mathscr{S}_{\mathrm{LALA}} + \mathscr{S}_{\mathrm{LATA}} + \ldots \tag{3.65}$$

where each $\mathscr{S}$ is a contribution to the $n = 2$ structure factor from the part of the density of states associated with the subscripted modes, and the ellipsis indicates we sum over all combinations

of modes. The first term of the sum in (3.65) is

$$\begin{aligned}\mathscr{S}_{\mathrm{LALA}} =& \frac{2\pi}{\Omega_c}\frac{q^4}{96c_{\mathrm{LA}}^6 q_{\mathrm{BZ}}^6 m_p^2}\Bigg(\omega^3\Theta(c_{\mathrm{LA}}q_{\mathrm{BZ}}-\omega)\\ &-\left(4c_{\mathrm{LA}}^3q_{\mathrm{BZ}}^3-6c_{\mathrm{LA}}^2q_{\mathrm{BZ}}^2\omega+\omega^3\right)\\ &\times\Theta(\omega-c_{\mathrm{LA}}q_{\mathrm{BZ}})\Theta(2c_{\mathrm{LA}}q_{\mathrm{BZ}}-\omega)\Bigg),\end{aligned} \tag{3.66}$$

and $\mathscr{S}_{\mathrm{TATA}}$ is given by $\mathscr{S}_{\mathrm{LALA}}$ with the replacement LA $\rightarrow$ TA and an additional overal factor of 4. The same procedure gives the LATA term as

$$\begin{aligned}\mathscr{S}_{\mathrm{LATA}} =& \frac{2\pi}{\Omega_c}\frac{q^4}{24c_{\mathrm{LA}}^3q_{\mathrm{BZ}}^6m_p^2}\Bigg(\frac{\omega^3}{c_{\mathrm{TA}}^3}\Theta(c_{\mathrm{TA}}q_{\mathrm{BZ}}-\omega)\\ &+\frac{-2c_{\mathrm{TA}}q_{\mathrm{BZ}}^3+3\omega q_{\mathrm{BZ}}^2}{c_{\mathrm{TA}}}\Theta(\omega-c_{\mathrm{TA}}q_{\mathrm{BZ}})\Theta(c_{\mathrm{LA}}q_{\mathrm{BZ}}-\omega)\\ &+\frac{-2(c_{\mathrm{LA}}^3+c_{\mathrm{TA}}^3)q_{\mathrm{BZ}}^3+3(c_{\mathrm{LA}}^2+c_{\mathrm{TA}}^2)q_{\mathrm{BZ}}^2\omega-\omega^3}{c_{\mathrm{TA}}^3}\\ &\times\Theta(\omega-c_{\mathrm{LA}}q_{\mathrm{BZ}})\Theta((c_{\mathrm{LA}}+c_{\mathrm{TA}})q_{\mathrm{BZ}}-\omega)\Bigg).\end{aligned} \tag{3.67}$$

as well as the LOLA term,

$$\begin{aligned}\mathscr{S}_{\mathrm{LOLA}} =& \frac{2\pi}{\Omega_c}\frac{a^5\left(q_{\mathrm{BZ}}^2q^4\right)}{768\pi^5c_{\mathrm{LA}}^3m_p^2\omega_{\mathrm{LO}}}(\omega-\omega_{\mathrm{LO}})\\ &\times\Theta(\omega-\omega_{\mathrm{LO}})\Theta((c_{\mathrm{LA}}q_{\mathrm{BZ}}+\omega_{\mathrm{LO}})-\omega).\end{aligned} \tag{3.68}$$

Again we may find $\mathscr{S}_{\mathrm{LOTA}}$, $\mathscr{S}_{\mathrm{TOLA}}$, and $\mathscr{S}_{\mathrm{TOTA}}$ by relabelings and inserting relevant factors of two for polarizations. Note that, since the incoherent approximation does not recover the q^6 scaling resulting from interference, we have written the structure factor here using $q_{\mathrm{BZ}} = 2\pi/a$ to make the comparison more explicit. At lowest order in x and for $A_1 \approx A_2$, such a comparison of (3.62) and (3.68) shows a relative factor of $40/\pi^3 \approx 1$ for the LOLA channel. Lastly, for the

remaining optical-optical channels we find

$$\begin{aligned}
\mathscr{S}_{\mathrm{LOLO}} &= \frac{2\pi}{\Omega_c}\frac{q^4}{144m_p^2\omega_{\mathrm{LO}}^2}\delta(\omega-2\omega_{\mathrm{LO}}) \\
\mathscr{S}_{\mathrm{LOTO}} &= \frac{2\pi}{\Omega_c}\frac{q^4}{36m_p^2\omega_{\mathrm{LO}}\omega_{\mathrm{TO}}}\delta(\omega-(\omega_{\mathrm{LO}}+\omega_{\mathrm{TO}})) \\
\mathscr{S}_{\mathrm{TOTO}} &= \frac{2\pi}{\Omega_c}\frac{q^4}{36m_p^2\omega_{\mathrm{TO}}^2}\delta(\omega-2\omega_{\mathrm{TO}}).
\end{aligned} \tag{3.69}$$

A comparison now of (3.61) and (3.69) shows the incoherent approximation gives a smaller structure factor by factors of $2\pi/5$ – $6\pi/5 \approx 2-4$.

3.B Impulse approximation

In this section we discuss how to obtain the impulse approximation form of the structure factor, (3.39) in Sec. 3.3.4. To achieve this we must approximate the t integral in (3.37) for large q. The expression in (3.37) can be written as

$$\mathscr{C}_{\ell d} = \frac{1}{V}e^{-2W_d(\mathbf{q})}\int_{-\infty}^{\infty}dt\, e^{f(t)}. \tag{3.70}$$

with

$$\begin{aligned}
\mathrm{Re}[f(t)] &\equiv \frac{q^2}{2m_d}\int d\omega'\frac{D_d(\omega')}{\omega'}\cos\big(\omega' t\big) \\
\mathrm{Im}[f(t)] &\equiv \frac{q^2}{2m_d}\int d\omega'\frac{D_d(\omega')}{\omega'}\sin\big(\omega' t\big) - \omega t.
\end{aligned} \tag{3.71}$$

From this, we see there is a global maximum in the real part and a global minimum in the modulus of the imaginary part at $t=0$. This allows us to perform a steepest-descent expansion about $t=0$, giving

$$\mathscr{C}_{\ell d} \approx \frac{1}{V}\int_{-\infty}^{\infty}dt\, e^{it\left(\frac{q^2}{2m_d}-\omega\right)-\frac{t^2}{2}\frac{q^2\bar{\omega}_d}{2m_d}}, \tag{3.72}$$

where again $\bar{\omega}_d = \int d\omega' \omega' D_d(\omega')$. Note that the leading term in the expansion about $t = 0$ cancelled the Debye Waller factor, assuming the form given in (3.24). Evaluating the above gives

$$\mathscr{C}_{\ell d} \approx \frac{1}{V}\sqrt{\frac{2\pi}{\Delta_d^2}} e^{-\frac{\left(\omega - \frac{q^2}{2m_d}\right)^2}{2\Delta_d^2}}, \tag{3.73}$$

which is the impulse approximation result.

In obtaining this form, we have assumed that any other local maxima in t gives a subdominant contribution to the $t = 0$ maximum. In particular, aside from the $t = 0$ point, which is a global maximum in $\mathrm{Re}[f(t)]$, there are local maxima in the real part which will generally be near integer multiples of $2\pi/\bar{\omega}_d$. The leading order contribution from each additional maxima t_{max} is given by evaluating the real part in the exponential at the location of the maxima.

This must necessarily be smaller than the $t = 0$ contribution since the following inequality is always satisfied

$$\int d\omega' \frac{D_d(\omega')}{\omega'} \cos\left(\omega' t_{\mathrm{max}}\right) < \int d\omega' \frac{D_d(\omega')}{\omega'}. \tag{3.74}$$

Since $t_{\mathrm{max}} \sim 2\pi/\bar{\omega}_d$, the left hand side will be suppressed by an $O(1)$ amount due to presence of the $\cos(\omega' t_{\mathrm{max}})$. Then, the contribution from the local maxima will be exponentially suppressed:

$$e^{\frac{q^2}{2m_d}\int d\omega' \frac{D_d(\omega')}{\omega'} \cos(\omega' t_{\mathrm{max}})} \ll e^{\frac{q^2}{2m_d}\int d\omega' \frac{D_d(\omega')}{\omega'}} \tag{3.75}$$

as long as the following condition is satisfied

$$\frac{q^2}{2m_d} \gg \frac{1}{\int d\omega' \frac{D_d(\omega')}{\omega'}} \sim \bar{\omega}_d. \tag{3.76}$$

Here we have taken $\int d\omega' \frac{D_d(\omega')}{\omega'} \sim 1/\bar{\omega}_d$ as a typical scale for this integral, although it will differ by an $O(1)$ factor. Therefore, as long as the free nuclear recoil energy $\omega = q^2/(2m_d)$ is well above the typical phonon energy $\bar{\omega}_d$ for a scattering off of atom d, the $t = 0$ maximum is

dominant and the impulse approximation should be accurate.

In the regime where $q^2/2m_d$ is comparable to $\bar{\omega}_d$, the contributions from the additional maxima in t can become important. Nevertheless, the impulse approximation is still accurate at large ω even in this case because of cancellations from the rapidly changing phase in $\mathrm{Im}[f(t)]$. When $\omega \gg \bar{\omega}_d$, then $\mathrm{Im}[f(t)] \approx -\omega t$ for t around $t_{\max} \sim 2\pi/\bar{\omega}_d$. This implies large oscillations of $f(t)$ around $t_{\max}$, which suppresses the contribution from these local maxima. On the other hand, if $\omega \lesssim \bar{\omega}_d$, there may be large corrections to the impulse approximation due to these additional maxima.

These effects were shown in Fig. 3.5a when comparing the multiphonon expansion result to the impulse approximation. The middle panel showed the result if $q = \sqrt{2m_d\bar{\omega}_d}$, in the $m_{\mathrm{Ga}} \approx m_{\mathrm{As}}$ approximation. For $\omega \gtrsim \bar{\omega}_d$ the structure factor falls smoothly and can be reasonably captured by the impulse approximation, while for $\omega \lesssim \bar{\omega}_d \approx 22$ meV or at the optical phonon energies 31 and 33 meV there are sharp peaks in the multiphonon response that are not captured by the impulse approximation. For $q = 2\sqrt{2m_d\bar{\omega}_d}$ the many multiphonon peaks merge and add up to a shape similar to the impulse approximation over the whole ω range. Practically, for our calculations, we use the impulse approximation for the structure factor at $q > 2\sqrt{2m_d\bar{\omega}_d}$. Though the approximation has small differences with the exact result when $q \sim 2\sqrt{2m_d\bar{\omega}_d}$, integrating over the allowed phase space for the rate largely washes out these differences.

3.C Implementation in `DarkELF`

In the main text, we presented the formulas in the manner which is most clear from the point of view of the various approximations and their regimes of validity. These formulas were not always suitable however for an efficient numerical implementation, which we address in this section. We also provide details on their implementation in the `DarkELF` package [74].

In the main text we gave the rate in the isotropic limit, (4.73). In order to calculate the rate for any mediator and to obtain the differential rate $dR/d\omega$, it is convenient to perform the

v-integral first and rewrite the rate as:

$$R = \frac{1}{4\pi\rho_T}\frac{\rho_\chi}{m_\chi}\frac{\sigma_p}{\mu_\chi^2}\int_{\omega_{\rm th}}^{\omega_+} d\omega \int_{q_-}^{q_+} dq\, q\, |\tilde{F}(q)|^2 S(q,\omega)\, \eta(v_{\rm min}(q,\omega)) \tag{3.77}$$

where now the integration limits are given by

$$q_\pm = m_\chi \left(v_{\rm max} \pm \sqrt{v_{\rm max}^2 - \frac{2\omega}{m_\chi}}\right) \tag{3.78}$$

$$\omega_+ = \frac{1}{2} m_\chi v_{\rm max}^2 \tag{3.79}$$

with $v_{\rm max} = v_{\rm esc} + v_e$ the maximum DM speed in the lab frame. The η function is given by

$$\eta(v_{\rm min}) = \int d^3\mathbf{v} \frac{f(\mathbf{v})}{v} \Theta(v - v_{\rm min}) \tag{3.80}$$

with $v_{\rm min}(q,\omega) = \frac{q}{2m_\chi} + \frac{\omega}{q}$.

To evaluate the rate using incoherent approximation, we provide look-up tables for the structure factor. At each n for the sum in (3.36), the q and ω parts of the integral are separable, so we can capture the ω-dependent part with the family of functions

$$F_{n,d}(\omega) \equiv \frac{1}{n!}\left(\prod_{i=1}^{n} \int d\omega_i \frac{D_d(\omega_i)}{\omega_i}\right) \delta\left(\sum_i \omega_i - \omega\right), \tag{3.81}$$

and calculate the rate in terms of functions $F_{n,d}$. These functions are simple to calculate numerically up to $n \leq 10$, which we have tabulated and provided in `DarkELF` as look-up tables to speed up the calculation. The combination $\bar{\omega}^n F_n(\omega)$ is shown in Fig. 3.11 for GaAs in the $m_{\rm Ga} \approx m_{\rm As}$ approximation. For increasingly high n, the $F_{n,d}$ become increasingly smooth.

We have added several additional functions to `DarkELF` for the differential and integrated rate calculations from the single phonon to the nuclear recoil regime. Tab. 3.1 describes some of the new relevant functions. These functions currently work for materials with up to two atoms

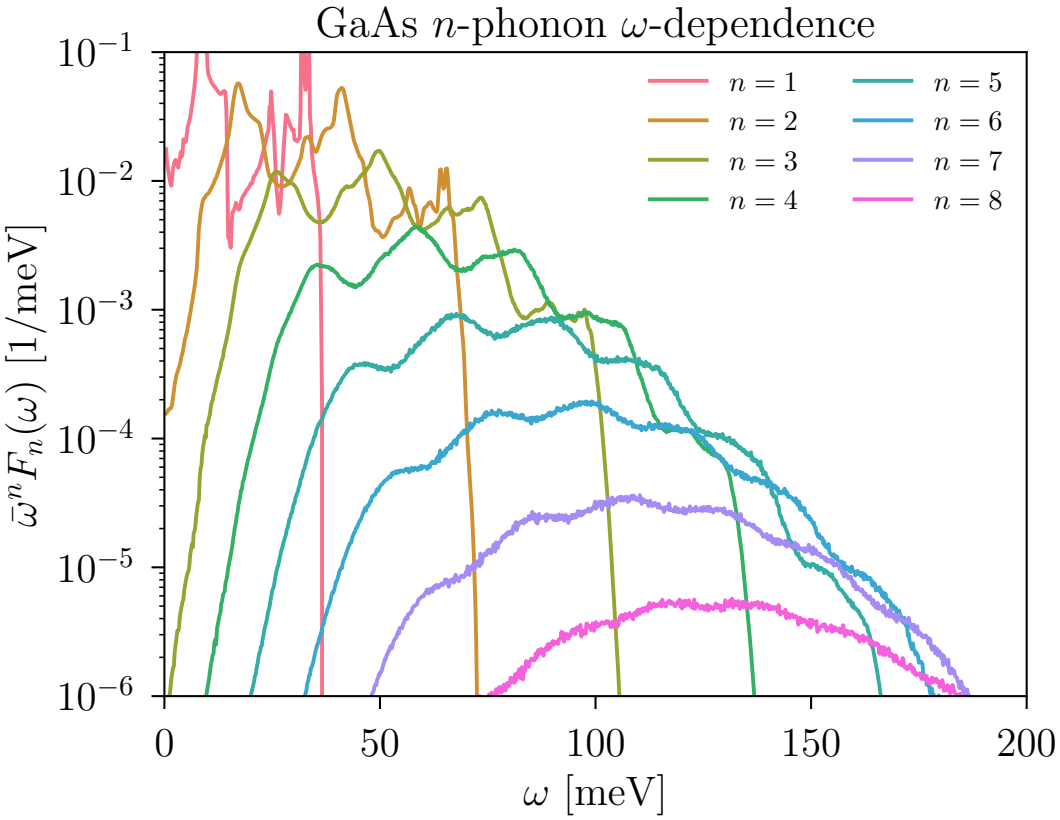

Figure 3.11. Here we have plotted $\bar{\omega}^n F_n(\omega)$, where $F_n(\omega)$ is the ω-dependent part of the structure factor in the incoherent approximation and given explicitly in (3.81). At fixed q, the structure factor decreases quickly with increasing ω.

per unit cell. We have included the necessary data files for the multiphonon calculation for GaN, Al, ZnS, GaAs, Si, and Ge from a combination of DFT and experimental sources. We also allow the user to input their own calculations or extractions of the (partial) density of states, as well as momentum-dependent dark matter-nucleon couplings. Before calculating multiphonon scattering rates in `DarkELF`, it is necessary to tabulate the auxiliary function (3.81) for each atom. This is done using the `DarkELF` function *create_Fn_omega*. This step is the most time consuming part of the calculation, so we provide these pre-tabulated for the aforementioned materials. For calculations with a user-supplied (partial) density of states, these tables must first be updated by running *create_Fn_omega*. `DarkELF` will save these new look-up tables for future computations, such that this step only need to be performed once. Next we describe the functions that return

important results. All of the following straightforwardly apply equations (3.77-3.80).

R_single_phonon: This function takes the energy threshold and DM-nucleon cross sections and outputs the rate in the long-wavelength single phonon regime using the analytic functions (3.30-3.31).

R_multiphonons_no_single: This function takes the energy threshold and DM-nucleon cross section as inputs and calculates the total integrated rate, excluding the single phonon processes at long wavelengths $q < q_{\mathrm{BZ}}$. In other words, this calculation includes only the purple (multiphonon expansion) and red (impulse approximation) phase space regions in Fig. 3.6.

sigma_multiphonons: This takes the energy threshold as input and returns the necessary DM-nucleon cross section to produce three events per kg-year for any number of phonons. In order to return this cross section, this function first calculates the total rate by summing the outputs of *R_single_phonon* and *R_multiphonons_no_single*, so it includes the entire calculation scheme depicted in Fig. 3.6.

_dR_domega_multiphonons_no_single: This function takes the energy transfer ω and DM-nucleon cross section and returns the differential rate $\frac{dR}{d\omega}$ at that energy excluding single phonons in the long wavelength regime. This comes from equation (3.77) without evaluating the ω integral. We exclude the single coherent phonon here since the long-wavelength approximation has delta functions in energy in the differential rate.

3.D Additional results

Here, we provide additional results for Ge, Si, and diamond. Concretely, Fig. 3.12 shows the density of states for these three materials, as extracted from [79]. Fig. 3.13 shows the differential scattering rate via a massive scalar mediator for two example DM masses in GaAs, Ge and Si targets. Finally, Figs. 3.14, 3.15, and 3.16 are the cross section plots corresponding to an integrated rate of 3 events/kg-year for Ge, Si, and diamond, respectively. The electron recoil cross sections shown (dashed black lines) are based on calculations in [83] for Ge, Si and in [86]

for diamond.

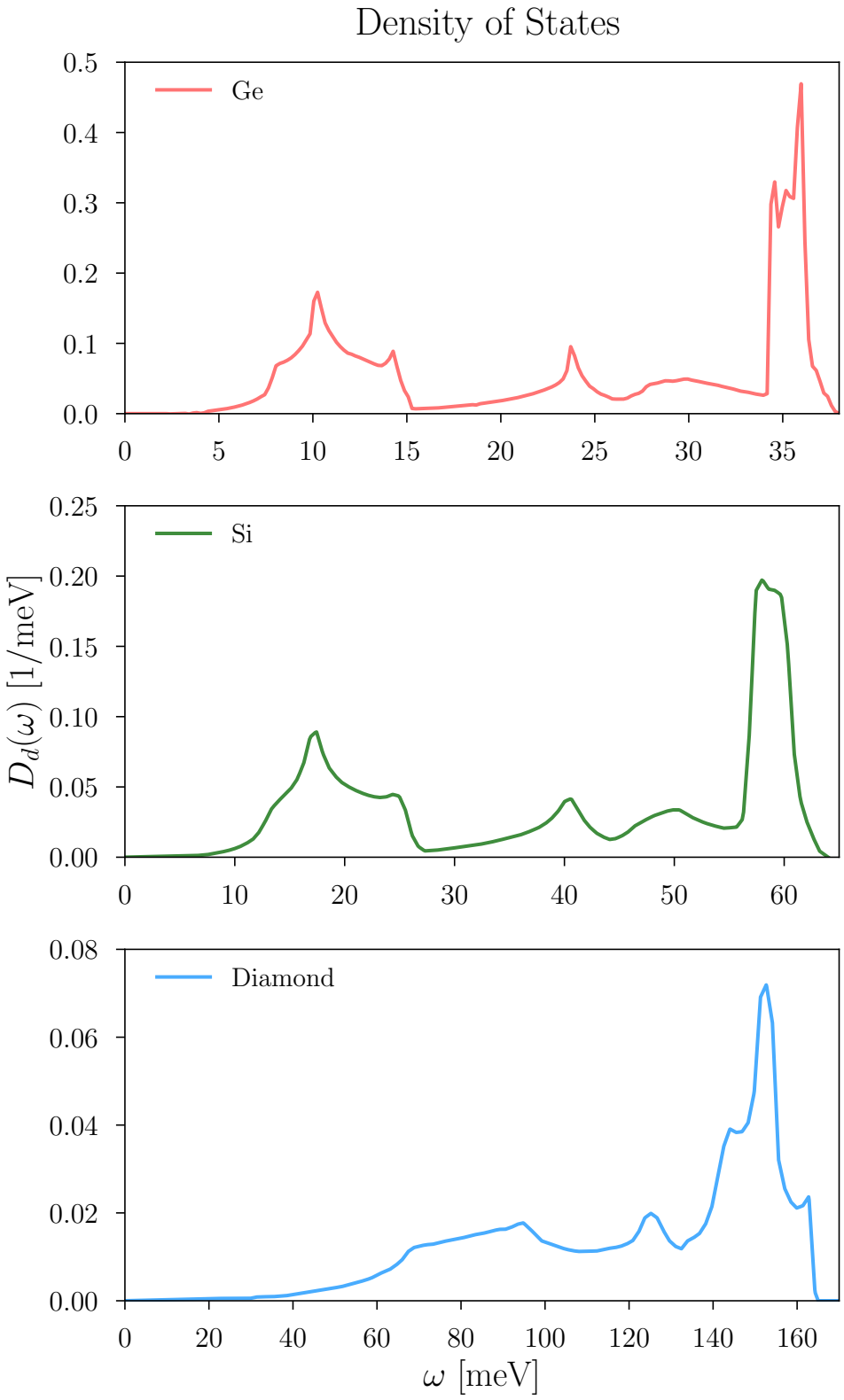

Figure 3.12. Densities of states for germanium, silicon, and diamond [79].

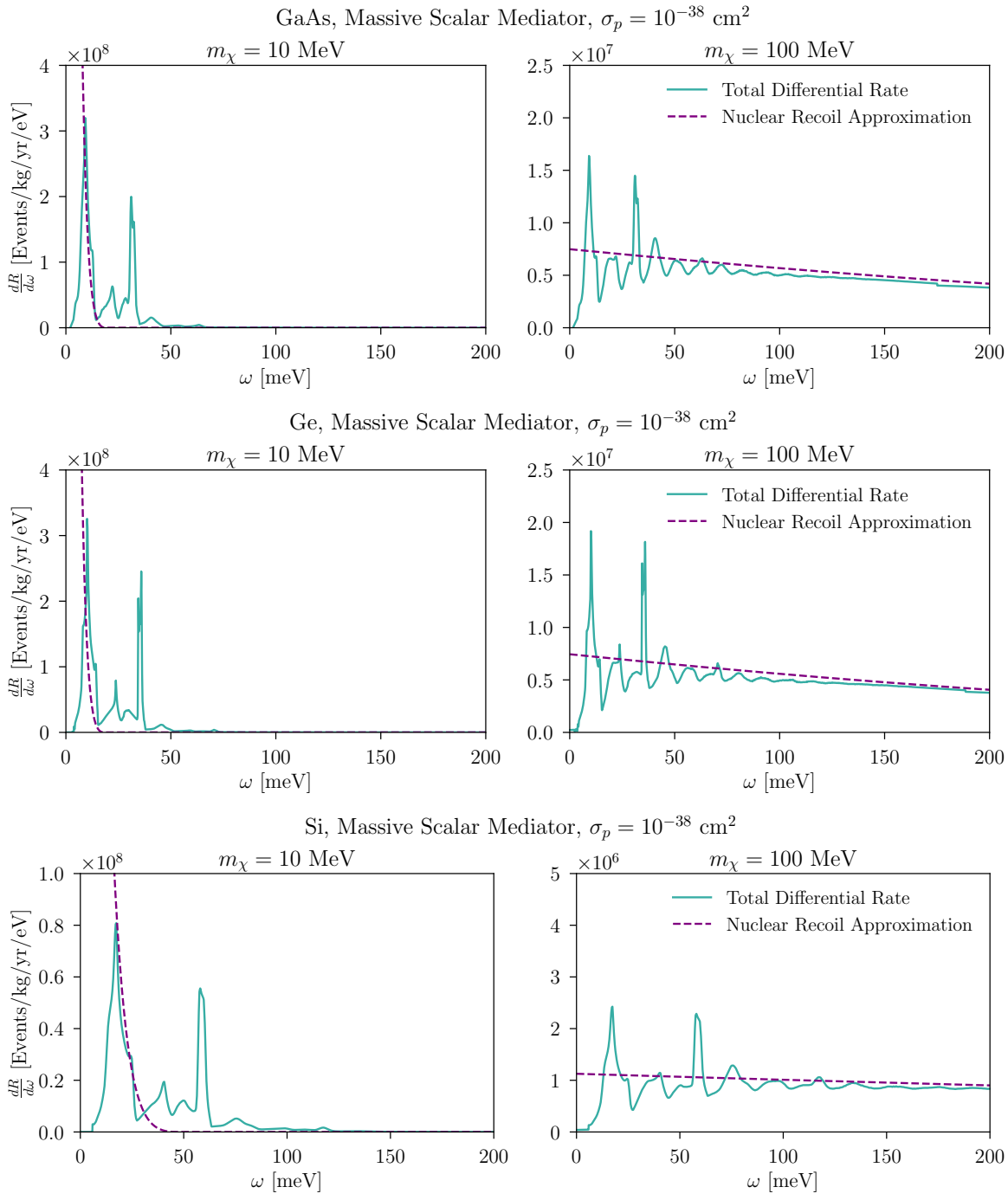

Figure 3.13. Differential rate for various materials and a massive scalar mediator, compared with the nuclear recoil approximation. The single phonon contribution from the long wavelength regime is not shown, since it gives a delta function contribution.

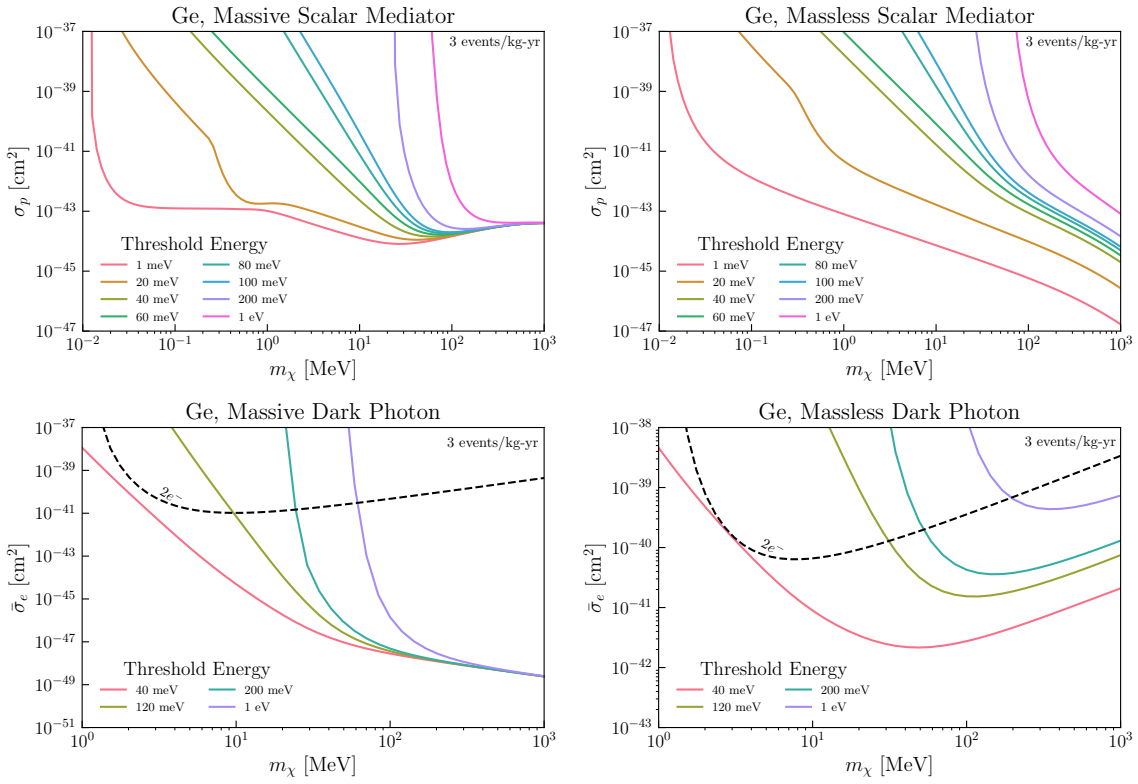

Figure 3.14. Cross section plots for a rate of 3 events/kg-year exposure for different thresholds in Ge.

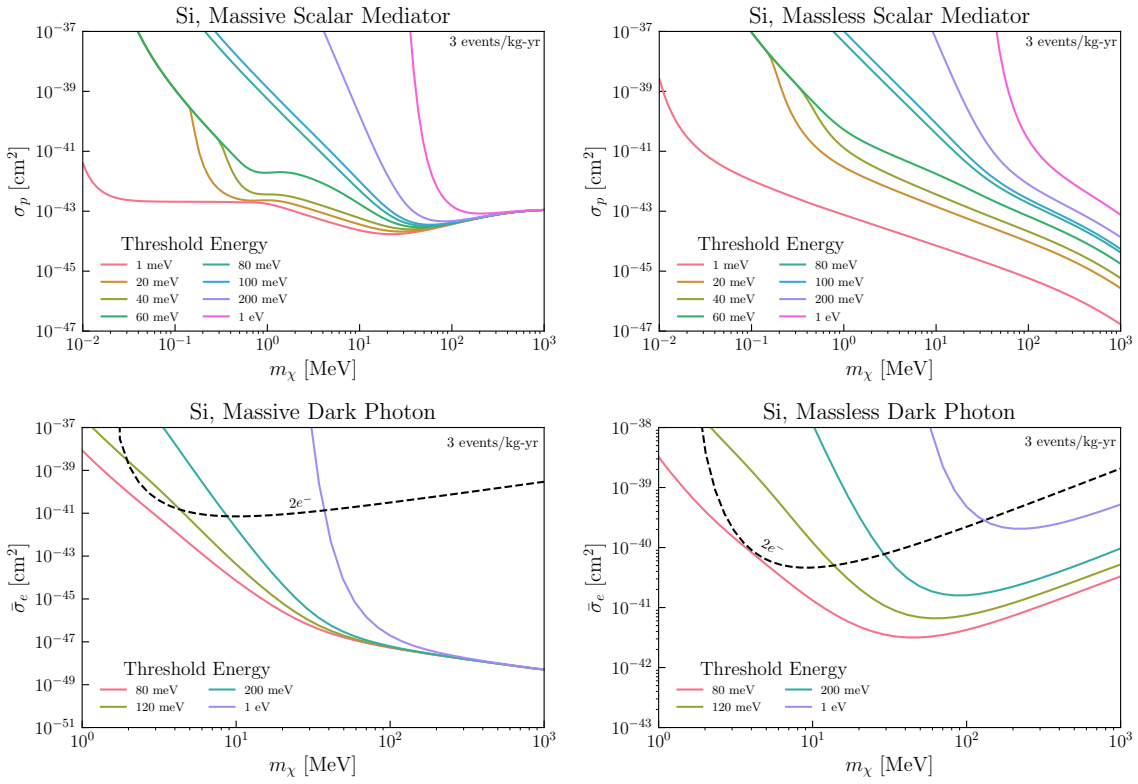

Figure 3.15. Cross section plots for a rate of 3 events/kg-year exposure for different thresholds in Si.

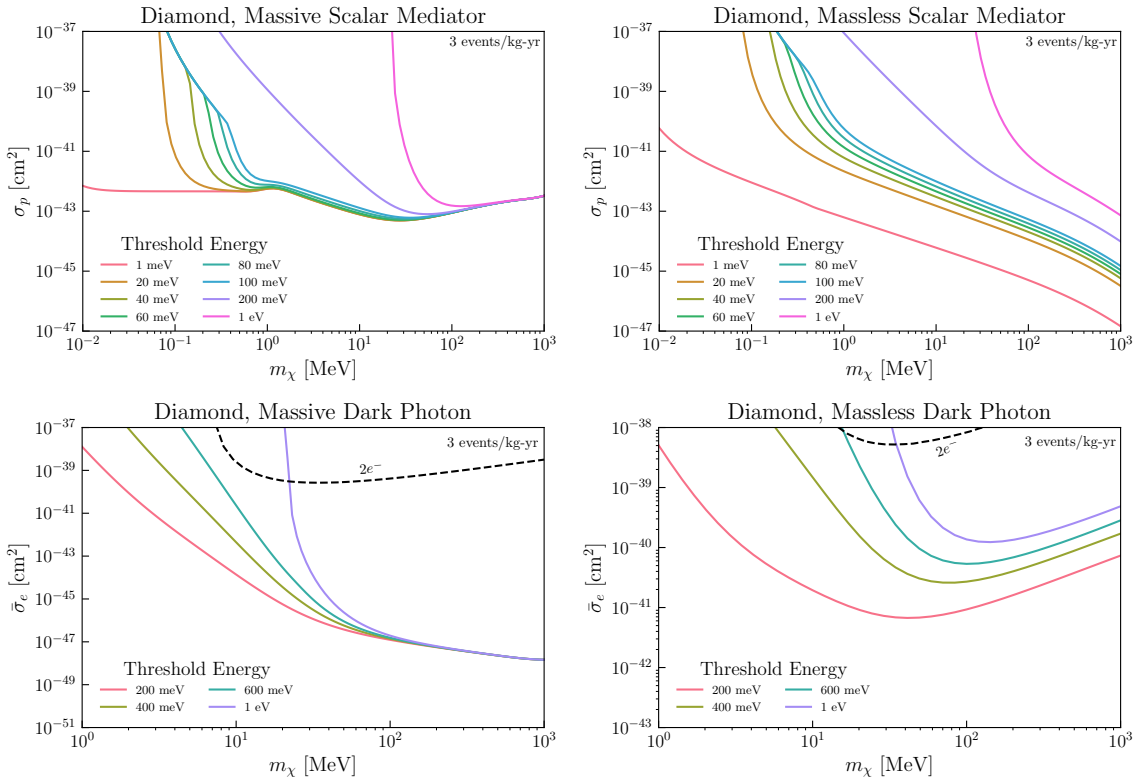

Figure 3.16. Cross section plots for a rate of 3 events/kg-year exposure for different thresholds in diamond.

Table 3.1. List of public functions in `DarkELF` related to multiphonon excitations from DM scattering. Only mandatory arguments are shown; for optional arguments and flags, see text and the documentation in repository. Some functions are only available for select materials, as indicated in the righthand column.

DM-multiphonon scattering

function	description	available for
`dRdomega_multiphonons_no_single(omega)`	Differential rate $dR/d\omega$ in 1/kg/yr/eV excluding long-wavelength single phonons	all except SiO_2, Al_2O_3
`R_multiphonons_no_single(omega)`	Total phonon rate in 1/kg-yr excluding long-wavelength single phonons	all except SiO_2, Al_2O_3
`sigma_multiphonons(omega)`	Nucleon cross section to produce 3 events/kg-yr	all except SiO_2, Al_2O_3

Chapter 4

Dark matter-crystal scattering, anharmonic effects on multiphonon production

4.1 Introduction

Over the past few decades, a significant theoretical and experimental effort has been dedicated to detect dark matter (DM), but the particle nature of DM still remains a mystery. Direct detection experiments look for the direct signatures left by halo DM depositing energy inside the detectors. Traditionally, such experiments have looked for elastic nuclear recoils induced by DM particles in detectors [87]. This strategy has had tremendous sensitivity for DM particles with masses higher than the GeV-scale that interact with nuclei [88, 89, 90]. However, in recent years it has also been recognized that sub-GeV dark matter models are also compelling and motivated dark matter candidates [91, 92, 93, 28, 94, 95, 96]. These DM particles would leave much lower energy nuclear recoils, motivating experimental efforts to lower the detector thresholds for nuclear recoils. Inelastic processes like the Migdal effect [97, 55, 98, 72, 99] or bremsstrahlung [56] provide alternative channels to detect nuclear scattering in the sub-GeV DM regime.

The majority of experiments achieving lower thresholds in nuclear recoils (down to $\sim$ 10 eV) are doing so with crystal targets [100, 101, 102, 103], although there is also progress in using liquid helium [104]. Future experiments like SPICE [37] will reach even lower thresholds by measuring athermal phonons produced in crystals like GaAs and Sapphire (i.e. Al_2O_3). In

crystal targets, DM-nucleus scattering can deviate substantially from the picture of a free nucleus undergoing elastic recoils. Nuclei (or atoms) are subject to forces from the rest of the lattice, which play a role at the lower energies relevant for sub-GeV DM. For recoil energies below the typical binding energy of the atom to the lattice ($\mathcal{O}(10$ eV$)$), the atoms are instead treated as being bound in a potential well. At even lower energies, the relevant degrees of freedom are the collective excitations of the lattice, known as phonons. In this regime, single phonon excitations with typical energies $\lesssim 0.1$ eV are possible.

In the DM scattering rate, crystal scattering effects are all encoded within a quantity known as the dynamic structure factor, $S(\mathbf{q},\omega)$. The differential cross section for a DM particle of velocity $\mathbf{v}$ and mass m_χ to scatter with energy deposition ω and momentum transfer $\mathbf{q}$ can be written in terms of $S(\mathbf{q},\omega)$ as:

$$\frac{d\sigma}{d^3\mathbf{q}d\omega} = \frac{b_p^2}{\mu_\chi^2}\frac{1}{v}\frac{\Omega_c}{2\pi}|\tilde{F}(\mathbf{q})|^2 S(\mathbf{q},\omega)\delta(\omega-\omega_\mathbf{q}), \tag{4.1}$$

Here b_p is the scattering length of the DM with a proton, μ_χ is the reduced DM-proton mass, $\Omega_c \equiv V/N$ is the volume of the unit cell in the crystal with total volume V and N unit cells, and $\omega_\mathbf{q} = \mathbf{q}\cdot\mathbf{v} - q^2/2m_\chi$ is equal to the energy ω lost by the DM particle when it transfers momentum $\mathbf{q}$ to the lattice. The $\mathbf{q}$-dependence of the DM-nucleus interaction is encapsulated in the DM form factor $\tilde{F}(\mathbf{q})$. $S(\mathbf{q},\omega)$ can thus be viewed as a form factor for the crystal response. For a recent review, see Ref. [43].

Understanding $S(\mathbf{q},\omega)$ in crystals is critical to direct detection of sub-GeV dark matter. Thus far, the limiting behavior of $S(\mathbf{q},\omega)$ is well understood [105]. In the limit of large ω and q ($\omega \gtrsim$ eV and $q \sim \sqrt{2m_N\omega}$ for nucleus of mass m_N), the structure factor behaves as $S(\mathbf{q},\omega) \propto \delta\left(q^2/(2m_N) - \omega\right)$, reproducing the cross section for free elastic recoils. At low ω comparable to the typical phonon energy ω_0 and q comparable to the inverse lattice spacing, $S(\mathbf{q},\omega)$ instead is dominated by single phonon production. The intermediate regime, particularly $q \sim \sqrt{2m_N\omega_0}$, is dominated by multiphonon production. For a large number of phonons being

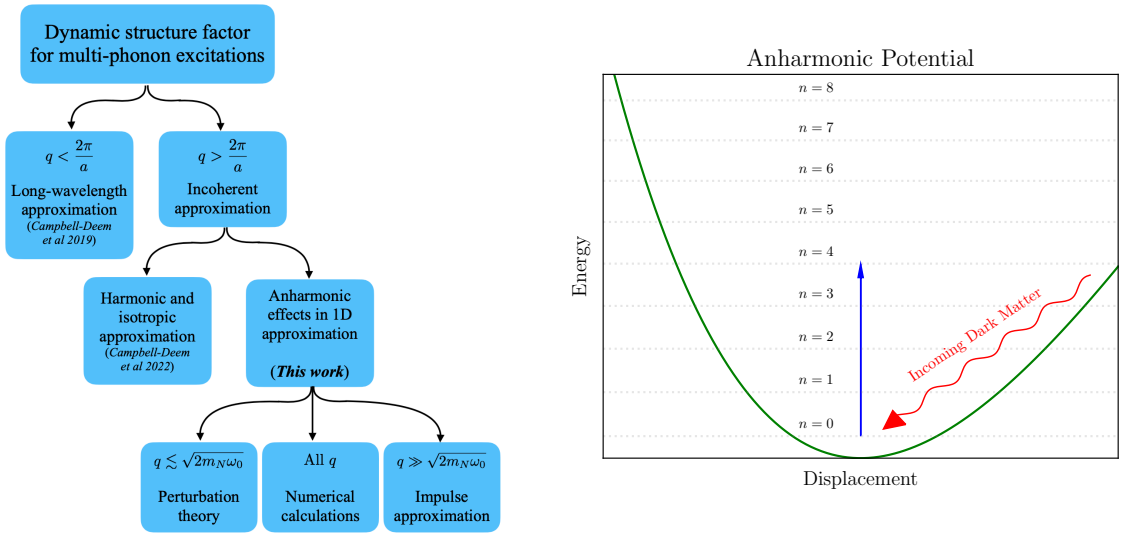

Figure 4.1. (**Left**) Due to the computational challenges of obtaining the multiphonon scattering rate in crystals, analytic approximations are valuable. Here we show a classification of regimes in which a multiphonon calculation has been performed, as well as approximations made in each case. In this work, we show that anharmonic corrections can be significant for $q \lesssim \sqrt{2m_N\omega_0}$ (Sec. 4.3.2) but are negligible when $q \gg \sqrt{2m_N\omega_0}$ (Sec. 4.3.3). We obtain results for all q using numerical calculations (Sec. 4.4.1). (**Right**) To estimate anharmonic effects, we take a toy model of dark matter scattering off an atom in a 1D anharmonic potential. We obtain the anharmonicity by fitting to empirical models of interatomic potentials.

produced, this should merge into the free nuclear recoil limit.

For DM masses below ∼MeV, the momentum-transfers are smaller than the typical inverse lattice spacing of crystals, $q < 2\pi/a \sim \mathcal{O}(\text{keV})$, where a is the lattice spacing. The dominant process is the production of a single phonon. In recent years, the single phonon contribution to $S(\mathbf{q}, \omega)$ has been computed extensively in a variety of materials, often using first-principles approaches for the phonons [57, 41, 58, 59, 60, 106, 61, 62, 63, 74, 107]. In most of the crystals, single phonons have a maximum energy of $\mathcal{O}(100\text{ meV})$, however, requiring extremely low experimental thresholds to detect them.

Production of multiphonons is an enticing channel to look for sub-GeV DM with detectors having thresholds higher than $\mathcal{O}(100\text{ meV})$. They are also important to understand in the near term as experiments lower their thresholds. However, multiphonon production has been more challenging to compute. The numerical first-principles approach taken for single phonon

production does not scale well with number of phonons being produced, where even the two-phonon rate becomes very complicated. Alternate analytic methods are thus valuable. In Fig. 4.1, we show a classification of the different regimes in which a multiphonon calculation has been performed, including this work. We discuss the details of these regimes and calculations below.

One analytic approach was taken in Ref. [42], which calculated the two-phonon rate in the long-wavelength limit, but this study was limited to the regime $q < 2\pi/a$ and focused on acoustic phonons only. For $q > 2\pi/a$, a different approximation is possible, the incoherent approximation, which drops interference terms between different atoms of the crystal in calculating $S(\mathbf{q}, \omega)$. Then scattering is dominated by recoiling off of individual atoms. This approach was taken in [105], which found a general n-phonon production rate scaling as $(q^2/(2m_N\omega_0))^n$. This result also showed how the free nuclear recoil cross section was reproduced in the multiphonon structure factor as $q \gg \sqrt{2m_N\omega_0}$.

However, one limitation of the multiphonon production rate in Ref. [105] was that it worked in the harmonic approximation, where higher order phonon interactions like the three-phonon interaction are neglected. Typical crystals have some anharmonicity which introduces phonon self-interactions, leading to various observable effects like phonon decays, thermal expansion, and thermal conductivity of crystals [108, 109, 110]. Using a simplified model of anharmonic phonon interactions, Ref. [105] estimated that anharmonic three-phonon interactions may give the dominant contribution to the two-phonon rate $q < 2\pi/a$, and are larger than the harmonic piece by almost an order of magnitude in the regime. On the other hand, we do not expect anharmonic effects to be important in the opposite limit of large q ($q \gg \sqrt{2m_N\omega_0}$), where the nucleus can be treated as a free particle. It is thus necessary to bridge these two extremes and estimate the anharmonic effects in the intermediate regime where multi-phonons dominate the scattering.

In this work, we estimate the anharmonic effects on the rate of multiphonon production by working in the incoherent approximation and $q > 2\pi/a$. In this limit, the multiphonon scattering rate looks similar to that of an atom in a potential [71], although the spectrum of states is smeared

out due to interactions between neighboring atoms. Given this similarity, we will take a toy model of an atom in a 1D potential. This gives a simple approach to including anharmonic effects, which is also illustrated in the right panel of Fig. 4.1. The anharmonic corrections to the atomic potential only capture a part of the contributions to anharmonic phonon interactions, but they have a similar size (in the appropriate dimensionless units) and should give a reasonable estimate of the size of the effect. We can therefore use this approach to estimate theoretical uncertainties and gain analytic understanding for the multiphonon production rate. However, the result should not be taken as a definitive calculation of the anharmonic corrections. Fortunately, we will find that anharmonic corrections are large only in certain parts of the phase space which are more challenging to observe, and that the multiphonon rate quickly converges to the harmonic result for DM masses above a few MeV.

The outline of this paper is as follows: In Sec. 4.2, we discuss the formalism of DM scattering in a crystal and the dynamic structure factor, which encodes the information about the crystal response. We consider the calculation of the structure factor under the incoherent approximation, and motivate the anharmonic 1D toy potentials we use in this paper. In Sec. 4.3, we study the behavior of the dynamic structure factor analytically for the anharmonic 1D potentials. Using perturbation theory, we show that anharmonic corrections can dominate for $q \ll \sqrt{2m_N\omega_0}$ and become more important for higher phonon number. In the opposite limit $q \gg \sqrt{2m_N\omega_0}$, we use the impulse approximation to show that anharmonic corrections are negligible and that the structure factor indeed approaches that of an elastic recoil. In Sec. 4.4, we present numerical results for the structure factor in anharmonic 1D potentials obtained from realistic atomic potentials in various crystals. In Sec. 4.4.1, we calculate the impacts of including anharmonic effects on DM scattering rates. We conclude in Sec. 4.5.

Appendix 4.A gives the details of the modeling of the interatomic forces on the lattice, used to extract 1D single atom potentials. Appendix 4.B gives additional details of the analytic perturbation theory estimates of the anharmonic structure factor. Appendix 4.C includes additional details relevant to the impulse approximation calculation. Appendix 4.D summarizes the

exactly solveable Morse potential model, which further validates the results in the main text.

4.2 Dark matter scattering in a crystal

Consider DM that interacts with nuclei in the crystal. We will parameterize the interaction with the lattice by a coupling strength $f_{\ell d}$ relative to that of a single proton, where ℓ denotes the lattice vector of a unit cell and d denotes the atoms in the unit cell. In the DM scattering cross section, (4.1), the material properties of the crystal are encoded in the structure factor $S(\mathbf{q},\omega)$ which is defined as,

$$S(\mathbf{q},\omega) \equiv \frac{2\pi}{V}\sum_f \Big|\sum_\ell \sum_d f_{\ell d}\langle \Phi_f | e^{i\mathbf{q}\cdot\mathbf{r}_{\ell d}}|0\rangle\Big|^2 \times \delta(E_f - E_0 - \omega), \tag{4.2}$$

where $|\Phi_f\rangle$ is the final excited state of the crystal with energy E_f and $\mathbf{r}_{\ell d}$ denotes the position of the scattered nucleus. The crystal is considered to be in the ground state $|0\rangle$ initially. Note for simplicity we assume a pure crystal where each atom has a unique coupling strength; the scattering is modified if there is a statistical distribution for the interaction strengths at each lattice site, for instance if different isotopes are present [105].

The states $|\Phi_f\rangle$ are the phonon eigenstates of the lattice Hamiltonian,

$$H_{\text{lattice}} = \sum_{\ell d} \frac{p_{\ell d}^2}{2m_{\ell d}} + V_{\text{lattice}} + E_0, \tag{4.3}$$

where the first term is the kinetic energy of the atoms in the lattice and the lattice potential V_{lattice}

in general is given by,

$$\begin{aligned} V_{\text{lattice}} = &\frac{1}{2}\sum_{\ell,d,\ell',d'}\sum_{\alpha,\beta} k^{(2)}_{\alpha\beta}(\ell d,\ell' d')\; u_\alpha(\ell d)\; u_\beta(\ell' d') \\ &+\frac{1}{3!}\sum_{\ell,d,\ell',d',\ell'',d''}\sum_{\alpha,\beta,\gamma} k^{(3)}_{\alpha\beta\gamma}(\ell d,\ell' d',\ell'' d'') \\ &\qquad\qquad \times u_\alpha(\ell d)\; u_\beta(\ell' d')\; u_\gamma(\ell'' d'') \\ &+ \ldots \end{aligned} \tag{4.4}$$

where the $u_\alpha(\ell d)$ is the displacement from the equilibrium position in the Cartesian direction α for the atom at the position d in the unit cell located at ℓ, and $k^{(2)}_{\alpha\beta}$, $k^{(3)}_{\alpha\beta\gamma}$ are the second-, and third-order force constants respectively. Note that as the displacements are considered around equilibrium, we do not have a term in the potential which is linear in the displacements.

A number of approximations are useful in evaluating $S(\mathbf{q},\omega)$. The first is the harmonic approximation, which amounts to keeping the terms up to second-order force constants and neglecting the higher order terms ($k^{(3)}_{\alpha\beta\gamma} = 0$). This vastly simplifies the Hamiltonian into a harmonic oscillator system, and has been used in most previous calculations of DM scattering in crystals. While this is generally an excellent approximation in crystals, including higher order terms in the Hamiltonian (anharmonicity) is necessary to explain a number of observable effects, as we will discuss further below.

The second approximation is the incoherent approximation, used for scattering with momentum transfers much bigger than the inverse lattice spacing of the crystal, $q \gg 2\pi/a$. In this limit, we drop the interference terms between different atoms in the crystal in (4.2). This amounts to summing over the squared matrix elements of individual atoms in the structure factor

in (4.2),

$$S(\mathbf{q},\omega) \approx \frac{2\pi}{V}\sum_f\sum_\ell\sum_d |f_{\ell d}|^2 \left|\langle\Phi_f|e^{i\mathbf{q}\cdot\mathbf{r}_{\ell d}}|0\rangle\right|^2 \times \delta(E_f - E_0 - \omega). \tag{4.5}$$

The calculation of the structure factor then simplifies to computing matrix elements $\left|\langle\Phi_f|e^{i\mathbf{q}\cdot\mathbf{r}_{\ell d}}|0\rangle\right|^2$ which are identical for the atoms in all unit cells ℓ.

Below, we will first discuss this calculation under the approximation of a harmonic crystal, before going on to setting up a model that accounts for anharmonicity in crystals.

4.2.1 Harmonic approximation

In the harmonic approximation, the lattice Hamiltonian can be written as a sum of harmonic oscillators in Fourier space [75],

$$H^{\text{Harmonic}}_{\text{lattice}} = \sum_\nu^{3n}\sum_{\mathbf{q}} \omega_{\mathbf{q},\nu}(\hat{a}^\dagger_{\mathbf{q},\nu}\hat{a}_{\mathbf{q},\nu} + \frac{1}{2}), \tag{4.6}$$

where the phonon eigenmodes of the lattice are labelled by the momentum $\mathbf{q}$ and the $3n$ branches ν with n being the number of atoms in the unit cell. The $\hat{a}^\dagger_{\mathbf{q},\nu}$ ($\hat{a}_{\mathbf{q},\nu}$) are the creation (annihilation) operators, and $\omega_{\mathbf{q},\nu}$ are the energies of the phonons. The lattice eigenstates that appear in (4.2) can then be written as,

$$|\Phi_n\rangle = \hat{a}^\dagger_{\mathbf{q}_1,\nu_1}\hat{a}^\dagger_{\mathbf{q}_2,\nu_2}...\hat{a}^\dagger_{\mathbf{q}_n,\nu_n}|0\rangle, \tag{4.7}$$

where $|\Phi_n\rangle$ is an n-phonon state. The displacement operators in this harmonic approximation are given by,

$$\mathbf{u}(\ell d) = \sum_{\nu}^{3n} \sum_{\mathbf{q}} \sqrt{\frac{1}{2Nm_d\omega_{\mathbf{q},\nu}}} \Big(\mathbf{e}_{\mathbf{q},\nu}(d)\, \hat{a}_{\mathbf{q},\nu}\, e^{i\mathbf{q}\cdot\mathbf{r}^0_{\ell d} - i\omega_{\mathbf{q},\nu}t} + \text{h.c.} \Big), \tag{4.8}$$

where the $\mathbf{e}_{\mathbf{q},\nu}(d)$ indicates the eigenvector of the displacement of atom d for that phonon. The equilibrium position of the atom is denoted by $\mathbf{r}^0_{\ell d}$. Using $\mathbf{r}_{\ell d} = \mathbf{r}^0_{\ell d} + \mathbf{u}(\ell d)$ inside (4.2), the dynamic structure factor can be calculated in the harmonic approximation. This approach has been applied to calculate single-phonon excitations using numerical results for phonon energies and eigenvectors [41, 58, 59, 60, 61, 62, 63], but becomes computationally much more burdensome for multi-phonons in the final state.

Under both the incoherent and harmonic approximations, it is possible to compute the multiphonon structure factor in (4.5). This was given in Ref. [105] as an expansion in the number of phonons produced n,

$$S(\mathbf{q},\omega) \approx 2\pi \sum_d n_d\, |f_d|^2 e^{-W_d(\mathbf{q})} \sum_n \frac{1}{n!} \left(\frac{q^2}{2m_d}\right)^n \times \left(\prod_{i=1}^{n} \int d\omega_i \frac{D_d(\omega_i)}{\omega_i} \right) \delta\left(\sum_{j=1}^{n} \omega_j - \omega \right), \tag{4.9}$$

where $D_d(\omega)$ is the partial density of states in the crystal, normalized to $\int d\omega D_d(\omega) = 1$. $W_d(\mathbf{q})$ is the Debye-Waller factor defined as,

$$W_d(\mathbf{q}) = \frac{q^2}{4m_d} \int d\omega'\, \frac{D_d(\omega')}{\omega'}. \tag{4.10}$$

(4.9) shows that with higher momentum q, there is an increased rate of multiphonons; the typical phonon number is $n \sim \frac{q^2}{2m\bar{\omega}}$ with $\bar{\omega}$ a typical phonon energy. In the limit of $n \gg 1$, this reproduces

the nuclear recoil limit.

In the incoherent approximation above, we still assumed the final states $|\Phi_f\rangle$ are the phonon eigenstates of the harmonic lattice Hamiltonian in (4.6). Let us now make a further approximation that the final states are isolated atomic states, where each atom is bound in a potential. Assuming an isotropic potential, and a single frequency ω_0 for the oscillators, a toy atomic Hamiltonian for atom d in the lattice can be written as,

$$H_d^{\text{toy}} = \frac{p_d^2}{2m_d} + \frac{1}{2} m_d \omega_0^2 r_d^2, \tag{4.11}$$

where $\mathbf{r}_d$ is the displacement of the atom d from its equilibrium position. Following (4.5), the dynamic structure factor can be written as,

$$\begin{aligned} S_{\text{toy}}(\mathbf{q},\omega) = 2\pi \sum_d n_d |f_d|^2 \sum_n \left| \langle \vec{n} | e^{i\mathbf{q}\cdot\mathbf{r}_d} | 0 \rangle \right|^2 \\ \times \delta(E_n - E_0 - \omega), \end{aligned} \tag{4.12}$$

where $|\vec{n}\rangle$ are the energy eigenstates of the toy harmonic Hamiltonian considered for atom d, with $\vec{n} = \{n_x, n_y, n_z\}$. The energies with respect to the ground state equilibrium are given by $E_n - E_0 = n\omega_0$ with $n = n_x + n_y + n_z$. We have also absorbed the sum over the lattice vector ℓ and the volume V into the density n_d of atom d in the lattice. As shown in [71], this structure factor is given by,

$$\begin{aligned} S_{\text{toy}}(\mathbf{q},\omega) \approx 2\pi \sum_d n_d |f_d|^2 e^{-2W_d^{\text{toy}}(q)} \\ \times \sum_n \frac{1}{n!} \left(\frac{q^2}{2m_d\omega_0} \right)^n \delta\left(n\omega_0 - \omega\right), \end{aligned} \tag{4.13}$$

where the Debye-Waller factor in the toy model is given by, $W_d^{\text{toy}}(q) = q^2/4m_d\omega_0$.

This picture can be simplified even further by considering a toy one-dimensional harmonic

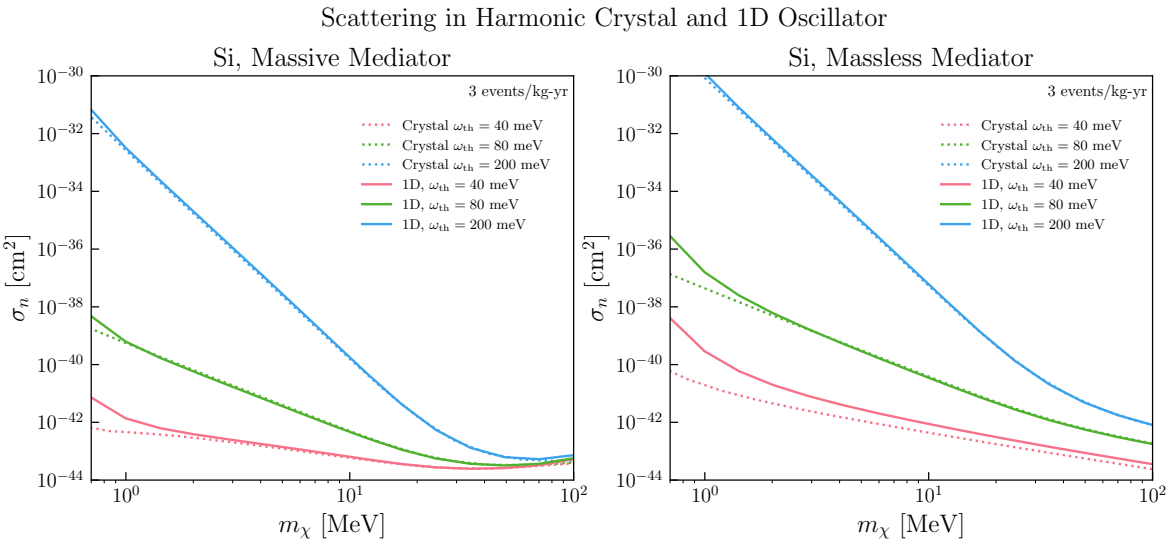

Figure 4.2. Comparison of scattering in a harmonic crystal to 1D harmonic oscillator. The dotted lines show the DM cross section reach computed using the multiphonon structure factor in a harmonic crystal, (4.9), and assuming the incoherent approximation [105]. Using the structure factor of the toy 1D harmonic oscillator in (4.13) combined with the energy smearing prescription in (4.16) gives a very similar result (solid lines). There are some small deviations at low momentum since we place a hard cut on the allowed momentum transfer $q > 2\pi/a \approx 2$ keV for the 1D oscillator.

potential for the atom d given by

$$V_d(x) = \frac{1}{2} m_d \omega_0^2 x^2. \tag{4.14}$$

Note that in general ω_0 will depend on the atom d within the unit cell, but we suppress this dependence for simplicity. The structure factor in this 1D case is exactly the same expression as the toy three-dimensional case in (4.13), as expected given the isotropic 3D potential assumed. A derivation of the 1D result is given in Sec. 4.3.1.

The toy model of DM scattering off a 1D harmonic potential gives a simple intuitive picture for the result in (4.9). We see a very similar form of the structure factor in (4.13), but with a discrete spectrum of states for the isolated oscillator of the toy model. By assuming that the final states are isolated atomic states, we have effectively neglected the interactions between atoms, and the excited states of all the atoms are discrete and degenerate. In a real material,

the interaction with neighboring atoms will lead to a splitting of the degenerate levels, and give a broad spectrum of allowed energy levels (the phonon spectrum). The interpretation for the structure factor is therefore also somewhat different in the two cases, as it gives a probability for exciting the nth excited state in an isolated oscillator. But we will still continue to refer the nth excited state as the n-phonon state to make the connection with the full incoherent structure factor in (4.9).

The similarity in the structure factor gives a route forward to including anharmonic effects, which is much easier to understand in the toy model. We can proceed by including anharmonic corrections to the 1D potential in (4.14), and in some cases obtain analytic results that illustrate their importance. In order to quantitatively estimate the impact on dark matter scattering rates, a few remaining ingredients are needed. In practice, the toy model can give very different results in certain parts of parameter space due to the discrete spectrum assumed and depending on the choice of ω_0. We therefore need a prescription to identify the appropriate ω_0 for the isolated oscillator, and to smear it out appropriately to mimic a real material.

Comparing Eqs. 4.9 and 4.13, we see that the complete structure factor can be attained by making a replacement

$$\frac{\delta(n\omega_0-\omega)}{\omega_0^n} \to \left(\prod_{i=1}^{n}\int d\omega_i \frac{D(\omega_i)}{\omega_i}\right)\delta\left(\sum_{j=1}^{n}\omega_j-\omega\right). \tag{4.15}$$

In this expression, we can identify $D(\omega)/(\omega\overline{\omega^{-1}})$ as a normalized probability distribution for ω, where $\overline{\omega^{-1}} = \int d\omega' D(\omega')/\omega'$. This distribution yields a mean value for ω of $(\overline{\omega^{-1}})^{-1}$. The right hand side of (4.15) is proportional to the joint probability distribution for total energy ω, and we can simplify it when $n \gg 1$ by applying the Central Limit Theorem. This allows us to replace the right hand side with a Gaussian, which simplifies computations:

$$\frac{\delta(n\omega_0-\omega)}{\omega_0^n} \to \frac{\left(\overline{\omega^{-1}}\right)^n}{\sqrt{2\pi n\sigma^2}} e^{-\frac{\left(\omega-n\overline{\omega^{-1}}^{-1}\right)^2}{2n\sigma^2}}\Theta(\omega_{\max}-\omega). \tag{4.16}$$

Note we have included a cutoff at multiples of the maximum allowed energy in the density of states, $\omega_{\max} = n \times (\min(\omega)|D(\omega) = 0)$ so that we do not include the region where $D(\omega_i) = 0$ on the right hand side of (4.15). The width of the Gaussian for $n = 1$ is given by

$$\sigma = \sqrt{\frac{\overline{\omega}}{\overline{\omega^{-1}}} - \frac{1}{\left(\overline{\omega^{-1}}\right)^2}} \tag{4.17}$$

and $\overline{\omega} = \int d\omega' D(\omega')\omega'$. This discussion therefore makes it clear that we should identify the frequency of the 1D toy model as $\omega_0 = 1/\overline{\omega^{-1}}$, which can be calculated numerically given the phonon density of states. This approach is validated in Fig. 4.2, where we compare our previous result using the full density of states [105] to the prescription described above. Note that small deviations at low mass arise from the lack of a cutoff at the Brillouin zone momentum in the previous density of states result. We reiterate that in this work, we shall include this Brillouin zone cutoff across all rate calculations since the incoherent approximation and subsequent approximations are only valid in this regime.

We will utilize this prescription to extend the multiphonon calculations for an anharmonic potential. To set up toy 1D anharmonic potentials, we first need to understand the anharmonic properties of typical crystals to extract the behavior of the potentials. We do this in the following subsection.

4.2.2 Anharmonic crystal properties

In general, a crystal lattice will exhibit some anharmonicity. Anharmonicity technically refers to the presence of non-zero force constants which are higher than second-order in the lattice potential in (4.4). For example, cubic anharmonicity in the crystal is parameterized by the third-order force constants $k^{(3)}_{\alpha\beta\gamma}(\ell d, \ell' d', \ell'' d'')$ in (4.4). Such force constants can be computed with DFT methods, similar to the harmonic case [111]. In the presence of such terms, the phonon eigenstates are no longer the harmonic phonon eigenstates of the crystal, and higher order phonon interactions, such as a three-phonon interaction, will be present. Calculating the full

dynamic structure factor in (4.5) for a crystal with such anharmonicity would require accounting for these higher order force tensors in both the matrix elements and in the final states, which quickly becomes a very challenging numerical problem. The rough size of the anharmonic force constants can be inferred from measurable crystal properties, however. We will briefly discuss some of the anharmonic effects below, and use them to justify our estimate of anharmonic effects.

An important effect of keeping cubic or higher order terms in (4.4) is to introduce interactions between the phonon modes which are the eigenstates of the harmonic Hamiltonian. For example, from (4.8), we can see that a cubic term in the displacements $\mathbf{u}(\ell d)$ will introduce three-phonon interactions like $\hat{a}^{\dagger}_{\mathbf{q},\nu}\hat{a}_{\mathbf{q}',\nu'}\hat{a}_{\mathbf{q}'',\nu''}$ (i.e. annihilation of two phonons to create a single phonon) or $\hat{a}^{\dagger}_{\mathbf{q},\nu}\hat{a}^{\dagger}_{\mathbf{q}',\nu'}\hat{a}_{\mathbf{q}'',\nu''}$ (i.e. decay of a single phonon into two phonons) in the Hamiltonian at the first order in the anharmonic force constant $k^{(3)}$. Phonon lifetimes in crystals are thus directly related to the anharmonic force constants, and can be measured to estimate the size of the anharmonicity [112, 110, 113].

Anharmonicity is also necessary to explain thermal expansion and conductivity in crystals. In particular, the linear volume expansion coefficient of crystals can be directly written in terms of the mode Gruneisen constants $\gamma_{\mathbf{q}\nu}$ which is defined for phonon modes labelled by the momentum $\mathbf{q}$ and branch index ν as [114],

$$\gamma_{\mathbf{q}\nu} = -\frac{V}{\omega_{\mathbf{q}\nu}}\frac{\partial \omega_{\mathbf{q}\nu}}{\partial V}. \tag{4.18}$$

Note that the change in volume in the equation above is at a fixed temperature. In a purely harmonic crystal, the phonon frequencies are determined by the second-order force constants which do not get modified with changes in volume, thus leading to zero Gruneisen constant. However, in the presence of cubic anharmonicity, the phonon frequencies are determined by the effective second-order force constants, which receive corrections depending on both the third-order force constants $k^{(3)}$ and the changes in volume, thus giving a non-zero Gruneisen constant [115]. An increase in volume leads to larger displacements of atoms, which typically

makes the effective second order constants and the phonon frequencies smaller, providing a positive Gruneisen constant. In the case of a non-zero Gruneisen constant, the free energy of the crystal, which has a harmonic contribution $\propto \Delta V^2$, receives a volume-dependent correction $\propto -\Delta V \gamma_{\mathbf{q}\nu} \bar{E}_{\mathbf{q}\nu}$, where $\bar{E}_{\mathbf{q}\nu}$ is the mean energy in the phonon mode $\mathbf{q}\nu$ at a particular temperature [108]. As the temperature increases, the mean energy $\bar{E}_{\mathbf{q}\nu}$ goes up, and thus this leads to a new equilibrium volume which minimizes the free energy. For a positive Gruneisen constant, this leads to thermal volume expansion.

The Gruneisen constants are thus directly related to the cubic force constants of the material, and have also been used to extract them [115]. Concretely, the relationship between the mode Gruneisen constants and the anharmonic force constants for weak anharmonicity can be shown to be [116],

$$\gamma_{\mathbf{q}\nu} = -\frac{1}{6\omega^2_{\mathbf{q},\nu}} \sum_{d,\ell' d',\ell'' d''} \sum_{\alpha\beta\delta} k^{(3)}_{\alpha\beta\delta}(\mathbf{0}d, \ell' d', \ell'' d'') \times \frac{e^{\beta}_{\mathbf{q},\nu}(d')^* e^{\delta}_{\mathbf{q},\nu}(d'')}{\sqrt{m_{d'} m_{d''}}} \, r^{0,\alpha}_{\mathbf{0}d} \, e^{i\mathbf{q}\cdot(\ell''-\ell')}, \tag{4.19}$$

where the $e^{\beta}_{\mathbf{q},\nu}(d)$ indicates the displacement of atom d in the Cartesian direction β for the phonon $\mathbf{q}\nu$, and $r^{0,\alpha}_{\mathbf{0}d}$ is the equilibrium position of atom d in the Cartesian direction α for the unit cell at the origin. To get a rough estimate of the maximum anharmonicity strength in the crystal, the relation in (4.19) can be inverted and written in terms of the maximal mode Gruneisen constant $\gamma^{\max}$ found in a crystal,

$$k^{(3)} \sim \frac{6 m_d \omega_0^2 \gamma^{\max}}{l}, \tag{4.20}$$

where ω_0 is the typical phonon energy of the lattice and l is the nearest neighbor distance. Now consider a typical displacements $\sim (\sqrt{2 m_d \omega_0})^{-1}$ of an atom in the crystal; the change in the

potential energy δV_{anh} due to anharmonic force constant estimated above is given by,

$$\begin{aligned}\frac{\delta V_{\text{anh}}}{\omega_0} &\sim \frac{1}{\omega_0}\frac{1}{3!}\,k^{(3)}(\sqrt{2m_d\omega_0})^{-3} \\ &\sim 0.02\left(\frac{m_d}{28\text{ GeV}}\right)^{-0.5}\left(\frac{\omega_0}{30\text{ meV}}\right)^{-0.5} \\ &\times\left(\frac{\gamma^{\max}}{1.5}\right)\left(\frac{l}{2.35\,\mathring{A}}\right)^{-1},\end{aligned} \tag{4.21}$$

where in the second line we use parameters for Si. We use an estimate for the maximal value of the mode Gruneisen constant in Si from [108] at 0K. In Ge, the maximal Gruneisen constant is similar to that in Si, while in GaAs, it could be as high as 3.5 for certain phonon modes [108]. The Gruneisen constant thus provides a rough estimate of the overall anharmonicity in the crystal, including the cubic terms which depend on displacements of multiple atoms.

In this paper, we will work with a toy model of anharmonic interactions similar to the 1D oscillator model in Sec. 4.2.1. In particular, we consider excitations for an isolated atom in a 1D anharmonic potential. The anharmonicity is controlled by force constant terms like $k^{(3)}_{\alpha\beta\gamma}(\ell d,\ell' d',\ell'' d'')$ with $\ell d = \ell' d' = \ell'' d''$ which characterize the modification to the potential of a single atom in a lattice. Since the Gruneisen constants involve a sum over many cubic force terms, we instead directly obtain the single-atom anharmonic force constants with an empirical model of the lattice.

We model the lattice assuming empirical interatomic potentials, which have been shown to accurately reproduce phonon dispersions and transport properties [117]. Concretely, we assume the Tersoff-Buckingham-Coulomb interatomic potential with the parameter set given in Ref. [117] (see Appendix 4.A for details). We then fix all atoms at their equilibrium positions except for one atom denoted by ℓd, which is displaced by a small distance in different directions. The single atom potential calculated from this procedure is shown in Fig. 4.3 for Si, with deviations from the harmonic potential that depend on the direction of displacement. The maximum anharmonicity is along the direction of the nearest neighbor atom. Along this direction,

we find that the typical change in the potential energy for an atom displaced by $r \sim (\sqrt{2m_d\omega_0})^{-1}$ is,

$$\frac{\delta V_{\text{anh}}}{\omega_0} \sim 0.01. \tag{4.22}$$

Comparing this estimate with (4.21), we see that the anharmonicity strength inferred from the potential of a single atom is roughly of the same size as the overall anharmonicity strength of the lattice inferred from the Gruneisen constant. Thus, even though we do not perform a full calculation of the structure factor for an anharmonic crystal including the modification of the phonon spectrum and the lattice states, the comparison above suggests that the effects in a full calculation are expected to be similar in magnitude to the effects we estimate in this work using single atom potentials.

4.2.3 Toy anharmonic potential

As shown in Sec. 4.2.1 for the harmonic crystal, the features of the dynamic structure factor under the incoherent approximation can be well-approximated with just a 1D toy potential for an individual atom. This gives a much simpler path to calculating DM scattering in anharmonic crystals for $q \gg 2\pi/a$, where many phonons may be produced. In contrast, prior work including anharmonicity focused on the limit $q \ll 2\pi/a$, restricted to two phonons [42], and does not scale well to large number of phonons. We can then stitch together the two approaches to gain a more complete understanding of anharmonic effects.

In this work, we take a 1D anharmonic potential and calculate the 1D structure factor, in order to simplify the problem as much as possible. Taking the 1D approximation is more subtle in the presence of anharmonicity since a generic potential in 3D is not separable, unlike the harmonic case. Denoting the small displacement around equilibrium by r, and the polar and azimuthal directions by θ and ϕ respectively, the potential energy for atom d in the lattice can be

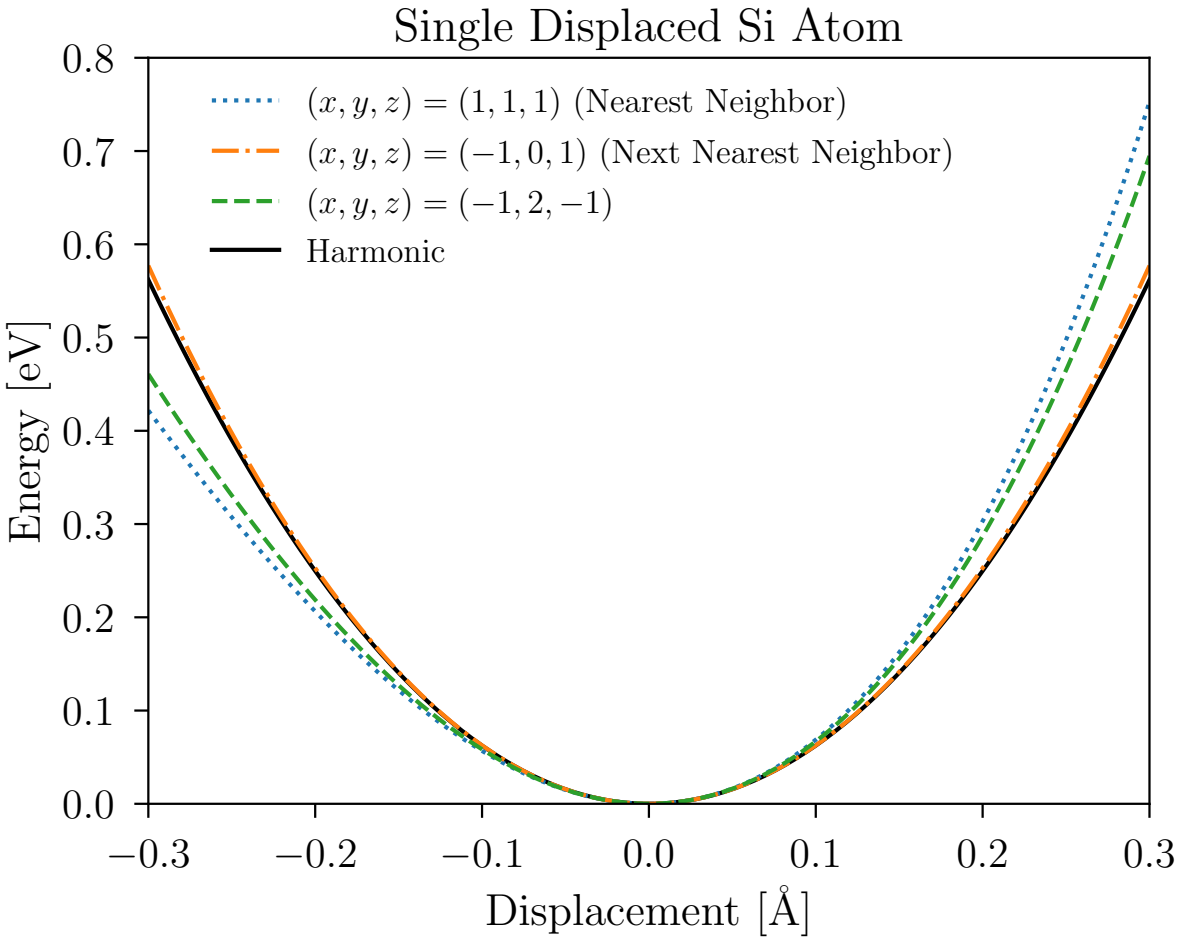

Figure 4.3. Single atomic potential: Potential of a single atom displaced along various directions with all other atoms at their equilibrium positions. In zincblende Si, the largest anharmonicity is in the direction of the nearest-neighbor atom, while the smallest anharmonicity is in the direction of the next-nearest-neighbor. We have also included a third direction orthogonal to the other two, with intermediate anharmonicity strength.

expanded in powers of r as,

$$V_d(r,\theta,\phi) = \frac{1}{2} m_d \omega_0^2 r^2 + \sum_{k\geq 3} \lambda_k \omega_0 f_k(\theta,\phi)(r\sqrt{2m_d\omega_0})^k, \tag{4.23}$$

where λ_k are dimensionless constants parameterizing the degree of anharmonicity at k^{th} order, and $f_k(\theta,\phi)$ are functions which specify the angular dependence and whose range is $[-1,1]$.

Solving the full 3D problem would require numerically finding the eigenstates of this general potential, while in the 1D case we can make much more progress analytically. We will therefore select directions of maximum anharmonicity and use this for our simplified 1D problem. Our expectation is that this gives a conservative estimate of the importance of anharmonic couplings, in that the full 3D calculation would give somewhat reduced effects.

As discussed in Sec. 4.2.2, we can extract realistic single atom potentials by modeling the interatomic potentials on the lattice and displacing a single atom (see Appendix 4.A for details). We typically find that, for small displacements around equilibrium, the anharmonicity is dominated by the cubic and quartic terms parametrized by λ_3 and λ_4, respectively. Motivated by these observations, we consider the following forms of toy potentials in our study:

- **Single cubic or quartic perturbations:** We first consider a harmonic potential with a single perturbation,

$$V_d(x) = \frac{1}{2} m_d \omega_0^2 x^2 + \lambda_k \omega_0 (\sqrt{2 m_d \omega_0} x)^k, \tag{4.24}$$

  where $k = 3$ or 4. This case is amenable to perturbation theory, and in Sec. 4.3.2, we apply it to discuss the power counting of anharmonic corrections.

- **Morse potential:** It is possible to obtain exact (non-perturbative) analytic results for the Morse potential defined by,

$$V_{\text{Morse}}(x) = B\left(e^{-2ax} - 2e^{-ax}\right), \tag{4.25}$$

  where a is a parameter controlling the width of the potential and B is the normalization. We fit these two parameters to the cubic anharmonicity estimated from the single atom potentials discussed earlier, and calculate the dynamic structure factor for this potential in App. 4.D.

- **Fit to realistic atomic potentials:** We numerically calculate the structure factor in a potential with both cubic and quartic terms, where the dimensionless anharmonic couplings are obtained by fitting to the actual single atom potential. The potential in this case is given by

$$V_d(x) = \frac{1}{2} m_d \omega_0^2 x^2 + \lambda_3 \omega_0 (\sqrt{2 m_d \omega_0} x)^3 + \lambda_4 \omega_0 (\sqrt{2 m_d \omega_0} x)^4. \tag{4.26}$$

We find that typically, $\lambda_3 \sim 0.01$, and $\lambda_4 \sim 10^{-4}$.

For the 1D toy potentials discussed above, we compute the 1D dynamic structure factor in the incoherent approximation ($q \gg 2\pi/a$):

$$S_{\text{toy}}(q,\omega) = 2\pi \sum_d n_d \, |f_d|^2 \sum_f \left| \left\langle \Phi_f \middle| e^{iqx} \middle| \Phi_0 \right\rangle \right|^2 \times \delta(E_f - E_0 - \omega). \tag{4.27}$$

Again, we have summed over all atoms of type d in the lattice and defined the number density of atom d by n_d. The wavefunctions $|\Phi\rangle$ are the eigenfunctions of the Hamiltonian,

$$H_{\text{toy}} = \frac{p^2}{2m_d} + V_d(x). \tag{4.28}$$

The computation of the dynamic structure factor then boils down to computing the ground state $|0\rangle$ and the excited eigenstates $|\Phi_f\rangle$ for this Hamiltonian, and calculating the structure factor under the incoherent approximation as in Eq. (4.27).

As discussed in Sec. 4.2.1, for a 1D toy model the phonon levels are discrete and in a real crystal there is a broad spectrum of energy levels. Similar to the harmonic case, we need a prescription to account for this smearing of energies. In the case with anharmonicity, the spectrum is shifted. The 1D toy model will instead give a modified energy-conserving delta

function:

$$\delta(f(n)\omega_0 - \omega), \tag{4.29}$$

where $f(n)\omega_0$ is the energy difference between the nth excited state and the ground state. $f(n)$ will depend on the exact form of the potential. Guided by the harmonic result, we again shall fix $\omega_0 = 1/\overline{\omega^{-1}}$ and introduce a width to the delta function in a similar fashion:

$$\delta(f(n)\omega_0 - \omega) \to \frac{1}{\sqrt{2\pi f(n)\sigma^2}} e^{-\frac{(\omega - f(n)\omega_0)^2}{2f(n)\sigma^2}}. \tag{4.30}$$

This is in the 1D approximation, and that including the full 3D anharmonic potential would be expected to have an additional effect on the spectrum of states. However, in practice the anharmonicity is sufficiently small that the shift of the spectrum is subdominant to the other anharmonic effects in the structure factor.

This forms the basis of the toy model we consider in this paper. Focusing on the high q regime where the incoherent approximation applies, we consider independent lattice sites and calculate scattering in them with 1D toy anharmonic potentials. We now describe different approaches to understand the dynamic structure factor in this setting.

4.3 Analytic results for structure factor

In this section, we study the features of the structure factor for a 1D anharmonic potential with analytic methods. This will allow us illustrate the general behavior for the limits $q \ll \sqrt{2m_d\omega_0}$ and $q \gg \sqrt{2m_d\omega_0}$.

First, we review the derivation of the structure factor for a 1D harmonic potential. For n-phonon production in the harmonic limit, the structure factor in the regime $q \gg \sqrt{2m_d\omega_0}$ is $\propto q^{2n}/(2m_d\omega_0)^n$. Treating the anharmonic 1D potential as a perturbation, we then show that the q dependence of the n-phonon term can be substantially modified in the regime $q \ll \sqrt{2m_d\omega_0}$, leading to large anharmonic corrections. In particular, we obtain the power counting of the

structure factor in powers of q and the anharmonicity parameter λ_k, which allows us to roughly identify the regime of q where we expect the anharmonic effects to be dominant. As we will see later, this proves useful to explain the numerical results for realistic potentials.

Finally, we will also use the impulse approximation to perform an analytic estimate of the structure factor in the regime $q > \sqrt{2m_d\omega_0}$. We show that the nuclear recoil limit is reproduced, with the structure factor approximated by a Gaussian envelope similar to the harmonic case. Anharmonic terms give rise to slightly modified shape of the Gaussian, which have negligible impact on scattering rates.

4.3.1 Harmonic oscillator

First, we briefly review the calculation of the dynamic structure factor in the harmonic approximation. In this case the potential $V_d(x)$ is given by

$$V_d(x) = \frac{1}{2} m_d \omega_0^2 x^2. \tag{4.31}$$

The energy E_n of the n-th excited state $|n\rangle$ of this simple harmonic oscillator is given by,

$$E_n = \left(n + \frac{1}{2}\right)\omega_0. \tag{4.32}$$

The structure factor in Eq. (4.27) thus becomes,

$$S_{\text{toy}}(q,\omega) = 2\pi \sum_d n_d \ |f_d|^2 \sum_n \left| \langle n|e^{iqx}|0\rangle \right|^2 \delta(n\omega_0 - \omega). \tag{4.33}$$

The matrix element can be evaluated in the following way,

$$\begin{aligned}\langle n|e^{iqx}|0\rangle &= \frac{1}{\sqrt{n!}}\langle 0|a^n e^{iqx}|0\rangle \\ &= \frac{1}{\sqrt{n!}}\langle 0|e^{iqx}\Big(a+\frac{iq}{\sqrt{2m_d\omega_0}}\Big)^n|0\rangle \\ &= \frac{1}{\sqrt{n!}}\Big(\frac{iq}{\sqrt{2m_d\omega_0}}\Big)^n\langle 0|e^{iqx}|0\rangle \\ &= \frac{1}{\sqrt{n!}}\Big(\frac{iq}{\sqrt{2m_d\omega_0}}\Big)^n e^{-\frac{q^2}{4m_d\omega_0}}, \end{aligned} \tag{4.34}$$

where we use $e^{-iqx}ae^{iqx} = a + \frac{iq}{\sqrt{2m_d\omega_0}}$ in the second equality. Plugging the above matrix element to the structure factor in (4.33) becomes,

$$\begin{aligned}S_{\rm toy}(q,\omega) &= 2\pi\sum_d n_d\ |f_d|^2 e^{-2W_d^{\rm toy}(q)} \\ &\quad\times\sum_n \frac{1}{n!}\left(\frac{q^2}{2m_d\omega_0}\right)^n \delta\left(n\omega_0-\omega\right), \end{aligned} \tag{4.35}$$

where $W_d^{\rm toy}(q) = q^2/(4m_d\omega_0)$ is the Debye-Waller factor in the toy model. The structure factor follows a Poisson distribution with mean number of phonons $\mu = q^2/(2m_d\omega_0)$, as also shown in the case of the 3-dimensional harmonic oscillator in [71].

4.3.2 Perturbation theory for anharmonic oscillator: $q \ll \sqrt{2m\omega_0}$

We now turn to more general case where small anharmonic terms are included in the 1D toy potential. An exact solution is no longer possible. But as we will see, in the kinematic regime $q \ll \sqrt{2m_d\omega_0}$, we can use perturbation theory to obtain the behavior of the structure factor and illustrate the importance of the anharmonic corrections as a function of momentum and energy deposition. Our goal in this section then is to obtain the power counting of the anharmonic contributions to the structure factor.

The toy Hamiltonian we consider is given by,

$$H_{\text{toy}} = \frac{p^2}{2m_d} + \frac{1}{2} m_d \omega_0^2 x^2 + \lambda_k \omega_0 (\sqrt{2 m_d \omega_0} x)^k. \tag{4.36}$$

We will concretely consider k equal to 3 and 4, corresponding to a leading cubic and quartic anharmonicity, respectively. Treating the dimensionless anharmonicity parameter λ_k as a perturbation, the eigenstates $|\Phi_n\rangle$ are given by

$$|\Phi_n\rangle = |n\rangle + \lambda_k \, |\psi_n^{(1)}\rangle + \lambda_k^2 \, |\psi_n^{(2)}\rangle + ..., \tag{4.37}$$

and E_n' are the perturbed energies,

$$E_n' = \left(n + \frac{1}{2}\right) \omega_0 + \lambda_k \, c_n^{(1)} + \lambda_k^2 \, c_n^{(2)} + ... \tag{4.38}$$

With time-independent perturbation theory, the dynamic structure factor can be explicitly computed at different orders in λ_k using (4.27). We defer the details of the explicit calculation to Appendix 4.B. Instead, from the structure of the expansion we can already learn about the relevant corrections. In general, we can express the dynamic structure factor as an expansion in both λ_k and $q^2/(2m_d\omega_0)$. At zeroth order in λ_k, we see from (4.35) that the n-phonon term appears with a q-scaling of $q^{2n}/(2m_d\omega_0)^n$. As we will show below, anharmonicity introduces departures from this q-scaling at higher orders of λ_k. In the kinematic regime under consideration ($q \ll \sqrt{2m_d\omega_0}$), powers of $q^2/(2m_d\omega_0)$ smaller than n can lead to large anharmonic corrections to the n-phonon term in the structure factor.[1] The aim of this section is thus to illustrate the behavior of the q-scaling at different orders of λ_k.

The general expression for the dynamic structure factor in the toy model can be written

[1]Perturbation theory in λ_k is still valid. For instance, the expansion in (4.37) still holds. But the harmonic contribution in the structure function could be suppressed by small q for multi-phonon states.

as,

$$S_{\text{toy}}(q,\omega) = 2\pi \sum_d n_d \, |f_d|^2 e^{-2W_d^{\text{toy}}(q)} \times \sum_n \delta(E_n' - E_0' - \omega) \left[\frac{1}{n!} \left(\frac{q^2}{2m_d\omega_0} \right)^n + \sum_{i \geq 1} \left(\frac{q^2}{2m_d\omega_0} \right)^i \left(a_{n,i} \, \lambda_k^{\nu(n,i)} + \mathscr{O}\left(\lambda_k^{\nu(n,i)+1} \right) \right) \right] \tag{4.39}$$

For each n, the harmonic contribution appears at $\mathscr{O}((q^2/(2m_d\omega_0))^n)$ as seen in (4.13); note that we do not include the Debye-Waller factor in this power counting discussion since it always appears as an overall factor. The anharmonic corrections are included here as an expansion in powers of $q^2/(2m_d\omega_0)$ which are denoted by i. From the orthogonality of the states $|\Phi_n\rangle$ with the ground states, we see that the dynamic structure factor should vanish for $q \to 0$, which in turn implies that $i \geq 1$. Each power i of $q^2/(2m_d\omega_0)$ appears with non-zero powers of λ_k, denoted by $\nu(n,i)$. Here the power $\nu(n,i)$ is the smallest *allowed* power of λ_k for a given phonon number n and the power i of $q^2/(2m_d\omega_0)$. However, numerical cancellations can sometimes force this leading behavior to vanish. Typically, the bigger the difference in i and n, the larger the power of λ_k that is required. We will explicitly see the behavior of the powers $\nu(n,i)$ for k equal to 3 and 4 below, but we first discuss the implications of this form.

For the single phonon structure factor (i.e. for $n = 1$), the anharmonic terms are always suppressed compared to the harmonic term because of the additional powers of λ_k and $q^2/(2m_d\omega_0)$. But for phonon numbers $n > 1$, it is possible for anharmonic contributions to dominate for $q \ll \sqrt{2m_d\omega_0}$. As a simple example, in the 3-phonon state, the harmonic contribution to the structure factor is proportional to $q^6/(2m_d\omega_0)^3$, while the aharmonic result contains $\lambda_3^2 q^4/(2m_d\omega_0)^2$. So when $q \ll \sqrt{2m_d\omega_0}$, the anharmonic effect can lead to a large correction to the dynamic structure factor.

In a generic n-phonon state, the harmonic piece scales as $(q^2/(2m_d\omega_0))^n$. Comparing this

with the anharmonic term $\propto \lambda_k^{\nu(n,i)} q^{2i}/(2m_d\omega_0)^i$, we note that the anharmonic term dominates the harmonic term for $q \ll \sqrt{2m_d\omega_0}\lambda_k^{\nu(n,i)/(2(n-i))}$. For small enough q, the behavior is governed by the anharmonic effects. Of course, at even smaller $q \sim q_{\rm BZ}$ one would expect the incoherent approximation to break down. For the values of λ in realistic materials, we find that the dominance of the anharmonic terms can happen for q above $q_{\rm BZ}$, particularly for larger n. These corrections become larger with n since the harmonic piece is progressively more suppressed in $q^2/(2m_d\omega_0)$.

We now illustrate the origin of the λ_k powers $\nu(n,i)$ with an example in the case of $k=3$. In this case, the perturbation $x^3 \sim (a+a^\dagger)^3$ implies the leading correction to the state can change the oscillator number by ± 1 or ± 3. Then the perturbed eigenstates have the schematic form:

$$|\Phi_n\rangle \sim |n\rangle + \lambda_3\left(|n-3\rangle + |n-1\rangle + |n+1\rangle + |n+3\rangle\right) + \mathscr{O}(\lambda_3^2). \tag{4.40}$$

We neglect the numerical prefactor in front of each state. Note that the terms are only present if the integer labelling the state is non-negative, for example for the ground state $|\Phi_0\rangle \sim |0\rangle + \lambda_3\left(|1\rangle + |3\rangle\right) + \mathscr{O}(\lambda_3^2)$. The matrix element appearing in the n-phonon structure factor can be expressed as,

$$\langle\Phi_n|e^{iqx}|\Phi_0\rangle \sim b_0 + \lambda_3 b_1 + \lambda_3^2 b_2 + \mathscr{O}(\lambda_3^3), \tag{4.41}$$

where the coefficients are schematically given by,

$$b_0 \sim \langle n|e^{iqx}|0\rangle \tag{4.42}$$

$$b_1 \sim \langle n-3|e^{iqx}|0\rangle + \langle n-1|e^{iqx}|0\rangle + \langle n+1|e^{iqx}|0\rangle + \langle n+3|e^{iqx}|0\rangle + \langle n|e^{iqx}|1\rangle + \langle n|e^{iqx}|3\rangle \tag{4.43}$$

In order for given term in the coefficient to be nonzero, a minimum number of powers of iqx are required in the series expansion for e^{iqx}. This therefore links the powers of q with powers of λ_3.

Taking $n = 3$ as an example, then $b_0 \propto (iq)^3$ at leading order in the q expansion. Meanwhile, $b_1 \propto (iq)^2 + (iq)^4 + ...$ Note that the matrix elements $\langle 0|e^{iqx}|0\rangle$ and $\langle 3|e^{iqx}|3\rangle$ in b_1 contain terms proportional to $(iq)^0$, but they cancel each other, consistent with a matrix element that always vanishes as $q \to 0$. Also note that the coefficients b_0, b_1 always alternate in even or odd powers of (iqx) and therefore alternate in being purely real or imaginary. The resulting matrix element squared thus goes as

$$\begin{aligned} |\langle \Phi_3|e^{iqx}|\Phi_0\rangle|^2 &\sim |b_0 + \lambda_3^2 b_2 + \mathscr{O}(\lambda_3^4)|^2 + |\lambda_3 b_1 + \mathscr{O}(\lambda_3^3)|^2, \\ &\sim q^6 + \lambda_3^2(q^4 + \mathscr{O}(q^6)) + \mathscr{O}(\lambda_3^4). \end{aligned} \tag{4.44}$$

For the cubic interaction, only even powers of λ_3 appear in the matrix element squared due to the alternating even and odd powers of (iqx) in the b coefficients. In this example, in order to achieve the minimum q scaling of q^2, higher powers of λ_3 are required, which will introduce more terms in the expansion. Here we see a correction to the matrix element squared at $O(q^2\lambda_3^4)$.

The explicit derivation of $\nu(n,i)$ is given in Appendix 4.B. The minimum power of λ_3 required to get the leading behavior $\propto q^2/(2m_d\omega_0)$ in the anharmonic terms is given by,

$$\nu(n,1) = \begin{cases} \max\left(4 \times \left\lceil \frac{(n-1)}{6} \right\rceil \ , \ 2\right) & \text{for odd } n \\ 4 \times \left\lceil \frac{(n+2)}{6} \right\rceil - 2 & \text{for even } n \end{cases} \tag{4.45}$$

The minimum power of λ_3 as a function of the phonon number n and the power i of $q^2/(2m_d\omega_0)$ for $i > 1$ is given by,

$$\nu(n,i) = \max\left(2 \times \left\lceil \frac{|n-i|}{3} \right\rceil \ , \ 2\right), \quad i > 1. \tag{4.46}$$

We show the expansion of the structure factor in the powers of λ_3 and $q^2/(2m_d\omega_0)$ schematically in Fig. 4.4, where we drop the numerical coefficients for all the terms and only illustrate the behavior of the powers of λ_3 and $q^2/(2m_d\omega_0)$. In the right part of the schematic, we show the behavior of the n-phonon term for $n > 3$, and in the left part of the schematic, we show the expansion for $n = 1$, 2, and 3.

The relationship between the powers in λ_3 and the powers of $q^2/(2m_d\omega_0)$ in (4.46) can also be understood in the following way. The powers of $q^2/(2m_d\omega_0)$ that appear at $\mathcal{O}(\lambda_3^\nu)$ can range from $n-3\nu/2$ to $n+3\nu/2$, with the minimum power allowed being 1, and ν being an even positive integer. Contributions from powers larger than n are suppressed in the kinematic regime $q \ll \sqrt{2m_d\omega_0}$. But powers smaller than n can lead to significant corrections in the same regime.

For example, the anharmonic contribution to the 2-phonon structure factor has a leading behavior $\propto \lambda_3^2 q^2/(2m_d\omega_0)$, which is expected to dominate the harmonic behavior $\propto q^4/(2m_d\omega_0)^2$ for small enough q (explicitly for $q \lesssim \sqrt{2m_d\omega_0}\lambda_3$). Assuming $m_d \sim 28$ GeV, $\omega_0 \sim 40$ meV, and a typical value of $\lambda_3 \sim 0.01$, we expect the anharmonic contribution to start to dominate for $q \lesssim 0.5$ keV. This kinematic regime does not strictly satisfy the conditions for the incoherent approximation which are assumed in this calculation. However, it is interesting to note here that the size of this anharmonic correction roughly matches onto the result for the 2-phonon structure factor in the long-wavelength limit ($q \ll 1/a$) [42, 105], where it was found that anharmonic interactions give up to an order of magnitude correction to the structure factor. At the edge of the Brillouin Zone $q \sim 2\pi/a \sim \mathcal{O}(\text{keV})$, with the typical values used above, we find in the toy model an $O(\sim 25\%)$ correction at the boundary of the valid region for the incoherent approximation.

For k equal to 4, which corresponds to a quartic perturbation to the harmonic potential, the calculation proceeds similarly to the cubic case discussed above, except for some key differences. All the coefficients b_i are either real or imaginary based on whether n is even or odd respectively, and hence the anharmonic corrections appear in all orders of λ_4. We thus have corrections at

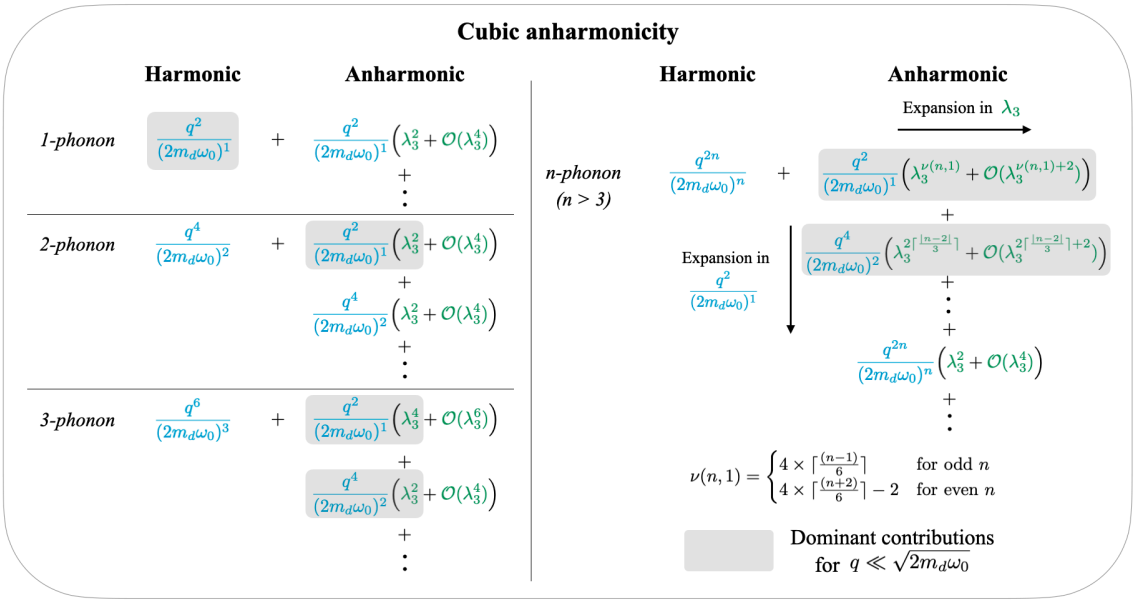

Figure 4.4. Expansion of the structure factor in phonon number n, powers of $q^2/(2m_d\omega_0)$, and powers of λ_3 for a cubic perturbation ($k = 3$ in (4.36)). The right part shows the general behavior of the n-phonon term for $n > 3$, while the left part shows the expansion for n =1, 2, and 3. Shaded terms show the dominant contributions when $q \ll \sqrt{2m_d\omega_0}$, which comes from the anharmonic terms for $n \geq 2$. Here we just illustrate the power counting; individual terms might not be present if there is a numerical cancellation in the coefficients.

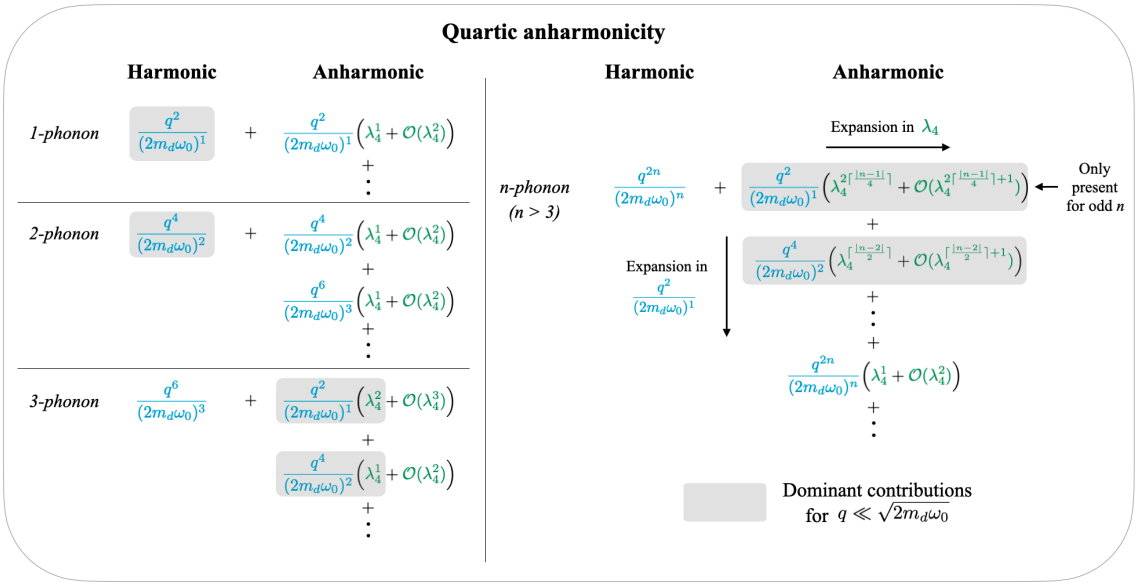

Figure 4.5. Expansion of the structure factor in phonon number n, $q^2/(2m_d\omega_0)$, and λ_4 for a quartic perturbation ($k = 4$ in (4.36)). The right part shows the general behavior of the n-phonon term for $n > 3$, while the left part shows the expansion for n =1, 2, and 3. Shaded terms show the dominant contributions when $q \ll \sqrt{2m_d\omega_0}$, which comes from the anharmonic terms for $n > 2$. Similar to the above, individual terms might not be present if there is a numerical cancellation in the coefficients.

$\mathcal{O}(\lambda_4)$. For even n, coefficients b_i only have even powers of q, and thus cannot generate terms $\propto q^2$ in the squared matrix element. The leading behavior for even n is thus $\propto q^4$. For odd n however, the leading behavior is $\propto q^2$, and the minimum power of λ_4 is given by,

$$\nu(n,1) = \max\left(2 \times \left\lceil \frac{(n-1)}{4} \right\rceil \ , \ 1\right). \tag{4.47}$$

For powers i greater than 1, the minimum power of λ_4 for any phonon number n is given by,

$$\nu(n, i>1) = \max\left(\left\lceil \frac{|n-i|}{2} \right\rceil \ , \ 1\right). \tag{4.48}$$

We show the expansion of the structure factor in the powers of λ_4 and $q^2/(2m_d\omega_0)$ schematically in Fig. 4.5, where we drop the numerical coefficients for all the terms and only illustrate the behavior of the powers of λ_4 and $q^2/(2m_d\omega_0)$. Similar to Fig. 4.4, we are only illustrating the

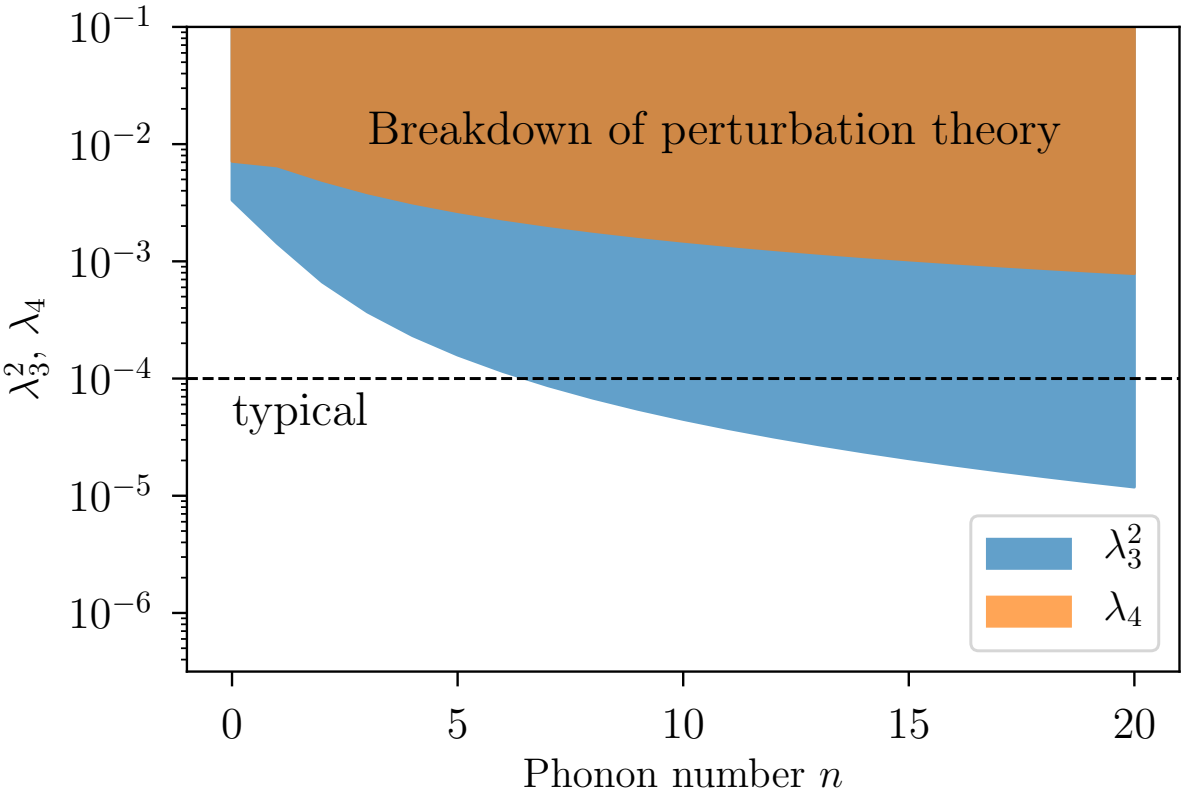

Figure 4.6. Perturbativity bound on λ_3^2 and λ_4 as a function of phonon number n. The bound is based on the criteria of (4.49) that the leading correction to the energy E_n is at most 10%. The dashed line shows the typical coupling sizes in Si and Ge crystals.

minimum allowed powers of λ_k in perturbation theory for $n > 3$. Due to numerical cancellations, the leading λ_k power can vanish in some cases.

Limitations of perturbation theory

Our analysis has focused on the regime $q \ll \sqrt{2m_d\omega_0}$ because this corresponds to a low mean phonon number. For large enough n, perturbation theory will start to break down. Equivalently, for a given n, perturbation theory will only be valid for λ_k sufficiently small.

For a particular phonon number n, if the energy correction in (4.38) is of the same order as the unperturbed energy eigenvalue $(n+\frac{1}{2})\omega_0$, the perturbation can no longer be treated as

small. Based on this, we set an upper bound on $|\lambda_k|$ by requiring that

$$|E'_n - \left(n+\frac{1}{2}\right)\omega_0| \sim 0.1 \times \left(n+\frac{1}{2}\right)\omega_0. \tag{4.49}$$

At leading order, the correction for k equal to 3 (i.e. a cubic perturbation) is given by

$$\begin{aligned} E'_n - \left(n+\frac{1}{2}\right)\omega_0 = \lambda_3^2\ \omega_0\ (9n^3 + 9(n+1)^3 \\ + (n+3)(n+2)(n+1) \\ + n(n-1)(n-2)) + \mathscr{O}(\lambda_3^4). \end{aligned} \tag{4.50}$$

The equivalent result for $k = 4$ reads,

$$\begin{aligned} E'_n - \left(n+\frac{1}{2}\right)\omega_0 = \lambda_4\ \omega_0\ ((n+1)(n+2) + (n+1)^2 \\ + 2(n+1)(n+2) + n^2 \\ + n(n-1)) + \mathscr{O}(\lambda_4^2). \end{aligned} \tag{4.51}$$

Using the equations above, we get the critical value of λ_3^2 and λ_4 compatible with the perturbation theory expansion. These are shown in Fig. 4.6. With the analytic structures of the energy corrections shown above, we see that the perturbativity bound on λ_3^2 (λ_4) has a scaling $\propto 1/n^2 (\propto 1/n)$, where n is the phonon number. For typical values of $\lambda_3 \sim 0.01$, we see that the perturbation theory is valid only up to $n \sim 6-7$. Furthermore, perturbation theory is impractical for calculating corrections at small q and very high phonon number n, since these corrections will be a very high order in the anharmonicity parameter.

To deal with these limitations, we consider two different approaches in this paper. Since high n is associated with high ω and q, in the next section we will use the impulse approximation to account for anharmonic effects at high q. In Appendix 4.D, we also study a special anharmonic potential, the Morse potential, where it is possible to obtain exact results. We use this as a case

study to validate the perturbation theory and impulse approximation results.

4.3.3 Impulse Approximation for $q \gg \sqrt{2m\omega_0}$

As we have shown, perturbation theory quickly goes out of control beyond the first few number of phonons. Resumming the anharmonic interaction is usually needed for the structure factor when q or ω is large. Consider the following phase space

$$\begin{aligned} \text{Impulse regime:} \quad & q \gg \sqrt{2m\omega_0}, \\ & \omega \sim \frac{q^2}{2m} + \mathscr{O}(\sqrt{\omega\omega_0}), \end{aligned} \tag{4.52}$$

It has previously been shown [105, 118] in the harmonic case, that one can calculate the structure factor by using a saddle point approximation in the time-integral representation of the structure factor. This is called the "impulse approximation" since the steepest-descent contour is dominated by small times, which can be interpreted physically as an impulse.

We begin with the structure factor in Eq. (4.27), which can be decomposed as contributions from each atom d, $S_{\text{toy}}(q,\omega) = \sum_d n_d |f_d|^2 S_{\text{toy},d}(q,\omega)$. Then we rewrite the energy conservation delta function as a time integral

$$\begin{aligned} & S_{\text{toy},d}(q,\omega) \\ & \equiv \sum_f \int dt\, e^{i(E_f - E_0 - \omega)t} \left| \left\langle \Phi_f \middle| e^{iqx} \middle| \Phi_0 \right\rangle \right|^2 \\ & = \int dt\, e^{-i\omega t} \sum_f \left\langle \Phi_0 \middle| e^{-iqx} \middle| \Phi_f \right\rangle \left\langle \Phi_f \middle| e^{iHt} e^{iqx} e^{-iHt} \middle| \Phi_0 \right\rangle \\ & = \int dt\, e^{-i\omega t} \left\langle \Phi_0 | e^{-iqx} e^{iqx(t)} | \Phi_0 \right\rangle, \end{aligned} \tag{4.53}$$

where in the second equality we use the fact that $|\Phi_0\rangle$ and $|\Phi_f\rangle$ are eigenfunctions of H, and in the third equality we use the completeness relation and the time-dependent position operator

$x(t) = e^{iHt} x e^{-iHt}$. The final expression is the well-known structure factor in the time domain. Using the above representation of the structure factor,

$$\begin{aligned} S_{\text{toy},d}(q,\omega) &= \int_{-\infty}^{\infty} dt \, \langle e^{-iqx} e^{iqx(t)} \rangle \, e^{-i\omega t} \\ &= \int_{-\infty}^{\infty} dt \, \langle e^{-iqx} e^{iHt} e^{iqx} \rangle \, e^{-i(E_0+\omega)t}, \end{aligned} \tag{4.54}$$

We can further simplify this using the fact that e^{iqx} acts as a translation operator on momentum p, $e^{-iqx} p e^{iqx} = p + q$. Applying the translation on the full Hamiltonian yields

$$e^{-iqx} H(x,p) e^{iqx} = H(x, p+q). \tag{4.55}$$

Here we generalize the impulse approximation to any 1D Hamiltonian, $H(x,p) = \frac{p^2}{2m} + V(x)$, which satisfies

$$H(x, p+q) = H(x,p) + \frac{q^2}{2m} + \frac{q}{m} p. \tag{4.56}$$

One can also generalize impulse approximation to a generic potential $V(x,p)$ as long as the above holds in the limit of large q.[2] In other words, we require that the Hamiltonian in the large momentum limit is dominated by the kinetic energy $\frac{p^2}{2m}$, not the potential. We can then obtain reliable theoretical predictions in the impulse regime even with large number of phonons.

Applying the above to Eq. (4.54), the structure function now reads

$$\begin{aligned} S_{\text{toy},d}(q,\omega) &= \int_{-\infty}^{\infty} dt \, \left\langle e^{iH(x,p+q)t} \right\rangle e^{-i(E_0+\omega)t} \\ &\approx \int_{-\infty}^{\infty} dt \, \left\langle e^{i\left(H + \frac{qp}{m}\right)t} \right\rangle e^{-i\left(E_0+\omega-\frac{q^2}{2m}\right)t}, \end{aligned} \tag{4.57}$$

where we translate the momentum in the first line and use Eq. (4.56) in the second line. Note

[2] In this case, the impluse regime in Eq. (4.52) needs to be replaced as $\omega \sim \frac{q^2}{2m} + \frac{q}{m}\langle p \rangle$ and we impose Eq. (4.56) holds up to $\mathcal{O}\left(\omega_0^2/q\right)$ correction.

that $H = H(x,p)$ throughout and we drop the argument for brevity. The last line is exact for potentials that depend only on x.

Now we can apply the saddle point approximation to evaluate the time integral. Defining $H' \equiv H + \frac{pq}{m}$, we can write

$$S_{\text{toy},d}(q,\omega) = \int_{-\infty}^{\infty} dt\, e^{f(t)}, \tag{4.58}$$

where

$$f(t) \equiv \ln\langle e^{iH't}\rangle - it\left(E_0 + \omega - \frac{q^2}{2m}\right). \tag{4.59}$$

In order to calculate this object, we can expand $\ln\langle e^{iH't}\rangle$ in small t. The first few terms in this expansion are given by

$$\begin{aligned}
f(0) &= 0 \\
f'(0) &= i\Big(\frac{q^2}{2m} - \omega\Big) \\
f''(0) &= i^2\Big(\langle H'^2\rangle - \langle H'\rangle^2\Big) \\
&= -\frac{q^2}{m^2}\Big(\langle p^2\rangle - \langle p\rangle^2\Big) \\
f^{(3)}(0) &= i^3\Big(\langle H'^3\rangle - 3\langle H'\rangle\langle H'^2\rangle + 2\langle H'\rangle^3\Big) \\
&= -i\Big(\frac{q^2}{m^2}\langle p[H,p]\rangle + \frac{q^3}{m^3}\langle p^3\rangle\Big) \\
f^{(4)}(0) &= i^4\Big(-6\langle H'\rangle^4 + 12\langle H'\rangle^2\langle H'^2\rangle^2 \\
&\qquad - 3\langle H'^2\rangle^2 - 4\langle H'\rangle\langle H'^3\rangle + \langle H'^4\rangle\Big) \\
&= -\frac{q^2}{m^2}\langle [p,H]^2\rangle + \frac{q^3}{m^3}\langle [[p,H],p^2]\rangle \\
&\qquad + \frac{q^4}{m^4}\Big(\langle p^4\rangle - 3\langle p^2\rangle^2\Big)
\end{aligned} \tag{4.60}$$

$\cdots$

In the harmonic approximation, only the terms proportional to q^2 are nonzero. As a result, only the first few expansion terms are needed as long as $t \ll \frac{1}{\omega_0}$ since $f^{(n+1)}/f^{(n)}$ is of order ω_0. Then one can solve for the saddle point t_I by solving $f'(t_I) \approx f'(0) + f''(0)t_I = 0$, which gives

$$it_I = \frac{m^2(\omega - \frac{q^2}{2m})}{q^2\sigma_p^2}, \tag{4.61}$$

where

$$\sigma_p^2 \equiv \langle p^2 \rangle - \langle p \rangle^2 = \langle p^2 \rangle. \tag{4.62}$$

In the last equality we use the fact that $\langle p \rangle = 0$ for a $V(x)$ potential since $\langle p \rangle \propto \langle [x, H] \rangle = 0$. Although t_I is formally imaginary, its magnitude is small and close to the origin in the impulse regime. Since there is no pole around this saddle point, we can approximate the time integral by the saddle point and find

$$\begin{aligned} S_{\text{toy},d}(q,\omega) &\approx \sqrt{\frac{2\pi}{-f''(t_I)}}\, e^{f(t_I)} \\ &= \frac{\sqrt{2\pi}m}{q\sigma_p} \exp\left(-\frac{m^2(\omega - \frac{q^2}{2m})^2}{2q^2\sigma_p^2}\right). \end{aligned} \tag{4.63}$$

For large energy depositions the Gaussian becomes narrowly peaked around $\omega = q^2/2m$, and this reproduces the nuclear recoil limit [105].

In the presence of anharmonic interactions, other powers of q will be present in the expansion of (4.60). In general, the $f^{(n)}$ term will have a q^n term with coefficient of $\mathscr{O}(\lambda)$. In this case, $f^{(n+1)}/f^{(n)} \sim q\sqrt{\omega_0/m}$. Higher orders will then be important in the expansion of $f(t)$ for sufficiently large q or t. For a given q, the higher order corrections become relevant for $|t| \gtrsim \sqrt{m/\omega_0}/q \sim 1/\sqrt{\omega\omega_0}$ in the impulse regime. Including these corrections is difficult in general, but we can continue to use the second order expansion giving (4.63) as long as $|t| \lesssim 1/\sqrt{\omega\omega_0}$. According to (4.61), this corresponds to a condition on how close ω is to

$q^2/(2m)$. Since $q^2 \sim 2m\omega$ and $\sigma_p^2 \sim m\omega_0$, this implies that

$$|t_I| \sim \frac{|\omega - \frac{q^2}{2m}|}{\omega\omega_0} \to |\omega - \frac{q^2}{2m}| \lesssim \sqrt{\omega\omega_0}. \tag{4.64}$$

We see that the distance of ω from $\frac{q^2}{2m}$ sets the size of t_I, which in turn tells us the regime for the validity for the approximation (4.63). The condition (4.64) is approximately the same condition that ω is within the Gaussian width in (4.63), and keeping terms in $f(t)$ only up to $f''(0)$ is self-consistent near $\omega = \frac{q^2}{2m}$.

Therefore, in the presence of anharmonic interactions, the above structure factor result (4.63) remains valid in the impulse regime (4.52). The only modification is in σ_p^2. Considering perturbations in $V(x)$ up to x^4 and recalling that the expectation value is with respect to the full ground state, we find that

$$\sigma_p^2 = \langle p^2 \rangle = \frac{m\omega_0}{2}\left(1 - 44\lambda_3^2 + 12\lambda_4 + \cdots\right) \tag{4.65}$$

at leading order in λ_3, λ_4. The nuclear recoil limit is again reproduced, with a small modification to the width of the Gaussian envelope due to anharmonic couplings. Note that in order to calculate the structure factor far from $\omega = \frac{q^2}{2m}$, we must include additional orders in $f(t)$ and t_I. We do not perform these higher order calculations for the final results in this paper since they have a negligible effect on the integrated rates, but we provide the procedure for completeness in App. 4.C.

Finally, we approximate the effect that introducing the full crystal lattice has on this single atom result. Up until the evaluation of various moments of H', the impulse approximation is fully model-independent. We just have to make an adjustment to the final evaluation of $\langle p^2 \rangle$. The states in the full crystal theory are smeared by the phonon density of states, so we calculate

$\langle p^2 \rangle$ via the following prescription

$$\begin{aligned}\langle p^2 \rangle &= \frac{m\omega_0}{2}\Big(1+g(\lambda)\Big) \\ &\xrightarrow{\text{crystal}} \int d\omega' D(\omega')\frac{m\omega'}{2}\Big(1+g(\lambda)\Big),\end{aligned} \tag{4.66}$$

where $g(\lambda)$ is the anharmonic correction calculated in the single-atom potential. Essentially, we have used the average single phonon energy to calculate $\langle p^2 \rangle$. In the harmonic limit, (4.63) then exactly matches the impulse result from [105].

In summary, in this section we have demonstrated the general behavior of anharmonic effects with q and ω. We have shown that they are indeed negligible at high q and $\omega \sim q^2/2m_d$, consistent with the intuition that scattering can be described by elastic recoils of a free nucleus. The effects grow for $q \ll \sqrt{2m_d\omega_0}$ and at low q they may dominate the structure factor. This roughly matches onto the results of Refs. [42, 105], which found that for $q < 2\pi/a$ anharmonic effects can have a large impact on the two-phonon rate .

4.4 Numerical results for 1D anharmonic oscillator

Having demonstrated the analytic behavior of the dynamic structure factor in the previous section, we now turn to obtaining numerical results using realistic potentials. We will perform concrete calculations for Si and Ge as representative materials while briefly commenting on others. As discussed in Sec. 4.2.2, we adopt an empirical model of interatomic interactions that encodes the anharmonicity in the potential. We use this empirical model to calculate a single atom potential, which we then use to evaluate the structure factor numerically.

As stated in Sec. 4.2.3, we start by fitting the single atom potential in a particular direction

onto a 1D potential of the form,

$$V_d(x) = \frac{1}{2} m_d \omega_0^2 x^2 + \lambda_3 \omega_0 (\sqrt{2 m_d \omega_0} x)^3 + \lambda_4 \omega_0 (\sqrt{2 m_d \omega_0} x)^4. \tag{4.67}$$

In the fit, $\omega_0, \lambda_3, \lambda_4$ are free parameters but in order to reproduce the harmonic limit, we then make the replacement $\omega_0 = 1/\overline{\omega^{-1}}$, which is calculated from the phonon density of states and gives a slightly different numerical value. This is motivated by the harmonic case discussed in Sec. 4.2.1. We do not consider anharmonic terms $\propto x^k$ for $k \geq 5$ as we observe that the anharmonic potential along any direction is dominated by the cubic and the quartic terms.

We find that the maximum anharmonicity is typically along the nearest neighbor direction $(x,y,z) = (1,1,1)$. For computing results, we will consider the potential along this direction, which represents maximum anharmonicity, as well as the potential in an orthogonal direction $(x,y,z) = (1,-2,1)$, which represents an intermediate value for the anharmonicity. Using the aforementioned interatomic models, we find anharmonicity strengths ranging from $\lambda_3 \sim 6 \times 10^{-3}$ to 10^{-2} and $\lambda_4 \sim (2-3) \times 10^{-4}$. For Si and Ge, the results are same for either atom in the unit cell.

Given the 1D potential in (4.67), we find exact solutions of the 1D eigenvalue and eigenvector problem using a simple finite difference method. We take a first order discretization of the Laplace operator and solve the discretized time-independent Schrödinger equation in a box. The box grid interval size must be small enough to resolve the maximum momentum scales of interest, which in this case depends on the highest excited state needed in the calculation. Also, the minimum box size required depends on the spatial extent of the highest excited state used. As seen in Sec. 4.3.3, the impulse approximation suffices for $q > \mathcal{O}(\text{few}) \times \sqrt{2 m_d \omega_0}$. Beyond this momentum, we no longer need to calculate excited states since the structure factor in the impulse limit is independent of the details of the highly excited states. The nth excited state is most relevant at momenta $q \sim \sqrt{n}\sqrt{2 m \omega_0}$. Therefore, to complete our calculation below

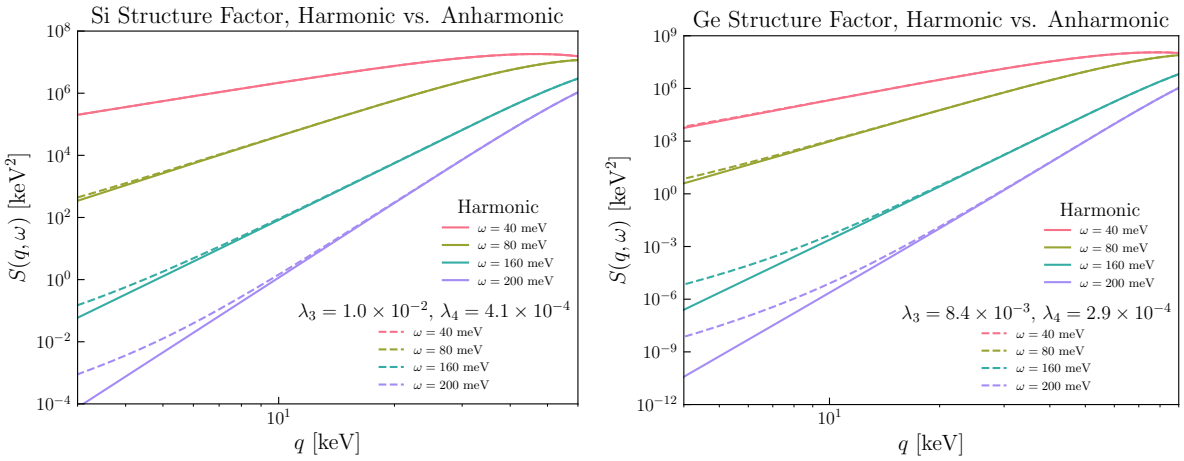

Figure 4.7. q**-dependence of structure factor:** We compare the structure factor in the harmonic and anharmonic cases, where in the latter case the structure factor is calculated numerically with the maximal anharmonicity. The lines from top to bottom show the structure factor at different ω, corresponding to an increasing minimum phonon number n. There are large corrections for $q \ll \sqrt{2m_d\omega_0}$ when anharmonic interactions are included (dashed), and the corrections become more significant as the threshold is increased. For $q \gg \sqrt{2m_d\omega_0}$, both cases converge to the same result. For Si, we have $\sqrt{2m_d\omega_0} \approx 40$ keV while for Ge, $\sqrt{2m_d\omega_0} \approx 50$ keV. For other materials, this quantity is listed in Table 4.1. The incoherent approximation momentum cutoff is $q_{\rm BZ} < 2\pi/a \sim 2.2$ keV for both crystals.

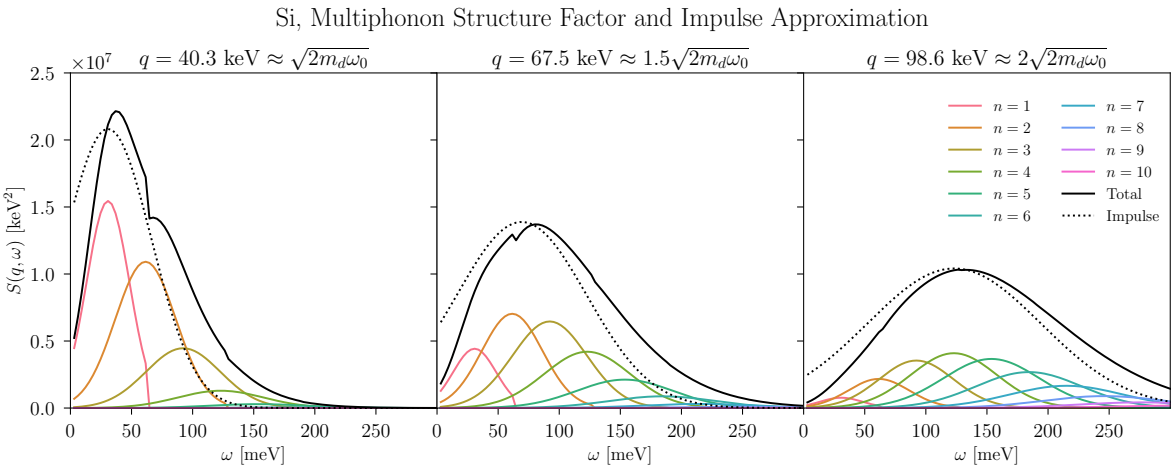

Figure 4.8. **ω-dependence of structure factor:** For different q values, we show the decomposition of the structure factor into individual n phonon terms, where the energy-conserving delta function has been smeared as in (4.68). Note that the maximum anharmonicity has been included in the numerical calculation, but the result is nearly identical to the harmonic result for these q values, as shown in Fig. 4.7. The dotted line shows the impulse approximation, which starts to become a good approximation as q increases above $\sqrt{2m_d\omega_0}$.

the impulse limit, we include the first 10 excited states. The results for these eigenstates are converged above a box size of $\sim 10/\sqrt{2m\omega_0}$ and grid size of $\sim 0.1/\sqrt{2m\omega_0}$.

We now use these numerical eigenstates and energies to calculate the structure factor in Eq. (4.27). We apply a prescription for the energy-conserving delta function similar to that used in the harmonic 1D oscillator, Eq. (4.15). The final result at momenta below the impulse regime ($q < 2\sqrt{2m\omega_0}$) is,

$$S(q,\omega) = 2\pi \sum_d n_d \, |f_d|^2 \sum_f \left| \left\langle \Phi_f \middle| e^{iqx} \middle| \Phi_0 \right\rangle \right|^2 \times \frac{1}{\sqrt{2\pi f(n)\sigma^2}} e^{-\frac{(\omega - f(n)\omega_0)^2}{2f(n)\sigma^2}} \times \Theta(\omega_{\max} - \omega), \tag{4.68}$$

where

$$\omega_0 = \left(\int d\omega \omega^{-1} D(\omega) \right)^{-1}, \tag{4.69}$$

$$\sigma = \sqrt{\frac{\int d\omega \omega D(\omega)}{\omega_0} - \frac{1}{\omega_0^2}}, \tag{4.70}$$

$$\omega_{\max} = f(n) \times (\min(\omega) | D(\omega) = 0) \tag{4.71}$$

and $f(n), |\Phi_0\rangle, |\Phi_f\rangle$ are given by the numerically solved eigenenergies and eigenstates, respectively. $D(\omega)$ is the single phonon density of states calculated with DFT [79]. In this work we assume equal couplings of DM with all nucleons so that $f_d = A_d$, where A_d is the atomic mass number. In the equations above, we have included a sum over all atoms in the unit cell d with density n_d, and in general the atomic potentials and density states can also depend on d, although for Si and Ge we do not include this.

In the impulse regime ($q > 2\sqrt{2m\omega_0}$), we have shown in Sec. 4.3.3 that the structure factor for any position-dependent potential is approximated by a Gaussian envelope,

$$S(q,\omega) \approx \sum_d n_d |f_d|^2 \sqrt{\frac{2\pi}{\frac{q^2}{m^2}\langle p^2 \rangle}} e^{-\frac{\left(\omega - \frac{q^2}{2m}\right)^2}{2\frac{q^2}{m^2}\langle p^2 \rangle}}, \tag{4.72}$$

where the the expectation values are all computed in the ground state and adjusted to the average single phonon energy via (4.66). Now we simply use the numerical ground state of the anharmonic potential (4.67) to calculate $\langle p^2 \rangle$ and therefore obtain the structure factor. Note that the anharmonic contribution is essentially negligible in the impulse limit, since corrections to $\langle p^2 \rangle$ are $\propto \lambda_3^2, \lambda_4$.

Fig. 4.7-4.8 shows numerical results on the structure factor for Si and Ge, taking the maximum anharmonicity in either case. In Fig. 4.7, the structure factor as a function of q is shown. As ω (and therefore minimum phonon number n) is increased, there is a larger anharmonic correction at small q. This can be understood by looking at the q scalings discussed in Sec. 4.3.2

and illustrated in Fig. 4.4 and Fig. 4.5. At low q and thus DM mass, the contributions from the anharmonic structure factor can give smaller powers of $\frac{q^2}{2m_d\omega_0}$ compared to the leading harmonic term $\left(\frac{q^2}{2m_d\omega_0}\right)^n$, so the enhancement grows with n. At high q, results converge to the harmonic result, consistent with our discussion of the impulse regime in Sec. 4.3.3. We see this also in Fig. 4.8, which shows the structure factor at different q. The impulse approximation becomes better as $q \gg \sqrt{2m_d\omega_0}$, and is indistinguishable from the harmonic case.

4.4.1 Impact on DM scattering rates

We now use the numerical results for the structure factor to compute the DM scattering rates for a range of DM masses and experimental thresholds. Our results are summarized in Figs. 4.9-4.10. We consider DM masses in the range $\sim 1-10$ MeV. The lower end of the mass range is chosen such that the momentum transfers are large enough to satisfy the condition for the incoherent approximation (i.e. $q > 2\pi/a$), while at the upper end of masses it is expected that scattering is described by the impulse approximation [105]. It is precisely this mass range where details of multiphonon production are important. We will also consider the two cases of scattering through heavy and light mediators. The goal will be to identify the region of parameter space where the anharmonic effects on the dynamic structure factor affect the scattering rates the most.

In the isotropic limit, the observed DM event rate per unit mass is given by [105]

$$R = \frac{1}{4\pi\rho_T}\frac{\rho_\chi}{m_\chi}\frac{\sigma_p}{\mu_\chi^2}\int d^3\mathbf{v}\frac{f(\mathbf{v})}{v}\int_{q_-}^{q_+}dq\int_{\omega_{\rm th}}^{\omega_+}d\omega\, q|\tilde{F}(q)|^2 S(q,\omega), \tag{4.73}$$

where ρ_χ is the DM energy density, ρ_T is the mass density of the target material, m_χ is the DM mass, μ_χ is the DM-nucleon reduced mass, σ_p is the DM-nucleon cross section, and $f(\mathbf{v})$ is the DM velocity distribution. The structure factor $S(q,\omega)$ is given by our numerical results (4.68)-(4.72) and the integration bounds are determined by the kinematically allowed phase

space

$$q_{\pm} \equiv m_\chi v \left(1 \pm \sqrt{1 - \frac{2\omega_{\rm th}}{m_\chi v^2}}\right), \tag{4.74}$$

$$\omega_+ \equiv qv - \frac{q^2}{2m_\chi}, \tag{4.75}$$

where the energy threshold of the experiment is denoted by $\omega_{\rm th}$. The q-dependence of the DM-nucleus interaction can be encapsulated in the DM form factor $\tilde{F}(q)$, where $\tilde{F}(q) = 1$ indicates an interaction through a heavy mediator, and $\tilde{F}(q) = q_0^2/q^2$ indicates an interaction through a light mediator for a reference momentum transfer of q_0.

Note that in general, the strength of the anharmonicity varies with the direction of the recoil of the nucleus, and the structure factor will depend on the direction of the momentum transfer. For simplicity, we are assuming that the anharmonicity strength is uniform in all directions. Our estimate with the maximum anharmonicity thus provides an upper bound on the anharmonic effects on DM scattering.

The DM mass sets the typical momentum-transfer scale q of the scattering, and the experimental energy threshold $\omega_{\rm th}$ sets the phonon number n. Hence, to identify the DM masses and experimental thresholds where anharmonic effects start to become important, we first need to understand the q-values where the anharmonic corrections are large for a particular phonon number n. We can estimate this using the perturbation theory results in Sec. 4.3.2. Note that in our numerical calculation, we find that λ_3 generally provides the larger anharmonic contribution, so we will focus on a purely cubic perturbation in this discussion.

For the analysis of a cubic perturbation discussed in Sec. 4.3.2, we showed that anharmonic effects introduced additional terms to the n-phonon structure factor of the form $\propto \lambda_3^{\nu(n,i)} \left(\frac{q^2}{2m_d\omega_0}\right)^i$, see (4.39). Therefore when q is lower than the scale

$$q \lesssim \sqrt{2m_d\omega_0}\lambda_3^{\nu(n,i)/(2(n-i))}, \tag{4.76}$$

terms in the anharmonic structure factor can be of comparable size to the harmonic structure factor. In order to find the largest q-scale where the anharmonic contribution starts to become relevant, we can evaluate (4.76) for all positive $i < n$, and find the minimum possible exponent of λ_3. For $n = 2$ or 3, the minimum exponent is achieved for $i = 1$, for which $\nu(n,1) = 2$. This gives a q-scaling of $q \sim \sqrt{2m_d\omega_0}\lambda_3^{1/(n-i)}$. This tells us that for the 2-phonon case, the anharmonic contribution should begin to become important at $q \sim \sqrt{2m_d\omega_0}\lambda_3$, while for the 3-phonon case, the anharmonic contribution becomes important at $q \sim \sqrt{2m_d\omega_0}\lambda_3^{1/2}$. For a larger number of phonons, this scaling is approximately $q \sim \sqrt{2m_d\omega_0}\lambda_3^{1/3}$. So we see that higher energy excitations have more significant anharmonic contributions at larger momentum transfers. Below the q-scale identified above, the anharmonic contributions are expected to increase substantially with decreasing q, as terms $\propto q^{2i}$ for $i < n$ dominate the harmonic scaling $\propto q^{2n}$.

We now recast our analysis concretely in terms of DM mass and experimental energy thresholds as follows. For both massive and massless mediators, the event rate for $n \geq 2$ phonons is always dominated by the large q portion of phase space and energy depositions near the threshold. Therefore the enhancement in the rate due to the anharmonicity roughly corresponds to the enhancement in structure factor evaluated at $S(q = 2m_\chi v, \omega = \omega_{\rm th})$, where v is the DM velocity. Inserting $q = 2m_\chi v$ into the condition in (4.76) gives a condition on the DM mass:

$$m_\chi \lesssim \begin{cases} \frac{\sqrt{2m_d\omega_0}\lambda_3}{2\times 10^{-3}} & n = 2 \\ \frac{\sqrt{2m_d\omega_0}\lambda_3^{1/2}}{2\times 10^{-3}} & n = 3 \\ \frac{\sqrt{2m_d\omega_0}\lambda_3^{1/3}}{2\times 10^{-3}} & n > 3, \end{cases} \tag{4.77}$$

where 10^{-3} is the typical DM velocity. In order to determine the appropriate phonon number n for a given $\omega_{\rm th}$ we must take into account the subtlety that each excitation energy is smeared across a width, as discussed in Sec. 4.2.3 and also given in (4.70). To solve for the smallest n

Table 4.1. Single phonon properties for various crystals. Using these energy scales, for a given experimental threshold we can estimate the DM masses where anharmonic effects become large, (4.76)-(4.79). For crystals with non-identical atoms in a unit cell, we show the quantities averaged across atoms. The relative importance of anharmonic effects in the different materials will mainly be governed by the different phonon energies ω_0.

Materials			
	ω_0 [meV]	σ [meV]	$\sqrt{2m_d\omega_0}$ [keV]
GaAs	16.9	9.5	48.8
Ge	18.2	10.6	49.6
Si	30.8	17.6	40.3
Diamond	109.6	35.8	49.7
Al_2O_3	51.6	20.4	51.1

that contributes appreciably above ω_{th}, we solve the following equation:

$$\omega_{\text{th}} = n\omega_0 + \sqrt{n}\sigma, \tag{4.78}$$

where σ is the single-phonon width as defined in (4.70) and we have for simplicity taken $f(n) = n$.

Applying (4.77)-(4.78) to Si with $\omega_0 = 31$ meV, $\sigma = 18$ meV, and $m_d = 26$ GeV, we find the following results

$$m_\chi \lesssim \begin{cases} 0.2\ \text{MeV}\frac{\lambda_3}{10^{-2}} & \omega_{\text{th}} = 80\ \text{meV} \\ 2.0\ \text{MeV}\left(\frac{\lambda_3}{10^{-2}}\right)^{1/2} & \omega_{\text{th}} = 120\ \text{meV} \\ 4.5\ \text{MeV}\left(\frac{\lambda_3}{10^{-2}}\right)^{1/3} & \omega_{\text{th}} \geq 160\ \text{meV} \end{cases} \tag{4.79}$$

Below these masses, anharmonic corrections become large. The last line applies for thresholds above 160 meV which corresponds to $n \geq 4$, and these n-phonon terms all give the same condition on DM mass. Note that this is only a heuristic, which does not include for example the combinatorial pre-factors or cancellations in the perturbation theory calculation. Nonetheless, we do see the same qualitative features in the complete numerical result which is given in Fig. 4.9.

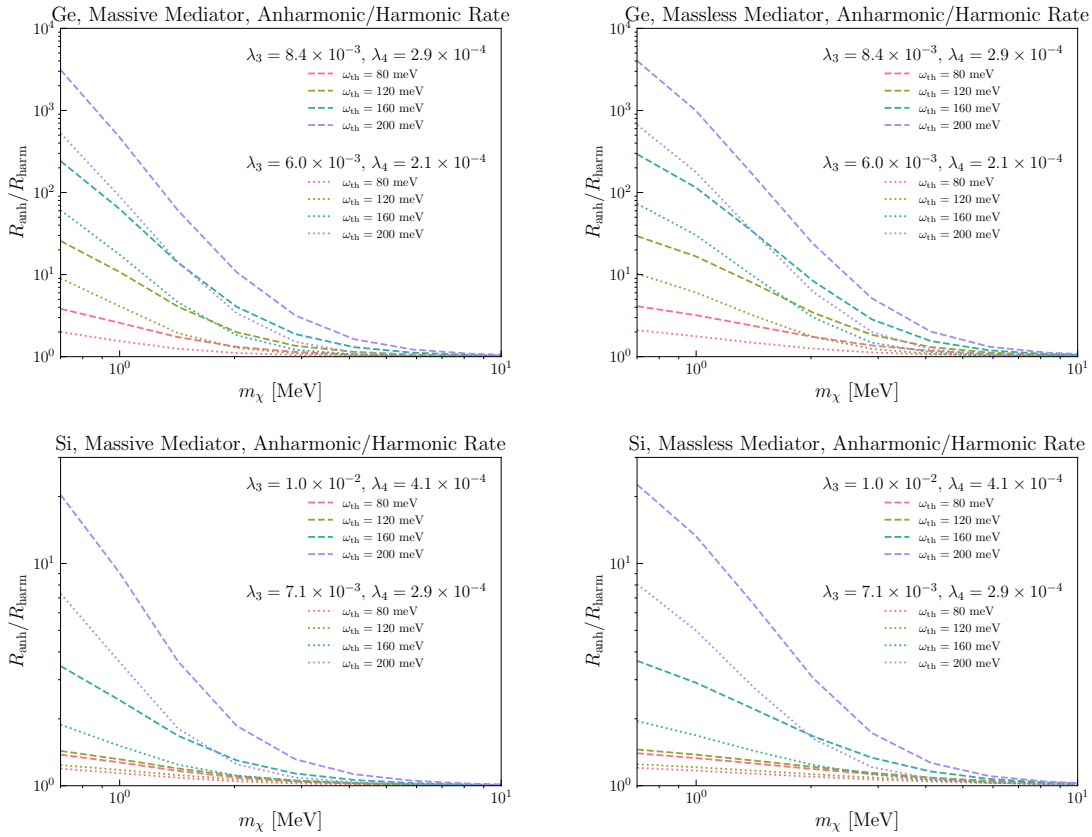

Figure 4.9. Ratio of anharmonic to harmonic rate. For each material (Ge and Si) we consider two representative values of the anharmonic couplings. The larger set corresponds to a direction of maximal anharmonicity while the other set corresponds to an orthogonal direction of intermediate anharmonicity. Anharmonic effects become more important for DM masses near the MeV scale and for larger energy thresholds.

In order to generalize (4.79) to other materials, we give the necessary energy scales in Tab. 4.1. Despite large differences in ω_0, the momentum scale $\sqrt{2m_d\omega_0}$ ends up being about the same in all crystals. Then the typical DM mass scale for anharmonic effects to become important is also about the same for a fixed phonon number n. However, the differences in ω_0 mean that the threshold corresponding to a given n can vary significantly. For a given threshold, GaAs and Ge have the largest phonon number. Since anharmonic corrections become more important with larger n, GaAs and Ge will therefore have larger anharmonic contributions compared to Diamond at the same threshold.

In Fig. 4.9, we present the ratio of scattering rates in the anharmonic case to the harmonic

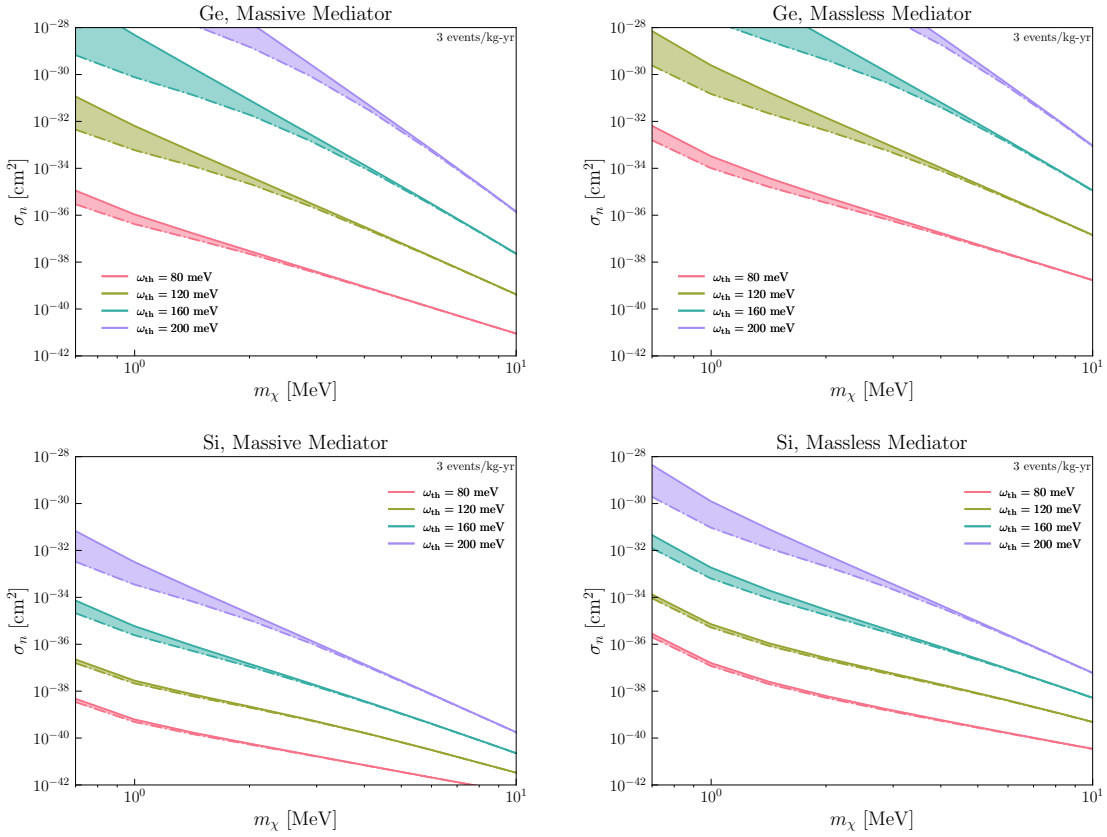

Figure 4.10. Cross section uncertainty. Comparison of the cross section corresponding to 3 events/kg-yr in the harmonic (solid) and anharmonic (dot-dashed) cases. The anharmonic result is shown for maximal anharmonicity, and so the shaded band represents our estimate of the theoretical uncertainty due to anharmonic effects. The effects are primarily important for high thresholds and low DM masses, corresponding to large σ_n, which is generally in tension with existing astrophysical or terrestrial constraints.

case in Si and Ge, taking two representative cases for the couplings. We also present the cross-sections corresponding to an observed rate of 3 events per kg-yr in Fig. 4.10. The bands depict the possible uncertainty that anharmonicity introduces to an experimental reach, with the solid line giving the harmonic result and the dot-dashed the result for maximal anharmonicity. We do not show the effects above the cross sections of $\sigma_n \gtrsim 10^{-28}$ cm^2 as for these large interaction strengths, the DM is expected to lose a significant energy in 1 km of Earth's crust through scattering, thus rendering DM with such cross sections unobservable in underground direct detection experiments [119].

For $m_\chi > 10$ MeV, the typical q becomes similar or larger than $\sqrt{2m_d\omega_0}$, where there is negligible difference in the anharmonic and harmonic structure factors. The rates will also start to be dominated by the impulse regime $q \gg \sqrt{2m_d\omega_0}$. In this case, the structure factor calculated with an anharmonic potential is nearly identical to that calculated in the harmonic case, as discussed in Sec. 4.3.3. We have also seen this behavior with numerical computations in Fig. 4.8. The anharmonic and harmonic scattering rates are also essentially identical for DM masses $m_\chi > 10$ MeV.

For DM masses $m_\chi < 10$ MeV (i.e. $q < \sqrt{2m_d\omega_0}$), the ratio of the anharmonic to harmonic rate begins to grow with decreasing DM mass. As the typical q decreases with decreasing DM mass, the leading anharmonic term $\propto \frac{q^2}{2m_d\omega_0}$ grows faster compared to the harmonic term $\propto \left(\frac{q^2}{2m_d\omega_0}\right)^n$ for $n \geq 2$. The effect is more pronounced for higher thresholds or equivalently higher n, since the harmonic term is even more suppressed. Therefore at larger thresholds, the anharmonic effects start becoming important already at larger masses and also grows much more quickly as the DM mass is decreased. For a given DM mass, this also implies that the spectrum of events will have larger anharmonic corrections on the high energy tail of events. However, the rates are also highly suppressed in this tail, and only observable for high scattering cross sections.

At DM masses $m_\chi < 1$ MeV, the slope of the ratio of the anharmonic rate to the harmonic rate starts to decrease slightly, which is an artifact of the Brillouin zone momentum cutoff that

we apply across all rate calculations. The incoherent and subsequent approximations are not guaranteed to be justified in this regime, so this effect should not be treated as physical. For sub-MeV DM masses, the phonons again should be treated as collective excitations, similar to the calculation of Ref. [42].

Lastly, we note an interesting feature that the anharmonic scattering rate is strictly greater than the harmonic rate in the entire parameter space that we probe. This is a consequence of the sign of the leading q-scaling term $\frac{q^2}{2m_d\omega_0}$. For the production of an excited state $|\Phi_f\rangle$ in the crystal, the term in the dynamic structure factor $\propto q^2$ can only come from the term $|\langle\Phi_f|iqx|\Phi_0\rangle|^2$, as the mixing term $\propto \langle\Phi_f|I|\Phi_0\rangle\langle\Phi_f|\frac{(iqx)^2}{2}|\Phi_0\rangle^*$ and its conjugate are zero from orthogonality. Thus, the sign of the term $\propto q^2$ in the anharmonic structure factor is strictly positive for producing an excited state, whereas there is no corresponding term $\propto q^2$ in the harmonic case for $n \geq 2$ phonons. Since we are probing the $q \ll \sqrt{2m_d\omega_0}$ regime, this leading term quickly dominates the structure factor. Thus, the anharmonic scattering rate exceeds the harmonic rate in this regime. A consequence of this is that we expect the harmonic crystal result gives a lower bound on the scattering.

4.5 Conclusions

Scattering of DM with nuclei in crystals necessarily goes through production of one or many phonons for DM masses smaller than ~ 100 MeV. Previous work has focused on calculating the multiphonon scattering rates in a harmonic crystal under the incoherent approximation (i.e. $q > q_{\rm BZ}$ or DM mass $\gtrsim$ MeV). In this work, we have studied the effects of anharmonicities in the crystal on the scattering rates, while still working within the incoherent approximation.

In order to obtain a tractable calculation of anharmonic effects, we have simplified the problem into a toy model of a single atom in a 1D anharmonic potential. In this toy model, scattering into multiphonons can still be well-approximated by applying a smearing on the spectrum of quantized states to account for the phonon spectrum of a lattice. We extract

anharmonic couplings by modeling the interatomic potentials of Si and Ge, which give rise to realistic single atom potentials. This approach allows us to obtain an analytic understanding and first estimate of the impact of anharmonicity, although the numerical results should not be taken as a definitive rate calculation.

We find that the harmonic crystal results of Ref. [105] can be safely assumed for DM masses down to ~ 10 MeV. Below ~ 10 MeV, this assumption cannot be taken for granted. In this regime, we find that anharmonic effects on the scattering rates increase with decreasing DM mass and increasing experimental thresholds. Anharmonic corrections up to two orders of magnitude are possible for DM masses $\sim$ a few MeV and for experimental thresholds $\sim$ a few times the typical single phonon energy of the crystal. These findings are consistent with Refs. [42, 105], which studied two-phonon production from sub-MeV DM and found up to an order of magnitude larger rate from anharmonic couplings.

The size of the corrections is dependent on the material through the anharmonicity strength of that crystal and also, non-trivially, through the typical single phonon energies of the material. For a particular energy threshold, crystals with lower single phonon energies exhibit larger corrections since they require larger phonon numbers to be produced. For example, anharmonic effects in Ge can be larger by almost an order of magnitude than those in Si for similar DM parameter space and thresholds, even though the anharmonic couplings in the two crystals are similar. This is a consequence of the difference in q scaling of the harmonic and anharmonic contributions, which become more pronounced with larger phonon number. Materials with low single-phonon energies, such as GaAs and Ge, therefore have the largest anharmonic effects. The effects will be reduced in Diamond and Al_2O_3, which have even higher single phonon energies than Si.

The relevance of anharmonic effects to direct detection experiments depends on the DM cross section. The effects are largest for low DM masses and high thresholds, in other words on the tails of the recoil spectrum where the rates are small. For a typical benchmark exposure of 1 kg-yr, the anharmonic corrections become sizeable for DM-nucleon cross sections above

$\sim 10^{-34}$ cm^2. Being agnostic about any terrestrial or astrophysical constraints on the DM model and only requiring the DM to be observable in underground direct detection experiments, the upper bound on the DM cross section is $\sigma_n \lesssim 10^{-28}$ cm^2 [119]. This comes from considering an overburden of $\sim$ km. On the other hand, these very high DM-nucleon cross sections are typically excluded by terrestrial and astrophysical constraints for the simplest sub-GeV dark matter models [34, 120]. DM-nucleon cross sections $\sigma_n \gtrsim 10^{-41}$ cm^2 ($\sigma_n \gtrsim 10^{-31}$ cm^2) are constrained for typical models with a heavy mediator (light dark photon mediator) for a DM mass $\sim$ MeV. With these constraints, we see from Fig. 4.10 that the anharmonic effects can only impart corrections of at most an order of magnitude for experiments with kg-yr exposure.

Experiments with exposures above kg-yr could see larger anharmonic effects, since they would be more sensitive to the events at high phonon number for MeV-scale DM. However, for solid-state direct detection experiments, achieving exposures significantly bigger than a kg-yr is challenging. Thus, for near-future crystal target experiments, we conclude that the anharmonic effects are only important up to $\mathcal{O}(1)$ factors at masses of $\sim$ a few MeV for the simplest DM models.

Acknowledgements

We are grateful to Simon Knapen and Xiaochuan Lu for useful discussions, and Simon Knapen for feedback on the draft. TL and EV were supported by Department of Energy grant DE-SC0022104. EV was also supported by a Sloan Scholar Fellowship. MS and CHS were supported by Department of Energy Grants DE-SC0009919 and DE-SC0022104. CHS was also supported by the Ministry of Education, Taiwan (MOE Yushan Young Scholar grant NTU-112V1039). Chapter 4, in full, is a reprint of the material as it appears in Tongyan Lin, Chia-Hsien Shen, Mukul Sholapurkar, and Ethan Villarama, Anharmonic effects in nuclear recoils from sub-GeV dark matter (e-print: 2309.10839 [hep-ph]), which is being prepared for journal submission. The dissertation author was one of the primary investigators and authors of this paper.

Appendix

4.A Interatomic potentials

In order to produce results for a real crystal, we adopt atomic potentials based on Ref. [117]. The interatomic potentials used here are a combination of various commonly used empirical potentials. We choose to use the Tersoff-Buckingham-Coulomb interatomic potential defined in Ref. [117] using the parameters in the set labeled "TBC-1", though other interatomic potentials may be chosen and give similar estimates for the anharmonicity strengths.

This potential includes a three-body Tersoff potential, originally defined in [121], which we restate here for reference.

$$\begin{aligned} E &= \frac{1}{2}\sum_i \sum_{i\neq j} V_{ij} \\ V_{ij} &= f_C(r_{ij})\big(f_R(r_{ij}) + b_{ij} f_A(r_{ij})\big), \end{aligned} \tag{4.80}$$

where the sum is over nearest-neighbor, and r_{ij} is the distance between neighbors i, j. The function f_C is a cutoff function that keeps the interaction short ranged, f_R and f_A are repulsive and attractive interactions, and b_{ij} is a three-body term that is a function of the bonding angle of

the third body with the atoms i, j. Explicitly, these functions are defined as

$$f_C(r) = \begin{cases} 1 & r < R - D \\ \frac{1}{2} - \frac{1}{2}\sin\left(\frac{\pi}{2}\frac{r-R}{D}\right) & R - D < r < R + D \\ 0 & r > R + D \end{cases} \tag{4.81}$$

$$f_R(r) = A\exp(-\lambda_1 r) \tag{4.82}$$

$$f_A(r) = -B\exp(-\lambda_2 r) \tag{4.83}$$

$$b_{ij} = \left(1 + \beta^n {\zeta_{ij}}^n\right)^{-\frac{1}{2n}} \tag{4.84}$$

$$\zeta_{ij} = \sum_{k \neq i,j} f_C(r_{ik})\, g\left[\theta_{ijk}\left(r_{ij}, r_{ik}\right)\right] \times \exp\left[{\lambda_3}^m \left(r_{ij} - r_{ik}\right)^m\right] \tag{4.85}$$

$$g(\theta) = 1 + \frac{c^2}{d^2} - \frac{c^2}{\left[d^2 + (\cos\theta - \cos\theta_0)^2\right]}, \tag{4.86}$$

where θ_{ijk} is the angle between the displacement vectors r_{ij} and r_{ik}. $R, D, A, B, \beta, n, c, d, \theta_0$, $\lambda_1, \lambda_2, \lambda_3$ are constants that can be found in Ref. [117]. Note that the notation in this section matches that of Ref. [117] and is standalone from the main text. Specifically, the parameters $\lambda_1, \lambda_2, \lambda_3$ are not to be confused with the anharmonicity strengths defined in the main text. In practice, anharmonicity arises from the asymmetry between the repulsive and attractive terms. The directional dependence of the anharmonicity strength is a result of the crystal's zincblende structure and bond angle-dependent potential.

The other components of this interatomic model include a long-range two-body Buckingham term

$$V(r) = Ce^{-r/\rho} - \frac{E}{r^6}, \tag{4.87}$$

and a screened Coulombic interaction defined by

$$V(r) = q^2\Big[\frac{\mathrm{erfc}(\alpha r)}{r} - \frac{\mathrm{erfc}(\alpha r_c)}{r_c} + \Big(\frac{\mathrm{erfc}(\alpha r_c)}{r_c^2} + \frac{2\alpha}{\sqrt{\pi}}\frac{e^{-\alpha^2 r_c^2}}{r_c}\Big)(r-r_c)\Big] \tag{4.88}$$

$$\times\,\Theta(r_c - r) \tag{4.89}$$

Here q is the effective atomic charge, α is a damping parameter, and r_c is a cutoff. As discussed in Ref. [117], the full interatomic potential model is a sum of the three aforementioned interactions. All of the free parameters are fit onto the actual second, third, and fourth order forces calculated from DFT. This gives an analytic interatomic potential that produces the correct single-phonon dispersions and also captures the anharmonicity in the potential by fitting onto the higher order interatomic forces from DFT.

4.B Power counting in perturbation theory

In this appendix, we work out the explicit relation between the powers of q^2 and λ_k in the perturbation theory calculation for the anharmonic Hamiltonian in (4.36).

The primary object we focus on in the dynamic structure factor is the squared matrix element $|\langle\Phi_n|e^{iqx}|\Phi_0\rangle|^2$, where $|\Phi_n\rangle$ are the eigenstates of the anharmonic Hamiltonian. With perturbation theory, the eigenstates can be expanded in powers of λ_k as in (4.37). The corrections to the nth final state up to second order in λ_k are given by,

$$|\psi_n^{(1)}\rangle = \sum_{k\neq n}\frac{V_{kn}}{(n-k)}|k\rangle, \tag{4.90}$$

$$|\psi_n^{(2)}\rangle = \sum_{k\neq n}\sum_{l\neq n}\frac{V_{kl}V_{ln}}{(n-k)(n-l)}|k\rangle - \frac{1}{2}|n\rangle\sum_{k\neq n}\frac{|V_{kn}|^2}{(n-k)^2},$$

where $V_{ij} \equiv \langle i|(\sqrt{2m_d\omega_0}x)^k|j\rangle$. In terms of the standard ladder operators of the harmonic

oscillator, V_{ij} are given by,

$$V_{ij} = \langle i|(a+a^{\dagger})^k|j\rangle\,. \tag{4.91}$$

This tells us that V_{ij} can only be non-zero when $i-j$ is one of the following: $-k$, $-k+2$,..., $k-2$, k.

With these selection rules, the corrections in Eqs. 4.90 can be schematically written as,

$$\begin{aligned} |\psi_n^{(1)}\rangle \sim\ & |n-k\rangle + |n-k+2\rangle + ... \\ & + |n+k-2\rangle + |n+k\rangle \end{aligned} \tag{4.92}$$

$$\begin{aligned} |\psi_n^{(2)}\rangle \sim\ & |n-2k\rangle + |n-2k+2\rangle + ... \\ & + |n+2k-2\rangle + |n+2k\rangle \end{aligned} \tag{4.93}$$

This pattern continues for higher orders in λ_k such that at $\mathcal{O}(\lambda_k^j)$, we have,

$$\begin{aligned} |\psi_n^{(j)}\rangle \sim\ & |n-(j\times k)\rangle + |n-(j\times k)+2\rangle + ... \\ & + |n+(j\times k)-2\rangle + |n+(j\times k)\rangle. \end{aligned} \tag{4.94}$$

Note that the sum should only include terms for which the integer labelling the state is non-negative. With the knowledge of the unperturbed states appearing in $|\Phi_n\rangle$, the matrix element $\langle\Phi_n|e^{iqx}|\Phi_0\rangle$ can also be expanded in λ_k,

$$\langle\Phi_n|e^{iqx}|\Phi_0\rangle \sim b_0 + \lambda_k b_1 + \lambda_k^2 b_2 + ..., \tag{4.95}$$

where the coefficients b_j are given by,

$$\begin{aligned} b_0 &\sim \langle n|e^{iqx}|0\rangle \\ b_1 &\sim \langle \psi_n^{(1)}|e^{iqx}|0\rangle + \langle n|e^{iqx}|\psi_0^{(1)}\rangle \\ b_2 &\sim \langle \psi_n^{(2)}|e^{iqx}|0\rangle + \langle \psi_n^{(1)}|e^{iqx}|\psi_0^{(1)}\rangle + \langle n|e^{iqx}|\psi_0^{(2)}\rangle \end{aligned} \tag{4.96}$$

In general, the coefficient b_j is schematically given by,

$$\begin{aligned} b_j \sim\ & \langle \psi_n^{(j)}|e^{iqx}|0\rangle + \langle \psi_n^{(j-1)}|e^{iqx}|\psi_0^{(1)}\rangle + ... \\ & + \langle \psi_n^{(1)}|e^{iqx}|\psi_0^{(j-1)}\rangle + \langle n|e^{iqx}|\psi_0^{(j)}\rangle. \end{aligned} \tag{4.97}$$

To study the powers of q appearing in b_j, we first need to understand the structure of the matrix element $\langle n_1|e^{iqx}|n_2\rangle$ for general eigenstates $|n_1\rangle$ and $|n_2\rangle$ of the unperturbed harmonic oscillator. This matrix element is given by the following,

$$\begin{aligned} \langle n_1|e^{iqx}|n_2\rangle = & \sum_{l=\frac{n_1-n_2+|n_1-n_2|}{2}}^{n_1} \frac{\sqrt{n_1!n_2!}}{l!(n_1-l)!(n_2-n_1+l)!}\times \\ & \Big(\frac{iq}{\sqrt{2m_d\omega_0}}\Big)^{n_2-n_1+2l} e^{-\frac{q^2}{4m_d\omega_0}}. \end{aligned} \tag{4.98}$$

We learn that the matrix element $\langle n_1|e^{iqx}|n_2\rangle$ contains powers of $iq/(\sqrt{2m_d\omega_0})$ ranging from $|n_1-n_2|$ to n_1+n_2. Note again that the Debye-Waller factor $e^{-\frac{q^2}{4m_d\omega_0}}$ is not included in this power counting since $e^{-\frac{q^2}{4m_d\omega_0}} \approx 1$ in the regime of interest.

Combining this information with the structure of b_j in (4.97) and the structure of $|\psi_n^{(j)}\rangle$ in (4.94), the powers of q in b_j can be identified:

$$\begin{aligned} b_j \sim e^{-\frac{q^2}{4m_d\omega_0}} \Big\{ & \Big(\frac{iq}{\sqrt{2m_d\omega_0}}\Big)^{n-jk} + \Big(\frac{iq}{\sqrt{2m_d\omega_0}}\Big)^{n-jk+2} \\ & + ... + \Big(\frac{iq}{\sqrt{2m_d\omega_0}}\Big)^{n+jk}\Big\}. \end{aligned} \tag{4.99}$$

Note that only those terms with powers of q larger or equal to 1 are present. Terms $\propto q^0$ have to cancel as they otherwise lead to q^0 terms in the squared matrix element $|\langle\Phi_n|e^{iqx}|\Phi_0\rangle|^2$, which is forbidden due to orthogonality of eigenstates.

As the kinematic regime under consideration is of $q \ll \sqrt{2m_d\omega_0}$, we will focus on powers of q less than n, which corresponds to the harmonic case. We see from the equation above that the lowest powers of q decrease with increasing values of j. Thus, higher order corrections in λ_k appear with lower powers in q. Eventually, at a sufficiently high power of λ_k, we get a coefficient b_j with the minimum power of q equal to 1. The squared matrix element can then be written in general as,

$$|\langle\Phi_n|e^{iqx}|\Phi_0\rangle|^2 = e^{-\frac{q^2}{2m_d\omega_0}} \times \left[\frac{1}{n!}\left(\frac{q^2}{2m_d\omega_0}\right)^n + \sum_{i\geq 1}\left(\frac{q^2}{2m_d\omega_0}\right)^i \left(a_{n,i}\,\lambda_k^{\nu(n,i)} + \mathscr{O}\left(\lambda_k^{\nu(n,i)+1}\right)\right)\right], \tag{4.100}$$

where the first term on the right hand side $\propto q^{2n}$ is the harmonic term, and the anharmonic corrections are expanded in powers of q^2 which are denoted by i, with $i \geq 1$. Every power i appears with a minimum *allowed* power $\nu(n,i)$ of λ_k.

To study the behavior of $\nu(n,i)$, we first note that, for even k, the matrix element $\langle\Phi_n|e^{iqx}|\Phi_0\rangle$ is purely real or purely imaginary, depending on whether n is even or odd respectively. For instance, if n is even, then b_0 is purely real. Higher orders in λ_k lead to insertions of $(a+a^\dagger)^k$ and therefore matrix elements where the difference in the harmonic oscillator states is also even, so that all coefficients b_j are real in this case. But for odd k, the b_j coefficients will alternate in being real and imaginary. This changes the structure of the squared matrix element depending on k, as we will see below.

Odd k: We will first consider odd k. In this case, the squared matrix element can be

written as,

$$|\langle\Phi_n|e^{iqx}|\Phi_0\rangle|^2 \sim |b_0+\lambda_k^2 b_2+\lambda_k^4 b_4+...|^2 + |\lambda_k b_1+\lambda_k^3 b_3+...|^2 \tag{4.101}$$

$$\sim |b_0|^2+\lambda_k^2(|b_1|^2+(b_0b_2^*+b_0^*b_2)) + \lambda_k^4(|b_2|^2+(b_0b_4^*+b_0^*b_4)+(b_1b_3^*+b_1^*b_3)) + \mathscr{O}(\lambda_k^6) \tag{4.102}$$

$$\sim e^{-\frac{q^2}{2m_d\omega_0}}\Big[\frac{1}{n!}\Big(\frac{q^2}{2m_d\omega_0}\Big)^n + \lambda_k^2\Big\{\Big(\frac{q^2}{2m_d\omega_0}\Big)^{n-k}+\Big(\frac{q^2}{2m_d\omega_0}\Big)^{n-k+1} + ...+\Big(\frac{q^2}{2m_d\omega_0}\Big)^{n+k}\Big\} + \lambda_k^4\Big\{\Big(\frac{q^2}{2m_d\omega_0}\Big)^{n-2k}+\Big(\frac{q^2}{2m_d\omega_0}\Big)^{n-2k+1} + ...+\Big(\frac{q^2}{2m_d\omega_0}\Big)^{n+2k}\Big\}+\mathscr{O}(\lambda_k^6)\Big]. \tag{4.103}$$

Thus we see that we get corrections at even orders in λ_k, with the lowest non-zero power being λ_k^2. In general, at $\mathscr{O}(\lambda_k^j)$ for an even $j=2j'$, the lowest power of q^2 is $n-(j'\times k)$, and the highest power is $n+(j'\times k)$. Note that only terms with positive powers of q^2 are present. The term $\propto q^2$ can also subtly cancel in some cases as there is no term $\propto q^0$ in coefficients b_j. We will deal with this case later below. But to get a power $i>1$ of q^2, the lowest non-zero j' is $\lceil\frac{|n-i|}{k}\rceil$, with the lowest j given by $2\times\lceil\frac{|n-i|}{k}\rceil$. Thus, in the squared matrix element, the lowest non-zero power $\nu(n,i)$ required is given by,

$$\nu(n,i)=\max\Big(2\times\lceil\frac{|n-i|}{k}\rceil\ ,\ 2\Big). \tag{4.104}$$

To get the lowest power $i=1$ of q^2 i.e. the term $\propto q^2$, the only possible way is to get the term $\propto q^1$ in the coefficient b_j as there is no term $\propto q^0$. For odd n, the term $\propto q^1$ in b_j can

only be generated at an even j, since that is the only way to satisfy $n - jk = 1$. For every even $j = 2j'$, the powers of q in b_j range from $n - (2k) \times j'$ to $n + (2k) \times j'$. The lowest j' to get a term $\propto q^1$ is then given by $\lceil \frac{|n-1|}{2k} \rceil$, with j given by $2 \times \lceil \frac{|n-1|}{2k} \rceil$. For an even n, the term $\propto q^1$ in b_j can only be generated for an odd j. For every odd $j = 2j' - 1$, the lowest power of q in b_j is $n + k - (2k) \times j'$. The lowest j' to get a term $\propto q^1$ is then given by $\lceil \frac{|n+k-1|}{2k} \rceil$, with j given by $2 \times \lceil \frac{|n+k-1|}{2k} \rceil - 1$. In the squared matrix element, the lowest non-zero power $\nu(n,1)$ required is given by,

$$\nu(n,1) = \begin{cases} \max\left(4 \times \lceil \frac{|n-1|}{2k} \rceil \ , \ 2\right) & \text{for odd } n \\ 4 \times \lceil \frac{|n+k-1|}{2k} \rceil - 2 & \text{for even } n \end{cases} \tag{4.105}$$

Even k: Now we consider even k. In this case, the squared matrix element is,

$$|\langle \Phi_n | e^{iqx} | \Phi_0 \rangle|^2 \sim |b_0 + \lambda_k b_1 + \lambda_k^2 b_2 + ...|^2 \tag{4.106}$$

$$\sim |b_0|^2 + \lambda_k((b_0 b_1^* + b_0^* b_1)) + \lambda_k^2(|b_1|^2 + (b_0 b_2^* + b_0^* b_2) + \mathcal{O}(\lambda_k^3) \tag{4.107}$$

$$\begin{aligned} \sim e^{-\frac{q^2}{2m_d\omega_0}} \Big[& \frac{1}{n!}\Big(\frac{q^2}{2m_d\omega_0}\Big)^n \\ & + \lambda_k \Big\{ \Big(\frac{q^2}{2m_d\omega_0}\Big)^{n-k/2} + \Big(\frac{q^2}{2m_d\omega_0}\Big)^{n-k/2+1} \\ & \quad + ... + \Big(\frac{q^2}{2m_d\omega_0}\Big)^{n+k/2} \Big\} \\ & + \lambda_k^2 \Big\{ \Big(\frac{q^2}{2m_d\omega_0}\Big)^{n-k} + \Big(\frac{q^2}{2m_d\omega_0}\Big)^{n-k+1} \\ & \quad + ... + \Big(\frac{q^2}{2m_d\omega_0}\Big)^{n+k} \Big\} + \mathcal{O}(\lambda_k^3) \Big]. \end{aligned} \tag{4.108}$$

Thus we see that we get corrections at all orders in λ_k, with the lowest non-zero power being λ_k. In general, at $\mathcal{O}(\lambda_k^j)$, the lowest power of q^2 is $n - (j \times k)/2$, and the highest power is $n + (j \times k)/2$. Following similar arguments to the case of odd k discussed earlier, $\nu(n,i)$ for

$i > 1$ is given by,

$$\nu(n,i) = \max\Big(\lceil \frac{|n-i|}{k/2} \rceil \ , \ 1\Big). \tag{4.109}$$

Another difference between the case of even k considered here and that of odd k is that we do not get an $i = 1$ term for even n, as all terms in the coefficients b_j contain even powers of q. This means that the leading term will always go as q^4, with a λ_k power determined by (4.109) for $i = 2$. For odd n, the lowest power of q in b_j is $n - k \times j$. Thus, in the squared matrix element, the lowest non-zero power $\nu(n,1)$ required is given by,

$$\nu(n,1) = \max\Big(2 \times \lceil \frac{|n-1|}{k} \rceil \ , \ 1\Big). \tag{4.110}$$

The calculations in this appendix up to this point consider the overall scaling behavior of the powers of q^2 and λ_k in the squared matrix element. We have neglected combinatorial factors at several steps in the calculations that enter into the numerical coefficients $a_{n,i}$ in (4.100). Sometimes, the numerical coefficients can also cancel with each other, and the naive leading behavior estimated in this section can vanish. In order to give concrete examples of the numerical coefficients, we perform explicit calculations of the squared matrix element using perturbation theory with $k = 3$ (i.e. a cubic perturbation), and phonon numbers $n = 1,\ 2,\ 3,$ and 4. We perform this explicit calculation only up to $\mathcal{O}(\lambda_3^2)$. The results of various numerical coefficients are presented below.

For a single-phonon production (i.e. $n = 1$), the coefficients $a_{n,i}$ are given by,

$$a_{1,1} = 44 \tag{4.111}$$

$$a_{1,2} = -82 \tag{4.112}$$

$$a_{1,3} = 5. \tag{4.113}$$

For a two-phonon production (i.e. $n = 2$), the coefficients are given by,

$$a_{2,1} = 8 \tag{4.114}$$

$$a_{2,2} = 59 \tag{4.115}$$

$$a_{2,3} = -56 \tag{4.116}$$

$$a_{2,4} = 2.5. \tag{4.117}$$

For a three-phonon production (i.e. $n = 3$), the coefficients are,

$$a_{3,2} = 18 \tag{4.118}$$

$$a_{3,3} = 37 \tag{4.119}$$

$$a_{3,4} = -23.04 \tag{4.120}$$

$$a_{3,5} = 0.77. \tag{4.121}$$

Note that we do not show the coefficient $a_{3,1}$ as it appears at $\mathcal{O}(\lambda_3^4)$. Finally, for a four-phonon production (i.e. $n = 4$), the coefficients are evaluated to be,

$$a_{4,1} = 0 \tag{4.122}$$

$$a_{4,2} = 0 \tag{4.123}$$

$$a_{4,3} = 0.097 \tag{4.124}$$

$$a_{4,4} = 0.05 \tag{4.125}$$

$$a_{4,5} = -0.012 \tag{4.126}$$

$$a_{4,6} = 1.81 \times 10^{-4}. \tag{4.127}$$

Note that the coefficients $a_{4,1}$ and $a_{4,2}$ amount to zero because of a numerical cancellation between the two terms in the b_1 coefficient in Eq. 4.96. The leading behavior of the terms

proportional to q^2 and q^4 in the structure factor is instead $q^2\lambda_3^6$ and $q^4\lambda_3^4$, respectively.

As these numerical coefficients appear through combinations and interferences of several combinatorial factors at various steps of the calculation, it is hard to provide a general expression for them. By looking at the examples above however, we can make some general observations. Typically, we see that the coefficients follow a pyramid structure, with $a_{n,i}$ being the largest for i near n, and decreasing with i away from n. We also find that the coefficients can vary by orders of magnitude from each other. The terms with i near n receive contributions from several individual matrix elements, and in general seem to be larger. We expect to see this pattern continue for higher phonon numbers as well. The exact values of these coefficients play a role in determining where the anharmonic corrections dominate, and so our power counting approach only gives an $O(1)$ estimate.

4.C Impulse approximation

In Sec. 4.3.3, we calculated the structure factor via the saddle point approximation in the regime defined by (4.52). This regime corresponded to values of ω near $\frac{q^2}{2m}$ and within the Gaussian width of (4.63). As discussed in the main text, in order to calculate the tail of the structure factor far from $\omega = \frac{q^2}{2m}$, more expansion terms are needed in f. Here we discuss this extension of the impulse approximation.

First, in the special case of a harmonic potential, we can start from the full result in Eq. (4.35). After rewriting the energy conservation delta function as a time integral, we find that

$$f(t) = -i\omega t + \frac{q^2}{2m_d\omega_0}(e^{i\omega_0 t} - 1) \tag{4.128}$$

Solving $f'(t) = 0$ gives the exact result

$$t_I = \frac{i}{\omega_0}\ln\left(\frac{q^2}{2m_d\omega}\right). \tag{4.129}$$

Using the saddle point approximation for $\omega \gg \omega_0$, we find

$$S_{\text{toy},d}(q,\omega) \sim \frac{1}{\sqrt{\omega\omega_0}} e^{-2W_{\text{toy}}(q)} \left(\frac{q^2}{2m\omega}\right)^{\frac{\omega}{\omega_0}} e^{\frac{\omega}{\omega_0}}. \tag{4.130}$$

The same result can also be derived by approximating the sum over phonon states as an integral in Eq. (4.35). The saddle point approximation for the harmonic oscillator holds as long as $\omega \gg \omega_0$, and we no longer have a condition on how close ω is to $\frac{q^2}{2m}$. In the impulse regime, $\omega \sim \frac{q^2}{2m}$, one can check that it reduces to the previous result in Eq. (4.63). We see in this exact result that the tail at large ω is Poissonian instead of Gaussian.

For general potentials, this exact analytic result is no longer possible, but we can still calculate corrections to the tail. First, we start by giving the exact saddle point equation:

$$0 = f'(t_I) = -i\left(E_0 + \omega - \frac{q^2}{2m}\right) + i\frac{\left\langle H' e^{iH't_I}\right\rangle}{\left\langle e^{iH't_I}\right\rangle} \tag{4.131}$$

which is valid at all orders. We begin by noticing that saddle point equation (4.131) is satisfied exactly at $\omega = \frac{q^2}{2m}$ by $t_I = 0$. Then, ω-derivatives of t_I at $\omega = \frac{q^2}{2m}$ can be found by taking ω-derivatives of (4.131) and solving for $t_I^{(n)}[\omega = \frac{q^2}{2m}]$. This allows us to calculate $t_I[\omega = \frac{q^2}{2m}]$ in an

iterative fashion. The first few terms are

$$
\begin{aligned}
t_I[\frac{q^2}{2m}] &= 0 \\
t_I'[\frac{q^2}{2m}] &= \frac{i}{\langle H'\rangle^2 - \langle H'^2\rangle} \\
t_I''[\frac{q^2}{2m}] &= i\frac{-2\langle H'\rangle^3 + 3\langle H'\rangle\langle H'^2\rangle - \langle H'^3\rangle}{\left(\langle H'\rangle^2 - \langle H'^2\rangle\right)^3} \\
t_I^{(3)}[\frac{q^2}{2m}] &= \frac{i}{\left(\langle H'\rangle^2 - \langle H'^2\rangle\right)^5}\times \\
&\quad \Big(6\langle H'\rangle^6 - 18\langle H'\rangle^4\langle H'^2\rangle + 3\langle H'^2\rangle^3 \\
&\quad + 8\langle H'\rangle^3\langle H'^3\rangle - 14\langle H'\rangle\langle H'^2\rangle\langle H'^3\rangle \\
&\quad + 3\langle H'^3\rangle^2 - \langle H'^2\rangle\langle H'^4\rangle \\
&\quad + \langle H'^2\rangle\left(12\langle H'^2\rangle^2 + \langle H'^4\rangle\right)\Big)
\end{aligned}
\tag{4.132}
$$

where $t_I^{(n)}$ denotes the nth ω-derivative of t_I. In the harmonic case, this series resums to (4.129). For general potentials, one can then use the expansions (4.60) and (4.132) to calculate

$$
S_{\text{toy},d}(q,\omega) \approx \sqrt{\frac{2\pi}{-f''(t_I)}}e^{f(t_I)} \tag{4.133}
$$

to a desired order.

4.D Exact results for Morse potential

The Morse potential is a special case of an anharmonic potential where the structure factor is analytically solvable. We will use this case to illustrate the behavior of the structure factor discussed in Sec. 4.3.2. We also use it to validate the numerical calculations used in our final results and check the validity of the impulse approximation in the regime where there are $n > 10$ phonons.

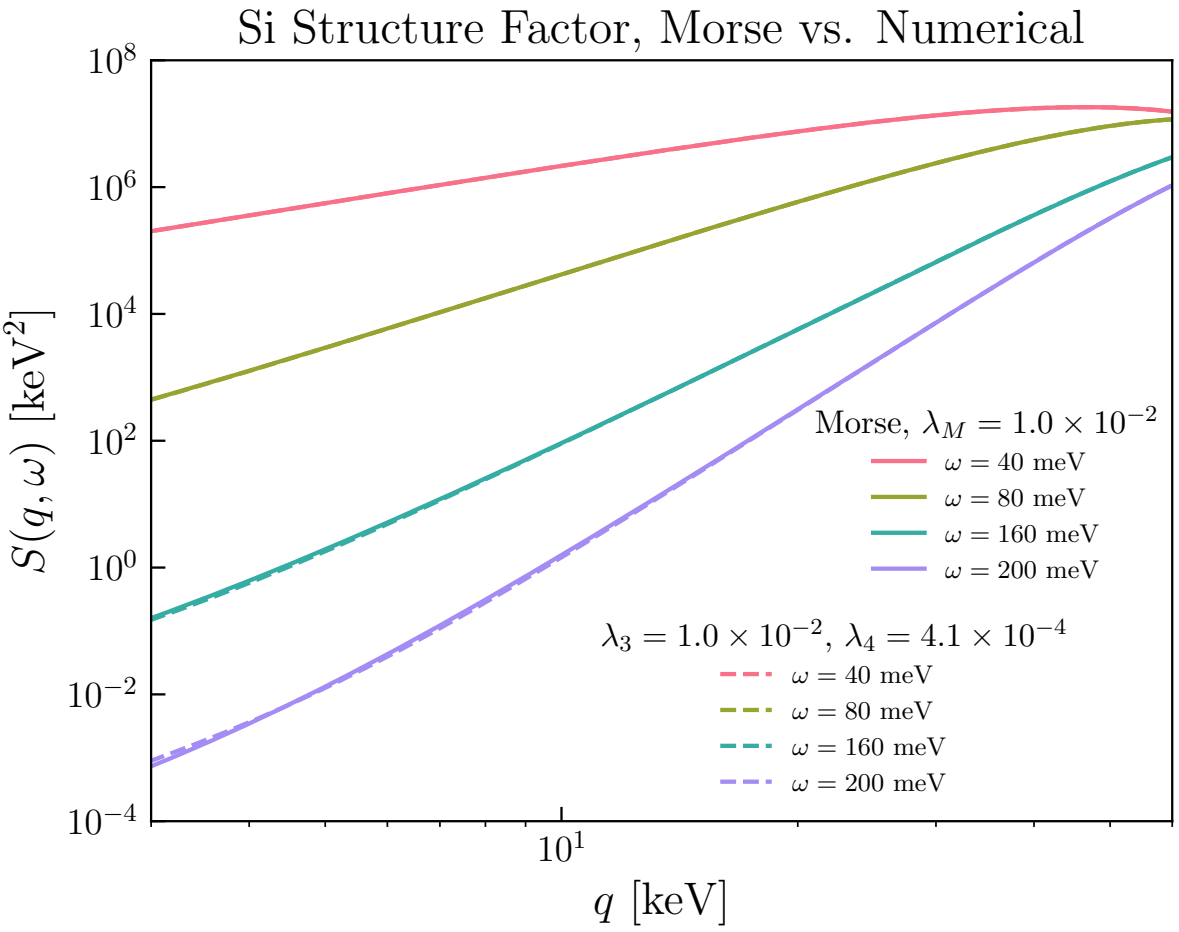

Figure 4.11. Comparison of analytic structure factor in the Morse potential and the numerical calculation for Si as described in Sec. 4.4. We find that the two methods give almost the same result due to the fact that the Morse potential well approximates the single-atom potential along the nearest-neighbor direction.

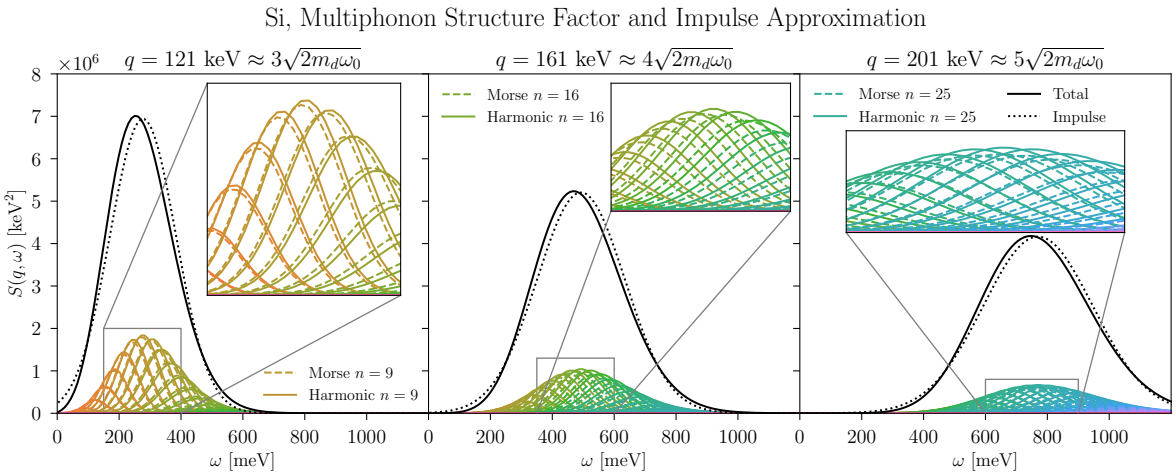

Figure 4.12. ω-dependence of structure factor for the Morse potential: Comparison of the Morse (dashed rainbow) and harmonic (solid rainbow) structure factor contributions from each individual excited state. The solid black line is the sum of contributions from the Morse potential, and dotted is the impulse envelope. Even though the energies of each individual Morse excited state are perturbed, the total structure factor remains essentially unchanged from the harmonic result. The small shift of order ω_0 between the exact result and impulse approximation results from dropping higher order terms in the impulse approximation as discussed in Sec. 4.3.3 and App. 4.C.

The Morse potential is defined as

$$V_{\text{Morse}} = B\left(e^{-2ax} - 2e^{-ax}\right), \tag{4.134}$$

where a is a parameter controlling the width of the potential and B is the normalization. Expanding this potential in powers of x gives

$$V_{\text{Morse}} = -B + Ba^2x^2 - Ba^3x^3 + \frac{7}{12}Ba^4x^4 + \ldots \tag{4.135}$$

Matching the quadratic and the cubic terms with (4.26), we find that

$$a = -4\lambda_3\sqrt{2m\omega_0} \tag{4.136}$$

$$B = \frac{\omega_0}{64\lambda_3^2}. \tag{4.137}$$

Note that the Morse potential has fewer free parameters than the anharmonic potential up to fourth order in the displacements, so we cannot simultaneously fit λ_4. Nonetheless, the realistic potential as obtained App. 4.A are well approximated by this Morse potential due to the dominance and Morse-like behavior of the f_R and f_A terms in the Tersoff part of the potential.

The Morse potential approximation of our anharmonic potential is then given by

$$V_{\text{Morse}} = \frac{\omega_0}{64\lambda_M^2}\left(e^{8\lambda_M\sqrt{2m\omega_0}} - 2e^{4\lambda_M\sqrt{2m\omega_0}x}\right), \tag{4.138}$$

where we take $\lambda_M = \lambda_3$ in order to fit up to third order anharmonicities. In this potential, the structure factor (4.68) is exactly calculable since the Morse eigenstates and eigenenergies are known analytically. These results [122] give squared matrix elements between the ground state and nth excited state of

$$\begin{aligned}|\langle\Phi_n|e^{iqx}|\Phi_0\rangle|^2 &= \frac{(2K-2n-1)(2K-1)}{n!\Gamma(2K)\Gamma(2K-n)} \\ &\times\left|\frac{\Gamma(n+\frac{i(q/\sqrt{2m\omega_0})}{4\lambda_M})\Gamma(2K+\frac{i(q/\sqrt{2m\omega_0})}{4\lambda_M}-n-1)}{\Gamma(\frac{iq/\sqrt{2m\omega_0}}{4\lambda_M})}\right|^2,\end{aligned} \tag{4.139}$$

with energy gaps

$$E_n - E_0 = \left(n - \frac{n(1+n)}{2K}\right)\omega_0, \tag{4.140}$$

where $K = \frac{1}{32\lambda_M^2}$.

Note that these formulae are only valid for $n < K - \frac{1}{2}$ since above this excited state, the eigenstates are unbound and have a different analytic form. For $\lambda_M \sim 0.01$, this condition requires $n \lesssim 312$, which corresponds to an energy gap of $\mathcal{O}(\text{eV})$. Recoil energies at this scale are comparable to the size of a typical lattice potential well and thus the free nuclear recoil approximation holds. Then, for typical anharmonicity strengths, the discrete states of the Morse potential that we have used in this analysis are sufficient to estimate the anharmonic effect in the multiphonon scattering regime.

Putting together expressions (4.139)-(4.146), (4.68), and (4.72) we can calculate the structure factor in the Morse potential in both the large and small q regime. We show these results for $\lambda_M = \lambda_3$ in Figs. 4.11 and 4.12. Fig. 4.11 provides a check for our numerical results in Sec. 4.4. Here we see that the numerical calculations and corresponding analytic Morse results are almost identical. There is a modified q scaling of the structure factor compared to the harmonic case, as was already illustrated in Fig. 4.7. We can also obtain this behavior analytically with the Morse potential. Expanding the expression (4.139) to leading order in q and subsequently in λ_M, we get explicitly,

$$|\langle 2|e^{iqx}|0\rangle|^2 = 8\lambda_M^2 q^2 + \dots \tag{4.141}$$

$$|\langle 3|e^{iqx}|0\rangle|^2 = \frac{512}{3}\lambda_M^4 q^2 + \dots \tag{4.142}$$

$$|\langle 4|e^{iqx}|0\rangle|^2 = 6144\lambda_M^6 q^2 + \dots, \tag{4.143}$$

$$|\langle 5|e^{iqx}|0\rangle|^2 = \frac{1572864}{5}\lambda_M^8 q^2 + \dots, \tag{4.144}$$

$$|\langle 6|e^{iqx}|0\rangle|^2 = 20971520\lambda_M^{10} q^2 + \dots, \tag{4.145}$$

where the ellipses include higher orders in both q and λ_M. The leading λ_M scalings are consistent with those illustrated in Fig. 4.4 for $n = 2$ and 3. For $n = 4$, the leading λ_M scaling differs from the power counting in Fig. 4.4, but matches with the explicit results obtained using perturbation theory as presented in Appendix 4.B. An exact numerical cancellation modifies the leading behavior to $\lambda_M^6 q^2$. We see that the leading behavior in q, λ_M for $n > 4$ also differs from the x^3-theory power counting, suggesting a generic presence of cancellations at lower orders of λ_3 for the q^2 dependence.

In Fig. 4.12, we demonstrate that the impulse approximation remains robust for $q \gg \sqrt{2m_d\omega_0}$ and $n > 10$ excited states. Note that we can also calculate corrections to $\langle p^2\rangle$ in the Morse ground state exactly:

$$\langle p^2\rangle = \frac{m\omega_0}{2}(1 - 16\lambda_M^2), \tag{4.146}$$

which is used in the impulse regime result (4.63). The impulse result is almost identical between the Morse and harmonic cases, since the Gaussian width is only corrected at order λ_M^2, which is $\sim 10^{-4}$. This is also borne out in the full calculation of the structure factor shown in Fig. 4.12.

Chapter 5

Signals of primordial black holes at gravitational wave interferometers

5.1 Abstract

Primordial black holes (PBHs) can form as a result of primordial scalar perturbations at small scales. This PBH formation scenario has associated gravitational wave (GW) signatures from second-order GWs induced by the primordial curvature perturbation, and from GWs produced during an early PBH dominated era. We investigate the ability of next generation GW experiments, including BBO, LISA, and CE, to probe this PBH formation scenario in a wide mass range. Measuring the stochastic GW background with GW observatories can constrain the allowed parameter space of PBHs for masses 10^9 - 10^{27} g. We also discuss possible GW sources from an unconstrained region where light PBHs ($< 10^9$g) temporarily dominate the energy density of the universe before evaporating. We show how PBH formation impacts the reach of GW observatories to the primordial power spectrum and provide constraints implied by existing PBH bounds.

5.2 Introduction

Primordial black holes (PBHs) may play an interesting role in astrophysics and cosmology [123, 124]. Much attention has been paid recently to the possibility of PBHs as dark

matter (DM) and as an explanation of recent LIGO/VIRGO [46] gravitational wave (GW) observations [125]. Such PBHs would need to be heavy enough to avoid Hawking evaporation on timescales comparable to the age of the Universe. Alternatively, there may have existed a significant population of light PBHs, which would have Hawking evaporated at early times. Though not corresponding to an observable PBH population today, light evaporating PBHs can be tied to other interesting phenomena, such as an early period of PBH domination [126, 127], baryogenesis [128, 129, 130, 131, 132], the production of dark radiation [127, 128, 129, 133, 134, 135, 131, 132], and perhaps the production of the observed DM density, either as a product of Hawking radiation [127, 128, 129, 133, 134, 135] or if evaporation ends in a stable relic [136, 137, 138, 139]. Such scenarios are challenging to probe. However, gravitational wave observations at interferometers can provide important insight into the formation and abundance of both evaporating and long-lived PBHs produced in the early Universe.

In this work, we will study the prospects for future GW interferometers to detect a gravitational wave background associated with PBH formation and, possibly, black hole domination, across a wide range of mass scales. The most well-studied PBH production mechanism is the collapse of primordial density perturbations from inflation. In this context, a sizable density perturbation associated with the formation of PBHs can source a stochastic GW background at second order in cosmological perturbation theory [140, 141, 142, 143, 144, 145, 146, 147]. Additionally, if the density perturbations are large enough to generate a substantial population of PBHs, a period of PBH domination can ensue, which provides additional mechanisms for producing primordial GWs. Such mechanisms have been the study of recent works including [148, 149, 150, 151]. We will elucidate on the combined impact of these sources in what follows.

There is a large corpus of existing literature dealing with GWs associated with PBH formation. Our study complements this past work in several ways. For one, we incorporate a treatment of the effects of a possible PBH-dominated era, which provides several additional mechanisms for generating GWs and affects the observational prospects. Secondly, we study

a larger range of PBH masses than is often considered, including very light PBHs which are sometimes neglected due to their evaporation at early times. Thirdly, we incorporate a state-of-the-art treatment relating the underlying inflationary perturbations to the resulting PBH mass spectrum and subsequent evolution. Finally, we present our results in a unified way alongside other observational constraints and prospects, facilitating a clear comparison of the corresponding GW interferometer reach to that of other observations sensitive to evaporating or long-lived PBHs.

Our study focuses on PBHs for which the underlying inflationary perturbations, or the effects of PBH domination, give rise to signals at GW interferometers. This occurs for sub-solar mass PBHs (assuming that the mass spectrum is approximately monochromatic), and so we will show results for masses below $\sim 10^{30}$ g. It is important to note, however, that heavier PBHs with masses above $\sim 10^{30}$ g can also induce an observable GW signal through various mechanisms. There is a vast corresponding literature covering this regime as well, especially in the context of the observed LIGO/VIRGO mergers (see e.g. [46, 152, 153]) and recent NANOGrav results [154, 155, 156, 157]. Such scenarios can also induce GW signals at interferometers if the mass function is sufficiently extended or the corresponding inflationary perturbations approximately scale-invariant [158], but we will not consider this possibility further, focusing instead on PBH populations with a nearly monochromatic mass function peaked well below the solar-mass regime.

Our study is organized as follows. Section 5.3 discusses various aspects of primordial black hole cosmology, and introduces the relevant parameter space. Section 5.4 details the relationship between the assumed underlying inflationary perturbations and the resulting black hole mass spectrum. Section 5.5 describes the various stochastic GW sources relevant at interferometer scales, including GWs from the formation and evaporation of PBHs, while the resulting observational prospects are discussed alongside other astrophysical and cosmological probes in Section 5.6. We conclude in Section 5.7. Our final results are summarized in Figs. 5.6-5.7.

5.3 Primordial Black Hole Cosmology

Primordial black holes could have meaningfully impacted our cosmic history in several ways. Depending on their mass and initial abundance, they may have led to an early period of black hole domination (BHD), injected entropy (including a possible dark radiation component [127]) as they evaporated, or survived long enough to constitute some fraction of the observed dark matter density. In this section, we discuss these various possibilities in the context of the PBH parameter space, compared with current constraints on PBHs.

We will describe the PBH parameter space in terms of characteristic mass $m_{\rm BH}$ and an initial fraction of the total energy density at time $t_\star$, with

$$\beta = \frac{\rho_{{\rm BH},\star}}{\rho_{r,\star}}. \tag{5.1}$$

Here $\rho_{r,\star}$ is the energy density in radiation at that time, and we will assume throughout that PBHs are formed in the early radiation-dominated FRW universe.

There are several mechanisms that could in principle give rise to an abundance of PBHs, but the most well-studied is the collapse of density fluctuations from inflation, whereby PBHs are formed when a large scalar perturbation enters the horizon. We will assume this mechanism throughout, taking a primordial curvature perturbation power spectrum that is peaked at a characteristic comoving wavenumber $k_\star$. We take $t_\star$ to be the time when the mode $k_\star$ enters the horizon, which is defined by the condition $k_\star \equiv a_\star H_\star$, with $a_\star$, $H_\star$ the FRW scale factor and Hubble parameter at horizon entry. The PBH mass is proportional to the horizon mass at this time:

$$m_{\rm BH} = \frac{4\pi\gamma_{\rm eff}}{3}\rho_{r,\star}H_\star^{-3}, \tag{5.2}$$

where $\gamma_{\rm eff}$ is an $O(1)$ prefactor inferred from numerical simulations and dependent on the spectrum of the primordial curvature perturbation. For a review on PBH formation and discussion of this γ parameter, see Refs. [160, 161, 124, 162], and references therein. It is important to note

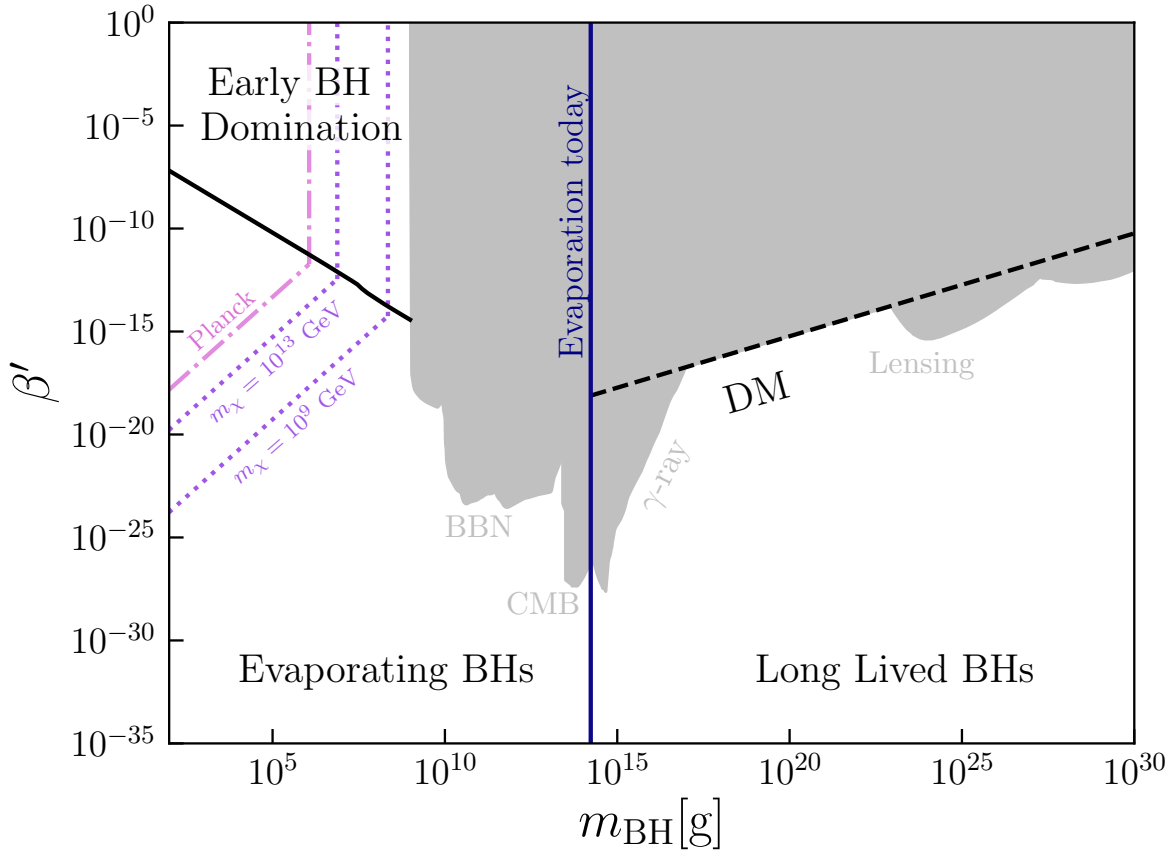

Figure 5.1. Range of PBH mass and β' considered in this work. β' is proportional to β, the initial fractional energy density in PBHs; see (5.3). The shaded region shows observational constraints for a monochromatic mass function, see text. The solid lines delineate different regimes of PBH cosmology, while the dashed line is where PBHs comprise all of the observed DM. The dotted lines are where Hawking radiation of the PBHs into particle DM produces $\Omega_{\rm DM}h^2 \simeq 0.1$; the two lines shown are for DM mass of $10^9\,$GeV and $10^{13}\,$GeV [127]. The dash-dotted line is where Planck-scale relics from BHs make up all of the DM [159].

that our $\gamma_{\rm eff}$ differs from the value of $\gamma \sim 0.2$ which appears sometimes in the literature. The difference arises from the fact that we define the PBH initial conditions at horizon entry of the mode $k_\star$, but more realistically, PBH formation happens over an extended period of time. In addition, the PBHs form with a distribution of masses, and here $m_{\rm BH}$ is defined by fitting to a lognormal mass distribution, given in (5.21). Examples of the PBH mass function and details about the time-dependent formation rate will be provided in Sec. 5.4. For now, we emphasize that the value of $\gamma_{\rm eff}$ depends on the amplitude and shape of the primordial curvature perturbation.

Both $\gamma_{\rm eff}$ and $g_\star$, the number of relativistic degrees of freedom at PBH formation, will enter into a number of quantities, making it useful to define the parameter

$$\beta' \equiv \sqrt{\gamma_{\rm eff}} \left(\frac{g_\star}{106.75}\right)^{-1/4} \left(\frac{h}{0.68}\right)^{-2} \beta, \tag{5.3}$$

where h is the dimensionless Hubble constant. Throughout this paper, we will generally suppress h dependence of quantities and use $h = 0.68$. In particular, the definition above is useful is because the relic density of long-lived PBHs is proportional to β'. We thus follow the convention of plotting observational constraints in terms of β' vs. $m_{\rm BH}$, and can thereby directly use the constraints of Ref. [160].

Assuming radiation domination, the temperature associated with $t_\star$ is

$$T_\star = 3 \times 10^8 \,{\rm GeV} \sqrt{\gamma_{\rm eff}} \left(\frac{10^{15}{\rm g}}{m_{\rm BH}}\right)^{1/2} \left(\frac{106.75}{g_\star}\right)^{1/4}. \tag{5.4}$$

Depending on the primordial power spectrum, the actual times associated with PBH formation will be slightly different from $t_\star$. As discussed above, this leads to different characteristic PBH masses, but these effects can be captured by the $\gamma_{\rm eff}$ parameter. Requiring $T_\star$ to be below a reheat scale $T_{\rm RH} \sim \sqrt{H_I M_{\rm pl}}$ with the scale of inflation $H_I \lesssim 10^{14}$ GeV implies that $m_{\rm BH} \gtrsim 1$ g, while requiring $T_\star$ to be well above BBN temperatures implies $m_{\rm BH} \lesssim 10^{34}$ g.

The relationship between $m_{\rm BH}$ and $k_\star$ can be derived by redshifting back from the present

day. If β' is sufficiently small such that the PBHs never dominate the energy density, then

$$k_\star \simeq \frac{5.4\times 10^{15}}{\text{Mpc}}\sqrt{\gamma_{\text{eff}}}\left(\frac{10^{15}\text{g}}{m_{\text{BH}}}\right)^{1/2} \quad , \quad \beta' < \beta'_{\text{min}}, \tag{5.5}$$

where we have neglected the (mild) dependence on $g_\star$ in this equation. β_{min} defines the condition for black hole domination, which we will give below in (5.9).

Throughout this study, we will approximate the PBH mass distribution as approximately monochromatic. The formation scenarios we consider have sufficiently small width in the PBH mass function, such that observational constraints and cosmological evolution are expected to be modified only at the $O(1)$ level by including a full mass function. We will also neglect the effect of mergers and accretion, so that once formed, the PBHs maintain an approximately fixed mass until they begin to evaporate. Given these assumptions, the subsequent cosmological evolution of the PBH population is governed by the parameters m_{BH} and β'. We can therefore map the $m_{\text{BH}} - \beta'$ plane into different cosmological scenarios, as shown in Fig. 5.1. In this paper, we will further map the gravitational wave reach from interferometers onto this plane.

Fig. 5.1 shows three qualitatively different scenarios: in the bottom right of the $m_{\text{BH}} - \beta'$ plane, PBHs are long-lived enough to exist today. The region to the left of the blue vertical line features PBHs that would have evaporated by today, while the upper left corner supports an early black hole-dominated epoch. The gray shaded parameter space is excluded by existing constraints. Note that for the parameter space shown, there is (or was) at least one PBH formed in our observable universe. We discuss each of these regions in turn below.

5.3.1 Long-lived PBHs

In the bottom right portion of the parameter space in Fig. 5.1, the PBHs are heavy and the initial abundance relatively small. Hawking radiation inevitably depletes the energy density of PBHs. However, the evaporation rate $dm_{\text{BH}}/dt \propto 1/m_{\text{BH}}^2$, so that heavy PBHs evaporate slowly. Sufficiently heavy PBHs can have lifetimes longer than the age of the Universe and exist as a

(meta-)stable relic today, making up a fraction (or all) of the observed dark matter density. The evaporation time $t_{\rm evap}$ for sufficiently heavy black holes is given approximately by [127]

$$t_{\rm evap} \simeq 4 \times 10^{-4}{\rm s} \times \left(\frac{m_{\rm BH}}{10^8\,{\rm g}}\right)^3 \tag{5.6}$$

assuming only photons and neutrinos are emitted (the other SM degrees of freedom are too heavy to be thermally produced via Hawking evaporation of long-lived heavy PBHs, since the Hawking radiation temperature is inversely proportional to $m_{\rm BH}$). From this, we see that PBHs will have lifetimes longer than the age of the Universe provided $m_{\rm BH} \gtrsim 4 \times 10^{14}$g. This region lies to the right of the blue vertical line in Fig. 5.1.

The long-lived population of PBHs can serve as a viable dark matter candidate. Since the effects of evaporation are negligible in this mass range, the energy density of PBHs simply redshifts as matter, $\rho_{\rm BH} \propto a^{-3}$ with a the FRW scale factor. Using entropy conservation, the PBH relic density today is given by

$$\Omega_{\rm BH} \approx 1.4 \times 10^{17} \beta' \left(\frac{10^{15}{\rm g}}{m_{\rm BH}}\right)^{1/2}. \tag{5.7}$$

The parameter values where PBHs are long-lived and satisfy $\Omega_{\rm BH}h^2 \simeq 0.12$ with $h = 0.68$ is indicated by the black dashed line in Fig. 5.1, and provides a particularly compelling target for GW interferometers and other astrophysical probes, as is well known (see e.g. [163, 164, 165]). Above the DM line in Fig. 5.1, the relic abundance of PBHs is too large and leads to overclosure. This is the strongest bound on the large-β region for $m_{\rm BH} \sim 10^{17} - 10^{23}$ g.

5.3.2 Evaporating PBHs

To the left of the blue vertical line in Fig. 5.1, $m_{\rm BH} < 4 \times 10^{14}$g and PBHs are light enough to evaporate on timescales smaller than the age of the Universe. In this regime, PBHs themselves are no longer a viable DM candidate, but can have other interesting effects. For

example, in Refs. [133, 127], it was shown that evaporating PBHs could source a significant amount of dark radiation. The same work also pointed out that PBH evaporation can also provide a non-thermal production mechanism for heavy DM candidates, potentially giving rise to the observed DM density. The dotted lines indicate the parameters which produce $\Omega_{\rm DM}h^2 \simeq 0.1$ for particle DM mass of 10^9 GeV (lower line) and 10^{13} GeV (upper line). Furthermore, it has been suggested that quantum gravity effects may halt PBH evaporation near the Planck scale, leaving behind a cold ∼Planck mass relic which is a possible DM candidate [166, 167]. The dash-dotted line in Fig. 5.1 indicates the parameters required for the Planck-scale remnants to produce $\Omega_{\rm DM}h^2 \simeq 0.1$.

5.3.3 Early black hole domination

Even if the PBHs evaporate away, if the primordial curvature perturbation is large enough, there will be a period of early black hole domination (BHD). Whether or not BHD occurs depends on if the energy density in black holes grows enough before they evaporate, so the minimum value of β for BHD is given by the ratio $T_{\rm RH}/T_\star$, where the reheating temperature $T_{\rm RH}$ is the temperature at the time of black hole evaporation (5.6). Assuming matter domination, we find

$$T_{\rm RH} = 2.8 \times 10^4\,{\rm GeV}\left(\frac{m_{\rm BH}}{10^4{\rm g}}\right)^{-3/2}, \tag{5.8}$$

so our condition on the energy density for a BHD era is

$$\beta'_{\rm min} \simeq 3 \times 10^{-10}\left(\frac{10^4{\rm g}}{m_{\rm BH}}\right). \tag{5.9}$$

For simplicity, we have suppressed the dependence on degrees of freedom and on h.

For $\beta' > \beta'_{\rm min}$, there is an additional BHD era where the scale factor evolves as in a matter-dominated era. This changes the relationship between the scale $k_\star$ and black hole mass

$m_{\rm BH}$, which now has β' dependence:

$$k_\star = \frac{2.4\times10^{20}}{\rm Mpc}\sqrt{\gamma_{\rm eff}}\left(\frac{10^{-7}}{\beta'}\right)^{1/3}\left(\frac{10^4\,{\rm g}}{m_{\rm BH}}\right)^{5/6},\ \beta' > \beta'_{\rm min} \tag{5.10}$$

since β' determines the time of the onset of a BHD era. In this region of parameter space, any gravitational waves generated at the time of PBH formation will be diluted by an additional redshifting factor given by

$$\frac{a_{\rm RH}}{a_{\rm BHD}} = 2.4\times10^3\left(\frac{\beta'}{10^{-7}}\right)^{4/3}\left(\frac{m_{\rm BH}}{10^4\,{\rm g}}\right)^{4/3}. \tag{5.11}$$

This has a significant impact on experimental reach from gravitational wave interferometers if $m_{\rm BH} < 10^9$ g and $\beta' > \beta'_{\rm min}$.

5.3.4 Constraints

Aside from the overclosure constraint, we show combined observational constraints on PBHs from Ref. [160]. These bounds are for a monochromatic mass function, and the observational constraints can change significantly for PBHs with extended mass functions and large enough widths [168]. In this work, we will restrict to formation scenarios where the width of the PBH mass function is not too large, such that constraints are not drastically different. We will discuss the width of the PBH mass function further in the following section.

We now briefly summarize where the constraints come from. If 10^9 g$< m_{\rm BH} < 4\times10^{14}$ g, then PBHs will evaporate during or after Big Bang Nucleosynthesis (BBN), but before today. This leads to injection of high energy particles that can impact BBN or the cosmic microwave background (CMB). These effects are the source of the strong constraints on β in the parameter space for evaporating BHs. The bounds are again taken from Ref. [160], although note that the BBN bounds have been updated in more recent work [169]. Bounds from observations of CMB anisotropies are strongest in the mass range of 3×10^{13} g to 2×10^{14} g, see for example Ref. [170].

For long-lived PBHs with mass 10^{14} g $\lesssim m_{\rm BH} \lesssim 10^{17}$ g, the bounds come from various galactic and extragalactic probes of cosmic rays or gamma rays produced in the Hawking radiation. More recent work has obtained stronger constraints with data from the INTEGRAL satellite [171]. At higher masses, there are constraints from lensing by PBHs. For 10^{23} g $\lesssim m_{\rm BH} \lesssim 10^{28}$ g, shown here are recently updated bounds [172] based on Subaru/HSC observations [173]. For 10^{28} g $\lesssim m_{\rm BH} \lesssim 10^{30}$ g, OGLE bounds [174] are shown.

5.4 Primordial black holes from Curvature Perturbations

In this work, we assume PBHs formed due to primordial curvature perturbations with Gaussian statistics. In cases with non-Gaussianity, the same curvature perturbation amplitude gives a larger energy density in PBHs [175]. We will consider a monochromatic curvature perturbation

$$\mathscr{P}(k) = A\delta\left(\log(k/k_\star)\right), \tag{5.12}$$

as well as a more realistic initial Gaussian perturbation

$$\mathscr{P}(k) = \frac{A}{\sqrt{2\pi\sigma^2}} \exp\left(-\frac{\log^2(k/k_\star)}{2\sigma^2}\right). \tag{5.13}$$

It has been shown in [176] that the maximum primordial curvature perturbation slope is $\propto k^4$ for single-field inflation, so only a Gaussian with $\sigma \gtrsim 1$ can result in this case. Multi-field inflation [177, 178, 179, 180] is required for growths steeper than k^4, which corresponds to a lognormal curvature perturbation of $\sigma < 1$. We will restrict to $\sigma \leq 2$ so that we can treat the black holes as forming at approximately the same time and so that we can compare with observational constraints on PBHs with nearly monochromatic mass functions.

In the section, we relate the primordial perturbations to the abundance and mass spectrum of the black holes, which can then be translated into parameters β and $\gamma_{\rm eff}$ defined in Sec. 5.3.

Because PBHs are forming from rare overdensities over the vast majority of the parameter space, the relationship between the primordial curvature perturbation and the PBH mass function depends sensitively on the treatment for the collapse of density fluctuations. There is an enormous literature dedicated to this topic, with varying results. Here we consider the Press-Schechter formalism with the parameters given in [162]. As shown in [162, 181], this gives a relationship between BH mass spectra and curvature perturbation that is consistent with other treatments of PBH formation, namely peaks theory and variations thereof.

In the Press-Schechter formalism, PBHs are formed whenever the density contrast exceeds a certain threshold. Therefore the initial energy density can be simply related to the probability distribution for density contrasts. Consider black holes formed at a particular time corresponding to a horizon size R. The initial fraction of the energy density in those black holes is given by

$$\beta_R = 2\int_{C_c}^{\infty} dC \frac{m}{M_H(R)} p(C), \tag{5.14}$$

where $M_H(R)$ is the horizon mass and C is a smoothed density contrast, defined below. $p(C)$ is the probability distribution for C, and the lower limit C_c is related to the density contrast threshold required for PBH formation. The black hole mass is related to the density contrast and horizon mass at formation by the critical collapse scaling relation:

$$m = M_H(R)K(C-C_c)^{\gamma}, \tag{5.15}$$

where K and γ are constants determined via numerical simulation. Here we use $K = 10, C_c = 2.5$, and $\gamma = 0.36$. The critical collapse relationship allows us to recast the integrand of (5.14) as a function of black hole mass m, which gives us the mass function of black holes formed at a certain horizon size, $d\beta_R/dm$.

To relate the curvature power spectrum in Fourier space to density contrasts in real space, we must smooth the power spectrum on horizon scales R with window function $W(k,R)$. The

variance of density contrasts on a scale R is given by

$$\sigma_0^2 = \int_0^\infty \frac{dk}{k} \frac{16}{81} (kR)^4 W^2(k,R) \mathscr{P}(k). \tag{5.16}$$

In Press-Schechter, the probability density for density contrasts is given in terms of this variance:

$$p(C) = \frac{1}{\sqrt{2\pi}\sigma_0} e^{-\frac{C^2}{2\sigma_0^2}}. \tag{5.17}$$

Note that the probability density $p(C)$ depends on the horizon size, which appears in the calculation of σ_0 through the smoothing of the primordial power spectrum. It has been noted that different choices of window functions can give rise to quite different required amplitudes for PBH formation [182], but [162] resolves these issues and shows that these differences are $< 10\%$ if one uses consistent quantities for smoothing and threshold density contrasts. In these calculations, we use the Gaussian window function.

The total effective energy density fraction in black holes is obtained by integrating (5.14) over PBHs formed at all horizon sizes, multiplied by a redshifting factor to account for the fact the black holes are forming in a radiation dominated era

$$\beta(t) = \int_0^\infty \frac{dR}{R} \frac{R(t)}{R} \beta_R, \tag{5.18}$$

where R is the horizon size. Note that this is slightly different from the true energy density at t, since integrating over all horizon sizes includes black holes forming at times greater than t. This is a negligible difference when evaluated at $t_\star$, since most black holes form before $t_\star$. Recall that the β parameter introduced in (5.1) is the effective PBH energy density evaluated at the horizon entry for the mode $k_\star$, and thus corresponds to $\beta(t_\star) \equiv \beta_\star$. Evaluating $\beta_\star$ from (5.18), we find

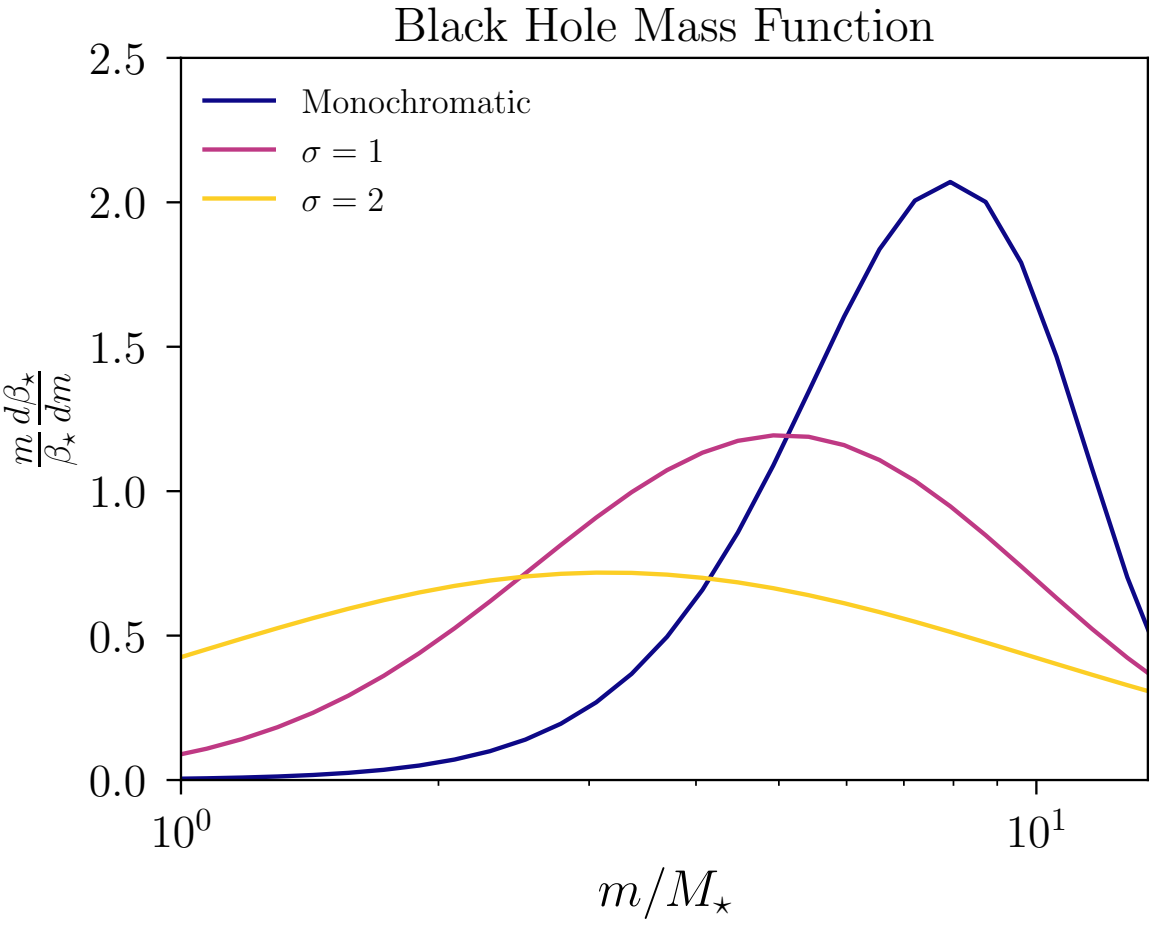

Figure 5.2. PBH mass function for different primordial curvature spectrum: the $\sigma = 1, 2$ lines are for the spectrum in (5.13). The amplitude is selected so that $\beta_\star \simeq 4 \times 10^{-7}$ for all cases here. $M_\star$ is the horizon mass associated with entry of the mode $k_\star$. Fitting these to log-normal mass functions gives peak BH masses of $m_{\rm BH} = \gamma_{\rm eff} M_\star$ with $\gamma_{\rm eff} \approx 7.6, 5.0, 3.1$ and widths $\sigma_m \approx 0.4, 0.7, 1.1$ for the monochromatic, $\sigma = 1$, and $\sigma = 2$ cases, respectively.

that the relationship to A is well-described by the following fitting function:

$$\beta_\star = aA^b \mathrm{Erfc}\left[\frac{c}{\sqrt{A}}\right], \tag{5.19}$$

where the fit parameters a, b, c will vary with the curvature perturbation width. Concretely, $a = 5.47, b = 0.51, c = 0.28$ for the monochromatic case; $a = 14.3, b = 0.66, c = 0.47$ for a Gaussian perturbation with $\sigma = 1$; and $a = 36.0, b = 0.91, c = 0.64$ for a Gaussian perturbation with $\sigma = 2$.

The PBH mass function is given by

$$\frac{1}{\beta(t)}\frac{d\beta(t)}{dm}. \tag{5.20}$$

and can be obtained by writing β_R as an integral over $d\beta_R/dm$ in (5.18). Examples of the resulting mass functions are shown in Fig. 5.2. In order to compare to existing observational bounds on PBHs with extended mass functions, we fit this mass distribution to a log-normal mass function given by

$$\frac{1}{\sqrt{2\pi}\sigma_m m}\exp\left(-\frac{\log^2(m/m_{\rm BH})}{2\sigma_m^2}\right). \tag{5.21}$$

The fit value $m_{\rm BH}$ is the characteristic black hole mass. $m_{\rm BH}$ can be written as some pre-factor $\gamma_{\rm eff}(\sigma,A)$ times $M_\star$ where $M_\star = 4\pi\rho_{r,\star}H_\star^{-3}/3$, the horizon mass corresponding to the entry of the mode $k_\star$.

Fig. 5.3 shows that $\gamma_{\rm eff}$ is an $O(\text{few})$ number that decreases with increasing curvature perturbation width and has a mild dependence on A. The width of the mass function, σ_m, also grows with the curvature perturbation width and A. For example, in Fig. 5.3, σ_m ranges from 0.4 to 1.1 going from a monochromatic to $\sigma = 2$ primordial spectrum for typical β values of interest for PBH observational constraints. Studies of PBH constraints with log-normal mass functions have shown that for $\sigma_m \lesssim 0.2$, observational bounds on the PBHs are nearly identical to that of a monochromatic mass function [168]. However, the shape of the constraints starts to deviate from the monochromatic case for $\sigma_m \sim 1$ and will be substantially different as σ_m is increased beyond 1. For this reason, we restrict to $\sigma < 2$ in the primordial power spectrum. Given the typical σ_m values for these primordial perturbations, the observational bounds on monochromatic black hole mass functions that we show from [168] are not exactly correct. In addition, some of the formulae in Sec. 5.3, such as the early black hole domination condition, are also not exact in the presence of an extended mass function. We neglect these model-dependent $O(1)$ differences given that we are working with many orders of magnitude in the total parameter space.

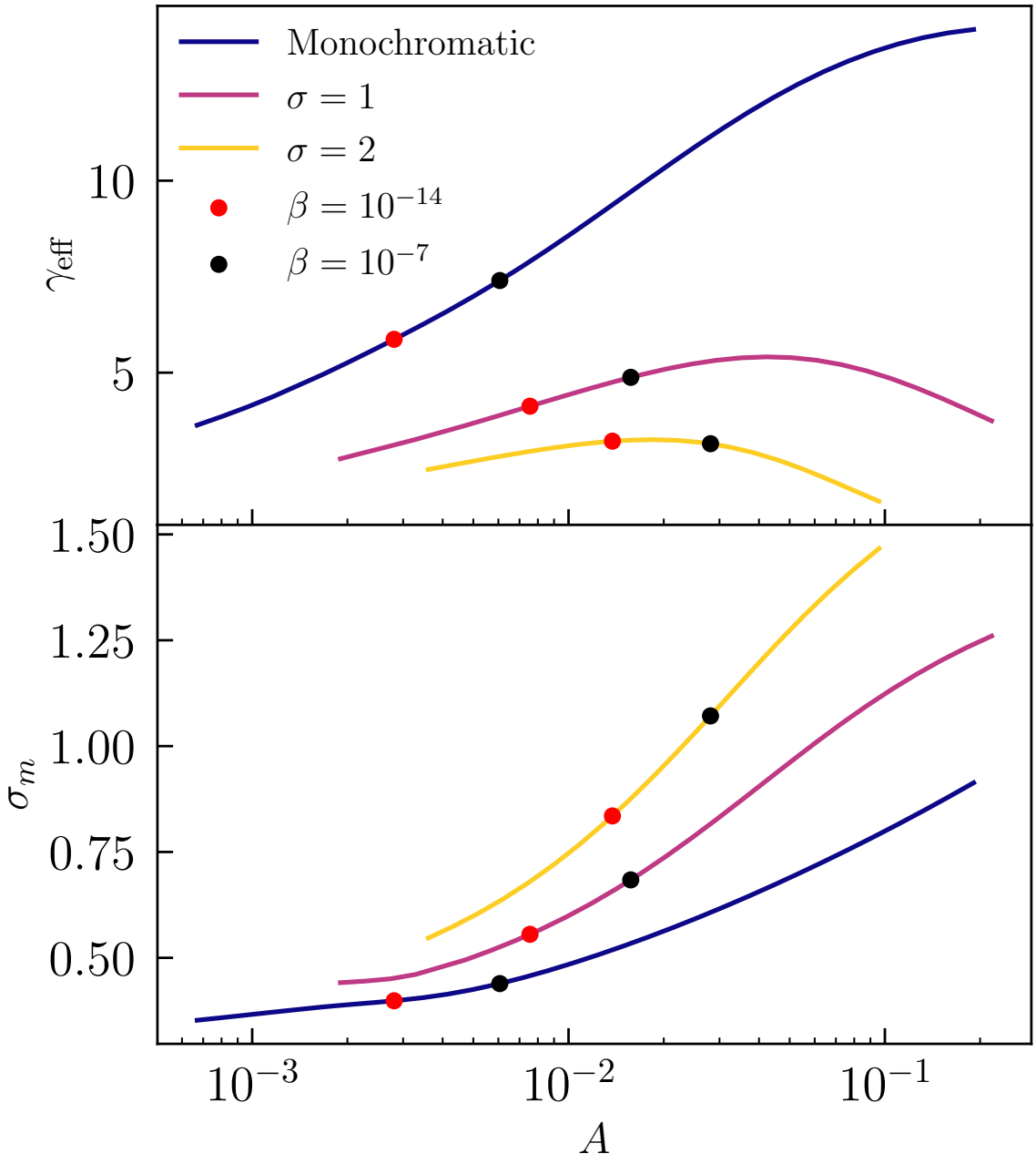

Figure 5.3. PBH mass function parameters as a function of the amplitude A and width of the primordial curvature spectrum. The peak BH mass is $\gamma_{\rm eff} M_\star$ and the width of the log-normal distribution is σ_m. The dots indicate the A values to produce $\beta_\star$ values of 10^{-7} and 10^{-14}.

5.5 Stochastic Gravitational Wave Spectrum

There are potentially multiple sources of stochastic gravitational waves associated with these PBHs. Assuming PBHs form due to a large primordial scalar perturbation, then gravitational waves can be generated at second-order in perturbation theory. These gravitational waves are dominantly produced around the time of PBH formation, and will determine the sensitivity in the absence of a BHD era. For sufficiently large density of PBHs such that there is a BHD era, then there are several additional effects. First, there can again be large scalar perturbations during the matter dominated-era due to the Poissonian distribution of PBHs, leading again to second-order gravitational waves. There may also be contributions from PBH clustering and evaporation at the end of a BHD era. These sources from the BHD era do not depend on the origin of the PBHs being from scalar perturbations, but they do in principle depend on the resulting mass function of the PBHs.

In this section, we detail each of these possible GW sources in turn. Note that aside from what is discussed here, there could also be GWs from Hawking radiation and PBH mergers [183, 184, 185, 186, 148, 187, 188], but these are generally at higher frequency and cannot be detected by GW interferometers for most of the PBH mass range we focus on. The GWs from mergers start to become detectable for some experiments at large masses near the very edge of our plots, but this contribution is more relevant for studies on solar mass PBHs.

5.5.1 Second-order gravitational waves from primordial scalar perturbations

Primordial scalar perturbations provide a source for the tensor modes at second order in perturbation theory, as first noted in [189]. In this section, we review the result following Ref. [190], and also account for differences in the parameter space where there is a black hole dominated era. Again, we assume the primordial perturbations obey Gaussian statistics throughout. For discussion of GWs resulting from non-Gaussian primordial perturbations, see

Refs. [175, 163].

As derived in detail in, *e.g.,* Refs. [146, 190, 191, 192, 193, 194], the equation of motion for each tensor mode polarization is given by

$$h''_{\mathbf{k}}(\eta) + 2\mathscr{H}h'_{\mathbf{k}}(\eta) + k^2 h_{\mathbf{k}}(\eta) = 4S_{\mathbf{k}}(\eta) \tag{5.22}$$

where η is the conformal time, $\mathscr{H} = aH$ is conformal Hubble parameter, and $S_{\mathbf{k}}(\eta)$ is a source term which depends quadratically on the first order scalar perturbations Φ. The tensor power spectrum and primordial power are related to the tensors and scalars by

$$\mathscr{P}_{\rm GW}(\eta,k)\delta^3(\mathbf{k}+\mathbf{k}') = \frac{k^3}{2\pi^2}\langle h_{\mathbf{k}}(\eta)h_{\mathbf{k}'}(\eta)\rangle, \tag{5.23}$$

$$\mathscr{P}(\eta,k)\delta^3(\mathbf{k}+\mathbf{k}') = \frac{k^3}{2\pi^2}\langle \Phi_{\mathbf{k}}(\eta)\Phi_{\mathbf{k}'}(\eta)\rangle. \tag{5.24}$$

The measurable quantity is the GW energy density fraction per logarithmic wavelength, which is given by

$$\Omega_{\rm GW} = \frac{1}{24}\left(\frac{k}{a(\eta)H(\eta)}\right)^2 \mathscr{P}_{\rm GW}(\eta,k) \tag{5.25}$$

where we have summed over both polarization modes.

We begin by considering a long-lasting radiation dominated (RD) era after horizon entry of the primordial perturbation. During radiation domination, the source term drops as $1/a^\gamma$ with $\gamma \approx 3$ [146] while for a freely propagating tensor mode $h \propto 1/a$. As a result, the power in the tensor modes will mainly be generated at horizon entry of the primordial perturbation, and well afterwards, they will behave as freely propagating gravitational waves. In this calculation, we will focus on those modes that enter the horizon during radiation domination and first study their evolution through RD. We will separately consider modes that enter the horizon during the PBH-dominated era below.

The GW dimensionless power spectrum in pure radiation-dominated (RD) is given

by [190, 191, 194]

$$\mathscr{P}_{\rm GW}(\eta,k) = 2\int_0^\infty dt \int_{-1}^1 ds\, \mathscr{P}(kv)\mathscr{P}(ku) I^2(s,t,x) \times \left[\frac{t(2+t)(s^2-1)}{(1-s+t)(1+s+t)}\right]^2 \tag{5.26}$$

where $\mathscr{P}$ is the initial perturbation, u and v are defined as $u = \frac{t+s+1}{2}$ and $v = \frac{t-s+1}{2}$, and $x = \eta k$. The I^2 term arises from second order perturbation theory as an integral over some combination of the Green's function for tensors and the transfer functions for the scalar modes. To consider k modes within the horizon such that the gravitational wave energy density is well-defined, we take the limit $x \to \infty$ (or $\eta k \gg 1$). In this limit and in a radiation-dominated era, I^2 can be explicitly written as

$$I^2(s,t,x) = \frac{288}{x^2}\frac{(s^2+t(2+t)-5)^4}{(s^2-(t+1)^2)^6}\left[\frac{\pi^2}{4}\Theta(t-(\sqrt{3}-1)) + \left(\frac{s^2-(t+1)^2}{s^2+t(2+t)-5} + \frac{1}{2}\log\left|\frac{-2+t(2+t)}{3-s^2}\right|\right)^2\right]. \tag{5.27}$$

From this result, we see that the power spectrum $\mathscr{P}_{\rm GW}$ scales as $\propto \frac{1}{\eta^2}$ in the $\eta k \gg 1$ limit. Since $a(\eta)H(\eta) = \frac{1}{\eta}$, we find that the GW energy density fraction in this limit is constant during RD:

$$\Omega_{\rm GW}^{RD} = \frac{1}{24}(k\eta)^2 \mathscr{P}_{\rm GW}(\eta,k)|_{x\to\infty} \tag{5.28}$$

corresponding to freely-propagating modes. Note that all dependence on the degrees of freedom is suppressed in the above equations and restored in the final expression below.

The GW spectrum in (5.28) applies during the early radiation dominated era. If there is a BHD era before standard MRE, we must include an additional factor of $a(\eta_{\rm BHD})/a(\eta_{\rm RH})$ to account for the different scaling of the energy density in matter-dominated era. This factor is just the ratio of scale factors between the beginning of black hole domination and the period of

reheating at the end of black hole domination.

Redshifting the energy density to today, we obtain the final result for the second-order GWs associated with the primordial perturbation:

$$\Omega_{\rm GW} = 1.4\,\Omega_{\gamma,0}\left(\frac{10.75}{g_\star}\right)^{1/3}\frac{1}{24}(k\eta)^2\,\mathscr{P}_{\rm GW}(\eta,k)|_{x\to\infty} \times \begin{cases} 1 & \beta' < \beta'_{\rm min} \\ \frac{a(\eta_{\rm BHD})}{a(\eta_{\rm RH})} & \beta' \geq \beta'_{\rm min} \end{cases}. \tag{5.29}$$

$g_\star$ is degrees of freedom at the horizon entry of the $k_\star$ mode, and $\Omega_{\gamma,0}$ is the abundance of photons today. We emphasize again that this applies for modes which have entered the horizon before PBH domination and therefore satisfy $k\eta_{\rm BHD} \gtrsim 1$, or equivalently $k \gtrsim \beta k_\star$. For the GWs produced at PBH formation, the experimental reach is primarily from tensor modes that are near the peak mode $k_\star$ or a few orders of magnitude below, so this result will suffice for our purposes.

Dependence on primordial perturbation

For sufficiently narrow primordial spectra, the BH mass function will not depend much on the details of the shape or width of the spectrum. The situation is quite different for the GW spectrum discussed in this section, however, where the infrared tail is quite sensitive to the width of the primordial spectrum.

Fig. 5.4 shows the GW spectrum for a monochromatic perturbation as well as Gaussians with a range of widths. For the monochromatic case, the spectrum goes as k^2 for $k \ll k_\star$. However, for a Gaussian primordial perturbation with width σ, the slope of the GW spectrum goes as k^2 for $\sigma k_\star \lesssim k \lesssim k_\star$, and goes as k^3 for $k \lesssim \sigma k_\star$ as also shown in [195]. The k^3 tail is a generic feature of gravitational waves produced at second order in a radiation dominated universe, as long as we have perturbations satisfying the conditions given in Ref. [196]. The important conditions here are that the source has finite width and that the k must be less than all characteristic scales associated with the source. The monochromatic case of course never

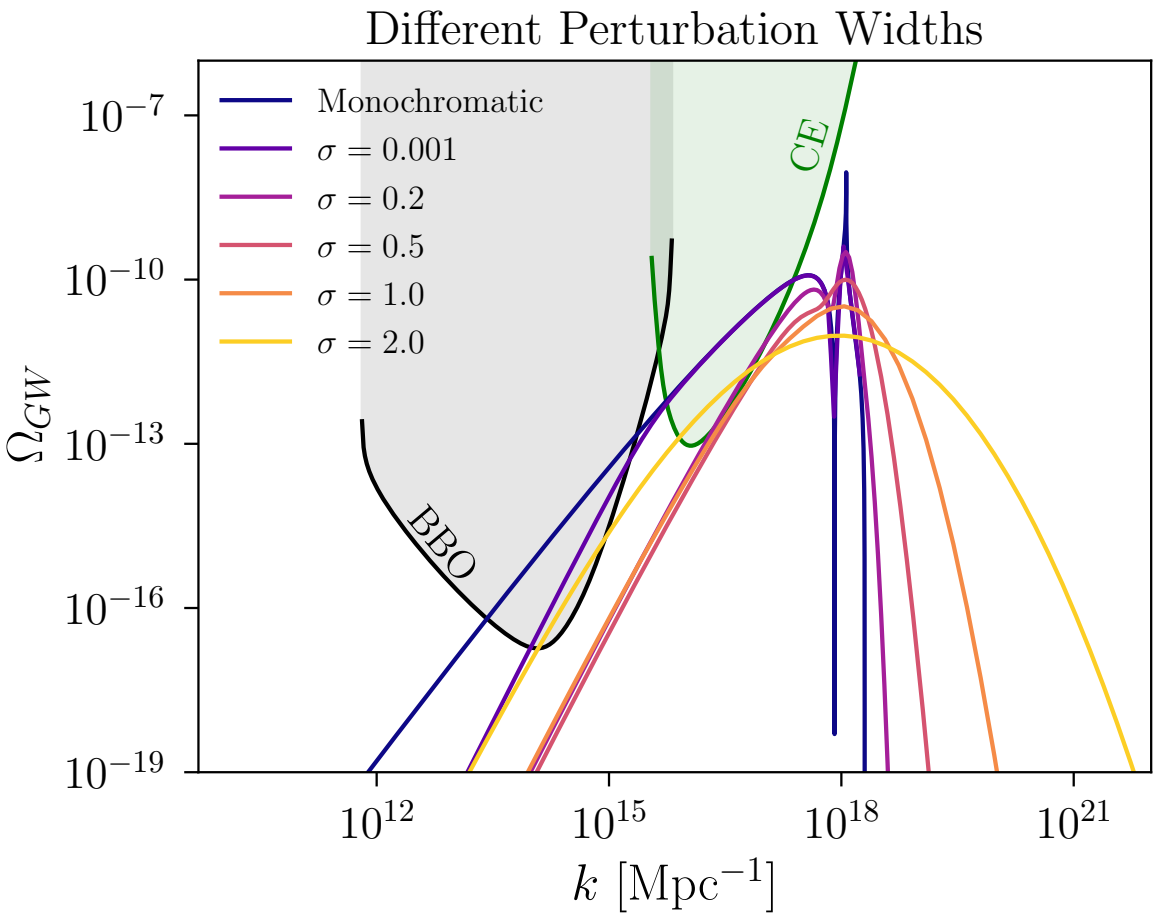

Figure 5.4. Gravitational wave spectrum induced at second order from the primordial scalar perturbations. $\Omega_{\rm GW}$ is the energy density per logarithmic wavelength today. The different lines show the dependence on the width of primordial curvature power spectrum, σ. For reference, we take $A = 0.003$, $k_\star = 10^{18}$ Mpc^{-1}. The black and green lines are power law integrated sensitivity curves for BBO and CE; for more details see Sec. 5.6.

satisfies these conditions, so it does not show this k^3 infrared scaling. In the finite width case, the condition that k is less than the characteristic scales associated with the source is satisfied for $k < \sigma k_\star$. This can be seen in the change in k scaling at $k \sim \sigma k_\star$ for the case $\sigma = 0.001$ in Fig. 5.4. For the other $O(1)$ values of σ, the possible region with k^2 scaling is not visible and instead the dominant behavior of the tail is the k^3 scaling. The width-dependence of the GW spectrum can thus have large impacts on GW detectability, even when the BH mass functions are similar.

In the monochromatic case, we can see the behavior for $k \ll k_\star$ by simply evaluating the integral (5.26) at the peak, where $s = 0$, $t = 2k/k_\star - 1$. Defining $\tilde{k} = k/k_\star$, then for $\tilde{k} \ll 1$, we have

$$\Omega_{\rm GW}^{RD} = A^2 \frac{3}{4}\tilde{k}^2 \left[\log^2\left(\frac{4}{3\tilde{k}^2}\right) - 4\log\left(\frac{4}{3\tilde{k}^2}\right) + \pi^2 + 4\right].$$

In the Gaussian case, we can analytically approximate the result via the Laplace method. Expanding the integrand about the peak $s = 0$, $t = \frac{2k_\star}{k}e^{-2\sigma^2} - 1$ and evaluating gives the following simple expression for the power spectrum for $\tilde{k} < \sigma$:

$$\Omega_{\rm GW}^{RD} = A^2 \frac{3\tilde{k}^3 e^{2\sigma^2} \log^3\left(\frac{4e^{-4\sigma^2}}{3\tilde{k}^2}\right)}{8\sqrt{2}\sigma} \times \left[\log^2\left(\frac{4e^{-4\sigma^2}}{3\tilde{k}^2}\right) + 2\sigma^2 \log\left(\frac{4e^{-4\sigma^2}}{3\tilde{k}^2}\right) + 4\sigma^2\right]^{-1/2} \tag{5.30}$$

which indeed goes as $\tilde{k}^3$.

5.5.2 Gravitational waves from PBH-dominated era

In addition to GWs produced at PBH formation, which dominates near the formation scale $k_\star$, there are also GWs generated during matter domination [197] that contribute at k below $k_\star$. We first consider GWs that arise from second order perturbation theory sourced by the scalar perturbations, with the difference in this case that the scalar perturbations are produced by the

gravitational potential of the PBHs themselves.

We will adapt our estimate from [197], including here an additional correction factor to restrict to the linear regime in perturbation theory. We first review Ref. [197], which directly computes the curvature power spectrum assuming a Poissonian distributed gas of PBHs. At formation, the density contrast in black holes can be treated as an isocurvature perturbation, which later evolves into a curvature perturbation. From [197], we have the following approximation for the perturbation at the onset of BHD:

$$\mathscr{P}_\Phi(k) = \frac{2}{3\pi}\left(\frac{k}{k_{\rm UV}}\right)^3 \left(5+\frac{4}{9}\frac{k^2}{\mathscr{H}_{\rm d}^2}\right)^{-2} \tag{5.31}$$

where $\mathscr{H}_{\rm d}$ is comoving Hubble at the onset of BHD and $k_{\rm UV}$ is the mean comoving BH separation scale,

$$k_{\rm UV} = \left(\frac{\beta}{\gamma_{\rm eff}}\right)^{1/3} k_\star. \tag{5.32}$$

Upon PBH formation, the black hole energy fraction grows, and the comoving Hubble when the black hole dominated era begins is $\mathscr{H}_{\rm d} = \beta k_\star$.

In order to calculate the contribution to the tensor power spectrum, we make the replacements $\mathscr{P} \to \mathscr{P}_\Phi$ and $I \to I_{\rm MD}$ in (5.26). Recall I arose in second order perturbation theory as an integral over a combination of the Green's function in RD and quadratic terms in the transfer function, so we must replace these with the solutions for the PBH era. This is the same as an matter-dominated (MD) era for our GW calculation, since BHs can be treated as a pressure-less non-relativistic fluid for modes $< k_{\rm UV} \ll k_\star$. The most important difference to note between the RD and MD eras is that the transfer function decays in RD but is constant in MD, so in the limit $x \to \infty$, $I^2_{\rm RD} \propto \frac{1}{x^2}$ as in (5.27), while $I^2_{\rm MD} = $ const. The source is constant and amplifies the resulting GWs from the BHD era.

For the BHD era, the energy density is $\Omega_{\rm GW} = (k/aH)^2 \mathscr{P}_{\rm GW}(k)/48$, which has a factor of 2 difference from the corresponding relationship for GWs generated in the RD era, (5.25).

While in the RD era there is an equal contribution from kinetic and gradient terms, in the MD era the kinetic terms are negligible when there is a constant source term. This is because the constant source forces the tensor modes to constant values at late times in the MD era. An approximate form for the GW spectrum today is then given by [197]

$$\begin{aligned}\Omega_{\rm GW} =& 4.4\times 10^{19}\,\Omega_{\gamma,0}\times\left(\frac{g_{\rm BHD}}{106.75}\right)^{-1/3}\left(\frac{g_{\rm RH}}{10.75}\right)^{-1/3}\\ &\times\left(\frac{m_{\rm BH}}{10^9\ {\rm g}}\right)^{4/3}(\beta')^{16/3}\\ &\times\begin{cases}\frac{k}{\mathscr{H}_{\rm d}} & k<8\mathscr{H}_{\rm d}\\ 8 & 8\mathscr{H}_{\rm d}<k<k_{\rm UV}\\ 0 & k>k_{\rm UV}\end{cases}\cdot\end{aligned} \tag{5.33}$$

Here we have assumed that the gravitational waves redshift as radiation after the transition from the PBH-dominated era to the radiation era. In general, there can be additional dampening or growth in the GW spectrum result depending on the details of the transition between the PBH and radiation dominated eras [198, 149]. For example, if there is a sufficiently narrow BH mass function, there is a rapid evaporation and a sudden change in the equation of state at the end of the MD era, leading to a significant enhancement in the spectrum relative to (5.33) [149, 150, 151]. This is the case if the BH mass function has $\sigma_m \lesssim 0.01$ [148], while we have log-normal mass functions with typical $\sigma_m \sim 0.4-1.2$.

However, it is not clear whether (5.33) applies for an extended MD era, because at some point during the MD era, density perturbations can become nonlinear. The density perturbation at black hole formation is given by

$$\delta(t_{\rm BHD}) \sim \sqrt{\frac{2}{3\pi}}\left(\frac{k}{k_{\rm UV}}\right)^{3/2} \tag{5.34}$$

and starts growing with the scale factor at $\mathrm{Max}[a_{\rm BHD}, a_k]$, where a_k is the scale factor at horizon

entry for that mode, since the density perturbation is frozen while outside of the horizon and can only grow in the BHD era. Once perturbations become nonlinear, the perturbation theory solution of the scalar modes with a constant source term is no longer valid. There may be GWs produced instead by collapse of nonlinear perturbations or mergers, as estimated in [199], but these require further numerical simulations to treat properly.

A lower bound on the possible GW spectrum can be obtained by restricting the source function to regions in k and time for which $\delta_k(t) < 1$. Setting the cutoff at $\delta_k = 1$ gives the cutoff scale factor $a_{\rm cut}(k)$:

$$\frac{a_{\rm cut}}{a_{\rm RH}} = \frac{a_{\rm BHD}}{a_{\rm RH}} \times \begin{cases} \sqrt{\frac{3\pi}{2}} \left(\frac{\mathscr{H}_{\rm d}}{k}\right)^2 \left(\frac{k_{\rm UV}}{k}\right)^{3/2} & k < \mathscr{H}_{\rm d} \\ \sqrt{\frac{3\pi}{2}} \left(\frac{k_{\rm UV}}{k}\right)^{3/2} & k > \mathscr{H}_{\rm d} \end{cases} . \tag{5.35}$$

Compared to the results of [197], cutting off the source function when density perturbations become nonlinear introduces an additional factor in (5.33) given by

$$R \approx \left(\text{Min} \left[\frac{a_{\rm BHD}}{a_{\rm RH}} \times \begin{cases} \sqrt{\frac{3\pi}{2}} \left(\frac{k_{\rm UV}}{6k_{\rm BHD}}\right)^{3/2} & k < 6\mathscr{H}_{\rm d} \\ \sqrt{\frac{3\pi}{2}} \left(\frac{k_{\rm UV}}{k}\right)^{3/2} & k > 6\mathscr{H}_{\rm d} \end{cases} , 1 \right] \right)^2 , \tag{5.36}$$

see Appendix 5.A for details. Here we have connected the results at $k \ll \mathscr{H}_{\rm d}$ and $k \gg \mathscr{H}_{\rm d}$ as the details in the intermediate regime are unimportant. With this approach, the source function is cut off well before the transition to radiation domination, leading to a strong dampening of the spectrum. Then the spectrum is far beneath the threshold required for experimental observability, such the details of how the source is cut off and the transition from the PBH to the RD era are not relevant for our calculation. We note that our estimate may be overly conservative, however. In addition, other sources of GWs will be present and can be many orders of magnitude larger when the perturbations are nonlinear [199]. We estimate one possible source of GWs generated at the end of the BHD era in the following subsection.

5.5.3 Gravitational waves from reheating

There can further be contributions to GWs from reheating of the universe due to PBH evaporation. One possibility is that GWs are produced when the nonlinear structures of the BHD era all evaporate into radiation. The idea is that the black holes slowly evaporate a fraction of their mass into radiation through the bulk of the BHD era. Then, at the end of the BHD era, the remaining mass contained within the halos evaporates and collides against the radiation fluid. This could produce a turbulent fluid with eddies that cascade down to smaller scales, which can induce GWs. In this section, we perform an order of magnitude estimate for this potential source. Detailed numerical simulations are required to determine if evaporation of the clustered PBHs indeed acts as an efficient source of turbulence.

The topic of GWs from turbulent events in the early universe has been studied in Refs. [200, 201]. Here we discuss the assumptions and calculations in these works and argue that the results can be used in estimating the GWs sourced by the PBHs at the end of their lifetime. In these studies, the picture is that during the early universe, a fraction of the available energy density is transformed into kinetic energy of the cosmological fluid. This kinetic energy is stirred on a length scale L_S over a time scale $\tau_{\rm stir}$. These quantities correspond to the characteristic length and duration of the turbulent source. The turbulent kinetic energy then cascades down to some damping scale determined by the fluid characteristics of the plasma.

In these works, the turbulent source is left generic and the only assumption is that the spectrum of the turbulence is Kolmogorov. We note that the Kolmogorov energy spectrum is a result from classical hydrodynamics and that relativistic turbulence is much less explored; nonetheless, we follow other works in assuming that classical theory provides an approximation for turbulence in a relativistic fluid. To summarize, the calculations of these studies depend on the scale and duration of turbulence, cosmological parameters and characteristics of the plasma during energy injection, and the model of the turbulence. The gravitational wave spectrum from turbulence is then calculated by solving the usual wave equation for tensor modes sourced by

the transverse traceless piece of the stress-energy tensor. Refs. [200] and [201] perform this analysis in Fourier and real space, respectively, arriving at approximately the same results with slight differences arising from different treatments in the time dependence of the turbulence. In particular, no assumption is made on the particle physics origin of the turbulence. For example, while Refs. [200, 201] discussed phase transitions as one possible source of GWs, the results have been applied to other scenarios such as decay of a scalar field reheating the universe [199].

We may apply these results to calculate GWs from Hawking evaporation in the BHD era, given the following physical picture. For the bulk of the BHD era, the universe will look like clusters of black holes with sparse radiation fluid freely streaming outwards. However, by the end of the BHD era, all of the mass in the black hole clusters then gets deposited into radiation, which is a possible source of turbulence. Since we expect the typical black hole mass function to have a fairly significant width as in Fig. 5.2, we approximate the turbulent source to last for around $\tau_{\rm stir} \approx t_{\rm evap}$. In addition, we take the length scale of the turbulence source L_S to be defined by the smallest comoving wavenumber that becomes non-linear by black hole evaporation, $k_{\rm NL}$. That is, $k_{\rm NL}$ is the comoving wavenumber that satisfies $a_{\rm cut} = a_{\rm RH}$ in (5.35), which gives

$$k_{\rm NL} = \begin{cases} \frac{3.2\times 10^{14}}{\rm Mpc}\left(\frac{m_{\rm BH}}{10^4 {\rm g}}\right)^{-\frac{17}{14}} & \beta' > \beta'_{\rm NL} \\ \frac{1\times 10^{16}}{\rm Mpc}\left(\frac{m_{\rm BH}}{10^4 {\rm g}}\right)^{-\frac{31}{18}}\left(\frac{\beta'}{10^{-7}}\right)^{-\frac{8}{9}} & \beta' < \beta'_{\rm NL} \end{cases} \tag{5.37}$$

where

$$\beta'_{\rm NL} = 5\times 10^{-6}\left(\frac{m_{\rm BH}}{10^4 {\rm g}}\right)^{-\frac{4}{7}} \tag{5.38}$$

is the minimum β' such that the largest non-linear mode enters the horizon after the BHD era starts.

As argued in [200], the relevant time-scale for production of gravitational waves from turbulence is given by the maximum of the turbulence duration $\tau_{\rm stir}$ and the dissipation time of the largest eddies τ_S. In the PBH evaporation scenario, the black hole mass function is wide

enough that the larger time-scale is on the order of the black hole evaporation time $t_{\rm evap}$. Then, the energy dissipation rate is given by

$$\varepsilon \sim \frac{\kappa\rho}{w t_{\rm evap}}, \tag{5.39}$$

where ρ is the energy density, κ is the efficiency factor of conversion to turbulent kinetic energy, and w is the enthalpy density of the radiation fluid. Note that this is highly approximate, as we've effectively treated the turbulence as uniformly injected over the time $t_{\rm evap}$ rather than modeling the exact time-dependence of the Hawking radiation, so the result should be treated as a very rough estimate. Another important quantity for the turbulence calculation is the Mach number defined in Ref. [201], which goes as

$$M \propto \left(\frac{\varepsilon}{k_{\rm NL}}\right)^{1/3} \propto \kappa^{1/3}\left(\frac{k_{\rm RH}}{k_{\rm NL}}\right)^{1/3}. \tag{5.40}$$

Typical Mach numbers for these early evaporating black holes are $M \sim 0.1 - 0.5$. The comoving wavenumber of the horizon at the end of evaporation $k_{\rm RH}$ can be calculated from (5.6) and is given by

$$k_{\rm RH} = \frac{4.9\times 10^{11}}{\rm Mpc}\left(\frac{m_{\rm BH}}{10^4}\right)^{-\frac{3}{2}}. \tag{5.41}$$

With these physical quantities in hand, we may apply the final result of Ref. [201] to our scenario. For clarity, we rewrite the original expression here and make explicit the replacements in our variables. The turbulence-sourced GW spectrum today is [201]

$$\begin{aligned} h_c \propto & \left(\frac{100\,\text{GeV}}{T_*}\right)\left(\frac{100}{g_*}\right)^{1/3}\times \\ & \left(\frac{H_*}{k_0}\right)^{3/2}(H_*\tau_{\rm stir})^{1/2}\left(k_0^3\omega H_{ijij}(\omega,\omega)\right)^{1/2}, \end{aligned} \tag{5.42}$$

where T_*, g_* are the temperature and degrees of freedom at the end of the turbulence, k_0 is the inverse length scale of the turbulent source, $\tau_{\rm stir}$ is the turbulence duration, ω is the angular

frequency of the gravitational waves at $t_{\rm evap}$, and the function H_{ijij} is approximated by

$$\frac{7M^3k_0^{-4}}{16\pi^{3/2}}\int_0^1 dx x^{11/4}\exp\Big[-\Big(\frac{\omega}{k_0M}\Big)^2 x\Big]\,\mathrm{Erfc}\Big[-\frac{\omega}{k_0M}\sqrt{x}\Big].$$

Then, taking $T_* = T_{\rm RH}$, $g_* = g_{\rm RH}$, $\tau_{\rm stir} = t_{\rm evap}$, and rewriting in terms of comoving quantities $H_* = k_{\rm RH}/a_{\rm RH}$, $k_0 = k_{\rm NL}/a_{\rm RH}$, $\omega = k_{\rm NL}/a_{\rm RH}$, and using the usual $\Omega_{\rm GW} = \frac{2\pi^2}{3H_)^2} f^2 h_c^2$, we have

$$\begin{aligned}\Omega_{\rm GW,turb} =& 4\times 10^{-22}\Big(\frac{100\,\mathrm{GeV}}{T_{\rm RH}}\Big)^2\Big(\frac{100}{g_{\rm RH}}\Big)^{2/3}\times \\ & \Big(\frac{k}{1\mathrm{Mpc}^{-1}}\Big)^2\Big(\frac{k_{\rm RH}}{k_{\rm NL}}\Big)^4\Big(\frac{k}{k_{\rm NL}}\times F(k)\Big)\end{aligned} \tag{5.43}$$

where $F(k)$ is given by

$$\frac{7M^3}{16\pi^{3/2}}\int_0^1 dx x^{11/4}\exp\Big[-\Big(\frac{k}{k_{\rm NL}M}\Big)^2 x\Big]\,\mathrm{Erfc}\Big[-\frac{k}{k_{\rm NL}M}\sqrt{x}\Big].$$

The function $F(k)$ is approximately constant below $k_{\rm NL}M$ and decays as $k^{-15/2}$ above $k_{\rm NL}M$, so the GW spectrum from turbulence peaks at $k_{\rm NL}M$. When the initial PBH abundance is well above the BHD line, the spectrum has no β' dependence. This is because at large β', the black hole dominated era starts early enough that $k_{\rm NL}$ is only dependent on the PBH mass. This can be seen from (5.37), which is β' independent above $\beta'_{\rm NL}$. Within 3-4 orders of magnitude in β' of the BHD line, there is a large suppression in this spectrum since the BHD era is much shorter and the halo sizes are smaller.

The spectrum in (5.43) should be regarded only as a rough estimate of the GWs from turbulence. For example, a large uncertainty arises from the dependence on the efficiency factor κ. There should also be an additional suppression from the expansion of the universe since the turbulence occurs over a Hubble time. Regardless, even with an optimistic efficiency factor $\kappa = 1$, our turbulence estimate in (5.43) is not strong enough to be detected even by BBO and does not appear in our reach plots.

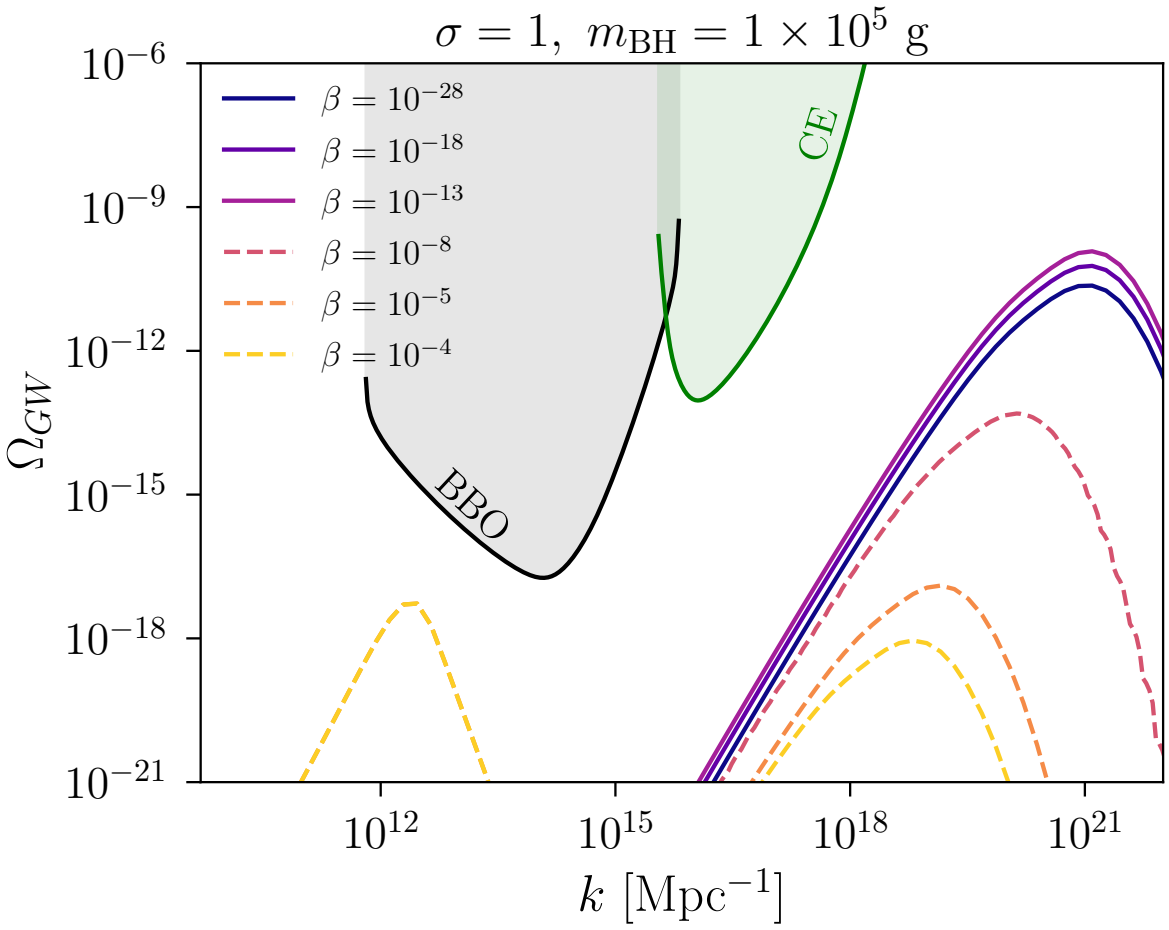

Figure 5.5. Total gravitational wave spectrum today from a Gaussian perturbation with $\sigma = 1$, for $m_{\rm BH} = 1 \times 10^5$g and different values of β. The solid lines are for small β with no BHD era. The dashed lines indicate the total resulting GWs when there is a BHD era. We see that when β increases, the dominant contribution shifts to the GWs from turbulence as discussed in Sec. 5.5.3. For this contribution, we assume an optimal efficiency of $\kappa = 1$, which gives a Mach number of $M \approx 0.2$. For β much larger than the minimum required for black hole domination, the turbulent contribution is identical.

5.5.4 Combined spectrum

In Fig. 5.5, we show the combined GW spectrum for a reference PBH mass of $m_{\rm BH} = 1 \times 10^5$g and assuming a primordial perturbation with lognormal width $\sigma = 1$. For small enough β, there is no BHD era, and the only GWs are those induced from the primordial perturbation, discussed in Sec. 5.5.1. The dashed lines show the GW spectrum where there is a BHD era. The BHD era leads to an overall redshifting of the GW spectrum associated with BH formation.

For this signal, it also leads to a peak frequency $k_\star$ which depends on β according to (5.10), leading to a peak at lower frequencies as β is increased. In addition, our rough estimate of the GW spectrum generated by turbulence at PBH evaporation is visible, giving a contribution that peaks at lower frequencies. The contribution from gravitational waves generated during the BHD era discussed in Sec. 5.5.2 peaks in a similar frequency range as the turbulent source, but has negligible amplitude when we implement a cutoff on nonlinear density perturbations. We emphasize again that our estimate of this latter contribution is likely too conservative and that a numerical study is required to calculate the GW spectrum from the black hole dominated non-linear regime.

5.6 Observational Bounds and Reach

In this section we discuss the experimental reach for various GW experiments on the stochastic GW background associated with PBHs. We show the sensitivity in terms of the parameter space for the primordial scalar perturbation, $(k_\star, A)$, as well as in the black hole mass and mass fraction parameter space, $(m_{\rm BH}, \beta')$. We also translate existing PBH bounds into the $(k_\star, A)$ plane.

5.6.1 Calculation of Observational Bounds

We calculate the expected observational bounds and observational reach from various current and proposed experiments following Refs. [202, 203]. We consider Big Bang Observer (BBO) [204, 205, 206, 207], Einstein Telescope (ET) [208, 209], Cosmic Explorer (CE) [210, 211], and the Laser Interferometer Space Antenna (LISA) [212, 213]. Other proposed interferometers that operate in a similar frequency range to LISA include TianQin [214, 215] and Taiji [216], while experiments that cover a similar range as BBO include DECIGO [217, 218], AION [219, 220], and AEDGE [219, 221]. We also note that current LIGO/VIRGO data has been used to search for a stochastic GW background [47], but the results do not add any constraints to the parameter space that we show.

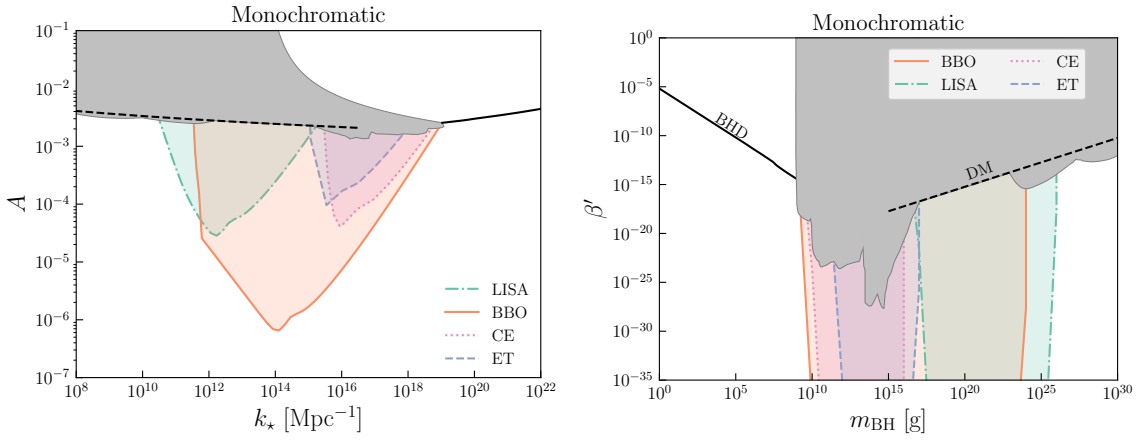

Figure 5.6. For monochromatic perturbations, the observational reach for experiments BBO, LISA, CE, ET are shown in the $(k_\star, A)$ plane for the primordial scalar perturbation (**left**) and in the $(\beta', m_{\rm BH})$ plane of PBH parameters (**right**). We assume an observational time of 1 year and a signal-to-noise ratio of 1 for each of the experiments. In both panels, the gray shaded regions are the existing PBH bounds that were shown in Fig. 5.1 and discussed in Sec. 5.3.4. The DM line (black, dashed) shows the parameters that would result in the saturation of current observed dark matter density today. The BHD line (black, solid) is the minimum β' at a given $m_{\rm BH}$ that would result in a period of black hole domination. Above the BHD line, none of the GW sources we have estimated are observable. For $m_{\rm BH} > 10^9$ g, the experimental reach comes from the second-order GWs induced by the primordial scalar perturbation. Note that pulsar timing arrays (PTA) have some observational reach near at $k_\star \sim 10^8$ Mpc^{-1} or $m_{\rm BH} \sim 10^{30}$ g, but we choose not to show this here as these reaches are most relevant for near solar mass PBHs.

An overview of the method to obtain the bounds can be found in [202]. We follow Appendix A of [203], which calculates the strain sensitivity curves for these experiments explicitly using the methods in [202]. The strain sensitivity curves and overlap reduction functions are used to calculate an effective GW background $\Omega_{\rm eff}$. The signal-to-noise (SNR) ratio for an expected stochastic GW spectrum $\Omega_{\rm GW}$ is then given by

$$\rho = \sqrt{nT}\left[\int_{f_{\rm min}}^{f_{\rm max}} df \left(\frac{\Omega_{\rm GW}}{\Omega_{\rm eff}}\right)^2\right]^{1/2} \tag{5.44}$$

where T is the observational time and we take the integral over the entire bandwidth of the experiment. n is 1 or 2 for auto-correlation (LISA, CE) and cross-correlation detections (BBO, ET), respectively. The spectrum $\Omega_{\rm GW}$ is function of initial perturbation amplitude A, scale $k_\star$,

and Gaussian width σ, so for some choice of σ, we can solve for the parameters that give a desired SNR. In this paper, we present results with $\rho = 1$ and $T = 1\,\mathrm{yr}$ for each experiment and assume a perfect subtraction of foreground GWs from active sources. For a given σ, we can then use the one-to-one correspondence between $(k_\star, A)$ and PBH parameters from Sec. 5.4 to show the same bounds in $(m_{\rm BH}, \beta')$ space.

5.6.2 Results

Our main results are shown in Fig. 5.6 for a monochromatic perturbation and Fig. 5.7 for a finite width Gaussian perturbation. The left panels show the existing bounds and experimental reach in the parameter space of primordial curvature perturbations, similar to Ref. [222], while the right panels are in the parameter space for PBHs. In both panels, the gray shaded region are existing bounds on PBHs, as previously shown in Fig. 5.1. Similar to Fig. 5.1, we again indicate where PBHs comprise all of the DM (dashed line) and the lower boundary to the region where we have a black-hole dominated (BHD) era (solid line). These features appear roughly inverted in the left and right panel due to the relationship between $m_{\rm BH}$ and $k_\star$. We note again that the correspondence between $k_\star$ and $m_{\rm BH}$ is different if BHD occurs. If BHD never occurs, we have $k_\star \sim m_{\rm BH}^{-1/2}$, while if BHD does occur we instead have $k_\star \sim m_{\rm BH}^{-5/6}\beta^{-1/3}$. This is why the PBH bounds depend on both A and $k_\star$ in the BHD era.

For black holes that evaporate after BBN ($m_{\rm BH} > 10^9$ g), gravitational wave interferometers are sensitive to the stochastic GW spectrum induced at second order from the primordial curvature perturbation. In this mass range, we see the broadest level of sensitivity for the largest curvature perturbation width ($\sigma = 2$), with the reach extending from $10^9 - 10^{28}$ g when all experiments are included. This is because the GW spectrum extends over a much wider frequency range, as seen in Fig. 5.4. The reach curves thus shrink with smaller σ in Fig. 5.7. However, once σ decreases below $\sigma \sim 0.01$, the reach actually improves again at small PBH mass, which can be seen in the sensitivities for the monochromatic perturbation in Fig. 5.6. This is because the k^2 infrared tail grows as σ decreases below $\sigma \sim 0.01$, as discussed in Sec 5.5.1.

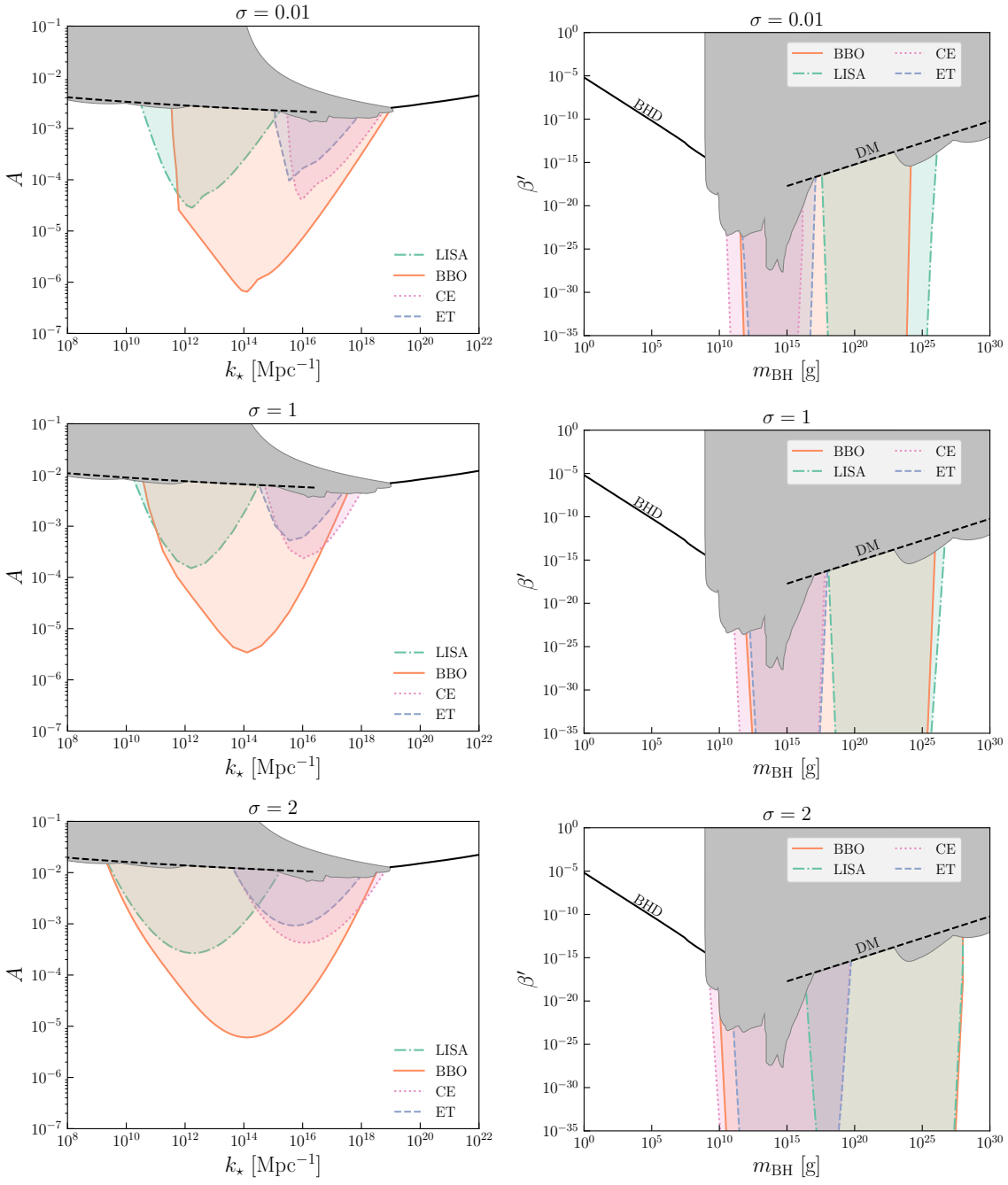

Figure 5.7. Similar to Fig. 5.6, but assuming a Gaussian perturbation as in Eq. 5.13. The different rows are for different curvature perturbation widths σ.

In the region of parameter space where the black holes are short-lived, the spectrum of stochastic GWs produced during or at the end of the BHD era is highly uncertain since density perturbations become nonlinear. At present, we do not find a detectable signal from any of the sources discussed in Secs. 5.5.2-5.5.3. However, more numerical work should be done to investigate what happens in a BHD era as density perturbations become non-linear and whether there are observable GW sources from the transition of the BHD to radiation era.

5.7 Conclusions

In this paper, we have investigated how generation GW interferometers can probe the parameter space of primordial black holes in the mass range of 10 g – 10^{28} g. Assuming that the black holes form from some generic primordial curvature perturbation at small scales generated by inflation, there are several possible stochastic GW signals, which we calculate as a function of the initial abundance and mean black hole mass. Second order gravitational waves from the primordial curvature perturbation can be used to probe primordial black hole masses in the range $10^9 - 10^{28}$ g down to very small β', depending on the experiment and curvature perturbation width. For black hole masses below 10^9 g, there are additional possible sources of GWs if β' is sufficiently large enough, such that there is an early black hole dominated era. We considered second order GWs generated from the black hole fluid curvature perturbation itself, as well as GWs produced from the turbulent fluid at the end of the BHD era. Based on our estimates, we did not find these to give rise to observable GWs. In addition, there may be GWs produced during the nonlinear evolution of the BHD era, from Hawking evaporation itself, mergers, or from a sharp transition from black hole dominated to radiation eras. Treating the BHD era properly and including all of these sources requires a numerical treatment.

Finally, we also presented results in terms of the curvature perturbation parameters and see that second order GWs allow us to probe perturbations at quite small scales. The stochastic GW spectrum is thus a promising way to probe inflationary scenarios giving rise to both short-

lived black holes, as well as long-lived black holes comprising some fraction of the dark matter today.

Acknowledgements

We thank David Langlois, Theodoros Papanikolaou, and Vincent Vennin for helpful discussions, and Vincent Vennin for valuable feedback on a draft of this work. JK is supported by the Department of Energy under grants DE-SC0019195 and DE-SC0009919. TL is supported by the Department of Energy under grant DE-SC0019195 and a UC Hellman fellowship. EV is supported by a Sloan Scholar Fellowship. Chapter 5, in full, is a reprint of the material as it appears in Jonathan Kozaczuk, Tongyan Lin, Ethan Villarama, Signals of primordial black holes at gravitational wave interferometers, Phys.Rev. D **105** (2022) no.12, 123023. The dissertation author was one of the primary investigators and authors of this paper.

Appendix

5.A GWs in BHD era

In this appendix, we briefly describe how we obtained (5.36), which we use to obtain a rough lower bound on second-order GWs sourced by scalar perturbations during the BHD era.

To obtain (5.36), we imposed k-dependent time cutoff on density perturbations. To apply this cutoff, we must re-calculate the quantity I, which now becomes

$$I(u,v,x) = \int_{x_d}^{x} d\bar{x} \frac{a(\bar{x})}{a(x)} k G_k(x,\bar{x}) F_k(u,v,\bar{x}) \times \Theta(x_{\rm cut}(vk) - \bar{x}) \Theta(x_{\rm cut}(uk) - \bar{x}). \tag{5.45}$$

where G_k and F_k are Green's functions defined in [197], $x = k\eta_{\rm RH}$, and $x_{\rm cut} = k\eta_{\rm cut}$ is given by

$$x_{\rm cut}(vk) = x \sqrt{ {\rm Min}\left[\frac{a_{\rm BHD}}{a_{\rm RH}} \times \begin{cases} \sqrt{\frac{3\pi}{2}} \left(\frac{\mathscr{H}_{\rm d}}{vk}\right)^2 \left(\frac{k_{\rm UV}}{vk}\right)^{3/2} & vk < \mathscr{H}_{\rm d} \\ \sqrt{\frac{3\pi}{2}} \left(\frac{k_{\rm UV}}{vk}\right)^{3/2} & vk > \mathscr{H}_{\rm d} \end{cases}, 1 \right]}. \tag{5.46}$$

This comes from applying (5.35) to the density perturbation vk. Evaluating I^2 as in Appendix B of [197] gives the leading term

$$I^2 \sim \frac{100}{9} \frac{(x_{\rm cut}(vk))^4}{x^4}, \tag{5.47}$$

which is similar to the result in [197], but with an additional suppression from the cutoff on non-

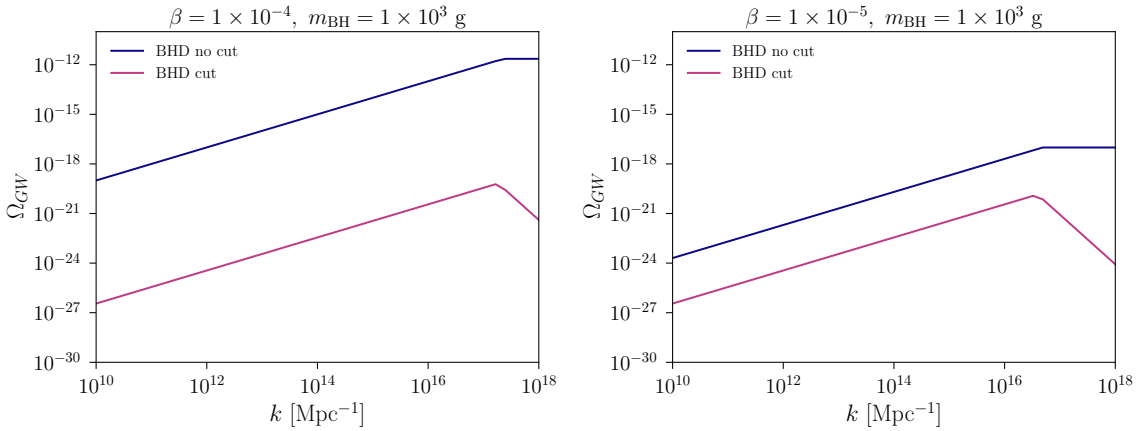

Figure 5.8. Comparison of GW spectra today from the BHD era and turbulence for $m_{\rm BH} = 10^3 \mathrm{g}, \sigma = 1$ and two values of β. The blue line is the pure BHD era result (5.33) without any modification to account for the fact that the density perturbations become non-linear. The magenta line is our conservative lower bound of the spectrum, which includes a cut-off when the density perturbations become non-linear. This introduces an additional suppression factor (5.36) to (5.33).

linear perturbations. Since (5.45) has two step functions we should have $\mathrm{Min}[x_{\rm cut}(vk), x_{\rm cut}(uk)]$, but the integrand always peaks near $u \sim v$ so we take both step functions to be the same.

We now evaluate the tensor spectrum with our modification to I^2. Here we provide simple estimates in the large and small k limits, similar to [197]. Since the integrand (aside from the I^2 factor) is peaked in u, v, we will treat I^2 as constant about the peak. Then the effect of the nonlinear cutoff is just to introduce a factor of $(x_{\rm cut}(vk)/x)^4$, evaluated at the peak value of v. For $k \gg k_{\rm BHD}$, the integrand is peaked at $u = v = 1$, so we can approximate $x_{\rm cut}(vk) \approx x_{\rm cut}(k)$. For $k \ll k_{\rm BHD}$, the integral is peaked at $u \sim v \sim \frac{6k_{\rm BHD}}{k}$ which gives $x_{\rm cut}(vk) \sim x_{\rm cut}(6k_{\rm BHD})$. Using (5.46) in these limits then gives (5.36), where we glued the solutions in the two limits together to obtain a continuous function. We have checked numerically that including the u, v dependence only leads to $O(\text{few})$ deviations from our analytic estimates.

Fig. 5.8 shows a comparison of the GW spectrum without the nonlinear cutoff, (5.33), and with the cutoff. With the nonlinear cutoff, our estimate of this GW signal is not detectable.

Chapter 6

Conclusions and Outlook

In the coming decades, advancements in solid state technologies may lead to new avenues of dark matter direct detection in the sub-GeV mass range. The primary result of this Dissertation is the calculation of experimental response rates in this light dark matter regime to the DM wind. In Chapter 3, we work in the harmonic crystal approximation and provide a complete prescription for calculating the crystal response across the entire energy-momentum phase space. In particular, we have shown how to calculate scattering rates in the multiphonon regime and that the response in this regime smoothly approaches the well-known nuclear recoil limit. The results of this work are neatly packaged in the `multiphonon` addition to the code `DarkELF`, which is gaining popularity with our colleagues in the experimental world. In Chapter 4, we allow for anharmonicities in the crystal potential and identify the DM mass regimes in which these anharmonicities are experimentally relevant. We have generalized methods from the harmonic case to demonstrate that the anharmonic corrections are negligible at DM masses ~ 10 MeV, but can introduce small $\mathcal{O}(1)$ enhancements at $\sim$ few MeV for near-future experiments. This work provides a fairly comprehensive theoretical understanding and a practical methodology for calculating LDM-crystal scattering rates, which will become increasingly important for probing LDM as experimental energy thresholds decrease.

Bibliography

[1] F. Zwicky, "Republication of: The redshift of extragalactic nebulae," *General Relativity and Gravitation*, vol. 41, no. 1, pp. 207–224, 2009.

[2] V. C. Rubin and W. K. Ford, Jr., "Rotation of the Andromeda Nebula from a Spectroscopic Survey of Emission Regions," *Astrophys. J.*, vol. 159, pp. 379–403, 1970.

[3] V. C. Rubin, N. Thonnard, and W. K. Ford, Jr., "Rotational properties of 21 SC galaxies with a large range of luminosities and radii, from NGC 4605 /R = 4kpc/ to UGC 2885 /R = 122 kpc/," *Astrophys. J.*, vol. 238, p. 471, 1980.

[4] R. Massey, T. Kitching, and J. Richard, "The dark matter of gravitational lensing," *Reports on Progress in Physics*, vol. 73, no. 8, p. 086901, 2010.

[5] V. Strait, M. Bradač, A. Hoag, K.-H. Huang, T. Treu, X. Wang, R. Amorin, M. Castellano, A. Fontana, B.-C. Lemaux, E. Merlin, K. B. Schmidt, T. Schrabback, A. Tomczack, M. Trenti, and B. Vulcani, "Mass and light of abell 370: A strong and weak lensing analysis," *The Astrophysical Journal*, vol. 868, p. 129, nov 2018.

[6] H. Hoekstra, H. K. C. Yee, and M. D. Gladders, "Properties of galaxy dark matter halos from weak lensing," *The Astrophysical Journal*, vol. 606, p. 67, may 2004.

[7] D. Munshi, P. Valageas, L. van Waerbeke, and A. Heavens, "Cosmology with weak lensing surveys," *Physics Reports*, vol. 462, no. 3, pp. 67–121, 2008.

[8] R. Mandelbaum, A. Slosar, T. Baldauf, U. Seljak, C. M. Hirata, R. Nakajima, R. Reyes, and R. E. Smith, "Cosmological parameter constraints from galaxy–galaxy lensing and galaxy clustering with the SDSS DR7," *Monthly Notices of the Royal Astronomical Society*, vol. 432, pp. 1544–1575, 04 2013.

[9] A. Leauthaud, J. Tinker, K. Bundy, P. S. Behroozi, R. Massey, J. Rhodes, M. R. George, J.-P. Kneib, A. Benson, R. H. Wechsler, M. T. Busha, P. Capak, M. Cortês, O. Ilbert, A. M. Koekemoer, O. L. Fèvre, S. Lilly, H. J. McCracken, M. Salvato, T. Schrabback, N. Scoville, T. Smith, and J. E. Taylor, "New constraints on the evolution of the stellar-to-dark matter connection: A combined analysis of galaxy–galaxy lensing, clustering, and stellar mass functions from z = 0.2 to z = 1*," *The Astrophysical Journal*, vol. 744, p. 159, dec 2011.

[10] D. Clowe, M. Bradač, A. H. Gonzalez, M. Markevitch, S. W. Randall, C. Jones, and D. Zaritsky, "A direct empirical proof of the existence of dark matter," *The Astrophysical Journal*, vol. 648, pp. L109–L113, aug 2006.

[11] Planck Collaboration, N. Aghanim, Y. Akrami, M. Ashdown, J. Aumont, C. Baccigalupi, M. Ballardini, A. J. Banday, R. B. Barreiro, N. Bartolo, S. Basak, R. Battye, K. Benabed, J. P. Bernard, M. Bersanelli, P. Bielewicz, J. J. Bock, J. R. Bond, J. Borrill, F. R. Bouchet, F. Boulanger, M. Bucher, C. Burigana, R. C. Butler, E. Calabrese, J. F. Cardoso, J. Carron, A. Challinor, H. C. Chiang, J. Chluba, L. P. L. Colombo, C. Combet, D. Contreras, B. P. Crill, F. Cuttaia, P. de Bernardis, G. de Zotti, J. Delabrouille, J. M. Delouis, E. Di Valentino, J. M. Diego, O. Doré, M. Douspis, A. Ducout, X. Dupac, S. Dusini, G. Efstathiou, F. Elsner, T. A. Enßlin, H. K. Eriksen, Y. Fantaye, M. Farhang, J. Fergusson, R. Fernandez-Cobos, F. Finelli, F. Forastieri, M. Frailis, A. A. Fraisse, E. Franceschi, A. Frolov, S. Galeotta, S. Galli, K. Ganga, R. T. Génova-Santos, M. Gerbino, T. Ghosh, J. González-Nuevo, K. M. Górski, S. Gratton, A. Gruppuso, J. E. Gudmundsson, J. Hamann, W. Handley, F. K. Hansen, D. Herranz, S. R. Hildebrandt, E. Hivon, Z. Huang, A. H. Jaffe, W. C. Jones, A. Karakci, E. Keihänen, R. Keskitalo, K. Kiiveri, J. Kim, T. S. Kisner, L. Knox, N. Krachmalnicoff, M. Kunz, H. Kurki-Suonio, G. Lagache, J. M. Lamarre, A. Lasenby, M. Lattanzi, C. R. Lawrence, M. Le Jeune, P. Lemos, J. Lesgourgues, F. Levrier, A. Lewis, M. Liguori, P. B. Lilje, M. Lilley, V. Lindholm, M. López-Caniego, P. M. Lubin, Y. Z. Ma, J. F. Macías-Pérez, G. Maggio, D. Maino, N. Mandolesi, A. Mangilli, A. Marcos-Caballero, M. Maris, P. G. Martin, M. Martinelli, E. Martínez-González, S. Matarrese, N. Mauri, J. D. McEwen, P. R. Meinhold, A. Melchiorri, A. Mennella, M. Migliaccio, M. Millea, S. Mitra, M. A. Miville-Deschênes, D. Molinari, L. Montier, G. Morgante, A. Moss, P. Natoli, H. U. Nørgaard-Nielsen, L. Pagano, D. Paoletti, B. Partridge, G. Patanchon, H. V. Peiris, F. Perrotta, V. Pettorino, F. Piacentini, L. Polastri, G. Polenta, J. L. Puget, J. P. Rachen, M. Reinecke, M. Remazeilles, A. Renzi, G. Rocha, C. Rosset, G. Roudier, J. A. Rubiño-Martín, B. Ruiz-Granados, L. Salvati, M. Sandri, M. Savelainen, D. Scott, E. P. S. Shellard, C. Sirignano, G. Sirri, L. D. Spencer, R. Sunyaev, A. S. Suur-Uski, J. A. Tauber, D. Tavagnacco, M. Tenti, L. Toffolatti, M. Tomasi, T. Trombetti, L. Valenziano, J. Valiviita, B. Van Tent, L. Vibert, P. Vielva, F. Villa, N. Vittorio, B. D. Wandelt, I. K. Wehus, M. White, S. D. M. White, A. Zacchei, and A. Zonca, "Planck 2018 results. VI. Cosmological parameters," *"Astron. Astrophys."*, vol. 641, p. A6, Sept. 2020.

[12] M. Davis, G. Efstathiou, C. S. Frenk, and S. D. White, "The evolution of large-scale structure in a universe dominated by cold dark matter," *Astrophysical Journal, Part 1 (ISSN 0004-637X), vol. 292, May 15, 1985, p. 371-394. Research supported by the Science and Engineering Research Council of England and NASA.*, vol. 292, pp. 371–394, 1985.

[13] G. R. Blumenthal, S. Faber, J. R. Primack, and M. J. Rees, "Formation of galaxies and large-scale structure with cold dark matter," *Nature*, vol. 311, no. 5986, pp. 517–525, 1984.

[14] C. J. Copi, D. N. Schramm, and M. S. Turner, "Big-bang nucleosynthesis and the baryon density of the universe," *Science*, vol. 267, no. 5195, pp. 192–199, 1995.

[15] K. Jedamzik and M. Pospelov, "Big Bang Nucleosynthesis and Particle Dark Matter," *New J. Phys.*, vol. 11, p. 105028, 2009.

[16] T. Lin, "Tasi lectures on dark matter models and direct detection," 2019.

[17] S. Tremaine and J. E. Gunn, "Dynamical role of light neutral leptons in cosmology," *Phys. Rev. Lett.*, vol. 42, pp. 407–410, Feb 1979.

[18] J. Preskill, M. B. Wise, and F. Wilczek, "Cosmology of the Invisible Axion," *Phys. Lett. B*, vol. 120, pp. 127–132, 1983.

[19] G. G. Di Cortona, E. Hardy, J. P. Vega, and G. Villadoro, "The qcd axion, precisely," *Journal of High Energy Physics*, vol. 2016, no. 1, pp. 1–37, 2016.

[20] A. Hook, "TASI Lectures on the Strong CP Problem and Axions," *PoS*, vol. TASI2018, p. 004, 2019.

[21] E. G. M. Ferreira, "Ultra-light dark matter," *Astron. Astrophys. Rev.*, vol. 29, no. 1, p. 7, 2021.

[22] L. Di Luzio, M. Giannotti, E. Nardi, and L. Visinelli, "The landscape of QCD axion models," *Phys. Rept.*, vol. 870, pp. 1–117, 2020.

[23] L. Roszkowski, E. M. Sessolo, and S. Trojanowski, "Wimp dark matter candidates and searches—current status and future prospects," *Reports on Progress in Physics*, vol. 81, no. 6, p. 066201, 2018.

[24] S. Dodelson and F. Schmidt, *Modern cosmology*. Academic press, 2020.

[25] G. Steigman, B. Dasgupta, and J. F. Beacom, "Precise Relic WIMP Abundance and its Impact on Searches for Dark Matter Annihilation," *Phys. Rev. D*, vol. 86, p. 023506, 2012.

[26] G. Jungman, M. Kamionkowski, and K. Griest, "Supersymmetric dark matter," *Physics Reports*, vol. 267, no. 5, pp. 195–373, 1996.

[27] G. Arcadi, M. Dutra, P. Ghosh, M. Lindner, Y. Mambrini, M. Pierre, S. Profumo, and F. S. Queiroz, "The waning of the wimp? a review of models, searches, and constraints," *The European Physical Journal C*, vol. 78, pp. 1–57, 2018.

[28] M. Pospelov, A. Ritz, and M. B. Voloshin, "Secluded WIMP Dark Matter," *Phys. Lett. B*, vol. 662, pp. 53–61, 2008.

[29] J. Alexander, M. Battaglieri, B. Echenard, R. Essig, M. Graham, E. Izaguirre, J. Jaros, G. Krnjaic, J. Mardon, D. Morrissey, T. Nelson, M. Perelstein, M. Pyle, A. Ritz, P. Schuster, B. Shuve, N. Toro, R. G. V. D. Water, D. Akerib, H. An, K. Aniol, I. J. Arnquist, D. M. Asner, H. O. Back, K. Baker, N. Baltzell, D. Banerjee, B. Batell, D. Bauer, J. Beacham, J. Benesch, J. Bjorken, N. Blinov, C. Boehm, M. Bondí, W. Bonivento, F. Bossi, S. J. Brodsky, R. Budnik, S. Bueltmann, M. H. Bukhari, R. Bunker, M. Carpinelli, C. Cartaro,

D. Cassel, G. Cavoto, A. Celentano, A. Chaterjee, S. Chaudhuri, G. Chiodini, H.-M. S. Cho, E. D. Church, D. A. Cooke, J. Cooley, R. Cooper, R. Corliss, P. Crivelli, F. Curciarello, A. D'Angelo, H. Davoudiasl, M. D. Napoli, R. D. Vita, A. Denig, P. deNiverville, A. Deshpande, R. Dharmapalan, B. Dobrescu, S. Donskov, R. Dupre, J. Estrada, S. Fegan, T. Ferber, C. Field, E. Figueroa-Feliciano, A. Filippi, B. Fornal, A. Freyberger, A. Friedland, I. Galon, S. Gardner, F.-X. Girod, S. Gninenko, A. Golutvin, S. Gori, C. Grab, E. Graziani, K. Griffioen, A. Haas, K. Harigaya, C. Hearty, S. Hertel, J. Hewett, A. Hime, D. Hitlin, Y. Hochberg, R. J. Holt, M. Holtrop, E. W. Hoppe, T. W. Hossbach, L. Hsu, P. Ilten, J. Incandela, G. Inguglia, K. Irwin, I. Jaegle, R. P. Johnson, Y. Kahn, G. Kalicy, Z.-B. Kang, V. Khachatryan, V. Kozhuharov, N. V. Krasnikov, V. Kubarovsky, E. Kuflik, N. Kurinsky, R. Laha, G. Lanfranchi, D. Li, T. Lin, M. Lisanti, K. Liu, M. Liu, B. Loer, D. Loomba, V. E. Lyubovitskij, A. Manalaysay, G. Mandaglio, J. Mans, W. J. Marciano, T. Markiewicz, L. Marsicano, T. Maruyama, V. A. Matveev, D. McKeen, B. McKinnon, D. McKinsey, H. Merkel, J. Mock, M. E. Monzani, O. Moreno, C. Nantais, S. Paul, M. Peskin, V. Poliakov, A. D. Polosa, M. Pospelov, I. Rachek, B. Radics, M. Raggi, N. Randazzo, B. Ratcliff, A. Rizzo, T. Rizzo, A. Robinson, A. Rubbia, D. Rubin, D. Rueter, T. Saab, E. Santopinto, R. Schnee, J. Shelton, G. Simi, A. Simonyan, V. Sipala, O. Slone, E. Smith, D. Snowden-Ifft, M. Solt, P. Sorensen, Y. Soreq, S. Spagnolo, J. Spencer, S. Stepanyan, J. Strube, M. Sullivan, A. S. Tadepalli, T. Tait, M. Taiuti, P. Tanedo, R. Tayloe, J. Thaler, N. V. Tran, S. Tulin, C. G. Tully, S. Uemura, M. Ungaro, P. Valente, H. Vance, J. Vavra, T. Volansky, B. von Krosigk, A. Whitbeck, M. Williams, P. Wittich, B. Wojtsekhowski, W. Xue, J. M. Yoon, H.-B. Yu, J. Yu, T.-T. Yu, Y. Zhang, Y. Zhao, Y. Zhong, and K. Zurek, "Dark Sectors 2016 Workshop: Community Report," 8 2016.

[30] M. Fabbrichesi, E. Gabrielli, and G. Lanfranchi, *The physics of the dark photon: a primer*. Springer, 2021.

[31] G. Arcadi, A. Djouadi, and M. Raidal, "Dark matter through the higgs portal," *Physics Reports*, vol. 842, pp. 1–180, 2020.

[32] L. Darmé, S. Rao, and L. Roszkowski, "Light dark higgs boson in minimal sub-gev dark matter scenarios," *Journal of High Energy Physics*, vol. 2018, no. 3, pp. 1–31, 2018.

[33] B. Dutta, S. Ghosh, and J. Kumar, "Sub-gev dark matter model," *Phys. Rev. D*, vol. 100, p. 075028, Oct 2019.

[34] S. Knapen, T. Lin, and K. M. Zurek, "Light Dark Matter: Models and Constraints," *Phys. Rev.*, vol. D96, no. 11, p. 115021, 2017.

[35] M. Schumann, "Direct detection of WIMP dark matter: concepts and status," *Journal of Physics G: Nuclear and Particle Physics*, vol. 46, p. 103003, aug 2019.

[36] J. Billard, M. Boulay, S. Cebriá n, L. Covi, G. Fiorillo, A. Green, J. Kopp, B. Majorovits, K. Palladino, F. Petricca, L. R. (chair), and M. Schumann, "Direct detection of dark matter—APPEC committee report," *Reports on Progress in Physics*, vol. 85, p. 056201, apr 2022.

[37] C. Chang, S. Derenzo, Y. Efremenko, W. Guo, S. Hertel, M. Garcia-Sciveres, R. Mahapatra, D. N. McKinsey, B. Penning, M. Pyle, P. Sorenson, A. Suzuki, G. Wang, and K. Zurek, "The tesseract dark matter project, snowmass loi."

[38] S. L. Watkins, *Athermal Phonon Sensors in Searches for Light Dark Matter*. PhD thesis, UC, Berkeley (main), 2022.

[39] C. W. Fink, S. L. Watkins, T. Aramaki, P. L. Brink, S. Ganjam, B. A. Hines, M. E. Huber, N. A. Kurinsky, R. Mahapatra, N. Mirabolfathi, W. A. Page, R. Partridge, M. Platt, M. Pyle, B. Sadoulet, B. Serfass, and S. Zuber, "Characterizing TES power noise for future single optical-phonon and infrared-photon detectors," *AIP Advances*, vol. 10, p. 085221, 08 2020.

[40] C. Kittel, *Introduction to solid state physics*. John Wiley & sons, inc, 2005.

[41] S. Griffin, S. Knapen, T. Lin, and K. M. Zurek, "Directional Detection of Light Dark Matter with Polar Materials," *Phys. Rev.*, vol. D98, no. 11, p. 115034, 2018.

[42] B. Campbell-Deem, P. Cox, S. Knapen, T. Lin, and T. Melia, "Multiphonon excitations from dark matter scattering in crystals," *Phys. Rev. D*, vol. 101, no. 3, p. 036006, 2020. [Erratum: Phys.Rev.D 102, 019904(E) (2020)].

[43] Y. Kahn and T. Lin, "Searches for light dark matter using condensed matter systems," 8 2021.

[44] B. P. Abbott, R. Abbott, T. D. Abbott, M. R. Abernathy, F. Acernese, K. Ackley, C. Adams, T. Adams, P. Addesso, R. X. Adhikari, V. B. Adya, C. Affeldt, M. Agathos, K. Agatsuma, N. Aggarwal, O. D. Aguiar, L. Aiello, A. Ain, P. Ajith, B. Allen, A. Allocca, P. A. Altin, S. B. Anderson, W. G. Anderson, K. Arai, M. A. Arain, M. C. Araya, C. C. Arceneaux, J. S. Areeda, N. Arnaud, K. G. Arun, S. Ascenzi, G. Ashton, M. Ast, S. M. Aston, P. Astone, P. Aufmuth, C. Aulbert, S. Babak, P. Bacon, M. K. M. Bader, P. T. Baker, F. Baldaccini, G. Ballardin, S. W. Ballmer, J. C. Barayoga, S. E. Barclay, B. C. Barish, D. Barker, F. Barone, B. Barr, L. Barsotti, M. Barsuglia, D. Barta, J. Bartlett, M. A. Barton, I. Bartos, R. Bassiri, A. Basti, J. C. Batch, C. Baune, V. Bavigadda, M. Bazzan, B. Behnke, M. Bejger, C. Belczynski, A. S. Bell, C. J. Bell, B. K. Berger, J. Bergman, G. Bergmann, C. P. L. Berry, D. Bersanetti, A. Bertolini, J. Betzwieser, S. Bhagwat, R. Bhandare, I. A. Bilenko, G. Billingsley, J. Birch, R. Birney, O. Birnholtz, S. Biscans, A. Bisht, M. Bitossi, C. Biwer, M. A. Bizouard, J. K. Blackburn, C. D. Blair, D. G. Blair, R. M. Blair, S. Bloemen, O. Bock, T. P. Bodiya, M. Boer, G. Bogaert, C. Bogan, A. Bohe, P. Bojtos, C. Bond, F. Bondu, R. Bonnand, B. A. Boom, R. Bork, V. Boschi, S. Bose, Y. Bouffanais, A. Bozzi, C. Bradaschia, P. R. Brady, V. B. Braginsky, M. Branchesi, J. E. Brau, T. Briant, A. Brillet, M. Brinkmann, V. Brisson, P. Brockill, A. F. Brooks, D. A. Brown, D. D. Brown, N. M. Brown, C. C. Buchanan, A. Buikema, T. Bulik, H. J. Bulten, A. Buonanno, D. Buskulic, C. Buy, R. L. Byer, M. Cabero, L. Cadonati, G. Cagnoli, C. Cahillane, J. C. Bustillo, T. Callister, E. Calloni, J. B. Camp, K. C. Cannon, J. Cao, C. D. Capano, E. Capocasa, F. Carbognani, S. Caride, J. C. Diaz, C. Casentini, S. Caudill,

M. Cavaglià, F. Cavalier, R. Cavalieri, G. Cella, C. B. Cepeda, L. C. Baiardi, G. Cerretani, E. Cesarini, R. Chakraborty, T. Chalermsongsak, S. J. Chamberlin, M. Chan, S. Chao, P. Charlton, E. Chassande-Mottin, H. Y. Chen, Y. Chen, C. Cheng, A. Chincarini, A. Chiummo, H. S. Cho, M. Cho, J. H. Chow, N. Christensen, Q. Chu, S. Chua, S. Chung, G. Ciani, F. Clara, J. A. Clark, F. Cleva, E. Coccia, P.-F. Cohadon, A. Colla, C. G. Collette, L. Cominsky, M. Constancio, A. Conte, L. Conti, D. Cook, T. R. Corbitt, N. Cornish, A. Corsi, S. Cortese, C. A. Costa, M. W. Coughlin, S. B. Coughlin, J.-P. Coulon, S. T. Countryman, P. Couvares, E. E. Cowan, D. M. Coward, M. J. Cowart, D. C. Coyne, R. Coyne, K. Craig, J. D. E. Creighton, T. D. Creighton, J. Cripe, S. G. Crowder, A. M. Cruise, A. Cumming, L. Cunningham, E. Cuoco, T. D. Canton, S. L. Danilishin, S. D'Antonio, K. Danzmann, N. S. Darman, C. F. Da Silva Costa, V. Dattilo, I. Dave, H. P. Daveloza, M. Davier, G. S. Davies, E. J. Daw, R. Day, S. De, D. DeBra, G. Debreczeni, J. Degallaix, M. De Laurentis, S. Deléglise, W. Del Pozzo, T. Denker, T. Dent, H. Dereli, V. Dergachev, R. T. DeRosa, R. De Rosa, R. DeSalvo, S. Dhurandhar, M. C. Díaz, L. Di Fiore, M. Di Giovanni, A. Di Lieto, S. Di Pace, I. Di Palma, A. Di Virgilio, G. Dojcinoski, V. Dolique, F. Donovan, K. L. Dooley, S. Doravari, R. Douglas, T. P. Downes, M. Drago, R. W. P. Drever, J. C. Driggers, Z. Du, M. Ducrot, S. E. Dwyer, T. B. Edo, M. C. Edwards, A. Effler, H.-B. Eggenstein, P. Ehrens, J. Eichholz, S. S. Eikenberry, W. Engels, R. C. Essick, T. Etzel, M. Evans, T. M. Evans, R. Everett, M. Factourovich, V. Fafone, H. Fair, S. Fairhurst, X. Fan, Q. Fang, S. Farinon, B. Farr, W. M. Farr, M. Favata, M. Fays, H. Fehrmann, M. M. Fejer, D. Feldbaum, I. Ferrante, E. C. Ferreira, F. Ferrini, F. Fidecaro, L. S. Finn, I. Fiori, D. Fiorucci, R. P. Fisher, R. Flaminio, M. Fletcher, H. Fong, J.-D. Fournier, S. Franco, S. Frasca, F. Frasconi, M. Frede, Z. Frei, A. Freise, R. Frey, V. Frey, T. T. Fricke, P. Fritschel, V. V. Frolov, P. Fulda, M. Fyffe, H. A. G. Gabbard, J. R. Gair, L. Gammaitoni, S. G. Gaonkar, F. Garufi, A. Gatto, G. Gaur, N. Gehrels, G. Gemme, B. Gendre, E. Genin, A. Gennai, J. George, L. Gergely, V. Germain, A. Ghosh, A. Ghosh, S. Ghosh, J. A. Giaime, K. D. Giardina, A. Giazotto, K. Gill, A. Glaefke, J. R. Gleason, E. Goetz, R. Goetz, L. Gondan, G. González, J. M. G. Castro, A. Gopakumar, N. A. Gordon, M. L. Gorodetsky, S. E. Gossan, M. Gosselin, R. Gouaty, C. Graef, P. B. Graff, M. Granata, A. Grant, S. Gras, C. Gray, G. Greco, A. C. Green, R. J. S. Greenhalgh, P. Groot, H. Grote, S. Grunewald, G. M. Guidi, X. Guo, A. Gupta, M. K. Gupta, K. E. Gushwa, E. K. Gustafson, R. Gustafson, J. J. Hacker, B. R. Hall, E. D. Hall, G. Hammond, M. Haney, M. M. Hanke, J. Hanks, C. Hanna, M. D. Hannam, J. Hanson, T. Hardwick, J. Harms, G. M. Harry, I. W. Harry, M. J. Hart, M. T. Hartman, C.-J. Haster, K. Haughian, J. Healy, J. Heefner, A. Heidmann, M. C. Heintze, G. Heinzel, H. Heitmann, P. Hello, G. Hemming, M. Hendry, I. S. Heng, J. Hennig, A. W. Heptonstall, M. Heurs, S. Hild, D. Hoak, K. A. Hodge, D. Hofman, S. E. Hollitt, K. Holt, D. E. Holz, P. Hopkins, D. J. Hosken, J. Hough, E. A. Houston, E. J. Howell, Y. M. Hu, S. Huang, E. A. Huerta, D. Huet, B. Hughey, S. Husa, S. H. Huttner, T. Huynh-Dinh, A. Idrisy, N. Indik, D. R. Ingram, R. Inta, H. N. Isa, J.-M. Isac, M. Isi, G. Islas, T. Isogai, B. R. Iyer, K. Izumi, M. B. Jacobson, T. Jacqmin, H. Jang, K. Jani, P. Jaranowski, S. Jawahar, F. Jiménez-Forteza, W. W. Johnson, N. K. Johnson-McDaniel, D. I. Jones, R. Jones, R. J. G. Jonker, L. Ju, K. Haris, C. V. Kalaghatgi, V. Kalogera, S. Kandhasamy, G. Kang, J. B. Kanner, S. Karki, M. Kasprzack, E. Katsavounidis, W. Katzman, S. Kaufer, T. Kaur, K. Kawabe, F. Kawazoe,

F. Kéfélian, M. S. Kehl, D. Keitel, D. B. Kelley, W. Kells, R. Kennedy, D. G. Keppel, J. S. Key, A. Khalaidovski, F. Y. Khalili, I. Khan, S. Khan, Z. Khan, E. A. Khazanov, N. Kijbunchoo, C. Kim, J. Kim, K. Kim, N.-G. Kim, N. Kim, Y.-M. Kim, E. J. King, P. J. King, D. L. Kinzel, J. S. Kissel, L. Kleybolte, S. Klimenko, S. M. Koehlenbeck, K. Kokeyama, S. Koley, V. Kondrashov, A. Kontos, S. Koranda, M. Korobko, W. Z. Korth, I. Kowalska, D. B. Kozak, V. Kringel, B. Krishnan, A. Królak, C. Krueger, G. Kuehn, P. Kumar, R. Kumar, L. Kuo, A. Kutynia, P. Kwee, B. D. Lackey, M. Landry, J. Lange, B. Lantz, P. D. Lasky, A. Lazzarini, C. Lazzaro, P. Leaci, S. Leavey, E. O. Lebigot, C. H. Lee, H. K. Lee, H. M. Lee, K. Lee, A. Lenon, M. Leonardi, J. R. Leong, N. Leroy, N. Letendre, Y. Levin, B. M. Levine, T. G. F. Li, A. Libson, T. B. Littenberg, N. A. Lockerbie, J. Logue, A. L. Lombardi, L. T. London, J. E. Lord, M. Lorenzini, V. Loriette, M. Lormand, G. Losurdo, J. D. Lough, C. O. Lousto, G. Lovelace, H. Lück, A. P. Lundgren, J. Luo, R. Lynch, Y. Ma, T. MacDonald, B. Machenschalk, M. MacInnis, D. M. Macleod, F. Magaña Sandoval, R. M. Magee, M. Mageswaran, E. Majorana, I. Maksimovic, V. Malvezzi, N. Man, I. Mandel, V. Mandic, V. Mangano, G. L. Mansell, M. Manske, M. Mantovani, F. Marchesoni, F. Marion, S. Márka, Z. Márka, A. S. Markosyan, E. Maros, F. Martelli, L. Martellini, I. W. Martin, R. M. Martin, D. V. Martynov, J. N. Marx, K. Mason, A. Masserot, T. J. Massinger, M. Masso-Reid, F. Matichard, L. Matone, N. Mavalvala, N. Mazumder, G. Mazzolo, R. McCarthy, D. E. McClelland, S. McCormick, S. C. McGuire, G. McIntyre, J. McIver, D. J. McManus, S. T. McWilliams, D. Meacher, G. D. Meadors, J. Meidam, A. Melatos, G. Mendell, D. Mendoza-Gandara, R. A. Mercer, E. Merilh, M. Merzougui, S. Meshkov, C. Messenger, C. Messick, P. M. Meyers, F. Mezzani, H. Miao, C. Michel, H. Middleton, E. E. Mikhailov, L. Milano, J. Miller, M. Millhouse, Y. Minenkov, J. Ming, S. Mirshekari, C. Mishra, S. Mitra, V. P. Mitrofanov, G. Mitselmakher, R. Mittleman, A. Moggi, M. Mohan, S. R. P. Mohapatra, M. Montani, B. C. Moore, C. J. Moore, D. Moraru, G. Moreno, S. R. Morriss, K. Mossavi, B. Mours, C. M. Mow-Lowry, C. L. Mueller, G. Mueller, A. W. Muir, A. Mukherjee, D. Mukherjee, S. Mukherjee, N. Mukund, A. Mullavey, J. Munch, D. J. Murphy, P. G. Murray, A. Mytidis, I. Nardecchia, L. Naticchioni, R. K. Nayak, V. Necula, K. Nedkova, G. Nelemans, M. Neri, A. Neunzert, G. Newton, T. T. Nguyen, A. B. Nielsen, S. Nissanke, A. Nitz, F. Nocera, D. Nolting, M. E. N. Normandin, L. K. Nuttall, J. Oberling, E. Ochsner, J. O'Dell, E. Oelker, G. H. Ogin, J. J. Oh, S. H. Oh, F. Ohme, M. Oliver, P. Oppermann, R. J. Oram, B. O'Reilly, R. O'Shaughnessy, C. D. Ott, D. J. Ottaway, R. S. Ottens, H. Overmier, B. J. Owen, A. Pai, S. A. Pai, J. R. Palamos, O. Palashov, C. Palomba, A. Pal-Singh, H. Pan, Y. Pan, C. Pankow, F. Pannarale, B. C. Pant, F. Paoletti, A. Paoli, M. A. Papa, H. R. Paris, W. Parker, D. Pascucci, A. Pasqualetti, R. Passaquieti, D. Passuello, B. Patricelli, Z. Patrick, B. L. Pearlstone, M. Pedraza, R. Pedurand, L. Pekowsky, A. Pele, S. Penn, A. Perreca, H. P. Pfeiffer, M. Phelps, O. Piccinni, M. Pichot, M. Pickenpack, F. Piergiovanni, V. Pierro, G. Pillant, L. Pinard, I. M. Pinto, M. Pitkin, J. H. Poeld, R. Poggiani, P. Popolizio, A. Post, J. Powell, J. Prasad, V. Predoi, S. S. Premachandra, T. Prestegard, L. R. Price, M. Prijatelj, M. Principe, S. Privitera, R. Prix, G. A. Prodi, L. Prokhorov, O. Puncken, M. Punturo, P. Puppo, M. Pürrer, H. Qi, J. Qin, V. Quetschke, E. A. Quintero, R. Quitzow-James, F. J. Raab, D. S. Rabeling, H. Radkins, P. Raffai, S. Raja, M. Rakhmanov, C. R. Ramet, P. Rapagnani, V. Raymond, M. Razzano, V. Re, J. Read, C. M. Reed, T. Regimbau, L. Rei, S. Reid, D. H. Reitze,

H. Rew, S. D. Reyes, F. Ricci, K. Riles, N. A. Robertson, R. Robie, F. Robinet, A. Rocchi, L. Rolland, J. G. Rollins, V. J. Roma, J. D. Romano, R. Romano, G. Romanov, J. H. Romie, D. Rosińska, S. Rowan, A. Rüdiger, P. Ruggi, K. Ryan, S. Sachdev, T. Sadecki, L. Sadeghian, L. Salconi, M. Saleem, F. Salemi, A. Samajdar, L. Sammut, L. M. Sampson, E. J. Sanchez, V. Sandberg, B. Sandeen, G. H. Sanders, J. R. Sanders, B. Sassolas, B. S. Sathyaprakash, P. R. Saulson, O. Sauter, R. L. Savage, A. Sawadsky, P. Schale, R. Schilling, J. Schmidt, P. Schmidt, R. Schnabel, R. M. S. Schofield, A. Schönbeck, E. Schreiber, D. Schuette, B. F. Schutz, J. Scott, S. M. Scott, D. Sellers, A. S. Sengupta, D. Sentenac, V. Sequino, A. Sergeev, G. Serna, Y. Setyawati, A. Sevigny, D. A. Shaddock, T. Shaffer, S. Shah, M. S. Shahriar, M. Shaltev, Z. Shao, B. Shapiro, P. Shawhan, A. Sheperd, D. H. Shoemaker, D. M. Shoemaker, K. Siellez, X. Siemens, D. Sigg, A. D. Silva, D. Simakov, A. Singer, L. P. Singer, A. Singh, R. Singh, A. Singhal, A. M. Sintes, B. J. J. Slagmolen, J. R. Smith, M. R. Smith, N. D. Smith, R. J. E. Smith, E. J. Son, B. Sorazu, F. Sorrentino, T. Souradeep, A. K. Srivastava, A. Staley, M. Steinke, J. Steinlechner, S. Steinlechner, D. Steinmeyer, B. C. Stephens, S. P. Stevenson, R. Stone, K. A. Strain, N. Straniero, G. Stratta, N. A. Strauss, S. Strigin, R. Sturani, A. L. Stuver, T. Z. Summerscales, L. Sun, P. J. Sutton, B. L. Swinkels, M. J. Szczepańczyk, M. Tacca, D. Talukder, D. B. Tanner, M. Tápai, S. P. Tarabrin, A. Taracchini, R. Taylor, T. Theeg, M. P. Thirugnanasambandam, E. G. Thomas, M. Thomas, P. Thomas, K. A. Thorne, K. S. Thorne, E. Thrane, S. Tiwari, V. Tiwari, K. V. Tokmakov, C. Tomlinson, M. Tonelli, C. V. Torres, C. I. Torrie, D. Töyrä, F. Travasso, G. Traylor, D. Trifirò, M. C. Tringali, L. Trozzo, M. Tse, M. Turconi, D. Tuyenbayev, D. Ugolini, C. S. Unnikrishnan, A. L. Urban, S. A. Usman, H. Vahlbruch, G. Vajente, G. Valdes, M. Vallisneri, N. van Bakel, M. van Beuzekom, J. F. J. van den Brand, C. Van Den Broeck, D. C. Vander-Hyde, L. van der Schaaf, J. V. van Heijningen, A. A. van Veggel, M. Vardaro, S. Vass, M. Vasúth, R. Vaulin, A. Vecchio, G. Vedovato, J. Veitch, P. J. Veitch, K. Venkateswara, D. Verkindt, F. Vetrano, A. Viceré, S. Vinciguerra, D. J. Vine, J.-Y. Vinet, S. Vitale, T. Vo, H. Vocca, C. Vorvick, D. Voss, W. D. Vousden, S. P. Vyatchanin, A. R. Wade, L. E. Wade, M. Wade, S. J. Waldman, M. Walker, L. Wallace, S. Walsh, G. Wang, H. Wang, M. Wang, X. Wang, Y. Wang, H. Ward, R. L. Ward, J. Warner, M. Was, B. Weaver, L.-W. Wei, M. Weinert, A. J. Weinstein, R. Weiss, T. Welborn, L. Wen, P. Weßels, T. Westphal, K. Wette, J. T. Whelan, S. E. Whitcomb, D. J. White, B. F. Whiting, K. Wiesner, C. Wilkinson, P. A. Willems, L. Williams, R. D. Williams, A. R. Williamson, J. L. Willis, B. Willke, M. H. Wimmer, L. Winkelmann, W. Winkler, C. C. Wipf, A. G. Wiseman, H. Wittel, G. Woan, J. Worden, J. L. Wright, G. Wu, J. Yablon, I. Yakushin, W. Yam, H. Yamamoto, C. C. Yancey, M. J. Yap, H. Yu, M. Yvert, A. Zadrożny, L. Zangrando, M. Zanolin, J.-P. Zendri, M. Zevin, F. Zhang, L. Zhang, M. Zhang, Y. Zhang, C. Zhao, M. Zhou, Z. Zhou, X. J. Zhu, M. E. Zucker, S. E. Zuraw, and J. Zweizig, "Observation of gravitational waves from a binary black hole merger," *Phys. Rev. Lett.*, vol. 116, p. 061102, Feb 2016.

[45] B. P. Abbott, R. Abbott, T. D. Abbott, S. Abraham, F. Acernese, K. Ackley, C. Adams, R. X. Adhikari, V. B. Adya, C. Affeldt, M. Agathos, K. Agatsuma, N. Aggarwal, O. D. Aguiar, L. Aiello, A. Ain, P. Ajith, G. Allen, A. Allocca, M. A. Aloy, P. A. Altin, A. Amato, A. Ananyeva, S. B. Anderson, W. G. Anderson, S. V. Angelova, S. Antier, S. Appert,

K. Arai, M. C. Araya, J. S. Areeda, M. Arène, N. Arnaud, K. G. Arun, S. Ascenzi, G. Ashton, S. M. Aston, P. Astone, F. Aubin, P. Aufmuth, K. AultONeal, C. Austin, V. Avendano, A. Avila-Alvarez, S. Babak, P. Bacon, F. Badaracco, M. K. M. Bader, S. Bae, P. T. Baker, F. Baldaccini, G. Ballardin, S. W. Ballmer, S. Banagiri, J. C. Barayoga, S. E. Barclay, B. C. Barish, D. Barker, K. Barkett, S. Barnum, F. Barone, B. Barr, L. Barsotti, M. Barsuglia, D. Barta, J. Bartlett, I. Bartos, R. Bassiri, A. Basti, M. Bawaj, J. C. Bayley, M. Bazzan, B. Bécsy, M. Bejger, I. Belahcene, A. S. Bell, D. Beniwal, B. K. Berger, G. Bergmann, S. Bernuzzi, J. J. Bero, C. P. L. Berry, D. Bersanetti, A. Bertolini, J. Betzwieser, R. Bhandare, J. Bidler, I. A. Bilenko, S. A. Bilgili, G. Billingsley, J. Birch, R. Birney, O. Birnholtz, S. Biscans, S. Biscoveanu, A. Bisht, M. Bitossi, M. A. Bizouard, J. K. Blackburn, J. Blackman, C. D. Blair, D. G. Blair, R. M. Blair, S. Bloemen, N. Bode, M. Boer, Y. Boetzel, G. Bogaert, F. Bondu, E. Bonilla, R. Bonnand, P. Booker, B. A. Boom, C. D. Booth, R. Bork, V. Boschi, S. Bose, K. Bossie, V. Bossilkov, J. Bosveld, Y. Bouffanais, A. Bozzi, C. Bradaschia, P. R. Brady, A. Bramley, M. Branchesi, J. E. Brau, T. Briant, J. H. Briggs, F. Brighenti, A. Brillet, M. Brinkmann, V. Brisson, P. Brockill, A. F. Brooks, D. D. Brown, S. Brunett, A. Buikema, T. Bulik, H. J. Bulten, A. Buonanno, D. Buskulic, M. J. Bustamante Rosell, C. Buy, R. L. Byer, M. Cabero, L. Cadonati, G. Cagnoli, C. Cahillane, J. Calderón Bustillo, T. A. Callister, E. Calloni, J. B. Camp, W. A. Campbell, M. Canepa, K. C. Cannon, H. Cao, J. Cao, E. Capocasa, F. Carbognani, S. Caride, M. F. Carney, G. Carullo, J. Casanueva Diaz, C. Casentini, S. Caudill, M. Cavaglià, F. Cavalier, R. Cavalieri, G. Cella, P. Cerdá-Durán, G. Cerretani, E. Cesarini, O. Chaibi, K. Chakravarti, S. J. Chamberlin, M. Chan, S. Chao, P. Charlton, E. A. Chase, E. Chassande-Mottin, D. Chatterjee, M. Chaturvedi, K. Chatziioannou, B. D. Cheeseboro, H. Y. Chen, X. Chen, Y. Chen, H.-P. Cheng, C. K. Cheong, H. Y. Chia, A. Chincarini, A. Chiummo, G. Cho, H. S. Cho, M. Cho, N. Christensen, Q. Chu, S. Chua, K. W. Chung, S. Chung, G. Ciani, A. A. Ciobanu, R. Ciolfi, F. Cipriano, A. Cirone, F. Clara, J. A. Clark, P. Clearwater, F. Cleva, C. Cocchieri, E. Coccia, P.-F. Cohadon, D. Cohen, R. Colgan, M. Colleoni, C. G. Collette, C. Collins, L. R. Cominsky, M. Constancio, L. Conti, S. J. Cooper, P. Corban, T. R. Corbitt, I. Cordero-Carrión, K. R. Corley, N. Cornish, A. Corsi, S. Cortese, C. A. Costa, R. Cotesta, M. W. Coughlin, S. B. Coughlin, J.-P. Coulon, S. T. Countryman, P. Couvares, P. B. Covas, E. E. Cowan, D. M. Coward, M. J. Cowart, D. C. Coyne, R. Coyne, J. D. E. Creighton, T. D. Creighton, J. Cripe, M. Croquette, S. G. Crowder, T. J. Cullen, A. Cumming, L. Cunningham, E. Cuoco, T. D. Canton, G. Dálya, S. L. Danilishin, S. D'Antonio, K. Danzmann, A. Dasgupta, C. F. Da Silva Costa, L. E. H. Datrier, V. Dattilo, I. Dave, M. Davier, D. Davis, E. J. Daw, D. DeBra, M. Deenadayalan, J. Degallaix, M. De Laurentis, S. Deléglise, W. Del Pozzo, L. M. DeMarchi, N. Demos, T. Dent, R. De Pietri, J. Derby, R. De Rosa, C. De Rossi, R. DeSalvo, O. de Varona, S. Dhurandhar, M. C. Díaz, T. Dietrich, L. Di Fiore, M. Di Giovanni, T. Di Girolamo, A. Di Lieto, B. Ding, S. Di Pace, I. Di Palma, F. Di Renzo, A. Dmitriev, Z. Doctor, F. Donovan, K. L. Dooley, S. Doravari, I. Dorrington, T. P. Downes, M. Drago, J. C. Driggers, Z. Du, J.-G. Ducoin, P. Dupej, S. E. Dwyer, P. J. Easter, T. B. Edo, M. C. Edwards, A. Effler, P. Ehrens, J. Eichholz, S. S. Eikenberry, M. Eisenmann, R. A. Eisenstein, R. C. Essick, H. Estelles, D. Estevez, Z. B. Etienne, T. Etzel, M. Evans, T. M. Evans, V. Fafone, H. Fair, S. Fairhurst, X. Fan, S. Farinon, B. Farr, W. M. Farr, E. J.

Fauchon-Jones, M. Favata, M. Fays, M. Fazio, C. Fee, J. Feicht, M. M. Fejer, F. Feng, A. Fernandez-Galiana, I. Ferrante, E. C. Ferreira, T. A. Ferreira, F. Ferrini, F. Fidecaro, I. Fiori, D. Fiorucci, M. Fishbach, R. P. Fisher, J. M. Fishner, M. Fitz-Axen, R. Flaminio, M. Fletcher, E. Flynn, H. Fong, J. A. Font, P. W. F. Forsyth, J.-D. Fournier, S. Frasca, F. Frasconi, Z. Frei, A. Freise, R. Frey, V. Frey, P. Fritschel, V. V. Frolov, P. Fulda, M. Fyffe, H. A. Gabbard, B. U. Gadre, S. M. Gaebel, J. R. Gair, L. Gammaitoni, M. R. Ganija, S. G. Gaonkar, A. Garcia, C. García-Quirós, F. Garufi, B. Gateley, S. Gaudio, G. Gaur, V. Gayathri, G. Gemme, E. Genin, A. Gennai, D. George, J. George, L. Gergely, V. Germain, S. Ghonge, A. Ghosh, A. Ghosh, S. Ghosh, B. Giacomazzo, J. A. Giaime, K. D. Giardina, A. Giazotto, K. Gill, G. Giordano, L. Glover, P. Godwin, E. Goetz, R. Goetz, B. Goncharov, G. González, J. M. Gonzalez Castro, A. Gopakumar, M. L. Gorodetsky, S. E. Gossan, M. Gosselin, R. Gouaty, A. Grado, C. Graef, M. Granata, A. Grant, S. Gras, P. Grassia, C. Gray, R. Gray, G. Greco, A. C. Green, R. Green, E. M. Gretarsson, P. Groot, H. Grote, S. Grunewald, P. Gruning, G. M. Guidi, H. K. Gulati, Y. Guo, A. Gupta, M. K. Gupta, E. K. Gustafson, R. Gustafson, L. Haegel, O. Halim, B. R. Hall, E. D. Hall, E. Z. Hamilton, G. Hammond, M. Haney, M. M. Hanke, J. Hanks, C. Hanna, M. D. Hannam, O. A. Hannuksela, J. Hanson, T. Hardwick, K. Haris, J. Harms, G. M. Harry, I. W. Harry, C.-J. Haster, K. Haughian, F. J. Hayes, J. Healy, A. Heidmann, M. C. Heintze, H. Heitmann, P. Hello, G. Hemming, M. Hendry, I. S. Heng, J. Hennig, A. W. Heptonstall, F. Hernandez Vivanco, M. Heurs, S. Hild, T. Hinderer, D. Hoak, S. Hochheim, D. Hofman, A. M. Holgado, N. A. Holland, K. Holt, D. E. Holz, P. Hopkins, C. Horst, J. Hough, E. J. Howell, C. G. Hoy, A. Hreibi, Y. Huang, E. A. Huerta, D. Huet, B. Hughey, M. Hulko, S. Husa, S. H. Huttner, T. Huynh-Dinh, B. Idzkowski, A. Iess, C. Ingram, R. Inta, G. Intini, B. Irwin, H. N. Isa, J.-M. Isac, M. Isi, B. R. Iyer, K. Izumi, T. Jacqmin, S. J. Jadhav, K. Jani, N. N. Janthalur, P. Jaranowski, A. C. Jenkins, J. Jiang, D. S. Johnson, N. K. Johnson-McDaniel, A. W. Jones, D. I. Jones, R. Jones, R. J. G. Jonker, L. Ju, J. Junker, C. V. Kalaghatgi, V. Kalogera, B. Kamai, S. Kandhasamy, G. Kang, J. B. Kanner, S. J. Kapadia, S. Karki, K. S. Karvinen, R. Kashyap, M. Kasprzack, S. Katsanevas, E. Katsavounidis, W. Katzman, S. Kaufer, K. Kawabe, N. V. Keerthana, F. Kéfélian, D. Keitel, R. Kennedy, J. S. Key, F. Y. Khalili, H. Khan, I. Khan, S. Khan, Z. Khan, E. A. Khazanov, M. Khursheed, N. Kijbunchoo, C. Kim, J. C. Kim, K. Kim, W. Kim, W. S. Kim, Y.-M. Kim, C. Kimball, E. J. King, P. J. King, M. Kinley-Hanlon, R. Kirchhoff, J. S. Kissel, L. Kleybolte, J. H. Klika, S. Klimenko, T. D. Knowles, P. Koch, S. M. Koehlenbeck, G. Koekoek, S. Koley, V. Kondrashov, A. Kontos, N. Koper, M. Korobko, W. Z. Korth, I. Kowalska, D. B. Kozak, V. Kringel, N. Krishnendu, A. Królak, G. Kuehn, A. Kumar, P. Kumar, R. Kumar, S. Kumar, L. Kuo, A. Kutynia, S. Kwang, B. D. Lackey, K. H. Lai, T. L. Lam, M. Landry, B. B. Lane, R. N. Lang, J. Lange, B. Lantz, R. K. Lanza, A. Lartaux-Vollard, P. D. Lasky, M. Laxen, A. Lazzarini, C. Lazzaro, P. Leaci, S. Leavey, Y. K. Lecoeuche, C. H. Lee, H. K. Lee, H. M. Lee, H. W. Lee, J. Lee, K. Lee, J. Lehmann, A. Lenon, N. Leroy, N. Letendre, Y. Levin, J. Li, K. J. L. Li, T. G. F. Li, X. Li, F. Lin, F. Linde, S. D. Linker, T. B. Littenberg, J. Liu, X. Liu, R. K. L. Lo, N. A. Lockerbie, L. T. London, A. Longo, M. Lorenzini, V. Loriette, M. Lormand, G. Losurdo, J. D. Lough, C. O. Lousto, G. Lovelace, M. E. Lower, H. Lück, D. Lumaca, A. P. Lundgren, R. Lynch, Y. Ma, R. Macas, S. Macfoy, M. MacInnis, D. M. Macleod, A. Macquet, F. Magaña Sandoval,

L. Magaña Zertuche, R. M. Magee, E. Majorana, I. Maksimovic, A. Malik, N. Man, V. Mandic, V. Mangano, G. L. Mansell, M. Manske, M. Mantovani, F. Marchesoni, F. Marion, S. Márka, Z. Márka, C. Markakis, A. S. Markosyan, A. Markowitz, E. Maros, A. Marquina, S. Marsat, F. Martelli, I. W. Martin, R. M. Martin, D. V. Martynov, K. Mason, E. Massera, A. Masserot, T. J. Massinger, M. Masso-Reid, S. Mastrogiovanni, A. Matas, F. Matichard, L. Matone, N. Mavalvala, N. Mazumder, J. J. McCann, R. McCarthy, D. E. McClelland, S. McCormick, L. McCuller, S. C. McGuire, J. McIver, D. J. McManus, T. McRae, S. T. McWilliams, D. Meacher, G. D. Meadors, M. Mehmet, A. K. Mehta, J. Meidam, A. Melatos, G. Mendell, R. A. Mercer, L. Mereni, E. L. Merilh, M. Merzougui, S. Meshkov, C. Messenger, C. Messick, R. Metzdorff, P. M. Meyers, H. Miao, C. Michel, H. Middleton, E. E. Mikhailov, L. Milano, A. L. Miller, A. Miller, M. Millhouse, J. C. Mills, M. C. Milovich-Goff, O. Minazzoli, Y. Minenkov, A. Mishkin, C. Mishra, T. Mistry, S. Mitra, V. P. Mitrofanov, G. Mitselmakher, R. Mittleman, G. Mo, D. Moffa, K. Mogushi, S. R. P. Mohapatra, M. Montani, C. J. Moore, D. Moraru, G. Moreno, S. Morisaki, B. Mours, C. M. Mow-Lowry, A. Mukherjee, D. Mukherjee, S. Mukherjee, N. Mukund, A. Mullavey, J. Munch, E. A. Muñiz, M. Muratore, P. G. Murray, A. Nagar, I. Nardecchia, L. Naticchioni, R. K. Nayak, J. Neilson, G. Nelemans, T. J. N. Nelson, M. Nery, A. Neunzert, K. Y. Ng, S. Ng, P. Nguyen, D. Nichols, A. B. Nielsen, S. Nissanke, A. Nitz, F. Nocera, C. North, L. K. Nuttall, M. Obergaulinger, J. Oberling, B. D. O'Brien, G. D. O'Dea, G. H. Ogin, J. J. Oh, S. H. Oh, F. Ohme, H. Ohta, M. A. Okada, M. Oliver, P. Oppermann, R. J. Oram, B. O'Reilly, R. G. Ormiston, L. F. Ortega, R. O'Shaughnessy, S. Ossokine, D. J. Ottaway, H. Overmier, B. J. Owen, A. E. Pace, G. Pagano, M. A. Page, A. Pai, S. A. Pai, J. R. Palamos, O. Palashov, C. Palomba, A. Pal-Singh, H.-W. Pan, B. Pang, P. T. H. Pang, C. Pankow, F. Pannarale, B. C. Pant, F. Paoletti, A. Paoli, M. A. Papa, A. Parida, W. Parker, D. Pascucci, A. Pasqualetti, R. Passaquieti, D. Passuello, M. Patil, B. Patricelli, B. L. Pearlstone, C. Pedersen, M. Pedraza, R. Pedurand, A. Pele, S. Penn, A. Perego, C. J. Perez, A. Perreca, H. P. Pfeiffer, M. Phelps, K. S. Phukon, O. J. Piccinni, M. Pichot, F. Piergiovanni, G. Pillant, L. Pinard, M. Pirello, M. Pitkin, R. Poggiani, D. Y. T. Pong, S. Ponrathnam, P. Popolizio, E. K. Porter, J. Powell, A. K. Prajapati, J. Prasad, K. Prasai, R. Prasanna, G. Pratten, T. Prestegard, S. Privitera, G. A. Prodi, L. G. Prokhorov, O. Puncken, M. Punturo, P. Puppo, M. Pürrer, H. Qi, V. Quetschke, P. J. Quinonez, E. A. Quintero, R. Quitzow-James, F. J. Raab, H. Radkins, N. Radulescu, P. Raffai, S. Raja, C. Rajan, B. Rajbhandari, M. Rakhmanov, K. E. Ramirez, A. Ramos-Buades, J. Rana, K. Rao, P. Rapagnani, V. Raymond, M. Razzano, J. Read, T. Regimbau, L. Rei, S. Reid, D. H. Reitze, W. Ren, F. Ricci, C. J. Richardson, J. W. Richardson, P. M. Ricker, G. M. Riemenschneider, K. Riles, M. Rizzo, N. A. Robertson, R. Robie, F. Robinet, A. Rocchi, L. Rolland, J. G. Rollins, V. J. Roma, M. Romanelli, R. Romano, C. L. Romel, J. H. Romie, K. Rose, D. Rosińska, S. G. Rosofsky, M. P. Ross, S. Rowan, A. Rüdiger, P. Ruggi, G. Rutins, K. Ryan, S. Sachdev, T. Sadecki, M. Sakellariadou, O. Salafia, L. Salconi, M. Saleem, F. Salemi, A. Samajdar, L. Sammut, E. J. Sanchez, L. E. Sanchez, N. Sanchis-Gual, V. Sandberg, J. R. Sanders, K. A. Santiago, N. Sarin, B. Sassolas, B. S. Sathyaprakash, P. R. Saulson, O. Sauter, R. L. Savage, P. Schale, M. Scheel, J. Scheuer, P. Schmidt, R. Schnabel, R. M. S. Schofield, A. Schönbeck, E. Schreiber, B. W. Schulte, B. F. Schutz, S. G. Schwalbe, J. Scott, S. M. Scott, E. Seidel, D. Sellers,

A. S. Sengupta, N. Sennett, D. Sentenac, V. Sequino, A. Sergeev, Y. Setyawati, D. A. Shaddock, T. Shaffer, M. S. Shahriar, M. B. Shaner, L. Shao, P. Sharma, P. Shawhan, H. Shen, R. Shink, D. H. Shoemaker, D. M. Shoemaker, S. ShyamSundar, K. Siellez, M. Sieniawska, D. Sigg, A. D. Silva, L. P. Singer, N. Singh, A. Singhal, A. M. Sintes, S. Sitmukhambetov, V. Skliris, B. J. J. Slagmolen, T. J. Slaven-Blair, J. R. Smith, R. J. E. Smith, S. Somala, E. J. Son, B. Sorazu, F. Sorrentino, T. Souradeep, E. Sowell, A. P. Spencer, A. K. Srivastava, V. Srivastava, K. Staats, C. Stachie, M. Standke, D. A. Steer, M. Steinke, J. Steinlechner, S. Steinlechner, D. Steinmeyer, S. P. Stevenson, D. Stocks, R. Stone, D. J. Stops, K. A. Strain, G. Stratta, S. E. Strigin, A. Strunk, R. Sturani, A. L. Stuver, V. Sudhir, T. Z. Summerscales, L. Sun, S. Sunil, J. Suresh, P. J. Sutton, B. L. Swinkels, M. J. Szczepańczyk, M. Tacca, S. C. Tait, C. Talbot, D. Talukder, D. B. Tanner, M. Tápai, A. Taracchini, J. D. Tasson, R. Taylor, F. Thies, M. Thomas, P. Thomas, S. R. Thondapu, K. A. Thorne, E. Thrane, S. Tiwari, S. Tiwari, V. Tiwari, K. Toland, M. Tonelli, Z. Tornasi, A. Torres-Forné, C. I. Torrie, D. Töyrä, F. Travasso, G. Traylor, M. C. Tringali, A. Trovato, L. Trozzo, R. Trudeau, K. W. Tsang, M. Tse, R. Tso, L. Tsukada, D. Tsuna, D. Tuyenbayev, K. Ueno, D. Ugolini, C. S. Unnikrishnan, A. L. Urban, S. A. Usman, H. Vahlbruch, G. Vajente, G. Valdes, N. van Bakel, M. van Beuzekom, J. F. J. van den Brand, C. Van Den Broeck, D. C. Vander-Hyde, J. V. van Heijningen, L. van der Schaaf, A. A. van Veggel, M. Vardaro, V. Varma, S. Vass, M. Vasúth, A. Vecchio, G. Vedovato, J. Veitch, P. J. Veitch, K. Venkateswara, G. Venugopalan, D. Verkindt, F. Vetrano, A. Viceré, A. D. Viets, D. J. Vine, J.-Y. Vinet, S. Vitale, T. Vo, H. Vocca, C. Vorvick, S. P. Vyatchanin, A. R. Wade, L. E. Wade, M. Wade, R. Walet, M. Walker, L. Wallace, S. Walsh, G. Wang, H. Wang, J. Z. Wang, W. H. Wang, Y. F. Wang, R. L. Ward, Z. A. Warden, J. Warner, M. Was, J. Watchi, B. Weaver, L.-W. Wei, M. Weinert, A. J. Weinstein, R. Weiss, F. Wellmann, L. Wen, E. K. Wessel, P. Weßels, J. W. Westhouse, K. Wette, J. T. Whelan, L. V. White, B. F. Whiting, C. Whittle, D. M. Wilken, D. Williams, A. R. Williamson, J. L. Willis, B. Willke, M. H. Wimmer, W. Winkler, C. C. Wipf, H. Wittel, G. Woan, J. Woehler, J. K. Wofford, J. Worden, J. L. Wright, D. S. Wu, D. M. Wysocki, L. Xiao, H. Yamamoto, C. C. Yancey, L. Yang, M. J. Yap, M. Yazback, D. W. Yeeles, H. Yu, H. Yu, S. H. R. Yuen, M. Yvert, A. K. Zadrożny, M. Zanolin, F. Zappa, T. Zelenova, J.-P. Zendri, M. Zevin, J. Zhang, L. Zhang, T. Zhang, C. Zhao, M. Zhou, Z. Zhou, X. J. Zhu, A. B. Zimmerman, Y. Zlochower, M. E. Zucker, and J. Zweizig, "Gwtc-1: A gravitational-wave transient catalog of compact binary mergers observed by ligo and virgo during the first and second observing runs," *Phys. Rev. X*, vol. 9, p. 031040, Sep 2019.

[46] R. Abbott, T. D. Abbott, S. Abraham, F. Acernese, K. Ackley, A. Adams, C. Adams, R. X. Adhikari, V. B. Adya, C. Affeldt, M. Agathos, K. Agatsuma, N. Aggarwal, O. D. Aguiar, L. Aiello, A. Ain, P. Ajith, S. Akcay, G. Allen, A. Allocca, P. A. Altin, A. Amato, S. Anand, A. Ananyeva, S. B. Anderson, W. G. Anderson, S. V. Angelova, S. Ansoldi, J. M. Antelis, S. Antier, S. Appert, K. Arai, M. C. Araya, J. S. Areeda, M. Arène, N. Arnaud, S. M. Aronson, K. G. Arun, Y. Asali, S. Ascenzi, G. Ashton, S. M. Aston, P. Astone, F. Aubin, P. Aufmuth, K. AultONeal, C. Austin, V. Avendano, S. Babak, F. Badaracco, M. K. M. Bader, S. Bae, A. M. Baer, S. Bagnasco, J. Baird, M. Ball, G. Ballardin, S. W. Ballmer, A. Bals, A. Balsamo, G. Baltus, S. Banagiri, D. Bankar, R. S. Bankar, J. C. Barayoga,

C. Barbieri, B. C. Barish, D. Barker, P. Barneo, S. Barnum, F. Barone, B. Barr, L. Barsotti, M. Barsuglia, D. Barta, J. Bartlett, I. Bartos, R. Bassiri, A. Basti, M. Bawaj, J. C. Bayley, M. Bazzan, B. R. Becher, B. Bécsy, V. M. Bedakihale, M. Bejger, I. Belahcene, D. Beniwal, M. G. Benjamin, T. F. Bennett, J. D. Bentley, F. Bergamin, B. K. Berger, G. Bergmann, S. Bernuzzi, C. P. L. Berry, D. Bersanetti, A. Bertolini, J. Betzwieser, R. Bhandare, A. V. Bhandari, D. Bhattacharjee, J. Bidler, I. A. Bilenko, G. Billingsley, R. Birney, O. Birnholtz, S. Biscans, M. Bischi, S. Biscoveanu, A. Bisht, M. Bitossi, M.-A. Bizouard, J. K. Blackburn, J. Blackman, C. D. Blair, D. G. Blair, R. M. Blair, O. Blanch, F. Bobba, N. Bode, M. Boer, Y. Boetzel, G. Bogaert, M. Boldrini, F. Bondu, E. Bonilla, R. Bonnand, P. Booker, B. A. Boom, R. Bork, V. Boschi, S. Bose, V. Bossilkov, V. Boudart, Y. Bouffanais, A. Bozzi, C. Bradaschia, P. R. Brady, A. Bramley, M. Branchesi, J. E. Brau, M. Breschi, T. Briant, J. H. Briggs, F. Brighenti, A. Brillet, M. Brinkmann, P. Brockill, A. F. Brooks, J. Brooks, D. D. Brown, S. Brunett, G. Bruno, R. Bruntz, A. Buikema, T. Bulik, H. J. Bulten, A. Buonanno, R. Buscicchio, D. Buskulic, R. L. Byer, M. Cabero, L. Cadonati, M. Caesar, G. Cagnoli, C. Cahillane, J. Calderón Bustillo, J. D. Callaghan, T. A. Callister, E. Calloni, J. B. Camp, M. Canepa, K. C. Cannon, H. Cao, J. Cao, G. Carapella, F. Carbognani, M. F. Carney, M. Carpinelli, G. Carullo, T. L. Carver, J. Casanueva Diaz, C. Casentini, S. Caudill, M. Cavaglià, F. Cavalier, R. Cavalieri, G. Cella, P. Cerdá-Durán, E. Cesarini, W. Chaibi, K. Chakravarti, C.-L. Chan, C. Chan, K. Chandra, P. Chanial, S. Chao, P. Charlton, E. A. Chase, E. Chassande-Mottin, D. Chatterjee, D. Chattopadhyay, M. Chaturvedi, K. Chatziioannou, A. Chen, H. Y. Chen, X. Chen, Y. Chen, H.-P. Cheng, C. K. Cheong, H. Y. Chia, F. Chiadini, R. Chierici, A. Chincarini, A. Chiummo, G. Cho, H. S. Cho, M. Cho, S. Choate, N. Christensen, Q. Chu, S. Chua, K. W. Chung, S. Chung, G. Ciani, P. Ciecielag, M. Cieślar, M. Cifaldi, A. A. Ciobanu, R. Ciolfi, F. Cipriano, A. Cirone, F. Clara, E. N. Clark, J. A. Clark, L. Clarke, P. Clearwater, S. Clesse, F. Cleva, E. Coccia, P.-F. Cohadon, D. E. Cohen, M. Colleoni, C. G. Collette, C. Collins, M. Colpi, M. Constancio, L. Conti, S. J. Cooper, P. Corban, T. R. Corbitt, I. Cordero-Carrión, S. Corezzi, K. R. Corley, N. Cornish, D. Corre, A. Corsi, S. Cortese, C. A. Costa, R. Cotesta, M. W. Coughlin, S. B. Coughlin, J.-P. Coulon, S. T. Countryman, B. Cousins, P. Couvares, P. B. Covas, D. M. Coward, M. J. Cowart, D. C. Coyne, R. Coyne, J. D. E. Creighton, T. D. Creighton, M. Croquette, S. G. Crowder, J. R. Cudell, T. J. Cullen, A. Cumming, R. Cummings, L. Cunningham, E. Cuoco, M. Curyło, T. D. Canton, G. Dálya, A. Dana, L. M. DaneshgaranBajastani, B. D'Angelo, B. Danila, S. L. Danilishin, S. D'Antonio, K. Danzmann, C. Darsow-Fromm, A. Dasgupta, L. E. H. Datrier, V. Dattilo, I. Dave, M. Davier, G. S. Davies, D. Davis, E. J. Daw, R. Dean, D. DeBra, M. Deenadayalan, J. Degallaix, M. De Laurentis, S. Deléglise, V. Del Favero, F. De Lillo, N. De Lillo, W. Del Pozzo, L. M. DeMarchi, F. De Matteis, V. D'Emilio, N. Demos, T. Denker, T. Dent, A. Depasse, R. De Pietri, R. De Rosa, C. De Rossi, R. DeSalvo, O. de Varona, S. Dhurandhar, M. C. Díaz, M. Diaz-Ortiz, N. A. Didio, T. Dietrich, L. Di Fiore, C. DiFronzo, C. Di Giorgio, F. Di Giovanni, M. Di Giovanni, T. Di Girolamo, A. Di Lieto, B. Ding, S. Di Pace, I. Di Palma, F. Di Renzo, A. K. Divakarla, A. Dmitriev, Z. Doctor, L. D'Onofrio, F. Donovan, K. L. Dooley, S. Doravari, I. Dorrington, T. P. Downes, M. Drago, J. C. Driggers, Z. Du, J.-G. Ducoin, P. Dupej, O. Durante, D. D'Urso, P.-A. Duverne, S. E. Dwyer, P. J. Easter, G. Eddolls, B. Edelman, T. B. Edo, O. Edy,

A. Effler, J. Eichholz, S. S. Eikenberry, M. Eisenmann, R. A. Eisenstein, A. Ejlli, L. Errico, R. C. Essick, H. Estellés, D. Estevez, Z. B. Etienne, T. Etzel, M. Evans, T. M. Evans, B. E. Ewing, V. Fafone, H. Fair, S. Fairhurst, X. Fan, A. M. Farah, S. Farinon, B. Farr, W. M. Farr, E. J. Fauchon-Jones, M. Favata, M. Fays, M. Fazio, J. Feicht, M. M. Fejer, F. Feng, E. Fenyvesi, D. L. Ferguson, A. Fernandez-Galiana, I. Ferrante, T. A. Ferreira, F. Fidecaro, P. Figura, I. Fiori, D. Fiorucci, M. Fishbach, R. P. Fisher, J. M. Fishner, R. Fittipaldi, M. Fitz-Axen, V. Fiumara, R. Flaminio, E. Floden, E. Flynn, H. Fong, J. A. Font, P. W. F. Forsyth, J.-D. Fournier, S. Frasca, F. Frasconi, Z. Frei, A. Freise, R. Frey, V. Frey, P. Fritschel, V. V. Frolov, G. G. Fronzé, P. Fulda, M. Fyffe, H. A. Gabbard, B. U. Gadre, S. M. Gaebel, J. R. Gair, J. Gais, S. Galaudage, R. Gamba, D. Ganapathy, A. Ganguly, S. G. Gaonkar, B. Garaventa, C. García-Quirós, F. Garufi, B. Gateley, S. Gaudio, V. Gayathri, G. Gemme, A. Gennai, D. George, J. George, R. N. George, L. Gergely, S. Ghonge, A. Ghosh, A. Ghosh, S. Ghosh, B. Giacomazzo, L. Giacoppo, J. A. Giaime, K. D. Giardina, D. R. Gibson, C. Gier, K. Gill, P. Giri, J. Glanzer, A. E. Gleckl, P. Godwin, E. Goetz, R. Goetz, N. Gohlke, B. Goncharov, G. González, A. Gopakumar, S. E. Gossan, M. Gosselin, R. Gouaty, B. Grace, A. Grado, M. Granata, V. Granata, A. Grant, S. Gras, P. Grassia, C. Gray, R. Gray, G. Greco, A. C. Green, R. Green, E. M. Gretarsson, H. L. Griggs, G. Grignani, A. Grimaldi, E. Grimes, S. J. Grimm, H. Grote, S. Grunewald, P. Gruning, J. G. Guerrero, G. M. Guidi, A. R. Guimaraes, G. Guixé, H. K. Gulati, Y. Guo, A. Gupta, A. Gupta, P. Gupta, E. K. Gustafson, R. Gustafson, F. Guzman, L. Haegel, O. Halim, E. D. Hall, E. Z. Hamilton, G. Hammond, M. Haney, M. M. Hanke, J. Hanks, C. Hanna, M. D. Hannam, O. A. Hannuksela, O. Hannuksela, H. Hansen, T. J. Hansen, J. Hanson, T. Harder, T. Hardwick, K. Haris, J. Harms, G. M. Harry, I. W. Harry, D. Hartwig, R. K. Hasskew, C.-J. Haster, K. Haughian, F. J. Hayes, J. Healy, A. Heidmann, M. C. Heintze, J. Heinze, J. Heinzel, H. Heitmann, F. Hellman, P. Hello, A. F. Helmling-Cornell, G. Hemming, M. Hendry, I. S. Heng, E. Hennes, J. Hennig, M. H. Hennig, F. Hernandez Vivanco, M. Heurs, S. Hild, P. Hill, A. S. Hines, S. Hochheim, E. Hofgard, D. Hofman, J. N. Hohmann, A. M. Holgado, N. A. Holland, I. J. Hollows, Z. J. Holmes, K. Holt, D. E. Holz, P. Hopkins, C. Horst, J. Hough, E. J. Howell, C. G. Hoy, D. Hoyland, Y. Huang, M. T. Hübner, A. D. Huddart, E. A. Huerta, B. Hughey, V. Hui, S. Husa, S. H. Huttner, B. M. Hutzler, R. Huxford, T. Huynh-Dinh, B. Idzkowski, A. Iess, S. Imperato, H. Inchauspe, C. Ingram, G. Intini, M. Isi, B. R. Iyer, V. Jaberian-Hamedan, T. Jacqmin, S. J. Jadhav, S. P. Jadhav, A. L. James, K. Jani, K. Janssens, N. N. Janthalur, P. Jaranowski, D. Jariwala, R. Jaume, A. C. Jenkins, M. Jeunon, J. Jiang, G. R. Johns, N. K. Johnson-McDaniel, A. W. Jones, D. I. Jones, J. D. Jones, P. Jones, R. Jones, R. J. G. Jonker, L. Ju, J. Junker, C. V. Kalaghatgi, V. Kalogera, B. Kamai, S. Kandhasamy, G. Kang, J. B. Kanner, S. J. Kapadia, D. P. Kapasi, C. Karathanasis, S. Karki, R. Kashyap, M. Kasprzack, W. Kastaun, S. Katsanevas, E. Katsavounidis, W. Katzman, K. Kawabe, F. Kéfélian, D. Keitel, J. S. Key, S. Khadka, F. Y. Khalili, I. Khan, S. Khan, E. A. Khazanov, N. Khetan, M. Khursheed, N. Kijbunchoo, C. Kim, G. J. Kim, J. C. Kim, K. Kim, W. S. Kim, Y.-M. Kim, C. Kimball, P. J. King, M. Kinley-Hanlon, R. Kirchhoff, J. S. Kissel, L. Kleybolte, S. Klimenko, T. D. Knowles, E. Knyazev, P. Koch, S. M. Koehlenbeck, G. Koekoek, S. Koley, M. Kolstein, K. Komori, V. Kondrashov, A. Kontos, N. Koper, M. Korobko, W. Z. Korth, M. Kovalam, D. B. Kozak, C. Krämer, V. Kringel, N. V. Kr-

ishnendu, A. Królak, G. Kuehn, A. Kumar, P. Kumar, R. Kumar, R. Kumar, K. Kuns, S. Kwang, B. D. Lackey, D. Laghi, E. Lalande, T. L. Lam, A. Lamberts, M. Landry, B. B. Lane, R. N. Lang, J. Lange, B. Lantz, R. K. Lanza, I. La Rosa, A. Lartaux-Vollard, P. D. Lasky, M. Laxen, A. Lazzarini, C. Lazzaro, P. Leaci, S. Leavey, Y. K. Lecoeuche, H. M. Lee, H. W. Lee, J. Lee, K. Lee, J. Lehmann, E. Leon, N. Leroy, N. Letendre, Y. Levin, A. Li, J. Li, K. J. L. Li, T. G. F. Li, X. Li, F. Linde, S. D. Linker, J. N. Linley, T. B. Littenberg, J. Liu, X. Liu, M. Llorens-Monteagudo, R. K. L. Lo, A. Lockwood, L. T. London, A. Longo, M. Lorenzini, V. Loriette, M. Lormand, G. Losurdo, J. D. Lough, C. O. Lousto, G. Lovelace, H. Lück, D. Lumaca, A. P. Lundgren, Y. Ma, R. Macas, M. MacInnis, D. M. Macleod, I. A. O. MacMillan, A. Macquet, I. Magaña Hernandez, F. Magaña Sandoval, C. Magazzù, R. M. Magee, E. Majorana, I. Maksimovic, S. Maliakal, A. Malik, N. Man, V. Mandic, V. Mangano, G. L. Mansell, M. Manske, M. Mantovani, M. Mapelli, F. Marchesoni, F. Marion, S. Márka, Z. Márka, C. Markakis, A. S. Markosyan, A. Markowitz, E. Maros, A. Marquina, S. Marsat, F. Martelli, I. W. Martin, R. M. Martin, M. Martinez, V. Martinez, D. V. Martynov, H. Masalehdan, K. Mason, E. Massera, A. Masserot, T. J. Massinger, M. Masso-Reid, S. Mastrogiovanni, A. Matas, M. Mateu-Lucena, F. Matichard, M. Matiushechkina, N. Mavalvala, E. Maynard, J. J. McCann, R. McCarthy, D. E. McClelland, S. McCormick, L. McCuller, S. C. McGuire, C. McIsaac, J. McIver, D. J. McManus, T. McRae, S. T. McWilliams, D. Meacher, G. D. Meadors, M. Mehmet, A. K. Mehta, A. Melatos, D. A. Melchor, G. Mendell, A. Menendez-Vazquez, R. A. Mercer, L. Mereni, K. Merfeld, E. L. Merilh, J. D. Merritt, M. Merzougui, S. Meshkov, C. Messenger, C. Messick, R. Metzdorff, P. M. Meyers, F. Meylahn, A. Mhaske, A. Miani, H. Miao, I. Michaloliakos, C. Michel, H. Middleton, L. Milano, A. L. Miller, M. Millhouse, J. C. Mills, E. Milotti, M. C. Milovich-Goff, O. Minazzoli, Y. Minenkov, L. M. Mir, A. Mishkin, C. Mishra, T. Mistry, S. Mitra, V. P. Mitrofanov, G. Mitselmakher, R. Mittleman, G. Mo, K. Mogushi, S. R. P. Mohapatra, S. R. Mohite, I. Molina, M. Molina-Ruiz, M. Mondin, M. Montani, C. J. Moore, D. Moraru, F. Morawski, G. Moreno, S. Morisaki, B. Mours, C. M. Mow-Lowry, S. Mozzon, F. Muciaccia, A. Mukherjee, D. Mukherjee, S. Mukherjee, S. Mukherjee, N. Mukund, A. Mullavey, J. Munch, E. A. Muñiz, P. G. Murray, S. L. Nadji, A. Nagar, I. Nardecchia, L. Naticchioni, R. K. Nayak, B. F. Neil, J. Neilson, G. Nelemans, T. J. N. Nelson, M. Nery, A. Neunzert, A. H. Nitz, K. Y. Ng, S. Ng, C. Nguyen, P. Nguyen, T. Nguyen, S. A. Nichols, S. Nissanke, F. Nocera, M. Noh, C. North, D. Nothard, L. K. Nuttall, J. Oberling, B. D. O'Brien, J. O'Dell, G. Oganesyan, G. H. Ogin, J. J. Oh, S. H. Oh, F. Ohme, H. Ohta, M. A. Okada, C. Olivetto, P. Oppermann, R. J. Oram, B. O'Reilly, R. G. Ormiston, L. F. Ortega, R. O'Shaughnessy, S. Ossokine, C. Osthelder, D. J. Ottaway, H. Overmier, B. J. Owen, A. E. Pace, G. Pagano, M. A. Page, G. Pagliaroli, A. Pai, S. A. Pai, J. R. Palamos, O. Palashov, C. Palomba, H. Pan, P. K. Panda, T. H. Pang, C. Pankow, F. Pannarale, B. C. Pant, F. Paoletti, A. Paoli, A. Paolone, W. Parker, D. Pascucci, A. Pasqualetti, R. Passaquieti, D. Passuello, M. Patel, B. Patricelli, E. Payne, T. C. Pechsiri, M. Pedraza, M. Pegoraro, A. Pele, S. Penn, A. Perego, C. J. Perez, C. Périgois, A. Perreca, S. Perriès, J. Petermann, D. Petterson, H. P. Pfeiffer, K. A. Pham, K. S. Phukon, O. J. Piccinni, M. Pichot, M. Piendibene, F. Piergiovanni, L. Pierini, V. Pierro, G. Pillant, F. Pilo, L. Pinard, I. M. Pinto, K. Piotrzkowski, M. Pirello, M. Pitkin, E. Placidi, W. Plastino, C. Pluchar, R. Poggiani, E. Polini, D. Y. T. Pong, S. Ponrathnam, P. Popolizio,

E. K. Porter, A. Poverman, J. Powell, M. Pracchia, A. K. Prajapati, K. Prasai, R. Prasanna, G. Pratten, T. Prestegard, M. Principe, G. A. Prodi, L. Prokhorov, P. Prosposito, L. Prudenzi, A. Puecher, M. Punturo, F. Puosi, P. Puppo, M. Pürrer, H. Qi, V. Quetschke, P. J. Quinonez, R. Quitzow-James, F. J. Raab, G. Raaijmakers, H. Radkins, N. Radulesco, P. Raffai, H. Rafferty, S. X. Rail, S. Raja, C. Rajan, B. Rajbhandari, M. Rakhmanov, K. E. Ramirez, T. D. Ramirez, A. Ramos-Buades, J. Rana, K. Rao, P. Rapagnani, U. D. Rapol, B. Ratto, V. Raymond, M. Razzano, J. Read, T. Regimbau, L. Rei, S. Reid, D. H. Reitze, P. Rettegno, F. Ricci, C. J. Richardson, J. W. Richardson, L. Richardson, P. M. Ricker, G. Riemenschneider, K. Riles, M. Rizzo, N. A. Robertson, F. Robinet, A. Rocchi, J. A. Rocha, S. Rodriguez, R. D. Rodriguez-Soto, L. Rolland, J. G. Rollins, V. J. Roma, M. Romanelli, R. Romano, C. L. Romel, A. Romero, I. M. Romero-Shaw, J. H. Romie, S. Ronchini, C. A. Rose, D. Rose, K. Rose, M. J. B. Rosell, D. Rosińska, S. G. Rosofsky, M. P. Ross, S. Rowan, S. J. Rowlinson, S. Roy, S. Roy, P. Ruggi, K. Ryan, S. Sachdev, T. Sadecki, J. Sadiq, M. Sakellariadou, O. S. Salafia, L. Salconi, M. Saleem, A. Samajdar, E. J. Sanchez, J. H. Sanchez, L. E. Sanchez, N. Sanchis-Gual, J. R. Sanders, L. Sandles, K. A. Santiago, E. Santos, T. R. Saravanan, N. Sarin, B. Sassolas, B. S. Sathyaprakash, O. Sauter, R. L. Savage, V. Savant, D. Sawant, S. Sayah, D. Schaetzl, P. Schale, M. Scheel, J. Scheuer, A. Schindler-Tyka, P. Schmidt, R. Schnabel, R. M. S. Schofield, A. Schönbeck, E. Schreiber, B. W. Schulte, B. F. Schutz, O. Schwarm, E. Schwartz, J. Scott, S. M. Scott, M. Seglar-Arroyo, E. Seidel, D. Sellers, A. S. Sengupta, N. Sennett, D. Sentenac, V. Sequino, A. Sergeev, Y. Setyawati, T. Shaffer, M. S. Shahriar, S. Sharifi, A. Sharma, P. Sharma, P. Shawhan, H. Shen, M. Shikauchi, R. Shink, D. H. Shoemaker, D. M. Shoemaker, K. Shukla, S. ShyamSundar, M. Sieniawska, D. Sigg, L. P. Singer, D. Singh, N. Singh, A. Singha, A. Singhal, A. M. Sintes, V. Sipala, V. Skliris, B. J. J. Slagmolen, T. J. Slaven-Blair, J. Smetana, J. R. Smith, R. J. E. Smith, S. N. Somala, E. J. Son, K. Soni, S. Soni, B. Sorazu, V. Sordini, F. Sorrentino, N. Sorrentino, R. Soulard, T. Souradeep, E. Sowell, A. P. Spencer, M. Spera, A. K. Srivastava, V. Srivastava, K. Staats, C. Stachie, D. A. Steer, J. Steinhoff, M. Steinke, J. Steinlechner, S. Steinlechner, D. Steinmeyer, S. P. Stevenson, G. Stolle-McAllister, D. J. Stops, M. Stover, K. A. Strain, G. Stratta, A. Strunk, R. Sturani, A. L. Stuver, J. Südbeck, S. Sudhagar, V. Sudhir, H. G. Suh, T. Z. Summerscales, H. Sun, L. Sun, S. Sunil, A. Sur, J. Suresh, P. J. Sutton, B. L. Swinkels, M. J. Szczepańczyk, M. Tacca, S. C. Tait, C. Talbot, A. J. Tanasijczuk, D. B. Tanner, D. Tao, A. Tapia, E. N. Tapia San Martin, J. D. Tasson, R. Taylor, R. Tenorio, L. Terkowski, M. P. Thirugnanasambandam, L. M. Thomas, M. Thomas, P. Thomas, J. E. Thompson, S. R. Thondapu, K. A. Thorne, E. Thrane, S. Tiwari, S. Tiwari, V. Tiwari, K. Toland, A. E. Tolley, M. Tonelli, Z. Tornasi, A. Torres-Forné, C. I. Torrie, I. T. e Melo, D. Töyrä, A. T. Tran, A. Trapananti, F. Travasso, G. Traylor, M. C. Tringali, A. Tripathee, A. Trovato, R. J. Trudeau, D. S. Tsai, K. W. Tsang, M. Tse, R. Tso, L. Tsukada, D. Tsuna, T. Tsutsui, M. Turconi, A. S. Ubhi, R. P. Udall, K. Ueno, D. Ugolini, C. S. Unnikrishnan, A. L. Urban, S. A. Usman, A. C. Utina, H. Vahlbruch, G. Vajente, A. Vajpeyi, G. Valdes, M. Valentini, V. Valsan, N. van Bakel, M. van Beuzekom, J. F. J. van den Brand, C. Van Den Broeck, D. C. Vander-Hyde, L. van der Schaaf, J. V. van Heijningen, M. Vardaro, A. F. Vargas, V. Varma, S. Vass, M. Vasúth, A. Vecchio, G. Vedovato, J. Veitch, P. J. Veitch, K. Venkateswara, J. Venneberg, G. Venugopalan, D. Verkindt, Y. Verma, D. Veske,

F. Vetrano, A. Viceré, A. D. Viets, A. Vijaykumar, V. Villa-Ortega, J.-Y. Vinet, S. Vitale, T. Vo, H. Vocca, C. Vorvick, S. P. Vyatchanin, A. R. Wade, L. E. Wade, M. Wade, R. C. Walet, M. Walker, G. S. Wallace, L. Wallace, S. Walsh, J. Z. Wang, S. Wang, W. H. Wang, Y. F. Wang, R. L. Ward, J. Warner, M. Was, N. Y. Washington, J. Watchi, B. Weaver, L. Wei, M. Weinert, A. J. Weinstein, R. Weiss, F. Wellmann, L. Wen, P. Weßels, J. W. Westhouse, K. Wette, J. T. Whelan, D. D. White, L. V. White, B. F. Whiting, C. Whittle, D. M. Wilken, D. Williams, M. J. Williams, A. R. Williamson, J. L. Willis, B. Willke, D. J. Wilson, M. H. Wimmer, W. Winkler, C. C. Wipf, G. Woan, J. Woehler, J. K. Wofford, I. C. F. Wong, J. Wrangel, J. L. Wright, D. S. Wu, D. M. Wysocki, L. Xiao, H. Yamamoto, L. Yang, Y. Yang, Z. Yang, M. J. Yap, D. W. Yeeles, A. Yoon, H. Yu, H. Yu, S. H. R. Yuen, A. Zadrożny, M. Zanolin, T. Zelenova, J.-P. Zendri, M. Zevin, J. Zhang, L. Zhang, R. Zhang, T. Zhang, C. Zhao, G. Zhao, Y. Zheng, M. Zhou, Z. Zhou, X. J. Zhu, A. B. Zimmerman, Y. Zlochower, M. E. Zucker, and J. Zweizig, "Gwtc-2: Compact binary coalescences observed by ligo and virgo during the first half of the third observing run," *Phys. Rev. X*, vol. 11, p. 021053, Jun 2021.

[47] A. Romero-Rodriguez, M. Martinez, O. Pujolàs, M. Sakellariadou, and V. Vaskonen, "Search for a scalar induced stochastic gravitational wave background in the third LIGO-Virgo observing run," 7 2021.

[48] Q. Arnaud, D. Asner, J.-P. Bard, A. Brossard, B. Cai, M. Chapellier, M. Clark, E. Corcoran, T. Dandl, A. Dastgheibi-Fard, K. Dering, P. Di Stefano, D. Durnford, G. Gerbier, I. Giomataris, P. Gorel, M. Gros, O. Guillaudin, E. Hoppe, A. Kamaha, I. Katsioulas, D. Kelly, R. Martin, J. McDonald, J.-F. Muraz, J.-P. Mols, X.-F. Navick, T. Papaevangelou, F. Piquemal, S. Roth, D. Santos, I. Savvidis, A. Ulrich, F. Vazquez de Sola Fernandez, and M. Zampaolo, "First results from the news-g direct dark matter search experiment at the lsm," *Astroparticle Physics*, vol. 97, pp. 54–62, 2018.

[49] W. Guo and D. N. McKinsey, "Concept for a dark matter detector using liquid helium-4," *Phys. Rev.*, vol. D87, no. 11, p. 115001, 2013.

[50] Y.-S. Liu, D. McKeen, and G. A. Miller, "Electrophobic Scalar Boson and Muonic Puzzles," *Phys. Rev. Lett.*, vol. 117, no. 10, p. 101801, 2016.

[51] S. A. Hertel, A. Biekert, J. Lin, V. Velan, and D. N. McKinsey, "Direct detection of sub-GeV dark matter using a superfluid ^{4}He target," *Phys. Rev. D*, vol. 100, no. 9, p. 092007, 2019.

[52] N. A. Kurinsky, T. C. Yu, Y. Hochberg, and B. Cabrera, "Diamond Detectors for Direct Detection of Sub-GeV Dark Matter," *Phys. Rev.*, vol. D99, no. 12, p. 123005, 2019.

[53] J. D. Vergados and H. Ejiri, "The role of ionization electrons in direct neutralino detection," *Phys. Lett. B*, vol. 606, pp. 313–322, 2005.

[54] R. Bernabei, P. Belli, F. Montecchia, F. Nozzoli, F. Cappella, A. Incicchitti, D. Prosperi, R. Cerulli, C. J. Dai, H. L. He, H. H. Kuang, J. M. Ma, X. D. Sheng, and Z. P. Ye, "On

electromagnetic contributions in wimp quests," *International Journal of Modern Physics A*, vol. 22, no. 19, pp. 3155–3168, 2007.

[55] M. Ibe, W. Nakano, Y. Shoji, and K. Suzuki, "Migdal Effect in Dark Matter Direct Detection Experiments," *JHEP*, vol. 03, p. 194, 2018.

[56] C. Kouvaris and J. Pradler, "Probing sub-GeV Dark Matter with conventional detectors," *Phys. Rev. Lett.*, vol. 118, no. 3, p. 031803, 2017.

[57] S. Knapen, T. Lin, M. Pyle, and K. M. Zurek, "Detection of Light Dark Matter With Optical Phonons in Polar Materials," *Phys. Lett.*, vol. B785, pp. 386–390, 2018.

[58] T. Trickle, Z. Zhang, K. M. Zurek, K. Inzani, and S. Griffin, "Multi-Channel Direct Detection of Light Dark Matter: Theoretical Framework," *JHEP*, vol. 03, p. 036, 2020.

[59] P. Cox, T. Melia, and S. Rajendran, "Dark matter phonon coupling," *Phys. Rev. D*, vol. 100, no. 5, p. 055011, 2019.

[60] S. M. Griffin, K. Inzani, T. Trickle, Z. Zhang, and K. M. Zurek, "Multichannel direct detection of light dark matter: Target comparison," *Phys. Rev.*, vol. D101, no. 5, p. 055004, 2020.

[61] T. Trickle, Z. Zhang, and K. M. Zurek, "Effective field theory of dark matter direct detection with collective excitations," *Phys. Rev. D*, vol. 105, no. 1, p. 015001, 2022.

[62] S. M. Griffin, Y. Hochberg, K. Inzani, N. Kurinsky, T. Lin, and T. C. Yu, "Silicon carbide detectors for sub-GeV dark matter," *Phys. Rev. D*, vol. 103, no. 7, p. 075002, 2021.

[63] A. Coskuner, T. Trickle, Z. Zhang, and K. M. Zurek, "Directional detectability of dark matter with single phonon excitations: Target comparison," *Phys. Rev. D*, vol. 105, no. 1, p. 015010, 2022.

[64] K. Schutz and K. M. Zurek, "Detectability of Light Dark Matter with Superfluid Helium," *Phys. Rev. Lett.*, vol. 117, no. 12, p. 121302, 2016.

[65] S. Knapen, T. Lin, and K. M. Zurek, "Light Dark Matter in Superfluid Helium: Detection with Multi-excitation Production," *Phys. Rev.*, vol. D95, no. 5, p. 056019, 2017.

[66] F. Acanfora, A. Esposito, and A. D. Polosa, "Sub-GeV Dark Matter in Superfluid He-4: an Effective Theory Approach," *Eur. Phys. J.*, vol. C79, no. 7, p. 549, 2019.

[67] A. Caputo, A. Esposito, and A. D. Polosa, "Sub-MeV Dark Matter and the Goldstone Modes of Superfluid Helium," *Phys. Rev.*, vol. D100, no. 11, p. 116007, 2019.

[68] A. Caputo, A. Esposito, F. Piccinini, A. D. Polosa, and G. Rossi, "Directional detection of light dark matter from three-phonon events in superfluid ^{4}He," *Phys. Rev. D*, vol. 103, no. 5, p. 055017, 2021.

[69] G. Baym, D. H. Beck, J. P. Filippini, C. J. Pethick, and J. Shelton, "Searching for low mass dark matter via phonon creation in superfluid ^{4}He," *Phys. Rev. D*, vol. 102, no. 3, p. 035014, 2020. [Erratum: Phys.Rev.D 104, 019901(E) (2021)].

[70] K. T. Matchev, J. Smolinsky, W. Xue, and Y. You, "Superfluid Effective Field Theory for dark matter direct detection," 8 2021.

[71] Y. Kahn, G. Krnjaic, and B. Mandava, "Dark Matter Detection with Bound Nuclear Targets: The Poisson Phonon Tail," *Phys. Rev. Lett.*, vol. 127, no. 8, p. 081804, 2021.

[72] S. Knapen, J. Kozaczuk, and T. Lin, "Migdal Effect in Semiconductors," *Phys. Rev. Lett.*, vol. 127, no. 8, p. 081805, 2021.

[73] K. V. Berghaus, R. Essig, Y. Hochberg, Y. Shoji, and M. Sholapurkar, "The Phonon Background from Gamma Rays in Sub-GeV Dark Matter Detectors," 12 2021.

[74] S. Knapen, J. Kozaczuk, and T. Lin, "DarkELF: A python package for dark matter scattering in dielectric targets," *Phys. Rev. D*, vol. 105, no. 1, p. 015014, 2022.

[75] H. Schober, "An introduction to the theory of nuclear neutron scattering in condensed matter," *Journal of Neutron Research*, vol. 17, pp. 109–357, 2014.

[76] G. L. Squires, *Introduction to the Theory of Thermal Neutron Scattering*. Mineola, New York: Dover Publications, Inc., 1996.

[77] A. Togo and I. Tanaka, "First principles phonon calculations in materials science," *Scr. Mater.*, vol. 108, pp. 1–5, Nov 2015.

[78] G. Placzek, B. R. A. Nijboer, and L. V. Hove, "Effect of short wavelength interference on neuteron scattering by dense systems of heavy nuclei," *Phys. Rev.*, vol. 82, pp. 392–403, May 1951.

[79] A. Jain, S. P. Ong, G. Hautier, W. Chen, W. D. Richards, S. Dacek, S. Cholia, D. Gunter, D. Skinner, G. Ceder, and K. a. Persson, "The Materials Project: A materials genome approach to accelerating materials innovation," *APL Materials*, vol. 1, no. 1, p. 011002, 2013.

[80] G. Kresse and J. Furthmüller, "Efficient iterative schemes for ab initio total-energy calculations using a plane-wave basis set," *Phys. Rev. B*, vol. 54, pp. 11169–11186, Oct 1996.

[81] Z.-L. Liang, C. Mo, F. Zheng, and P. Zhang, "A phonon-mediated description of the Migdal effect in semiconductor detectors," 5 2022.

[82] P. J. Brown, A. G. Fox, E. N. Maslen, M. A. O'Keefe, and B. T. M. Willis, *Intensity of diffracted intensities*, ch. 6.1, pp. 554–595. American Cancer Society, 2006.

[83] S. Knapen, J. Kozaczuk, and T. Lin, "Dark matter-electron scattering in dielectrics," 1 2021.

[84] R. Essig, M. Fernandez-Serra, J. Mardon, A. Soto, T. Volansky, and T.-T. Yu, "Direct Detection of sub-GeV Dark Matter with Semiconductor Targets," *JHEP*, vol. 05, p. 046, 2016.

[85] G. Srivastava, "Phonon conductivity of insulators and semiconductors," *Journal of Physics and Chemistry of Solids*, vol. 41, no. 4, pp. 357–368, 1980.

[86] Z.-L. Liang, C. Mo, F. Zheng, and P. Zhang, "Describing Migdal effect with bremsstrahlung-like process and many-body effects," 11 2020.

[87] M. W. Goodman and E. Witten, "Detectability of Certain Dark Matter Candidates," *Phys. Rev. D*, vol. 31, p. 3059, 1985.

[88] E. Aprile, K. Abe, F. Agostini, S. Ahmed Maouloud, L. Althueser, B. Andrieu, E. Angelino, J. R. Angevaare, V. C. Antochi, D. Antón Martin, F. Arneodo, L. Baudis, A. L. Baxter, M. Bazyk, L. Bellagamba, R. Biondi, A. Bismark, E. J. Brookes, A. Brown, S. Bruenner, G. Bruno, R. Budnik, T. K. Bui, C. Cai, J. M. R. Cardoso, D. Cichon, A. P. Cimental Chavez, A. P. Colijn, J. Conrad, J. J. Cuenca-García, J. P. Cussonneau, V. D'Andrea, M. P. Decowski, P. Di Gangi, S. Di Pede, S. Diglio, K. Eitel, A. Elykov, S. Farrell, A. D. Ferella, C. Ferrari, H. Fischer, M. Flierman, W. Fulgione, C. Fuselli, P. Gaemers, R. Gaior, A. Gallo Rosso, M. Galloway, F. Gao, R. Glade-Beucke, L. Grandi, J. Grigat, H. Guan, M. Guida, R. Hammann, A. Higuera, C. Hils, L. Hoetzsch, N. F. Hood, J. Howlett, M. Iacovacci, Y. Itow, J. Jakob, F. Joerg, A. Joy, N. Kato, M. Kara, P. Kavrigin, S. Kazama, M. Kobayashi, G. Koltman, A. Kopec, F. Kuger, H. Landsman, R. F. Lang, L. Levinson, I. Li, S. Li, S. Liang, S. Lindemann, M. Lindner, K. Liu, J. Loizeau, F. Lombardi, J. Long, J. A. M. Lopes, Y. Ma, C. Macolino, J. Mahlstedt, A. Mancuso, L. Manenti, F. Marignetti, T. Marrodán Undagoitia, K. Martens, J. Masbou, D. Masson, E. Masson, S. Mastroianni, M. Messina, K. Miuchi, K. Mizukoshi, A. Molinario, S. Moriyama, K. Morå, Y. Mosbacher, M. Murra, J. Müller, K. Ni, U. Oberlack, B. Paetsch, J. Palacio, R. Peres, C. Peters, J. Pienaar, M. Pierre, V. Pizzella, G. Plante, J. Qi, J. Qin, D. Ramírez García, R. Singh, L. Sanchez, J. M. F. dos Santos, I. Sarnoff, G. Sartorelli, J. Schreiner, D. Schulte, P. Schulte, H. Schulze Eißing, M. Schumann, L. Scotto Lavina, M. Selvi, F. Semeria, P. Shagin, S. Shi, E. Shockley, M. Silva, H. Simgen, A. Takeda, P.-L. Tan, A. Terliuk, D. Thers, F. Toschi, G. Trinchero, C. Tunnell, F. Tönnies, K. Valerius, G. Volta, C. Weinheimer, M. Weiss, D. Wenz, C. Wittweg, T. Wolf, V. H. S. Wu, Y. Xing, D. Xu, Z. Xu, M. Yamashita, L. Yang, J. Ye, L. Yuan, G. Zavattini, M. Zhong, and T. Zhu, "First dark matter search with nuclear recoils from the xenonnt experiment," *Phys. Rev. Lett.*, vol. 131, p. 041003, Jul 2023.

[89] J. Aalbers, D. S. Akerib, C. W. Akerlof, A. K. Al Musalhi, F. Alder, A. Alqahtani, S. K. Alsum, C. S. Amarasinghe, A. Ames, T. J. Anderson, N. Angelides, H. M. Araújo, J. E. Armstrong, M. Arthurs, S. Azadi, A. J. Bailey, A. Baker, J. Balajthy, S. Balashov, J. Bang, J. W. Bargemann, M. J. Barry, J. Barthel, D. Bauer, A. Baxter, K. Beattie, J. Belle, P. Beltrame, J. Bensinger, T. Benson, E. P. Bernard, A. Bhatti, A. Biekert, T. P. Biesiadzinski, H. J. Birch, B. Birrittella, G. M. Blockinger, K. E. Boast, B. Boxer,

R. Bramante, C. A. J. Brew, P. Brás, J. H. Buckley, V. V. Bugaev, S. Burdin, J. K. Busenitz, M. Buuck, R. Cabrita, C. Carels, D. L. Carlsmith, B. Carlson, M. C. Carmona-Benitez, M. Cascella, C. Chan, A. Chawla, H. Chen, J. J. Cherwinka, N. I. Chott, A. Cole, J. Coleman, M. V. Converse, A. Cottle, G. Cox, W. W. Craddock, O. Creaner, D. Curran, A. Currie, J. E. Cutter, C. E. Dahl, A. David, J. Davis, T. J. R. Davison, J. Delgaudio, S. Dey, L. de Viveiros, A. Dobi, J. E. Y. Dobson, E. Druszkiewicz, A. Dushkin, T. K. Edberg, W. R. Edwards, M. M. Elnimr, W. T. Emmet, S. R. Eriksen, C. H. Faham, A. Fan, S. Fayer, N. M. Fearon, S. Fiorucci, H. Flaecher, P. Ford, V. B. Francis, E. D. Fraser, T. Fruth, R. J. Gaitskell, N. J. Gantos, D. Garcia, A. Geffre, V. M. Gehman, J. Genovesi, C. Ghag, R. Gibbons, E. Gibson, M. G. D. Gilchriese, S. Gokhale, B. Gomber, J. Green, A. Greenall, S. Greenwood, M. G. D. van der Grinten, C. B. Gwilliam, C. R. Hall, S. Hans, K. Hanzel, A. Harrison, E. Hartigan-O'Connor, S. J. Haselschwardt, M. A. Hernandez, S. A. Hertel, G. Heuermann, C. Hjemfelt, M. D. Hoff, E. Holtom, J. Y.-K. Hor, M. Horn, D. Q. Huang, D. Hunt, C. M. Ignarra, R. G. Jacobsen, O. Jahangir, R. S. James, S. N. Jeffery, W. Ji, J. Johnson, A. C. Kaboth, A. C. Kamaha, K. Kamdin, V. Kasey, K. Kazkaz, J. Keefner, D. Khaitan, M. Khaleeq, A. Khazov, I. Khurana, Y. D. Kim, C. D. Kocher, D. Kodroff, L. Korley, E. V. Korolkova, J. Kras, H. Kraus, S. Kravitz, H. J. Krebs, L. Kreczko, B. Krikler, V. A. Kudryavtsev, S. Kyre, B. Landerud, E. A. Leason, C. Lee, J. Lee, D. S. Leonard, R. Leonard, K. T. Lesko, C. Levy, J. Li, F.-T. Liao, J. Liao, J. Lin, A. Lindote, R. Linehan, W. H. Lippincott, R. Liu, X. Liu, Y. Liu, C. Loniewski, M. I. Lopes, E. Lopez Asamar, B. López Paredes, W. Lorenzon, D. Lucero, S. Luitz, J. M. Lyle, P. A. Majewski, J. Makkinje, D. C. Malling, A. Manalaysay, L. Manenti, R. L. Mannino, N. Marangou, M. F. Marzioni, C. Maupin, M. E. McCarthy, C. T. McConnell, D. N. McKinsey, J. McLaughlin, Y. Meng, J. Migneault, E. H. Miller, E. Mizrachi, J. A. Mock, A. Monte, M. E. Monzani, J. A. Morad, J. D. Morales Mendoza, E. Morrison, B. J. Mount, M. Murdy, A. S. J. Murphy, D. Naim, A. Naylor, C. Nedlik, C. Nehrkorn, F. Neves, A. Nguyen, J. A. Nikoleyczik, A. Nilima, J. O'Dell, F. G. O'Neill, K. O'Sullivan, I. Olcina, M. A. Olevitch, K. C. Oliver-Mallory, J. Orpwood, D. Pagenkopf, S. Pal, K. J. Palladino, J. Palmer, M. Pangilinan, N. Parveen, S. J. Patton, E. K. Pease, B. Penning, C. Pereira, G. Pereira, E. Perry, T. Pershing, I. B. Peterson, A. Piepke, J. Podczerwinski, D. Porzio, S. Powell, R. M. Preece, K. Pushkin, Y. Qie, B. N. Ratcliff, J. Reichenbacher, L. Reichhart, C. A. Rhyne, A. Richards, Q. Riffard, G. R. C. Rischbieter, J. P. Rodrigues, A. Rodriguez, H. J. Rose, R. Rosero, P. Rossiter, T. Rushton, G. Rutherford, D. Rynders, J. S. Saba, D. Santone, A. B. M. R. Sazzad, R. W. Schnee, P. R. Scovell, D. Seymour, S. Shaw, T. Shutt, J. J. Silk, C. Silva, G. Sinev, K. Skarpaas, W. Skulski, R. Smith, M. Solmaz, V. N. Solovov, P. Sorensen, J. Soria, I. Stancu, M. R. Stark, A. Stevens, T. M. Stiegler, K. Stifter, R. Studley, B. Suerfu, T. J. Sumner, P. Sutcliffe, N. Swanson, M. Szydagis, M. Tan, D. J. Taylor, R. Taylor, W. C. Taylor, D. J. Temples, B. P. Tennyson, P. A. Terman, K. J. Thomas, D. R. Tiedt, M. Timalsina, W. H. To, A. Tomás, Z. Tong, D. R. Tovey, J. Tranter, M. Trask, M. Tripathi, D. R. Tronstad, C. E. Tull, W. Turner, L. Tvrznikova, U. Utku, J. Va'vra, A. Vacheret, A. C. Vaitkus, J. R. Verbus, E. Voirin, W. L. Waldron, A. Wang, B. Wang, J. J. Wang, W. Wang, Y. Wang, J. R. Watson, R. C. Webb, A. White, D. T. White, J. T. White, R. G. White, T. J. Whitis, M. Williams, W. J. Wisniewski, M. S. Witherell, F. L. H. Wolfs, J. D. Wolfs, S. Woodford, D. Woodward, S. D. Worm, C. J. Wright, Q. Xia, X. Xiang,

Q. Xiao, J. Xu, M. Yeh, J. Yin, I. Young, P. Zarzhitsky, A. Zuckerman, and E. A. Zweig, "First dark matter search results from the lux-zeplin (lz) experiment," *Phys. Rev. Lett.*, vol. 131, p. 041002, Jul 2023.

[90] Y. Meng, Z. Wang, Y. Tao, A. Abdukerim, Z. Bo, W. Chen, X. Chen, Y. Chen, C. Cheng, Y. Cheng, X. Cui, Y. Fan, D. Fang, C. Fu, M. Fu, L. Geng, K. Giboni, L. Gu, X. Guo, K. Han, C. He, J. He, D. Huang, Y. Huang, Z. Huang, R. Hou, X. Ji, Y. Ju, C. Li, M. Li, S. Li, S. Li, Q. Lin, J. Liu, X. Lu, L. Luo, W. Ma, Y. Ma, Y. Mao, N. Shaheed, X. Ning, N. Qi, Z. Qian, X. Ren, C. Shang, G. Shen, L. Si, W. Sun, A. Tan, A. Wang, M. Wang, Q. Wang, S. Wang, S. Wang, W. Wang, X. Wang, M. Wu, W. Wu, J. Xia, M. Xiao, X. Xiao, P. Xie, B. Yan, X. Yan, J. Yang, Y. Yang, C. Yu, J. Yuan, Y. Yuan, D. Zhang, M. Zhang, P. Zhang, T. Zhang, L. Zhao, Q. Zheng, J. Zhou, N. Zhou, X. Zhou, and Y. Zhou, "Dark matter search results from the pandax-4t commissioning run," *Phys. Rev. Lett.*, vol. 127, p. 261802, Dec 2021.

[91] C. Boehm, T. A. Enßlin, and J. Silk, "Can annihilating dark matter be lighter than a few GeVs?," *Journal of Physics G: Nuclear and Particle Physics*, vol. 30, pp. 279–285, jan 2004.

[92] C. Bœhm and P. Fayet, "Scalar dark matter candidates," *Nuclear Physics B*, vol. 683, pp. 219–263, apr 2004.

[93] P. Fayet, "Light spin-$\frac{1}{2}$ or spin-0 dark matter particles," *Phys. Rev. D*, vol. 70, p. 023514, Jul 2004.

[94] J. L. Feng and J. Kumar, "The WIMPless Miracle: Dark-Matter Particles without Weak-Scale Masses or Weak Interactions," *Phys. Rev. Lett.*, vol. 101, p. 231301, 2008.

[95] D. E. Kaplan, M. A. Luty, and K. M. Zurek, "Asymmetric Dark Matter," *Phys. Rev.*, vol. D79, p. 115016, 2009.

[96] R. Essig, J. Mardon, and T. Volansky, "Direct Detection of Sub-GeV Dark Matter," *Phys. Rev.*, vol. D85, p. 076007, 2012.

[97] A. Migdal, "Ionizatsiya atomov pri yadernykh reaktsiyakh," *Sov. Phys. JETP*, vol. 9, p. 1163, 1939.

[98] R. Essig, J. Pradler, M. Sholapurkar, and T.-T. Yu, "Relation between the Migdal Effect and Dark Matter-Electron Scattering in Isolated Atoms and Semiconductors," *Phys. Rev. Lett.*, vol. 124, no. 2, p. 021801, 2020.

[99] K. V. Berghaus, A. Esposito, R. Essig, and M. Sholapurkar, "The Migdal effect in semiconductors for dark matter with masses below $\sim$ 100 MeV," *JHEP*, vol. 01, p. 023, 2023.

[100] I. Alkhatib, D. W. P. Amaral, T. Aralis, T. Aramaki, I. J. Arnquist, I. Ataee Langroudy, E. Azadbakht, S. Banik, D. Barker, C. Bathurst, D. A. Bauer, L. V. S. Bezerra, R. Bhattacharyya, T. Binder, M. A. Bowles, P. L. Brink, R. Bunker, B. Cabrera, R. Calkins, R. A.

Cameron, C. Cartaro, D. G. Cerdeño, Y.-Y. Chang, M. Chaudhuri, R. Chen, N. Chott, J. Cooley, H. Coombes, J. Corbett, P. Cushman, F. De Brienne, M. L. di Vacri, M. D. Diamond, E. Fascione, E. Figueroa-Feliciano, C. W. Fink, K. Fouts, M. Fritts, G. Gerbier, R. Germond, M. Ghaith, S. R. Golwala, H. R. Harris, N. Herbert, B. A. Hines, M. I. Hollister, Z. Hong, E. W. Hoppe, L. Hsu, M. E. Huber, V. Iyer, D. Jardin, A. Jastram, V. K. S. Kashyap, M. H. Kelsey, A. Kubik, N. A. Kurinsky, R. E. Lawrence, A. Li, B. Loer, E. Lopez Asamar, P. Lukens, D. MacDonell, D. B. MacFarlane, R. Mahapatra, V. Mandic, N. Mast, A. J. Mayer, H. Meyer zu Theenhausen, E. M. Michaud, E. Michielin, N. Mirabolfathi, B. Mohanty, J. D. Morales Mendoza, S. Nagorny, J. Nelson, H. Neog, V. Novati, J. L. Orrell, S. M. Oser, W. A. Page, P. Pakarha, R. Partridge, R. Podviianiuk, F. Ponce, S. Poudel, M. Pyle, W. Rau, E. Reid, R. Ren, T. Reynolds, A. Roberts, A. E. Robinson, T. Saab, B. Sadoulet, J. Sander, A. Sattari, R. W. Schnee, S. Scorza, B. Serfass, D. J. Sincavage, C. Stanford, J. Street, D. Toback, R. Underwood, S. Verma, A. N. Villano, B. von Krosigk, S. L. Watkins, L. Wills, J. S. Wilson, M. J. Wilson, J. Winchell, D. H. Wright, S. Yellin, B. A. Young, T. C. Yu, E. Zhang, H. G. Zhang, X. Zhao, L. Zheng, J. Camilleri, Y. G. Kolomensky, and S. Zuber, "Light dark matter search with a high-resolution athermal phonon detector operated above ground," *Phys. Rev. Lett.*, vol. 127, p. 061801, Aug 2021.

[101] G. Angloher, S. Banik, G. Benato, A. Bento, A. Bertolini, R. Breier, C. Bucci, J. Burkhart, L. Canonica, A. D'Addabbo, S. Di Lorenzo, L. Einfalt, A. Erb, F. v. Feilitzsch, N. Ferreiro Iachellini, S. Fichtinger, D. Fuchs, A. Fuss, A. Garai, V. M. Ghete, S. Gerster, P. Gorla, P. V. Guillaumon, S. Gupta, D. Hauff, M. Ješkovský, J. Jochum, M. Kaznacheeva, A. Kinast, H. Kluck, H. Kraus, A. Langenkämper, M. Mancuso, L. Marini, L. Meyer, V. Mokina, A. Nilima, M. Olmi, T. Ortmann, C. Pagliarone, L. Pattavina, F. Petricca, W. Potzel, P. Povinec, F. Pröbst, F. Pucci, F. Reindl, J. Rothe, K. Schäffner, J. Schieck, D. Schmiedmayer, S. Schönert, C. Schwertner, M. Stahlberg, L. Stodolsky, C. Strandhagen, R. Strauss, I. Usherov, F. Wagner, M. Willers, and V. Zema, "Results on sub-gev dark matter from a 10 ev threshold cresst-iii silicon detector," *Phys. Rev. D*, vol. 107, p. 122003, Jun 2023.

[102] A. H. Abdelhameed, G. Angloher, P. Bauer, A. Bento, E. Bertoldo, C. Bucci, L. Canonica, A. D'Addabbo, X. Defay, S. Di Lorenzo, A. Erb, F. v. Feilitzsch, S. Fichtinger, N. Ferreiro Iachellini, A. Fuss, P. Gorla, D. Hauff, J. Jochum, A. Kinast, H. Kluck, H. Kraus, A. Langenkämper, M. Mancuso, V. Mokina, E. Mondragon, A. Münster, M. Olmi, T. Ortmann, C. Pagliarone, L. Pattavina, F. Petricca, W. Potzel, F. Pröbst, F. Reindl, J. Rothe, K. Schäffner, J. Schieck, V. Schipperges, D. Schmiedmayer, S. Schönert, C. Schwertner, M. Stahlberg, L. Stodolsky, C. Strandhagen, R. Strauss, C. Türkoğlu, I. Usherov, M. Willers, and V. Zema, "First results from the cresst-iii low-mass dark matter program," *Phys. Rev. D*, vol. 100, p. 102002, Nov 2019.

[103] A. Aguilar-Arevalo, D. Amidei, D. Baxter, G. Cancelo, B. A. C. Vergara, A. E. Chavarria, J. C. D'Olivo, J. Estrada, F. Favela-Perez, R. Gaïor, Y. Guardincerri, E. W. Hoppe, T. W. Hossbach, B. Kilminster, I. Lawson, S. J. Lee, A. Letessier-Selvon, A. Matalon, P. Mitra, C. T. Overman, A. Piers, P. Privitera, K. Ramanathan, J. Da Rocha, Y. Sarkis, M. Settimo,

R. Smida, R. Thomas, J. Tiffenberg, M. Traina, R. Vilar, and A. L. Virto, "Results on low-mass weakly interacting massive particles from an 11 kg d target exposure of damic at snolab," *Phys. Rev. Lett.*, vol. 125, p. 241803, Dec 2020.

[104] R. Anthony-Petersen, A. Biekert, C. L. Chang, Y. Chang, L. Chaplinsky, A. Dushkin, C. W. Fink, M. Garcia-Sciveres, W. Guo, S. A. Hertel, X. Li, J. Lin, R. Mahapatra, W. Matava, D. N. McKinsey, D. Z. Osterman, P. K. Patel, B. Penning, H. D. Pinckney, M. Platt, M. Pyle, Y. Qi, M. Reed, G. R. C. Rischbieter, R. K. Romani, A. Serafin, B. Serfass, R. J. Smith, P. Sorensen, B. Suerfu, A. Suzuki, V. Velan, G. Wang, Y. Wang, S. L. Watkins, and M. R. Williams, "Applying superfluid helium to light dark matter searches: Demonstration of the herald detector concept," 2023.

[105] B. Campbell-Deem, S. Knapen, T. Lin, and E. Villarama, "Dark matter direct detection from the single phonon to the nuclear recoil regime," *Phys. Rev. D*, vol. 106, no. 3, p. 036019, 2022.

[106] A. Mitridate, T. Trickle, Z. Zhang, and K. M. Zurek, "Detectability of Axion Dark Matter with Phonon Polaritons and Magnons," *Phys. Rev. D*, vol. 102, no. 9, p. 095005, 2020.

[107] A. Mitridate, K. Pardo, T. Trickle, and K. M. Zurek, "Effective Field Theory for Dark Matter Absorption on Single Phonons," 8 2023.

[108] G. P. Srivastava, *The physics of phonons*. Routledge, 2019.

[109] A. Debernardi, "Anharmonic effects in the phonons of iii–v semiconductors: first principles calculations," *Solid State Communications*, vol. 113, no. 1, pp. 1–10, 1999.

[110] B. Wei, Q. Sun, C. Li, and J. Hong, "Phonon anharmonicity: a pertinent review of recent progress and perspective," *Science China Physics, Mechanics & Astronomy*, vol. 64, no. 11, p. 117001, 2021.

[111] A. Debernardi and S. Baroni, "Third-order density-functional perturbation theory: A practical implementation with applications to anharmonic couplings in si," *Solid State Communications*, vol. 91, no. 10, pp. 813–816, 1994.

[112] D. S. Kim, O. Hellman, N. Shulumba, C. N. Saunders, J. Y. Y. Lin, H. L. Smith, J. E. Herriman, J. L. Niedziela, D. L. Abernathy, C. W. Li, and B. Fultz, "Temperature-dependent phonon lifetimes and thermal conductivity of silicon by inelastic neutron scattering and ab initio calculations," *Phys. Rev. B*, vol. 102, p. 174311, Nov 2020.

[113] J. W. L. Pang, W. J. L. Buyers, A. Chernatynskiy, M. D. Lumsden, B. C. Larson, and S. R. Phillpot, "Phonon lifetime investigation of anharmonicity and thermal conductivity of uo_2 by neutron scattering and theory," *Phys. Rev. Lett.*, vol. 110, p. 157401, Apr 2013.

[114] A. Mayer and R. Wehner, "Calculation of grüneisen constants in si," *physica status solidi (b)*, vol. 126, no. 1, pp. 91–103, 1984.

[115] C. H. Lee and C. K. Gan, "Anharmonic interatomic force constants and thermal conductivity from grüneisen parameters: An application to graphene," *Physical Review B*, vol. 96, jul 2017.

[116] K. Esfarjani, G. Chen, and H. T. Stokes, "Heat transport in silicon from first-principles calculations," *Phys. Rev. B*, vol. 84, p. 085204, Aug 2011.

[117] A. Rohskopf, H. R. Seyf, K. Gordiz, T. Tadano, and A. Henry, "Empirical interatomic potentials optimized for phonon properties," *npj Computational Materials*, vol. 3, no. 1, p. 27, 2017.

[118] J. M. F. Gunn and M. Warner, "The effect of high momentum transfer on scattering from oscillators and crystals," *Zeitschrift für Physik B Condensed Matter*, vol. 56, no. 1, pp. 13–20, 1984.

[119] T. Emken, R. Essig, C. Kouvaris, and M. Sholapurkar, "Direct detection of strongly interacting sub-GeV dark matter via electron recoils," *Journal of Cosmology and Astroparticle Physics*, vol. 2019, pp. 070–070, sep 2019.

[120] D. Green and S. Rajendran, "The Cosmology of Sub-MeV Dark Matter," *JHEP*, vol. 10, p. 013, 2017.

[121] J. Tersoff, "New empirical approach for the structure and energy of covalent systems," *Phys. Rev. B*, vol. 37, pp. 6991–7000, Apr 1988.

[122] M. Berrondo, A. Palma, and J. López-Bonilla, "Matrix elements for the morse potential using ladder operators," *International Journal of Quantum Chemistry*, vol. 31, no. 2, pp. 243–249, 1987.

[123] B. Carr and F. Kuhnel, "Primordial Black Holes as Dark Matter: Recent Developments," *Ann. Rev. Nucl. Part. Sci.*, vol. 70, pp. 355–394, 2020.

[124] A. M. Green and B. J. Kavanagh, "Primordial Black Holes as a dark matter candidate," 7 2020.

[125] S. Bird, I. Cholis, J. B. Muñoz, Y. Ali-Haïmoud, M. Kamionkowski, E. D. Kovetz, A. Raccanelli, and A. G. Riess, "Did LIGO detect dark matter?," *Phys. Rev. Lett.*, vol. 116, no. 20, p. 201301, 2016.

[126] R. Anantua, R. Easther, and J. T. Giblin, "GUT-Scale Primordial Black Holes: Consequences and Constraints," *Phys. Rev. Lett.*, vol. 103, p. 111303, 2009.

[127] D. Hooper, G. Krnjaic, and S. D. McDermott, "Dark Radiation and Superheavy Dark Matter from Black Hole Domination," *JHEP*, vol. 08, p. 001, 2019.

[128] T. Fujita, M. Kawasaki, K. Harigaya, and R. Matsuda, "Baryon asymmetry, dark matter, and density perturbation from primordial black holes," *Phys. Rev. D*, vol. 89, no. 10, p. 103501, 2014.

[129] L. Morrison, S. Profumo, and Y. Yu, "Melanopogenesis: Dark Matter of (almost) any Mass and Baryonic Matter from the Evaporation of Primordial Black Holes weighing a Ton (or less)," *JCAP*, vol. 05, p. 005, 2019.

[130] Y. Hamada and S. Iso, "Baryon asymmetry from primordial black holes," *PTEP*, vol. 2017, no. 3, p. 033B02, 2017.

[131] P. Gondolo, P. Sandick, and B. Shams Es Haghi, "Effects of primordial black holes on dark matter models," *Phys. Rev. D*, vol. 102, no. 9, p. 095018, 2020.

[132] P. Sandick, B. S. Es Haghi, and K. Sinha, "Asymmetric Reheating by Primordial Black Holes," 8 2021.

[133] O. Lennon, J. March-Russell, R. Petrossian-Byrne, and H. Tillim, "Black Hole Genesis of Dark Matter," *JCAP*, vol. 04, p. 009, 2018.

[134] I. Masina, "Dark matter and dark radiation from evaporating primordial black holes," *Eur. Phys. J. Plus*, vol. 135, no. 7, p. 552, 2020.

[135] A. Arbey, J. Auffinger, P. Sandick, B. Shams Es Haghi, and K. Sinha, "Precision calculation of dark radiation from spinning primordial black holes and early matter-dominated eras," *Phys. Rev. D*, vol. 103, no. 12, p. 123549, 2021.

[136] J. H. MacGibbon, "Can Planck-mass relics of evaporating black holes close the universe?," *Nature*, vol. 329, pp. 308–309, 1987.

[137] J. D. Barrow, E. J. Copeland, and A. R. Liddle, "The Cosmology of black hole relics," *Phys. Rev. D*, vol. 46, pp. 645–657, 1992.

[138] B. J. Carr, J. H. Gilbert, and J. E. Lidsey, "Black hole relics and inflation: Limits on blue perturbation spectra," *Phys. Rev. D*, vol. 50, pp. 4853–4867, 1994.

[139] B. V. Lehmann, C. Johnson, S. Profumo, and T. Schwemberger, "Direct detection of primordial black hole relics as dark matter," *JCAP*, vol. 10, p. 046, 2019.

[140] S. Matarrese, O. Pantano, and D. Saez, "A General relativistic approach to the nonlinear evolution of collisionless matter," *Phys. Rev. D*, vol. 47, pp. 1311–1323, 1993.

[141] S. Matarrese, O. Pantano, and D. Saez, "General relativistic dynamics of irrotational dust: Cosmological implications," *Phys. Rev. Lett.*, vol. 72, pp. 320–323, 1994.

[142] S. Matarrese, S. Mollerach, and M. Bruni, "Second order perturbations of the Einstein-de Sitter universe," *Phys. Rev. D*, vol. 58, p. 043504, 1998.

[143] H. Noh and J.-c. Hwang, "Second-order perturbations of the Friedmann world model," *Phys. Rev. D*, vol. 69, p. 104011, 2004.

[144] C. Carbone and S. Matarrese, "A Unified treatment of cosmological perturbations from super-horizon to small scales," *Phys. Rev. D*, vol. 71, p. 043508, 2005.

[145] K. Nakamura, "Second-order gauge invariant cosmological perturbation theory: Einstein equations in terms of gauge invariant variables," *Prog. Theor. Phys.*, vol. 117, pp. 17–74, 2007.

[146] D. Baumann, P. J. Steinhardt, K. Takahashi, and K. Ichiki, "Gravitational Wave Spectrum Induced by Primordial Scalar Perturbations," *Phys. Rev. D*, vol. 76, p. 084019, 2007.

[147] C. Yuan and Q.-G. Huang, "A topic review on probing primordial black hole dark matter with scalar induced gravitational waves," *iScience*, vol. 24, no. 8, p. 102860, 2021.

[148] K. Inomata, M. Kawasaki, K. Mukaida, T. Terada, and T. T. Yanagida, "Gravitational Wave Production right after a Primordial Black Hole Evaporation," *Phys. Rev. D*, vol. 101, no. 12, p. 123533, 2020.

[149] K. Inomata, K. Kohri, T. Nakama, and T. Terada, "Enhancement of gravitational waves induced by scalar perturbations due to a sudden transition from an early matter era to the radiation era," *Phys. Rev. D*, vol. 100, p. 043532, Aug 2019.

[150] G. Domenech, C. Lin, and M. Sasaki, "Gravitational wave constraints on the primordial black hole dominated early universe,"

[151] G. Domènech, V. Takhistov, and M. Sasaki, "Exploring Evaporating Primordial Black Holes with Gravitational Waves," 5 2021.

[152] S. Clesse and J. García-Bellido, "Detecting the gravitational wave background from primordial black hole dark matter," *Phys. Dark Univ.*, vol. 18, pp. 105–114, 2017.

[153] K. Inomata, M. Kawasaki, K. Mukaida, Y. Tada, and T. T. Yanagida, "Inflationary primordial black holes for the LIGO gravitational wave events and pulsar timing array experiments," *Phys. Rev. D*, vol. 95, no. 12, p. 123510, 2017.

[154] Z. Arzoumanian, P. T. Baker, H. Blumer, B. Bécsy, A. Brazier, P. R. Brook, S. Burke-Spolaor, S. Chatterjee, S. Chen, J. M. Cordes, N. J. Cornish, F. Crawford, H. Thankful Cromartie, M. E. Decesar, P. B. Demorest, T. Dolch, J. A. Ellis, E. C. Ferrara, W. Fiore, E. Fonseca, N. Garver-Daniels, P. A. Gentile, D. C. Good, J. S. Hazboun, A. Miguel Holgado, K. Islo, R. J. Jennings, M. L. Jones, A. R. Kaiser, D. L. Kaplan, L. Z. Kelley, J. Shapiro Key, N. Laal, M. T. Lam, T. W. Lazio, D. R. Lorimer, J. Luo, R. S. Lynch, D. R. Madison, M. A. Mclaughlin, C. M. Mingarelli, C. Ng, D. J. Nice, T. T. Pennucci, N. S. Pol, S. M. Ransom, P. S. Ray, B. J. Shapiro-Albert, X. Siemens, J. Simon, R. Spiewak, I. H. Stairs, D. R. Stinebring, K. Stovall, J. P. Sun, J. K. Swiggum, S. R. Taylor, J. E. Turner, M. Vallisneri, S. J. Vigeland, and C. A. Witt, "The NANOGrav 12.5 yr Data Set: Search for an Isotropic Stochastic Gravitational-wave Background," *Astrophys.J.Lett.*, vol. 905, no. 2, p. L34, 2020.

[155] V. De Luca, G. Franciolini, and A. Riotto, "NANOGrav Data Hints at Primordial Black Holes as Dark Matter," *Phys. Rev. Lett.*, vol. 126, no. 4, p. 041303, 2021.

[156] K. Kohri and T. Terada, "Solar-Mass Primordial Black Holes Explain NANOGrav Hint of Gravitational Waves," *Phys. Lett. B*, vol. 813, p. 136040, 2021.

[157] V. Vaskonen and H. Veermäe, "Did nanograv see a signal from primordial black hole formation?," *Phys. Rev. Lett.*, vol. 126, p. 051303, Feb 2021.

[158] S. Clesse, J. García-Bellido, and S. Orani, "Detecting the Stochastic Gravitational Wave Background from Primordial Black Hole Formation," 12 2018.

[159] A. M. Green and A. R. Liddle, "Constraints on the density perturbation spectrum from primordial black holes," *Phys. Rev. D*, vol. 56, pp. 6166–6174, 1997.

[160] B. Carr, K. Kohri, Y. Sendouda, and J. Yokoyama, "Constraints on Primordial Black Holes," 2 2020.

[161] B. J. Carr, K. Kohri, Y. Sendouda, and J. Yokoyama, "New cosmological constraints on primordial black holes," *Phys. Rev. D*, vol. 81, p. 104019, 2010.

[162] A. D. Gow, C. T. Byrnes, P. S. Cole, and S. Young, "The power spectrum on small scales: Robust constraints and comparing PBH methodologies," *JCAP*, vol. 02, p. 002, 2021.

[163] R.-g. Cai, S. Pi, and M. Sasaki, "Gravitational Waves Induced by non-Gaussian Scalar Perturbations," *Phys. Rev. Lett.*, vol. 122, no. 20, p. 201101, 2019.

[164] N. Bartolo, V. De Luca, G. Franciolini, M. Peloso, D. Racco, and A. Riotto, "Testing primordial black holes as dark matter with LISA," *Phys. Rev. D*, vol. 99, no. 10, p. 103521, 2019.

[165] N. Bartolo, V. De Luca, G. Franciolini, A. Lewis, M. Peloso, and A. Riotto, "Primordial Black Hole Dark Matter: LISA Serendipity," *Phys. Rev. Lett.*, vol. 122, no. 21, p. 211301, 2019.

[166] A. R. Liddle and A. M. Green, "Cosmological constraints from primordial black holes," *Phys. Rept.*, vol. 307, pp. 125–131, 1998.

[167] B. J. Carr, J. H. Gilbert, and J. E. Lidsey, "Black hole relics and inflation: Limits on blue perturbation spectra," *Physical Review D*, vol. 50, p. 4853–4867, Oct 1994.

[168] B. Carr, M. Raidal, T. Tenkanen, V. Vaskonen, and H. Veermäe, "Primordial black hole constraints for extended mass functions," *Phys. Rev. D*, vol. 96, no. 2, p. 023514, 2017.

[169] C. Keith, D. Hooper, N. Blinov, and S. D. McDermott, "Constraints on Primordial Black Holes From Big Bang Nucleosynthesis Revisited," *Phys. Rev. D*, vol. 102, no. 10, p. 103512, 2020.

[170] P. Stöcker, M. Krämer, J. Lesgourgues, and V. Poulin, "Exotic energy injection with ExoCLASS: Application to the Higgs portal model and evaporating black holes," *JCAP*, vol. 03, p. 018, 2018.

[171] R. Laha, J. B. Muñoz, and T. R. Slatyer, "INTEGRAL constraints on primordial black holes and particle dark matter," *Phys. Rev. D*, vol. 101, no. 12, p. 123514, 2020.

[172] N. Smyth, S. Profumo, S. English, T. Jeltema, K. McKinnon, and P. Guhathakurta, "Updated Constraints on Asteroid-Mass Primordial Black Holes as Dark Matter," *Phys. Rev. D*, vol. 101, no. 6, p. 063005, 2020.

[173] H. Niikura, M. Takada, N. Yasuda, R. H. Lupton, T. Sumi, S. More, T. Kurita, S. Sugiyama, A. More, M. Oguri, and M. Chiba, "Microlensing constraints on primordial black holes with subaru/HSC andromeda observations," *Nature Astronomy*, vol. 3, pp. 524–534, apr 2019.

[174] H. Niikura, M. Takada, S. Yokoyama, T. Sumi, and S. Masaki, "Constraints on Earth-mass primordial black holes from OGLE 5-year microlensing events," *Phys. Rev. D*, vol. 99, no. 8, p. 083503, 2019.

[175] J. Garcia-Bellido, M. Peloso, and C. Unal, "Gravitational Wave signatures of inflationary models from Primordial Black Hole Dark Matter," *JCAP*, vol. 09, p. 013, 2017.

[176] C. T. Byrnes, P. S. Cole, and S. P. Patil, "Steepest growth of the power spectrum and primordial black holes," *JCAP*, vol. 06, p. 028, 2019.

[177] G. A. Palma, S. Sypsas, and C. Zenteno, "Seeding primordial black holes in multifield inflation," *Phys. Rev. Lett.*, vol. 125, p. 121301, Sep 2020.

[178] J. Fumagalli, S. Renaux-Petel, J. W. Ronayne, and L. T. Witkowski, "Turning in the landscape: a new mechanism for generating Primordial Black Holes," 4 2020.

[179] M. Braglia, X. Chen, and D. K. Hazra, "Probing Primordial Features with the Stochastic Gravitational Wave Background," *JCAP*, vol. 03, p. 005, 2021.

[180] M. Braglia, D. K. Hazra, F. Finelli, G. F. Smoot, L. Sriramkumar, and A. A. Starobinsky, "Generating PBHs and small-scale GWs in two-field models of inflation," *JCAP*, vol. 08, p. 001, 2020.

[181] S. Young, "The primordial black hole formation criterion re-examined: Parametrisation, timing and the choice of window function," *Int. J. Mod. Phys. D*, vol. 29, no. 02, p. 2030002, 2019.

[182] K. Ando, K. Inomata, and M. Kawasaki, "Primordial black holes and uncertainties in the choice of the window function," *Phys. Rev. D*, vol. 97, p. 103528, May 2018.

[183] M. Raidal, V. Vaskonen, and H. Veermäe, "Gravitational Waves from Primordial Black Hole Mergers," *JCAP*, vol. 09, p. 037, 2017.

[184] A. L. Miller, S. Clesse, F. De Lillo, G. Bruno, A. Depasse, and A. Tanasijczuk, "Probing planetary-mass primordial black holes with continuous gravitational waves," *Phys. Dark Univ.*, vol. 32, p. 100836, 2021.

[185] V. De Luca, G. Franciolini, P. Pani, and A. Riotto, "The Minimum Testable Abundance of Primordial Black Holes at Future Gravitational-Wave Detectors," 6 2021.

[186] J. L. Zagorac, R. Easther, and N. Padmanabhan, "GUT-Scale Primordial Black Holes: Mergers and Gravitational Waves," *JCAP*, vol. 06, p. 052, 2019.

[187] O. Pujolas, V. Vaskonen, and H. Veermäe, "Prospects for probing gravitational waves from primordial black hole binaries," 7 2021.

[188] S. Mukherjee, M. S. P. Meinema, and J. Silk, "Prospects of discovering sub-solar primordial black holes using the stochastic gravitational wave background from third-generation detectors," 7 2021.

[189] K. Tomita, "Non-Linear Theory of Gravitational Instability in the Expanding Universe," *Progress of Theoretical Physics*, vol. 37, pp. 831–846, May 1967.

[190] K. Kohri and T. Terada, "Semianalytic calculation of gravitational wave spectrum nonlinearly induced from primordial curvature perturbations," *Phys. Rev. D*, vol. 97, no. 12, p. 123532, 2018.

[191] J. R. Espinosa, D. Racco, and A. Riotto, "A Cosmological Signature of the SM Higgs Instability: Gravitational Waves," *JCAP*, vol. 09, p. 012, 2018.

[192] E. Bugaev and P. Klimai, "Induced gravitational wave background and primordial black holes," *Physical Review D*, vol. 81, Jan 2010.

[193] R. Saito and J. Yokoyama, "Gravitational-wave constraints on the abundance of primordial black holes," *Progress of Theoretical Physics*, vol. 123, p. 867–886, May 2010.

[194] G. Domènech, "Induced gravitational waves in a general cosmological background," *Int. J. Mod. Phys. D*, vol. 29, no. 03, p. 2050028, 2020.

[195] C. Yuan, Z.-C. Chen, and Q.-G. Huang, "Log-dependent slope of scalar induced gravitational waves in the infrared regions," *Phys. Rev. D*, vol. 101, p. 043019, Feb 2020.

[196] R.-G. Cai, S. Pi, and M. Sasaki, "Universal infrared scaling of gravitational wave background spectra," *Phys. Rev. D*, vol. 102, no. 8, p. 083528, 2020.

[197] T. Papanikolaou, V. Vennin, and D. Langlois, "Gravitational waves from a universe filled with primordial black holes," *JCAP*, vol. 03, p. 053, 2021.

[198] K. Inomata, K. Kohri, T. Nakama, and T. Terada, "Gravitational Waves Induced by Scalar Perturbations during a Gradual Transition from an Early Matter Era to the Radiation Era," *JCAP*, vol. 10, p. 071, 2019.

[199] K. Jedamzik, M. Lemoine, and J. Martin, "Generation of gravitational waves during early structure formation between cosmic inflation and reheating," *JCAP*, vol. 04, p. 021, 2010.

[200] A. Kosowsky, A. Mack, and T. Kahniashvili, "Gravitational radiation from cosmological turbulence," *Phys. Rev. D*, vol. 66, p. 024030, 2002.

[201] G. Gogoberidze, T. Kahniashvili, and A. Kosowsky, "The Spectrum of Gravitational Radiation from Primordial Turbulence," *Phys. Rev. D*, vol. 76, p. 083002, 2007.

[202] E. Thrane and J. D. Romano, "Sensitivity curves for searches for gravitational-wave backgrounds," *Phys. Rev. D*, vol. 88, no. 12, p. 124032, 2013.

[203] K. Schmitz, "New Sensitivity Curves for Gravitational-Wave Signals from Cosmological Phase Transitions," *JHEP*, vol. 01, p. 097, 2021.

[204] J. Crowder and N. J. Cornish, "Beyond LISA: Exploring future gravitational wave missions," *Phys. Rev. D*, vol. 72, p. 083005, 2005.

[205] V. Corbin and N. J. Cornish, "Detecting the cosmic gravitational wave background with the big bang observer," *Class. Quant. Grav.*, vol. 23, pp. 2435–2446, 2006.

[206] G. M. Harry, P. Fritschel, D. A. Shaddock, W. Folkner, and E. S. Phinney, "Laser interferometry for the big bang observer," *Class. Quant. Grav.*, vol. 23, pp. 4887–4894, 2006. [Erratum: Class.Quant.Grav. 23, 7361 (2006)].

[207] K. Yagi and N. Seto, "Detector configuration of DECIGO/BBO and identification of cosmological neutron-star binaries," *Phys. Rev. D*, vol. 83, p. 044011, 2011. [Erratum: Phys.Rev.D 95, 109901 (2017)].

[208] M. Maggiore, C. V. D. Broeck, N. Bartolo, E. Belgacem, D. Bertacca, M. A. Bizouard, M. Branchesi, S. Clesse, S. Foffa, J. Garcí a-Bellido, S. Grimm, J. Harms, T. Hinderer, S. Matarrese, C. Palomba, M. Peloso, A. Ricciardone, and M. Sakellariadou, "Science case for the einstein telescope," *Journal of Cosmology and Astroparticle Physics*, vol. 2020, pp. 050–050, mar 2020.

[209] M. Punturo, M. Abernathy, F. Acernese, B. Allen, N. Andersson, K. Arun, F. Barone, B. Barr, M. Barsuglia, M. Beker, N. Beveridge, S. Birindelli, S. Bose, L. Bosi, S. Braccini, C. Bradaschia, T. Bulik, E. Calloni, G. Cella, E. Chassande Mottin, S. Chelkowski, A. Chincarini, J. Clark, E. Coccia, C. Colacino, J. Colas, A. Cumming, L. Cunningham, E. Cuoco, S. Danilishin, K. Danzmann, G. De Luca, R. De Salvo, T. Dent, R. De Rosa, L. Di Fiore, A. Di Virgilio, M. Doets, V. Fafone, P. Falferi, R. Flaminio, J. Franc, F. Frasconi, A. Freise, P. Fulda, J. Gair, G. Gemme, A. Gennai, A. Giazotto, K. Glampedakis, M. Granata, H. Grote, G. Guidi, G. Hammond, M. Hannam, J. Harms, D. Heinert, M. Hendry, I. Heng, E. Hennes, S. Hild, J. Hough, S. Husa, S. Huttner, G. Jones, F. Khalili, K. Kokeyama, K. Kokkotas, B. Krishnan, M. Lorenzini, H. Lück, E. Majorana, I. Mandel, V. Mandic, I. Martin, C. Michel, Y. Minenkov, N. Morgado, S. Mosca, B. Mours, H. Müller–Ebhardt, P. Murray, R. Nawrodt, J. Nelson, R. Oshaughnessy, C. D. Ott, C. Palomba, A. Paoli, G. Parguez, A. Pasqualetti, R. Passaquieti, D. Passuello, L. Pinard, R. Poggiani, P. Popolizio, M. Prato, P. Puppo, D. Rabeling, P. Rapagnani, J. Read, T. Regimbau, H. Rehbein, S. Reid, L. Rezzolla, F. Ricci, F. Richard, A. Rocchi,

S. Rowan, A. Rüdiger, B. Sassolas, B. Sathyaprakash, R. Schnabel, C. Schwarz, P. Seidel, A. Sintes, K. Somiya, F. Speirits, K. Strain, S. Strigin, P. Sutton, S. Tarabrin, A. Thüring, J. van den Brand, C. van Leewen, M. van Veggel, C. van den Broeck, A. Vecchio, J. Veitch, F. Vetrano, A. Vicere, S. Vyatchanin, B. Willke, G. Woan, P. Wolfango, and K. Yamamoto, "The Einstein Telescope: a third-generation gravitational wave observatory," *Classical and Quantum Gravity*, vol. 27, p. 194002, Oct. 2010.

[210] D. Reitze, R. X. Adhikari, S. Ballmer, B. Barish, L. Barsotti, G. Billingsley, D. A. Brown, Y. Chen, D. Coyne, R. Eisenstein, M. Evans, P. Fritschel, E. D. Hall, A. Lazzarini, G. Lovelace, J. Read, B. S. Sathyaprakash, D. Shoemaker, J. Smith, C. Torrie, S. Vitale, R. Weiss, C. Wipf, and M. Zucker, "Cosmic Explorer: The U.S. Contribution to Gravitational-Wave Astronomy beyond LIGO," *Bulletin of the AAS*, vol. 51, sep 30 2019. https://baas.aas.org/pub/2020n7i035.

[211] B. P. Abbott, R. Abbott, T. D. Abbott, M. R. Abernathy, K. Ackley, C. Adams, P. Addesso, R. X. Adhikari, V. B. Adya, C. Affeldt, N. Aggarwal, O. D. Aguiar, A. Ain, P. Ajith, B. Allen, P. A. Altin, S. B. Anderson, W. G. Anderson, K. Arai, M. C. Araya, C. C. Arceneaux, J. S. Areeda, K. G. Arun, G. Ashton, M. Ast, S. M. Aston, P. Aufmuth, C. Aulbert, S. Babak, P. T. Baker, S. W. Ballmer, J. C. Barayoga, S. E. Barclay, B. C. Barish, D. Barker, B. Barr, L. Barsotti, J. Bartlett, I. Bartos, R. Bassiri, J. C. Batch, C. Baune, A. S. Bell, B. K. Berger, G. Bergmann, C. P. L. Berry, J. Betzwieser, S. Bhagwat, R. Bhandare, I. A. Bilenko, G. Billingsley, J. Birch, R. Birney, S. Biscans, A. Bisht, C. Biwer, J. K. Blackburn, C. D. Blair, D. G. Blair, R. M. Blair, O. Bock, C. Bogan, A. Bohe, C. Bond, R. Bork, S. Bose, P. R. Brady, V. B. Braginsky, J. E. Brau, M. Brinkmann, P. Brockill, J. E. Broida, A. F. Brooks, D. A. Brown, D. D. Brown, N. M. Brown, S. Brunett, C. C. Buchanan, A. Buikema, A. Buonanno, R. L. Byer, M. Cabero, L. Cadonati, C. Cahillane, J. Calderón Bustillo, T. Callister, J. B. Camp, K. C. Cannon, J. Cao, C. D. Capano, S. Caride, S. Caudill, M. Cavaglià, C. B. Cepeda, S. J. Chamberlin, M. Chan, S. Chao, P. Charlton, B. D. Cheeseboro, H. Y. Chen, Y. Chen, C. Cheng, H. S. Cho, M. Cho, J. H. Chow, N. Christensen, Q. Chu, S. Chung, G. Ciani, F. Clara, J. A. Clark, C. G. Collette, L. Cominsky, J. Constancio, M., D. Cook, T. R. Corbitt, N. Cornish, A. Corsi, C. A. Costa, M. W. Coughlin, S. B. Coughlin, S. T. Countryman, P. Couvares, E. E. Cowan, D. M. Coward, M. J. Cowart, D. C. Coyne, R. Coyne, K. Craig, J. D. E. Creighton, J. Cripe, S. G. Crowder, A. Cumming, L. Cunningham, T. Dal Canton, S. L. Danilishin, K. Danzmann, N. S. Darman, A. Dasgupta, C. F. Da Silva Costa, I. Dave, G. S. Davies, E. J. Daw, S. De, D. DeBra, W. Del Pozzo, T. Denker, T. Dent, V. Dergachev, R. T. DeRosa, R. DeSalvo, R. C. Devine, S. Dhurandhar, M. C. Díaz, I. Di Palma, F. Donovan, K. L. Dooley, S. Doravari, R. Douglas, T. P. Downes, M. Drago, R. W. P. Drever, J. C. Driggers, S. E. Dwyer, T. B. Edo, M. C. Edwards, A. Effler, H. B. Eggenstein, P. Ehrens, J. Eichholz, S. S. Eikenberry, W. Engels, R. C. Essick, T. Etzel, M. Evans, T. M. Evans, R. Everett, M. Factourovich, H. Fair, S. Fairhurst, X. Fan, Q. Fang, B. Farr, W. M. Farr, M. Favata, M. Fays, H. Fehrmann, M. M. Fejer, E. Fenyvesi, E. C. Ferreira, R. P. Fisher, M. Fletcher, Z. Frei, A. Freise, R. Frey, P. Fritschel, V. V. Frolov, P. Fulda, M. Fyffe, H. A. G. Gabbard, J. R. Gair, S. G. Gaonkar, G. Gaur, N. Gehrels, P. Geng, J. George,

L. Gergely, A. Ghosh, A. Ghosh, J. A. Giaime, K. D. Giardina, K. Gill, A. Glaefke, E. Goetz, R. Goetz, L. Gondan, G. González, A. Gopakumar, N. A. Gordon, M. L. Gorodetsky, S. E. Gossan, C. Graef, P. B. Graff, A. Grant, S. Gras, C. Gray, A. C. Green, H. Grote, S. Grunewald, X. Guo, A. Gupta, M. K. Gupta, K. E. Gushwa, E. K. Gustafson, R. Gustafson, J. J. Hacker, B. R. Hall, E. D. Hall, G. Hammond, M. Haney, M. M. Hanke, J. Hanks, C. Hanna, M. D. Hannam, J. Hanson, T. Hardwick, G. M. Harry, I. W. Harry, M. J. Hart, M. T. Hartman, C. J. Haster, K. Haughian, M. C. Heintze, M. Hendry, I. S. Heng, J. Hennig, J. Henry, A. W. Heptonstall, M. Heurs, S. Hild, D. Hoak, K. Holt, D. E. Holz, P. Hopkins, J. Hough, E. A. Houston, E. J. Howell, Y. M. Hu, S. Huang, E. A. Huerta, B. Hughey, S. Husa, S. H. Huttner, T. Huynh-Dinh, N. Indik, D. R. Ingram, R. Inta, H. N. Isa, M. Isi, T. Isogai, B. R. Iyer, K. Izumi, H. Jang, K. Jani, S. Jawahar, L. Jian, F. Jiménez-Forteza, W. W. Johnson, D. I. Jones, R. Jones, L. Ju, K. Haris, C. V. Kalaghatgi, V. Kalogera, S. Kandhasamy, G. Kang, J. B. Kanner, S. J. Kapadia, S. Karki, K. S. Karvinen, M. Kasprzack, E. Katsavounidis, W. Katzman, S. Kaufer, T. Kaur, K. Kawabe, M. S. Kehl, D. Keitel, D. B. Kelley, W. Kells, R. Kennedy, J. S. Key, F. Y. Khalili, S. Khan, Z. Khan, E. A. Khazanov, N. Kijbunchoo, C.-W. Kim, C. Kim, J. Kim, K. Kim, N. Kim, W. Kim, Y. M. Kim, S. J. Kimbrell, E. J. King, P. J. King, J. S. Kissel, B. Klein, L. Kleybolte, S. Klimenko, S. M. Koehlenbeck, V. Kondrashov, A. Kontos, M. Korobko, W. Z. Korth, D. B. Kozak, V. Kringel, C. Krueger, G. Kuehn, P. Kumar, R. Kumar, L. Kuo, B. D. Lackey, M. Landry, J. Lange, B. Lantz, P. D. Lasky, M. Laxen, A. Lazzarini, S. Leavey, E. O. Lebigot, C. H. Lee, H. K. Lee, H. M. Lee, K. Lee, A. Lenon, J. R. Leong, Y. Levin, J. B. Lewis, T. G. F. Li, A. Libson, T. B. Littenberg, N. A. Lockerbie, A. L. Lombardi, L. T. London, J. E. Lord, M. Lormand, J. D. Lough, H. Lück, A. P. Lundgren, R. Lynch, Y. Ma, B. Machenschalk, M. MacInnis, D. M. Macleod, F. Magaña-Sandoval, L. Magaña Zertuche, R. M. Magee, V. Mandic, V. Mangano, G. L. Mansell, M. Manske, S. Márka, Z. Márka, A. S. Markosyan, E. Maros, I. W. Martin, D. V. Martynov, K. Mason, T. J. Massinger, M. Masso-Reid, F. Matichard, L. Matone, N. Mavalvala, N. Mazumder, R. McCarthy, D. E. McClelland, S. McCormick, S. C. McGuire, G. McIntyre, J. McIver, D. J. McManus, T. McRae, S. T. McWilliams, D. Meacher, G. D. Meadors, A. Melatos, G. Mendell, R. A. Mercer, E. L. Merilh, S. Meshkov, C. Messenger, C. Messick, P. M. Meyers, H. Miao, H. Middleton, E. E. Mikhailov, A. L. Miller, A. Miller, B. B. Miller, J. Miller, M. Millhouse, J. Ming, S. Mirshekari, C. Mishra, S. Mitra, V. P. Mitrofanov, G. Mitselmakher, R. Mittleman, S. R. P. Mohapatra, B. C. Moore, C. J. Moore, D. Moraru, G. Moreno, S. R. Morriss, K. Mossavi, C. M. Mow-Lowry, G. Mueller, A. W. Muir, A. Mukherjee, D. Mukherjee, S. Mukherjee, N. Mukund, A. Mullavey, J. Munch, D. J. Murphy, P. G. Murray, A. Mytidis, R. K. Nayak, K. Nedkova, T. J. N. Nelson, A. Neunzert, G. Newton, T. T. Nguyen, A. B. Nielsen, A. Nitz, D. Nolting, M. E. N. Normandin, L. K. Nuttall, J. Oberling, E. Ochsner, J. O'Dell, E. Oelker, G. H. Ogin, J. J. Oh, S. H. Oh, F. Ohme, M. Oliver, P. Oppermann, R. J. Oram, B. O'Reilly, R. O'Shaughnessy, D. J. Ottaway, H. Overmier, B. J. Owen, A. Pai, S. A. Pai, J. R. Palamos, O. Palashov, A. Pal-Singh, H. Pan, C. Pankow, F. Pannarale, B. C. Pant, M. A. Papa, H. R. Paris, W. Parker, D. Pascucci, Z. Patrick, B. L. Pearlstone, M. Pedraza, L. Pekowsky, A. Pele, S. Penn, A. Perreca, L. M. Perri, M. Phelps, V. Pierro, I. M. Pinto, M. Pitkin, M. Poe, A. Post, J. Powell, J. Prasad, V. Predoi, T. Prestegard, L. R. Price, M. Prijatelj, M. Principe, S. Priv-

itera, L. Prokhorov, O. Puncken, M. Pürrer, H. Qi, J. Qin, S. Qiu, V. Quetschke, E. A. Quintero, R. Quitzow-James, F. J. Raab, D. S. Rabeling, H. Radkins, P. Raffai, S. Raja, C. Rajan, M. Rakhmanov, V. Raymond, J. Read, C. M. Reed, S. Reid, D. H. Reitze, H. Rew, S. D. Reyes, K. Riles, M. Rizzo, N. A. Robertson, R. Robie, J. G. Rollins, V. J. Roma, G. Romanov, J. H. Romie, S. Rowan, A. Rüdiger, K. Ryan, S. Sachdev, T. Sadecki, L. Sadeghian, M. Sakellariadou, M. Saleem, F. Salemi, A. Samajdar, L. Sammut, E. J. Sanchez, V. Sandberg, B. Sandeen, J. R. Sanders, B. S. Sathyaprakash, P. R. Saulson, O. E. S. Sauter, R. L. Savage, A. Sawadsky, P. Schale, R. Schilling, J. Schmidt, P. Schmidt, R. Schnabel, R. M. S. Schofield, A. Schönbeck, E. Schreiber, D. Schuette, B. F. Schutz, J. Scott, S. M. Scott, D. Sellers, A. S. Sengupta, A. Sergeev, D. A. Shaddock, T. Shaffer, M. S. Shahriar, M. Shaltev, B. Shapiro, P. Shawhan, A. Sheperd, D. H. Shoemaker, D. M. Shoemaker, K. Siellez, X. Siemens, D. Sigg, A. D. Silva, A. Singer, L. P. Singer, A. Singh, R. Singh, A. M. Sintes, B. J. J. Slagmolen, J. R. Smith, N. D. Smith, R. J. E. Smith, E. J. Son, B. Sorazu, T. Souradeep, A. K. Srivastava, A. Staley, M. Steinke, J. Steinlechner, S. Steinlechner, D. Steinmeyer, B. C. Stephens, R. Stone, K. A. Strain, N. A. Strauss, S. Strigin, R. Sturani, A. L. Stuver, T. Z. Summerscales, L. Sun, S. Sunil, P. J. Sutton, M. J. Szczepańczyk, D. Talukder, D. B. Tanner, M. Tápai, S. P. Tarabrin, A. Taracchini, R. Taylor, T. Theeg, M. P. Thirugnanasambandam, E. G. Thomas, M. Thomas, P. Thomas, K. A. Thorne, E. Thrane, V. Tiwari, K. V. Tokmakov, K. Toland, C. Tomlinson, Z. Tornasi, C. V. Torres, C. I. Torrie, D. Töyrä, G. Traylor, D. Trifirò, M. Tse, D. Tuyenbayev, D. Ugolini, C. S. Unnikrishnan, A. L. Urban, S. A. Usman, H. Vahlbruch, G. Vajente, G. Valdes, D. C. Vander-Hyde, A. A. van Veggel, S. Vass, R. Vaulin, A. Vecchio, J. Veitch, P. J. Veitch, K. Venkateswara, S. Vinciguerra, D. J. Vine, S. Vitale, T. Vo, C. Vorvick, D. V. Voss, W. D. Vousden, S. P. Vyatchanin, A. R. Wade, L. E. Wade, M. Wade, M. Walker, L. Wallace, S. Walsh, H. Wang, M. Wang, X. Wang, Y. Wang, R. L. Ward, J. Warner, B. Weaver, M. Weinert, A. J. Weinstein, R. Weiss, L. Wen, P. Weßels, T. Westphal, K. Wette, J. T. Whelan, B. F. Whiting, R. D. Williams, A. R. Williamson, J. L. Willis, B. Willke, M. H. Wimmer, W. Winkler, C. C. Wipf, H. Wittel, G. Woan, J. Woehler, J. Worden, J. L. Wright, D. S. Wu, G. Wu, J. Yablon, W. Yam, H. Yamamoto, C. C. Yancey, H. Yu, M. Zanolin, M. Zevin, L. Zhang, M. Zhang, Y. Zhang, C. Zhao, M. Zhou, Z. Zhou, X. J. Zhu, M. E. Zucker, S. E. Zuraw, J. Zweizig, (LIGO Scientific Collaboration, and J. Harms, "Exploring the sensitivity of next generation gravitational wave detectors," *Classical and Quantum Gravity*, vol. 34, p. 044001, Feb. 2017.

[212] P. Amaro-Seoane, H. Audley, S. Babak, J. Baker, E. Barausse, P. Bender, E. Berti, P. Binetruy, M. Born, D. Bortoluzzi, J. Camp, C. Caprini, V. Cardoso, M. Colpi, J. Conklin, N. Cornish, C. Cutler, K. Danzmann, R. Dolesi, L. Ferraioli, V. Ferroni, E. Fitzsimons, J. Gair, L. G. Bote, D. Giardini, F. Gibert, C. Grimani, H. Halloin, G. Heinzel, T. Hertog, M. Hewitson, K. Holley-Bockelmann, D. Hollington, M. Hueller, H. Inchauspe, P. Jetzer, N. Karnesis, C. Killow, A. Klein, B. Klipstein, N. Korsakova, S. L. Larson, J. Livas, I. Lloro, N. Man, D. Mance, J. Martino, I. Mateos, K. McKenzie, S. T. McWilliams, C. Miller, G. Mueller, G. Nardini, G. Nelemans, M. Nofrarias, A. Petiteau, P. Pivato, E. Plagnol, E. Porter, J. Reiche, D. Robertson, N. Robertson, E. Rossi, G. Russano, B. Schutz, A. Sesana, D. Shoemaker, J. Slutsky, C. F. Sopuerta, T. Sumner, N. Tamanini,

I. Thorpe, M. Troebs, M. Vallisneri, A. Vecchio, D. Vetrugno, S. Vitale, M. Volonteri, G. Wanner, H. Ward, P. Wass, W. Weber, J. Ziemer, and P. Zweifel, "Laser interferometer space antenna," 2017.

[213] J. Baker, J. Bellovary, P. L. Bender, E. Berti, R. Caldwell, J. Camp, J. W. Conklin, N. Cornish, C. Cutler, R. DeRosa, M. Eracleous, E. C. Ferrara, S. Francis, M. Hewitson, K. Holley-Bockelmann, A. Hornschemeier, C. Hogan, B. Kamai, B. J. Kelly, J. S. Key, S. L. Larson, J. Livas, S. Manthripragada, K. McKenzie, S. T. McWilliams, G. Mueller, P. Natarajan, K. Numata, N. Rioux, S. R. Sankar, J. Schnittman, D. Shoemaker, D. Shoemaker, J. Slutsky, R. Spero, R. Stebbins, I. Thorpe, M. Vallisneri, B. Ware, P. Wass, A. Yu, and J. Ziemer, "The laser interferometer space antenna: Unveiling the millihertz gravitational wave sky," 2019.

[214] J. Luo, L.-S. Chen, H.-Z. Duan, Y.-G. Gong, S. Hu, J. Ji, Q. Liu, J. Mei, V. Milyukov, M. Sazhin, C.-G. Shao, V. T. Toth, H.-B. Tu, Y. Wang, Y. Wang, H.-C. Yeh, M.-S. Zhan, Y. Zhang, V. Zharov, and Z.-B. Zhou, "TianQin: a space-borne gravitational wave detector," *Classical and Quantum Gravity*, vol. 33, p. 035010, jan 2016.

[215] Z.-C. Liang, Y.-M. Hu, Y. Jiang, J. Cheng, J.-d. Zhang, and J. Mei, "Science with the TianQin Observatory: Preliminary Results on Stochastic Gravitational-Wave Background," 7 2021.

[216] W.-H. Ruan, Z.-K. Guo, R.-G. Cai, and Y.-Z. Zhang, "Taiji program: Gravitational-wave sources," *Int. J. Mod. Phys. A*, vol. 35, no. 17, p. 2050075, 2020.

[217] N. Seto, S. Kawamura, and T. Nakamura, "Possibility of direct measurement of the acceleration of the universe using 0.1-Hz band laser interferometer gravitational wave antenna in space," *Phys. Rev. Lett.*, vol. 87, p. 221103, 2001.

[218] S. Kawamura, M. Ando, N. Seto, S. Sato, T. Nakamura, K. Tsubono, N. Kanda, T. Tanaka, J. Yokoyama, I. Funaki, K. Numata, K. Ioka, T. Takashima, K. Agatsuma, T. Akutsu, K.-s. Aoyanagi, K. Arai, A. Araya, H. Asada, Y. Aso, D. Chen, T. Chiba, T. Ebisuzaki, Y. Ejiri, M. Enoki, Y. Eriguchi, M.-K. Fujimoto, R. Fujita, M. Fukushima, T. Futamase, T. Harada, T. Hashimoto, K. Hayama, W. Hikida, Y. Himemoto, H. Hirabayashi, T. Hiramatsu, F.-L. Hong, H. Horisawa, M. Hosokawa, K. Ichiki, T. Ikegami, K. T. Inoue, K. Ishidoshiro, H. Ishihara, T. Ishikawa, H. Ishizaki, H. Ito, Y. Itoh, K. Izumi, I. Kawano, N. Kawashima, F. Kawazoe, N. Kishimoto, K. Kiuchi, S. Kobayashi, K. Kohri, H. Koizumi, Y. Kojima, K. Kokeyama, W. Kokuyama, K. Kotake, Y. Kozai, H. Kunimori, H. Kuninaka, K. Kuroda, S. Kuroyanagi, K.-i. Maeda, H. Matsuhara, N. Matsumoto, Y. Michimura, O. Miyakawa, U. Miyamoto, S. Miyoki, M. Y. Morimoto, T. Morisawa, S. Moriwaki, S. Mukohyama, M. Musha, S. Nagano, I. Naito, K. Nakamura, H. Nakano, K. Nakao, S. Nakasuka, Y. Nakayama, K. Nakazawa, E. Nishida, K. Nishiyama, A. Nishizawa, Y. Niwa, T. Noumi, Y. Obuchi, M. Ohashi, N. Ohishi, M. Ohkawa, K. Okada, N. Okada, K. Oohara, N. Sago, M. Saijo, R. Saito, M. Sakagami, S.-i. Sakai, S. Sakata, M. Sasaki, T. Sato, M. Shibata, H. Shinkai, A. Shoda, K. Somiya, H. Sotani, N. Sugiyama, Y. Suwa,

R. Suzuki, H. Tagoshi, F. Takahashi, K. Takahashi, K. Takahashi, R. Takahashi, R. Takahashi, T. Takahashi, H. Takahashi, T. Akiteru, T. Takano, N. Tanaka, K. Taniguchi, A. Taruya, H. Tashiro, Y. Torii, M. Toyoshima, S. Tsujikawa, Y. Tsunesada, A. Ueda, K.-i. Ueda, M. Utashima, Y. Wakabayashi, K. Yagi, H. Yamakawa, K. Yamamoto, T. Yamazaki, C.-M. Yoo, S. Yoshida, T. Yoshino, and K.-X. Sun, "The Japanese space gravitational wave antenna: DECIGO," *Classical and Quantum Gravity*, vol. 28, p. 094011, May 2011.

[219] L. Badurina, O. Buchmueller, J. Ellis, M. Lewicki, C. McCabe, and V. Vaskonen, "Prospective Sensitivities of Atom Interferometers to Gravitational Waves and Ultralight Dark Matter," 8 2021.

[220] L. Badurina, E. Bentine, D. Blas, K. Bongs, D. Bortoletto, T. Bowcock, K. Bridges, W. Bowden, O. Buchmueller, C. Burrage, J. Coleman, G. Elertas, J. Ellis, C. Foot, V. Gibson, M. Haehnelt, T. Harte, S. Hedges, R. Hobson, M. Holynski, T. Jones, M. Langlois, S. Lellouch, M. Lewicki, R. Maiolino, P. Majewski, S. Malik, J. March-Russell, C. McCabe, D. Newbold, B. Sauer, U. Schneider, I. Shipsey, Y. Singh, M. Uchida, T. Valenzuela, M. van der Grinten, V. Vaskonen, J. Vossebeld, D. Weatherill, and I. Wilmut, "AION: an atom interferometer observatory and network," *Journal of Cosmology and Astroparticle Physics*, vol. 2020, pp. 011–011, may 2020.

[221] Y. A. El-Neaj, C. Alpigiani, S. Amairi-Pyka, H. Araújo, A. Balaž, A. Bassi, L. Bathe-Peters, B. Battelier, A. Belić, E. Bentine, J. Bernabeu, A. Bertoldi, R. Bingham, D. Blas, V. Bolpasi, K. Bongs, S. Bose, P. Bouyer, T. Bowcock, W. Bowden, O. Buchmueller, C. Burrage, X. Calmet, B. Canuel, L.-I. Caramete, A. Carroll, G. Cella, V. Charmandaris, S. Chattopadhyay, X. Chen, M. L. Chiofalo, J. Coleman, J. Cotter, Y. Cui, A. Derevianko, A. D. Roeck, G. S. Djordjevic, P. Dornan, M. Doser, I. Drougkakis, J. Dunningham, I. Dutan, S. Easo, G. Elertas, J. Ellis, M. E. Sawy, F. Fassi, D. Felea, C.-H. Feng, R. Flack, C. Foot, I. Fuentes, N. Gaaloul, A. Gauguet, R. Geiger, V. Gibson, G. Giudice, J. Goldwin, O. Grachov, P. W. Graham, D. Grasso, M. van der Grinten, M. Gündogan, M. G. Haehnelt, T. Harte, A. Hees, R. Hobson, J. Hogan, B. Holst, M. Holynski, M. Kasevich, B. J. Kavanagh, W. von Klitzing, T. Kovachy, B. Krikler, M. Krutzik, M. Lewicki, Y.-H. Lien, M. Liu, G. G. Luciano, A. Magnon, M. A. Mahmoud, S. Malik, C. McCabe, J. Mitchell, J. Pahl, D. Pal, S. Pandey, D. Papazoglou, M. Paternostro, B. Penning, A. Peters, M. Prevedelli, V. Puthiya-Veettil, J. Quenby, E. Rasel, S. Ravenhall, J. Ringwood, A. Roura, D. Sabulsky, M. Sameed, B. Sauer, S. A. Schäffer, S. Schiller, V. Schkolnik, D. Schlippert, C. Schubert, H. R. Sfar, A. Shayeghi, I. Shipsey, C. Signorini, Y. Singh, M. Soares-Santos, F. Sorrentino, T. Sumner, K. Tassis, S. Tentindo, G. M. Tino, J. N. Tinsley, J. Unwin, T. Valenzuela, G. Vasilakis, V. Vaskonen, C. Vogt, A. Webber-Date, A. Wenzlawski, P. Windpassinger, M. Woltmann, E. Yazgan, M.-S. Zhan, X. Zou, and J. Zupan, "AEDGE: Atomic experiment for dark matter and gravity exploration in space," *EPJ Quantum Technology*, vol. 7, mar 2020.

[222] K. Inomata and T. Nakama, "Gravitational waves induced by scalar perturbations as probes of the small-scale primordial spectrum," *Phys. Rev. D*, vol. 99, no. 4, p. 043511, 2019.